METHODOLOGIES FOR ENHANCING ULTRASONIC NDE OF COARSE-GRAINED MATERIALS

by

Bo Xiao

Thesis submitted to the University of Strathclyde for

the degree of Doctor of Philosophy

Department of Electronic and Electrical Engineering

University of Strathclyde

Glasgow G1 1XW

May 2016

Abstract

Ultrasonic non-destructive evaluation (NDE) is employed extensively across many industries to ensure the integrity of safety critical infrastructures. Where the structure is formed of coarse-grained materials, such as austenitic steel and Inconel, ultrasonic NDE presents a significant challenge arising from their heterogeneous structures and elastic anisotropy. The Thesis addresses two longstanding problems encountered in ultrasonic NDE of coarse-grained materials: phase aberration and backscattering noise.

Phase aberration denotes that the wavefronts from elements of a phased array undergo phases shifts. A phase aberration correction approach based on microstructural characterisation and finite element modelling is evaluated in the third chapter. The validation of an emerging microstructural characterisation technique is presented. This embodies two approaches to simplifying measured crystallographic orientation data to construct finite element models, a reduction of computational overhead by 20 times is achieved whilst maintaining model fidelity.

The split-spectrum processing (SSP) technique has been widely used to suppress backscattering noise by employing a bank of bandpass filters followed by a combination operator. However, conventional combination algorithms are either ineffective or sensitive to the variations of material characteristics. The use of two artificial neural network (ANN) techniques and the best linear unbiased estimator (BLUE), as the combination algorithms of SSP is investigated in the fourth and fifth chapters, in order to improve its robustness and performance. The performance of two ANN techniques in terms of effectiveness in improving SNR and computational efficiency are compared to instruct the selection between the two techniques in various cases. The BLUE algorithm can improve image contrast by an average of 80% for combining three sub-band images. Another algorithm based on the statistical analysis of frequency components is also proposed in the sixth chapter to reduce speckle level. This algorithm is observed to reduce speckle level by an average of 15 dB.

Acknowledgements

I would like to express my great appreciation to my two supervisors, Dr Richard O'Leary and Prof Anthony Gachagan. Thanks for their supervision and guidance in the last four years. Richard offered me invaluable suggestions to my academic writing and was patient to me when I lost myself during the course of my work. Anthony enthusiastically supplied me inspirations and encouragement.

I would also like to thank Rui Gongzhang, Timothy Lardner and Dr Jerzy Dziewierz with whom I worked closely. Thanks to Rui for providing a lot of great ideas and suggestions to my work. He was always there to help when I was stuck in problems. Thanks to Timothy and Jerzy for their assistance in acquiring experimental data in my early Ph.D.

I am grateful to Dr Wenqi Li and Dr Timothy Burnett for their support to my work.

I would like to thank Rolls Royce, Shell, National Nuclear Laboratories, AMEC, and Weidlinger Associates for financial and technical support. E. ON Technologies, Siemens AG and Doosan Babcock are also acknowledged for providing test samples.

Special thanks to my parents, Caiting Xiao and Hongxia Zhang, for their endless love and the sacrifice that they made for me. A huge thank you to my girlfriend, Xiaofen Song, who unconditionally supported me during the several critical months of my Thesis.

Table of Contents

List of Figures

List of Tables

CHAPTER 1. Introduction

This chapter firstly gives a general overview of NDE techniques with emphasis on the development and applications of ultrasound inspection. Subsequently, the problems encountered in ultrasonic inspection of coarse-grained materials are described. Finally, Thesis outline and contribution to knowledge are introduced along with the publications arising from the Thesis.

1.1 Non-destructive evaluation

NDE consists of a broad range of techniques aiming to detect and characterise flaws in materials, components or structures [1, 2]. The essential feature of NDE is that the test process produces no physical damage to the objects. The term NDE is often exchangeable with non-destructive testing (NDT). NDE procedures are widely used in the quality control of manufactured products, in-service inspections and also condition monitoring of operating components.

1.1.1 Background of NDE

NDE history dates back to more than 150 years ago. One of the earliest NDE methods was called as "Oil and Whiting" for crack detection in the railway industry [3]. Inspectors immersed a cleaned object into diluted oil and then wiped out the oil on the object surface. The object surface was then coated with a white chalk. The residual oil that had penetrated the surface-breaking cracks caused discoloration of the white chalk thus allowing such cracks to be more readily identified. This method is considered as a precursor to modern liquid penetrant testing (PT) as they share some principles, such

as using "capillary action" to allow oil/liquid to enter the surface breaking cracks. In the year of 1895, Wilhelm Rontgen discovered "an unknown kind of radiation" which now is known as X-rays [4]. In the subsequent few decades, scientists developed radiographic testing (RT) and imaging techniques operating with X-ray beams [5].

Modern NDE began in the 1920s from when inspectors started to gain the awareness of the presence of various inspection methods. A milestone in the NDE development arrived during World War II. That is, the establishment of the American Industrial Radium and X-ray Society (now named as the American Society for Non-destructive Testing) indicated that NDE became as an independent discipline.

As some NDE techniques have greatly improved over time, the purpose of NDE has extended from the basic flaw detection in in-service components to the quality control of original equipment manufacturer (OEM) products. One such example is that NDE techniques can be employed to evaluate the conformance of as-manufactured composites to their design specifications which opens the opportunity to use both lighter and more cost-effective OEM composites in the aerospace industry [2, 6]. The evolution of NDE techniques is also manifested in that they are required not only to detect flaws but also to characterise flaws, e.g., obtain quantitative information of the flaws such as size and orientation. With the knowledge of the characteristics of a fatigue crack flaw and load cycles, fracture mechanics based models can be applied to predict the growth rate of the crack and the remaining service life of the fatigue component [7].

Contemporary NDE techniques are used in a diverse range of fields, including nuclear power generation, civil engineering, aerospace, petrochemical industry, manufacturing and so on [8].

1.1.2 NDE techniques

Contemporary NDE techniques encompass a diverse array of techniques, including PT, RT, eddy current testing (ECT), magnetic particle inspection (MPI), ultrasonic testing (UT) and so on. The working principle of PT has been described. The working principle, as well as the advantages and disadvantages of ECT, MPI, RT, UT, are introduced as below.

1.1.2.1   ECT

In standard ECT, a specimen is placed near to a circular coil. Eddy current is induced in the specimen if an alternating current is passed through the coil. The presence of defects can be identified from the change of magnitude and phase of the eddy current [9]. ECT can be performed without contacting specimen surface so it is particularly advantageous in inspecting products with corrosion conditions or at elevated temperature environment. However, ECT is only applicable to electrically conductive materials and can only detect surface-breaking and subsurface flaws due to limited penetration of the eddy current.

1.1.2.2   MPI

A specimen is magnetised as the first step of MPI. A surface-breaking defect will create a local flux leakage field. The iron particles will be attracted by and so cluster at the flux leakage field, hence forming visible flaw indications [10]. MPI can provide immediate indications of surface-breaking imperfections of the specimen with less expense. However, it is restricted to ferromagnetic materials and is unable to inspect some commonly used materials such as austenitic stainless steel. Furthermore, it can only detect surface-breaking defects.

1.1.2.3   RT

In RT, a specimen is sandwiched between a Gamma or X-ray radiation source and a detection film. The radiated ray penetrates through the specimen and is captured by the detection film. The changes in atomic number or density of the specimen result in different intensity in the detection film, from which the defects can be identified [5]. RT can detect both surface-breaking and internal flaws. Disadvantages of RT include the hazard of the radiation to inspectors and the high cost arising from the necessary plant downtime. Traditional RT is unable to provide information on defect depth. X-ray computed tomography gives an indication of defect depth at a premium both regarding cost and time.

1.1.2.4   UT

In UT, the transmission and reception of ultrasound are typically afforded by transducers made of piezoelectric materials coupled to the surface of the specimen. The

transmitter emits a short ultrasound pulse with centre frequencies usually ranging from 0.1 MHz to 25 MHz, into a specimen. If a flaw is present within the propagation path of the pulse in the specimen, some of the sound energy will be reflected and/or diffracted by the flaw and then captured by the receiver. In many cases, coupling media including gels, various oils and water may be applied between the transducer and specimen surface to enhance the ultrasound energy transfer efficiency. UT is often more cost-effective than RT and can be performed in-situ using portable devices. Also, UT has no radiation hazard and typically needs access to only one side of the specimen. However, the coarse grains found in certain materials, e.g., concrete, austenitic steels, result in an acoustically noisy propagation channel which may mask flaws and cause spurious indications [11].

1.1.3 Development of UT

Ultrasound pulse-echo is a fundamental and widely used UT mode. In a pulse-echo system, a single-element ultrasonic transducer emits an ultrasound pulse and receives the sound wave reflected back from discontinuities within the specimen. The received signals are displayed in the form of the amplitude of the received echo as a function of time-of-flight (TOF). This is the A-scan presentation. The envelope of an A-scan is extracted in some cases which is usually referred to the envelope-detected A-scan whilst the original A-scan is referred to as the radio-frequency (RF) A-scan. Fig. 1.1 shows the presentations of an RF A-scan and an envelope-detected A-scan.

The position and size of a defect can be estimated from the TOF and the amplitude of the received echo in the A-scan, respectively. However, defect sizing based on the received amplitude is often unreliable since the amplitude is strongly dependent on the orientation of the defect relative to the ultrasound beam direction. The time-of-flight diffraction (TOFD) technique uses the TOF of an ultrasonic pulse instead of signal amplitude to determine the size and position of a defect [12]. TOFD systems employ the pitch-catch UT mode. That is, as shown in Fig. 1.2, a pair of single-element transducers are placed on opposite sides of the region under inspection and on the same side of the specimen - one is used as the transmitter and the other one is used as the receiver. For an undamaged specimen, the receiver will receive two signals: one is the

reflection of the backwall of the specimen and the other is the lateral wave propagating along the surface of the specimen. If a defect is present in the specimen, the top and bottom tips of the defect will diffract the ultrasound beam and contribute two additional signals that will also be detected at the receiver. Through simple trigonometric calculations, the depths of the two defect tips can be calculated using the measured TOFs of the ultrasonic pulse, the size of the defect is, therefore, determined [12].
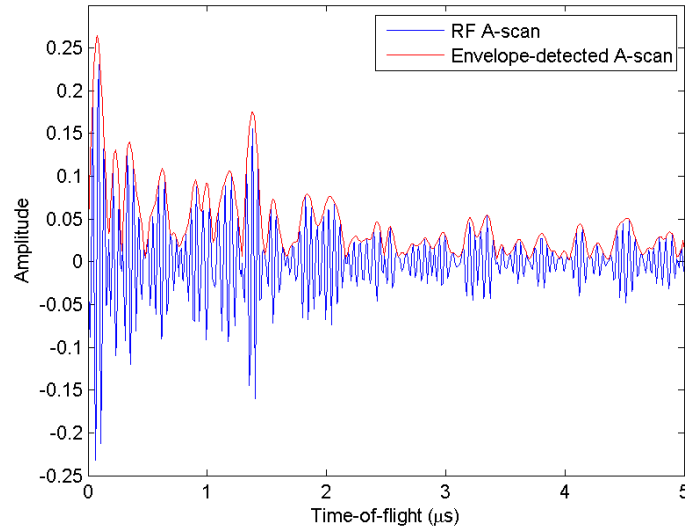
Fig. 1.1: Presentations of an RF A-scan and an envelope-detected A-scan
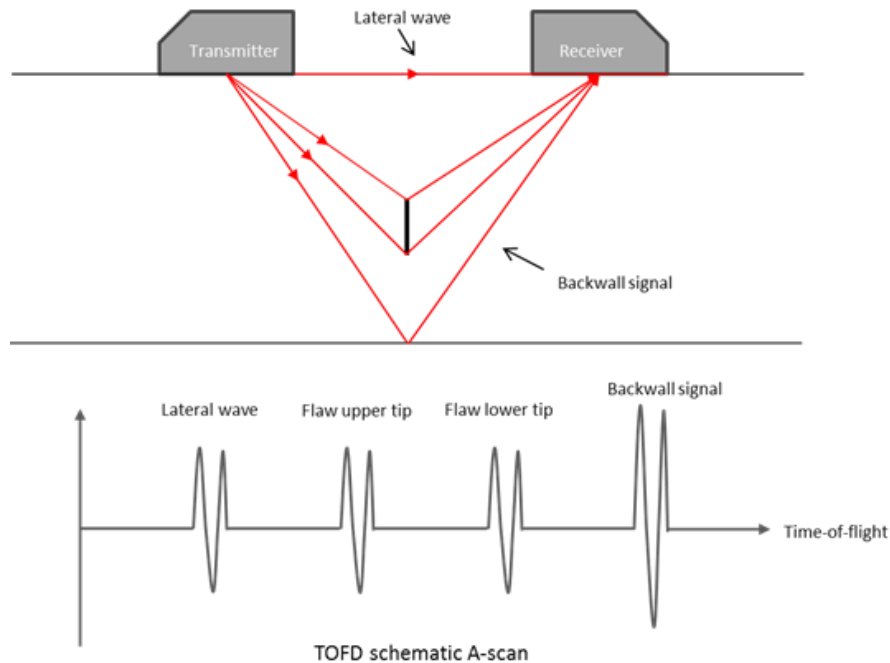
Fig. 1.2: Schematic diagram of time-of-flight diffraction technique

5

Interpretation of A-scan traces requires one to have a great deal of experience in analysing ultrasonic data. B-scan imaging which displays a cross-sectional profile through one vertical slice of the specimen is easier to interpret. To produce a B-scan image, the sound beam is scanned along the surface of the specimen and an A-scan trace is acquired at each scanning location, then beamforming is applied to construct a B-scan image from the acquired A-scan traces. B-scan imaging requires a conventional monolithic probe (i.e., a single-element transducer) to move mechanically along the surface of the specimen. Alternatively, a phased array probe can be employed to electronically scan the sound beam along the surface of the specimen removing the requirement for mechanical scanning. Therefore, the use of phased array probes can greatly speed up the inspection of a component [13].

Commercial phased array probes firstly appeared in the early 1970s for medical diagnostic imaging [14]. A phased array probe consists of a number of small elements each of which is individually addressable. Except faster inspection speed, another key advantage of phased array probes over monolithic probes is that they provide higher flexibility in the inspection. Particularly, they can steer and focus ultrasound beams via electronic control of the element excitation scheme, a schematic of such an excitation scheme is depicted in Fig. 1.3. Beam steering allows for specimens to be inspected at a range of angles without moving the probe. This can greatly facilitate the inspection of materials with complex geometry and also significantly increases flaw detectability [13]. As shown in Fig. 1.3, a phased array can steer and focus the ultrasound beams at a location beyond the edge of the array, greatly increasing inspection coverage. Moreover, beam focusing significantly enhance the signal-to-noise ratio (SNR) and improve the spatial resolution at the focal point. The disadvantages of phased array probes over monolithic probes include a higher capital cost of the probes and the associated drive and reception electronics.
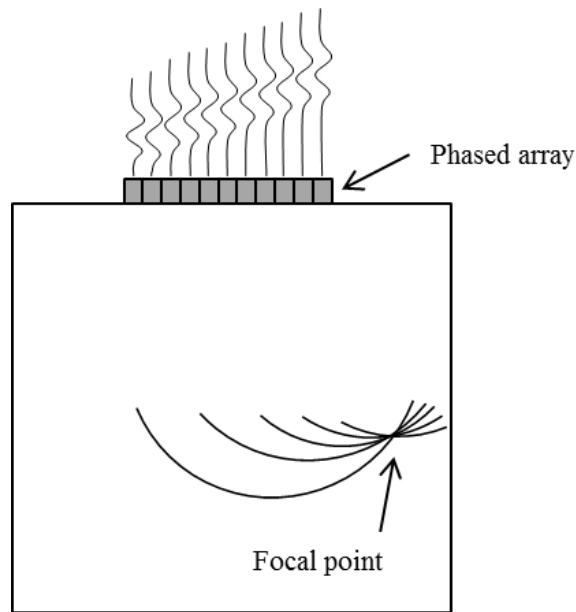
Fig. 1.3: Schematic plot of beam steering and focusing through electronic control of excitation scheme

In UT, a coupling liquid such as water may be applied to couple the sound field in the component under inspection with reduced losses. However, the coupling liquid can flow into the component such as in carbon-fibre–reinforced polymer (CFRP) used in the aerospace industry and mask the presence of flaws like delamination. Moreover, some components such as honeycomb structures cannot be wet. Air-coupled method can be applied to inspect such components [15]. Air-coupled inspection typically employs the through-transmission UT mode where a pair of transducers are placed on the opposite sides of the component - one is used as the transmitter and the other one is used as the receiver. Due to the huge acoustic impedance mismatch between air and any solid component, transducers and electronics have to design to maximise transmission efficiency and reception sensitivity.

In order to automate ultrasonic inspection in the nuclear industry, the two complimentary software packages named Micropulse Inspection Processing Software (MIPS) and Graphical Ultrasonic Image Data Evaluation (GUIDE) have been developed over 30 years for automatically acquiring and analysing data, respectively [16, 17]. Being used by many companies such as EDF Energy (London, UK), Doosan Babcock (Renfrew, UK), MIPS and GUIDE have been accepted as the UK Nuclear Industry standard for the inspection of safety critical component.

7

1.2   Problem definition

1.2.1   Coarse-grained materials

Coarse-grained microstructures can form in many metalworking processes such as casting and welding. In a common process of metal casting, molten metal is poured into a mould with a designated shape and size and then cooled down to a solid state. When the solidification commences, atoms of the molten metal start to bond together at random nucleation sites and begin to form crystals. For each individual crystal, the constitutive atoms are typically distributed in a repeating pattern in three-dimensional space. As the solidification proceeds, the crystals grow separately in size until adjacent crystals come into contact with each other. Due to the randomness of the locations of the nucleation sites and the growth direction of the crystals, the crystals are formed in various size and orientation, forming polycrystalline materials [18]. A crystal is usually referred to as a grain in engineering materials and the interface between adjacent grains is named a grain boundary.

The average grain size of a polycrystalline material is dependent on the number of nucleation sites which is a function of the cooling rate and the presence of impurities [19]. Slow cooling generally allows the grains to grow larger (a coarse-grained microstructure) whilst rapid cooling generally results in smaller grains (a fine-grained microstructure). Alloying elements which can induce nucleation are often added to increase the number of grains thus to refine the grain size [19]. Fine-grained materials have more grains, therefore, have a larger area of grain boundaries than the coarse-grained counterparts. Since grain boundaries are the barriers to the movement of dislocations, coarse-grained materials typically exhibit lower hardness, ductility and strength than the fine-grained counterparts.

Fine- and coarse-grained materials exhibit different elastic properties. Each grain itself is typically elastically anisotropic. For a fine-grained material, since there are a large number of randomly oriented grains in the medium, at the microscopic scale the grains can exhibit anisotropy. However, at the macroscopic scale, grain anisotropy tends to cancel out and the overall material often behaves as elastically isotropic. In contrast, for

a coarse-grained material, the anisotropic properties of the grains are unable to cancel each other out so that the material is elastically anisotropic.

1.2.2 UT of coarse-grained materials

Coarse-grained materials such as austenitic steel and concrete are extensively used to form parts of safety critical infrastructures across many industries so that it is absolutely vital to ensure their integrity. However, UT of such materials suffers from various undesirable effects due to their anisotropic and inhomogeneous microstructures – examples include the local variations in the velocity of the propagating wavefront, beam skewing, and beam scattering and so on. These undesirable effects result in three major problems: phase aberration, backscattering noise and attenuation. The three problems lead to UT of coarse-grained materials extremely challenging.

1.2.2.1 Phase aberration

The problem of phase aberration occurs when attempting to focus the ultrasound pulses emitted by different elements of a phased array. As shown in Fig. 1.3, to focus the beam at a point of interest, a bank of time delays is applied to array elements to ensure that the wavefront of each element arrives at the focal point in phase and at the appropriate point in time. The bank of time delays is typically calculated based on the difference in geometric path length of the array elements to the focal point for, an often assumed, constant ultrasound velocity in the direction of propagation. This bank of time delays is often referred to as an isotropic focal law.

However, for the coarse-grained materials where elastic anisotropy can be observed, the spatial fluctuation in the elastic properties of the material as well as the effect of beam skewing and distortion arising from the interaction of the wavefront with grain boundaries, give rise to concomitant variations in the velocity of the propagating wavefront. The resultant effect is that the sound velocity exhibits a degree of direction dependence. Therefore, the wavefront propagating from each element of the array arrives at the desired focal point at a different time than anticipated by the isotropic focal law. As a result, the wavefront undergoes a phase shift that degrades constructive interference required for focusing. This problem in array imaging is termed phase

aberration [20]. The phase aberration problem is particularly prominent for the coarse-grained materials with preferred crystallographic orientations due to the large variability of the sound velocity in different directions. Such materials include austenitic steel welds, which are characterised by elongated columnar-grained microstructures. This will be discussed in more details in Section 3.4.2.2.

Phase aberration leads to the shifting and widening, or more severely, the fragmentation of the mainlobe, which is the acoustic pressure in the direction of the programmed angle. Phase aberration also leads to the increase of the sidelobe, which is produced by the leakage of acoustic pressure from array elements at different angles from the mainlobe. In UT imaging, the distorted mainlobe and increased sidelobe would give rise to inaccuracy in defect positioning and sizing. Moreover, phase aberration reduces the mainlobe amplitude, indicating the reduced sensitivity of the UT imaging system to small defects.

1.2.2.2   Backscattering noise

UT typically suffers to some extent from noise interference in the acquisition process. There are two contributing factors to noise: incoherent noise and coherent noise. Incoherent noise typically arises in the drive and reception electronics and is usually caused by thermal effects on electronic circuitry. It is time-variant, and from a statistical perspective, it follows a Gaussian distribution and is zero mean. Therefore, it can be removed at the acquisition stage by applying time domain signal averaging. In most cases, the incoherent noise is considered to be negligible in comparison to coherent noise.

Coherent noise arises since numerous grain boundaries of coarse-grained materials diffusively scatter the sound wave as the wave travels through the medium. The backscattered waves interfere with each other and form noisy signals in an A-scan trace. These noisy signals are usually referred to as grain noise. Grain noise is time-invariant so that it cannot be eliminated by applying time domain averaging. Moreover, since the flaw echoes and grain noise occupy similar portions of the frequency band of the transduction system, conventional bandpass filtering techniques also fail to suppress grain noise without affecting the information comprising the flaw echoes [21]. When beamforming techniques are applied to a set of A-scan traces to construct a B-scan

image, grain noise in the A-scan traces aggregates to form speckle pattern on the B-scan image [11, 22].

The grain noise and speckle pattern can significantly decrease SNR and defect detectability, indicating the reduced probability of detection (POD). Furthermore, they can give rise to spurious indications of flaws and hence the increased probability of false alarm (PFA), which can result in unnecessary plant downtime and repairs. Generally, the amplitude of backscattering noise is proportional to the fourth power of inspection frequency and the cubic power of grain diameter [23]. Using lower frequency to inspect can reduce the amplitude of backscattering noise, but at the price of degraded spatial resolution.

1.2.2.3   Acoustic attenuation

The problem of attenuation is a combination result of the grain scattering and beam absorption. Grain scattering denotes that the sound wavefront is redirected and beam absorption refers to that ultrasound energy is converted to other forms of energy, such as thermal energy. Attenuation detrimentally decreases the sound penetration depth so that the inspection range is reduced. Using lower frequency to inspect can decrease attenuation and so increase the sound penetration depth, but again at the price of spatial resolution.

1.3   Thesis outline

The overall aim of this Thesis is to improve defect detection by improving existing and developing new methodologies to address the two problems in the UT of coarse-grained materials using bulk waves: phase aberration and backscattering noise. The Thesis consists of seven chapters which are introduced as below.

Chapter 1 gives a general overview of NDE techniques with emphasis on ultrasound inspection. Three problems, i.e., phase aberration, backscattering noise and attenuation, faced by ultrasound inspection of coarse-grained materials are described.

Chapter 2 introduces background knowledge related to the research topics of the Thesis.

Existing methods for phase aberration correction and the reduction of grain noise and speckle are reviewed and the potential improvement areas are identified. Finally, experimental arrangements and the specifications of a number of material samples to be studied in the reminder of the Thesis will be described.

Chapter 3 investigates an approach to correcting phase aberration in both columnar-grained and equiaxed-grained materials (coarse-grained materials with random orientation). This approach uses an accurate finite element model of the material under inspection to estimate the elemental phase shifts of the phased array. The material model is constructed using crystallographic orientation data of the material acquired by two microstructural characterisation techniques: Electron Backscatter Diffraction (EBSD) and Spatially Resolved Acoustic Spectroscopy (SRAS). Validation of the emerging SRAS technique is presented. Two approaches to processing orientation data are proposed in order to establish computationally efficient finite element models of coarse-grained materials. A strategy of estimating the elemental phase shifts through simulation analysis is explored.

Chapter 4, 5 and 6 focus on developing and evaluating innovative approaches for the reduction of grain noise and speckle.

Chapter 4 firstly presents an analytical model describing grain scattering process, followed by the evaluation of the prevalent split-spectrum processing (SSP) technique for grain noise reduction. The combination of SSP with artificial neural network (ANN) techniques is proposed to improve the performance of SSP in terms of grain noise suppression. The efficacy and efficiency of two ANN models, i.e. multi-layer perceptron (MLP) and radial basis function (RBF), used in conjunction with SSP are compared at various conditions.

Chapter 5 proposes the combination of a statistical signal processing algorithm, best linear unbiased estimator (BLUE), with SSP to attain enhanced speckle reduction. Parametric studies of the BLUE techniques are performed in order to give an indication of the optimal value ranges of the two parameters of BLUE.

Chapter 6 proposes an innovative signal processing algorithm for speckle reduction, called distribution dissimilarity imaging (DDI). This algorithm measures the

dissimilarity coefficient between a reference distribution and the statistical distribution of the magnitudes of frequency components. The dissimilarity coefficient is associated with the possibility of the presence of a flaw. Two DDI approaches with a different measure of the distribution dissimilarity are investigated.

Chapter 7 concludes the Thesis and provides suggestions of future work to the work presented in Chapter 3~6.

It should be noted that the work presented in the Thesis is attempting to improve defect detection only and is unrelated to defect characterisation. However, it can be considered as complementary to defect characterisation since the higher sensitivity and SNR exhibited by improved defect detection can undoubtedly facilitate defect characterisation.

1.4   Contributions to knowledge

- The accuracy of the emerging SRAS technique in characterising the microstructure of complex polycrystalline materials has been validated through comparing with the well-established EBSD technique. SRAS is more practically applicable in phase aberration correction than EBSD since it has no restriction on sample size and needs less surface preparation.

- Two approaches to processing the orientation data of equiaxed-grained materials acquired by EBSD and SRAS have been implemented, in order to construct an accurate and cost-effective finite element model of the materials. They have remarkably reduced the computational overhead of the wave propagation simulation in equiaxed-grained materials whilst maintaining model fidelity.

- A new time reversal method has been proposed and it provides a more reliable and rapid solution of the establishment of anisotropic focal laws in the simulation than conventional approaches. The simulation results have shown that equiaxed-grained materials are almost free from the phase aberration problem and the focusing quality of columnar-grained materials can be restored using the

anisotropic focal laws generated in the simulations.

- Three signal and imaging processing algorithms have been developed to increase SNR and image contrast to allow coarse-grained materials to be inspected with reduced error and greater confidence.

- The performance of SSP can be enhanced by combining it with ANN techniques. Most of the previous research focus on the MLP model whereas other ANN models have been rarely explored. The comparison of the MLP model and RBF model used in conjunction with SSP in terms of SNR improvement and computational efficiency have been presented. RBF model is observed to have higher SNR improvement when less noise training samples are used and the flaw location is known. MLP model is found to be superior when more noise training samples are used and the flaw location is known as well as when the sample location is unknown. RBF model is observed to be 35 times more efficient than MLP model on average.

- The statistical signal processing algorithms have received little consideration in the NDE community. The combination of SSP with BLUE has been investigated. BLUE has been observed to provide higher image contrast enhancement than conventional approaches whilst the spatial resolution is maintained. The optimal value ranges of the parameters of BLUE have been provided via parametric studies. It has been observed that BLUE can also effectively reduce sidelobe level used in conjunction with SSP.

- It has been observed in DDI analysis that the presence of a flaw can change the statistical distribution of the magnitudes of frequency components. Two DDI approaches with a different measure of distribution dissimilarity have been investigated. Both DDI approaches remarkably reduce the speckle intensity, offering better image quality than the conventional delay-and-sum approaches.

1.5 Publications

1. B. Xiao, M. Li, R. Gongzhang, R. L. O'Leary and A. Gachagan, "Image denoising via spectral distribution similarity analysis for ultrasonic non-destructive evaluation", in *Review of Progress in Quantitative Nondestructive Evaluation*, 2014, pp. 1941-1947.

2. R. Gongzhang, M. Li, B. Xiao, T. Lardner and A. Gachagan, "Robust frequency diversity based algorithm for clutter noise reduction of ultrasonic signals using multiple sub-spectrum phase coherence", in *Review of Progress in Quantitative Nondestructive Evaluation*, 2014, pp. 1948-1955.

3. B. Xiao, R. L. O'Leary, A. Gachagan, W. Li, T. Burnett, "Accurate finite element model of equiaxed-grain engineering material for ultrasonic inspection", in *IEEE International Ultrasonics Symposium (IUS)*, 2014, pp. 1364-1367.

4. R. Gongzhang, A. Gachagan, B. Xiao, "Clutter noise reduction for phased array imaging using frequency-spatial polarity coherence", in *Review of Progress in Quantitative Nondestructive Evaluation*, 2015, pp. 1648-1656.

5. B. Xiao, R. Gongzhang, T. Lardner, R. L. O'Leary and A. Gachagan, "Ultrasonic imaging of coarse-grained materials using adaptive frequency compounding", *NDT&E International*, 2016. (submitted)

CHAPTER 2. Literature review

2.1 Introduction

Firstly, background knowledge relevant to the research topics of the Thesis is introduced in this chapter, in order to provide some key information and terminology. Subsequently, the literature review of existing methods for phase aberration correction and the reduction of grain noise and speckle is presented. Next, the research gaps in phase aberration correction and noise reduction are defined and the general descriptions of Chapter 3~6 are presented. The experimental arrangement of data acquisition and the specifications of material samples used in the Thesis are described in the end.

2.2 Background knowledge

This section provides a review of the techniques typically employed in ultrasonic NDE, it is presented in order to define key terminology and nomenclature that will be employed throughout the literature review and Thesis. The first two subsections introduce the phased array techniques and commonly used array imaging algorithms. The next two subsections present some key information on crystallography and microstructural characterisation techniques. Some modelling techniques are described in the final subsection.

2.2.1 Phased array techniques

As described in Chapter 1, phased array probes are faster and more flexible in inspection than monolithic probes. These advantages have led to a dramatic increase in

the uptake of phased array probes by the NDE community. Present phased array transducers for NDE applications typically employ piezoelectric composite materials. Piezoelectric composites consist of a diced piezoelectric material substrate and a polymer material filling the void of the substrate. Ceramic materials such as PZT (Lead Zirconate Titanate) are commonly used as the active piezoelectric material within the device and an epoxy resin is typically selected as the passive polymer phase [24]. The advantages of piezoelectric composite materials over single piezoelectric ceramic materials include the increased electromechanical coupling efficiency, increased bandwidth, opportunity to tailor the transducers to the imaging task, etc.

Piezoelectric composites can be categorised according to the connectivity of the two constitutive materials. Connectivity is defined as the number of dimensions in which a constitutive material is continuous – by convention the first number represents the connectivity of the ceramic component and the second number represents the connectivity of the polymer. Fig. 2.1 shows a schematic diagram of a 1-3 connectivity piezoelectric composite [25-27].
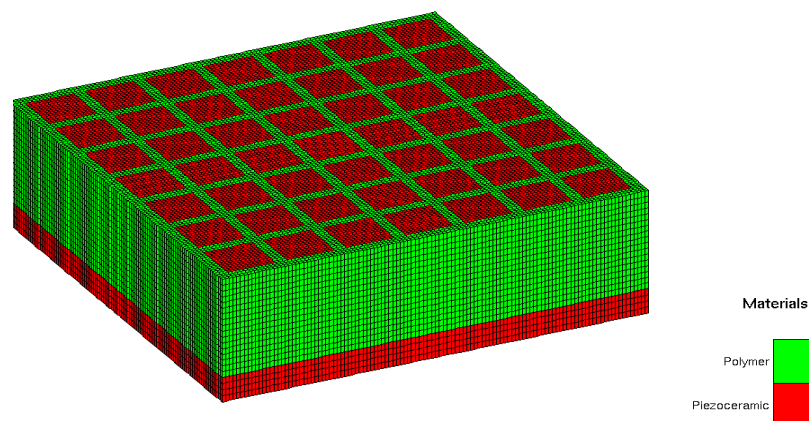
Fig. 2.1: Schematic representation of a piezoelectric composite with 1-3 connectivity.

A phased array probe is an assembly of ranging from 16 to as many as 256 individually addressable elements - each element is electrically isolated from its neighbours. When connected to appropriate drive electronics, each element can be excited in a specific order, defined by the focal law, to affect focusing and steering of the beam in the load medium, as depicted in Fig. 1.3.

Phased array elements can be arranged in either one- or two-dimensional patterns [13]. Fig. 2.2(a) shows the schematic diagram of the geometry of a 1D array with nine elements, each element is denoted as a rectangle in the diagram. Throughout the Thesis, the Cartesian coordinate system in Fig. 2.2 is used. Here, the axial direction z is the direction of wave propagation and x and y are the lateral and elevation directions, respectively. The beam is scanned in the x direction and the produced B-scan image is in the x-z plane. Typical 1D arrays for NDE use have their length in the y direction, L, much longer than their element width, e. Fig. 2.2(b) shows the schematic diagram of a 2D matrix array with 16 square elements evenly distrusted in the x-y plane. 2D array probes are able to generate 3D images of the inspected volume. They can steer and focus the ultrasound beam in 3D space in the front of array surface, they, therefore, can provide more accurate defect sizing than 1D array probes. 1D array probes have been used exclusively in the work that will be presented in the following chapters, although there is no reason why they cannot be extended to 2D array probes or other complex array layouts.
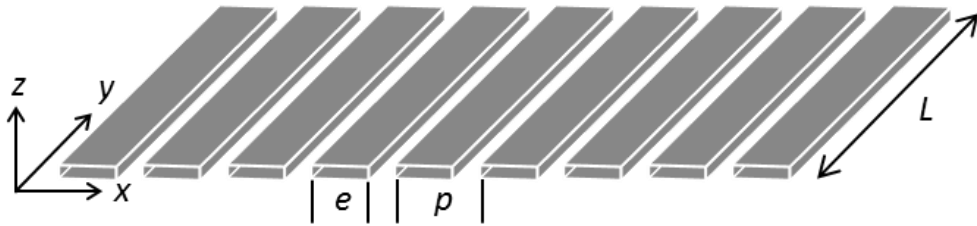
(a)
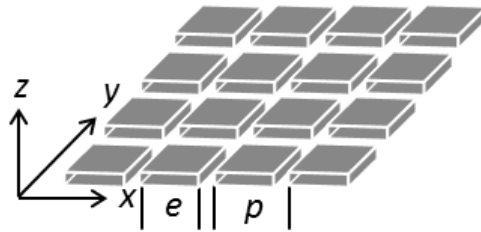
(b)

Fig. 2.2: Schematic geometry of (a): a 1D array with nine elements; (b): a 2D array with 16 square elements

The array geometry is required to be prudently designed to avoid problems such as grating lobes. Grating lobes denote the beam patterns formed at an angle to the mainlobe and are generated due to the periodic spacing of the small individual array elements [28]. The angular positions of the grating lobes, $\beta_{grating}$, can be described by

$$\beta_{grating} = \sin^{-1}\left(m\lambda/p\right), \text{m}= \pm 1, \pm 2, \pm 3,....$$

Eq. 2.1

where λ is the ultrasound wavelength corresponding to the central frequency of the array, p is the element pitch size which is the distance between the centres of two adjacent elements, as shown in Fig. 2.2. The value of p must be smaller than $\lambda/2$ to avoid the formation of grating lobes [28].

A backing layer is usually bonded to the rear face of the active elements of a phased array. It aims to maximise the energy loss at the rear face of the array and has the effect of reducing the ring-down time of the array. It, therefore, shortens the length of the emitted pulse leading to an increase in bandwidth and axial resolution of the array, this is achieved at the expense of sensitivity [28].

In some cases, one or more matching layers are attached at the front face of a phased array, aiming to maximise energy transfer efficiency between the probe and the load material [29-31]. The matching layer can improve the sensitivity of the array to small defects in the specimen. The simplest guideline in designing a matching layer is to maximise the transmission coefficient, T_i, which is formulated as

$$T_i = \frac{4}{2 + \left(\frac{Z_1}{Z_3} + \frac{Z_3}{Z_1}\right)\cos^2 kL + \left(\frac{Z_2{}^2}{Z_1 Z_3} + \frac{Z_1 Z_3}{Z_2{}^2}\right)\sin^2 kL}$$

Eq. 2.2

where Z_1, Z_2 and Z_3 are the acoustic impedances of the composite material layer, matching layer and the load material, respectively, L and k are the thickness and wavenumber of the matching layer, respectively. If L is equal to an odd number of quarter wavelengths and $Z_2 = \sqrt{Z_1 Z_3}$, perfect transmission ($T_i=1$) may be obtained.

2.2.2 Array imaging algorithms

Phased array probes are conventionally employed to emulate monolithic probes. That is, a number of array elements are excited with pre-defined time delays to form a physically focused and/or steered wavefront in the medium during the inspection. The received signals are summed and the results are stitched together to form B-scan images in real time during inspection.

Holmes et al. proposed a data acquisition approach which enables B-scan images to be generated offline in post-processing [32]. The data acquisition approach is named full matrix capture (FMC). FMC data are acquired by sequentially firing each element of a phased array while all elements are used as receivers. For a phased array with N elements, N^2 RF A-scan traces are acquired and form the FMC data volume for a given specimen and array position/orientation. The FMC data acquisition approach enables the beam focusing and steering to be emulated offline via post-processing FMC data. In such cases, the ultrasound beam is synthetically focused and steered offline with no physically focused or steered wavefront generated during the inspection. Comparing with conventional phased array systems, the FMC approach requires much easier inspection arrangement due to no requirement for the computation of complicated focal laws and has the potential to offer larger inspection coverage.

Note that if the performance of each element of an array is assumed to be consistent, data redundancy is observed in FMC data. That is, the A-scan trace from a transmitter-receiver pair XY is a temporal reciprocal of the A-scan trace from the pair YX. Therefore, FMC data could be reduced into half matrix captured (HMC) data by removing either the lower or the upper triangular section of the matrix.

Array imaging algorithms include the plane B-scan, focused B-scan, sectorial B-scan, and the total focusing method (TFM) [32]. The first three algorithms can be applied as standard inspection techniques in conventional phased array systems and can also be implemented by post-processing FMC data. TFM constructs images from FMC data so that it can only be applied in post-processing. The four image algorithms are introduced and compared below.

2.2.2.1   Plane B-scan

Plane B-scan is the most fundamental array inspection technique. To obtain enhanced sensitivity and lateral resolution, a group of elements which is termed an aperture are fired simultaneously, as shown in Fig. 2.3(a). The received time domain signals by all the elements in the aperture are then summed to generate a single A-scan trace. The aperture is shifted along the array by an element at each time of excitation. All the acquired A-scan traces are stitched to form a plane B-scan image. The lateral resolution of a plane B-scan image is equal to the array pitch size.

In post-processing of FMC data, results are computed from the A-scan traces of only pulse-echo mode (i.e., transmitter and receiver are the same element) acquired by the elements in an aperture. The image intensity at an arbitrary location (x_1, z_1) in a Cartesian coordinate system as indicated in Fig. 2.3(a) could be computed as:

$$a(x_1, z_1) = \sum_{tx=1, rx=tx}^{N} h_{tx,rx} \left({2z_1}/{c} \right) \qquad \text{Eq. 2.3}$$

where N is the number of array elements in the aperture, $h_{tx,rx}$ is the A-scan trace of a transmitter-receiver pair (*tx=rx* for plane B-scan), and c is the propagation velocity of the ultrasound wave. Plane B-scan does not employ focusing in neither transmission nor reception so that it gives poor lateral resolution when compared to other algorithms.

2.2.2.2   Focused B-scan

In conventional phased array systems, the elements within an aperture are applied with a symmetric focal law in transmission to focus the beam at a particular depth, as illustrated in Fig. 2.3(b). The received time domain signals undergo the same time delay as on transmission and are then summed to generate a single A-scan trace. Then all of the A-scan traces are stitched to form a focused B-scan image, usually focusing at a particular depth or feature within the field of view.

In post-processing of FMC data, results are often computed from A-scan traces of both pulse-echo mode and pitch-catch mode (i.e., transmitter and receiver are two different elements). If the beam is focused at the location (x_1, z_1), as shown in Fig. 2.3(b), the image intensity at an arbitrary location (x_1, z_n) can be computed as

$$a(x_1, z_n)$$

$$= \sum_{tx=1}^{N} \sum_{rx=1}^{N} h_{tx,rx} \left(\frac{\sqrt{(x_{tx} - x_1)^2 + z_1{}^2} + \sqrt{(x_{rx} - x_1)^2 + z_1{}^2} + 2(Z_n - Z_1)}{c} \right) \quad \text{Eq. 2.4}$$

where x_{tx} is the lateral coordinate of the transmitter, and x_{rx} is the lateral coordinate of the receiver, other symbols are as previously defined.

A focused B-scan image has a better lateral resolution at the focal depth than a plane B-scan image. Resolution at other depths could be improved by applying focal laws with different time delay sequences in transmission and/or reception. This is often termed Dynamic Depth Focusing (DDF). Applying different focal laws in transmission leads to multiple firings which reduces the frame rate. Applying different focal laws in reception results in no frame rate penalty, with the only limitation being computational resources. Therefore, DDF is usually implemented with coarser and finer focal control in transmission and reception, respectively [33].

In post-processing of FMC data, infinite focal laws can be applied in both transmission and reception. If one focal law is applied in transmission to focus the beam at (x_1, z_1) and numerous focal laws are applied in reception, the DDF image intensity at an arbitrary location (x_1, z_n) is given as

$$a(x_1, z_n)$$

$$= \sum_{tx=1}^{N} \sum_{rx=1}^{N} h_{tx,rx} \left(\frac{\sqrt{(x_{tx} - x_1)^2 + z_1{}^2} + \sqrt{(x_{rx} - x_1)^2 + z_n{}^2} + z_n - z_1}{c} \right) \quad \text{Eq. 2.5}$$

Focused B-scan is similar to the synthetic aperture focusing technique (SAFT) which is widely used in medical diagnostic imaging, both radar and sonar systems [22]. In SAFT, a monolithic probe is laterally moved to form a synthetic aperture, and a pulse-echo A-scan is acquired at each lateral location. All the A-scan traces are post-processed to produce a focused B-scan image.

2.2.2.3   Sectorial B-scan

Sectorial B-scan steers the ultrasound beam with a certain angle to facilitate the inspection of a component not immediately underneath the aperture. In conventional phased array systems, in transmission the elements within an aperture are applied with time delay sequences to steer the beam in a certain direction, as illustrated in Fig. 2.3(c).

The received time domain signals by the aperture are applied with same time delays as in transmission and then summed up to generate a single A-scan trace. An A-scan trace is obtained at each incremental steering angle and all the A-scan traces are combined as a sectorial B-scan image. Unlike plan and focused B-scan, sector B-scan conducts an angular sweep so that a polar coordinate system (r, θ) is often employed, where r and θ represent the axial and angular coordinates, respectively, as illustrated in Fig. 2.3(c).

In post-processing of FMC data, the image intensity at an arbitrary location (r_1, θ_1), where r_1 is the distance from the aperture centre to the point and θ_1 is the angle between the aperture surface normal and the steered beam, can be computed as

$$a(r_1, \theta_1) = \sum_{tx=1}^{N} \sum_{rx=1}^{N} h_{tx,rx} \left(\frac{2r_1 + x_{tx} \sin \theta_1 + x_{rx} \sin \theta_1}{c} \right) \qquad \text{Eq. 2.6}$$
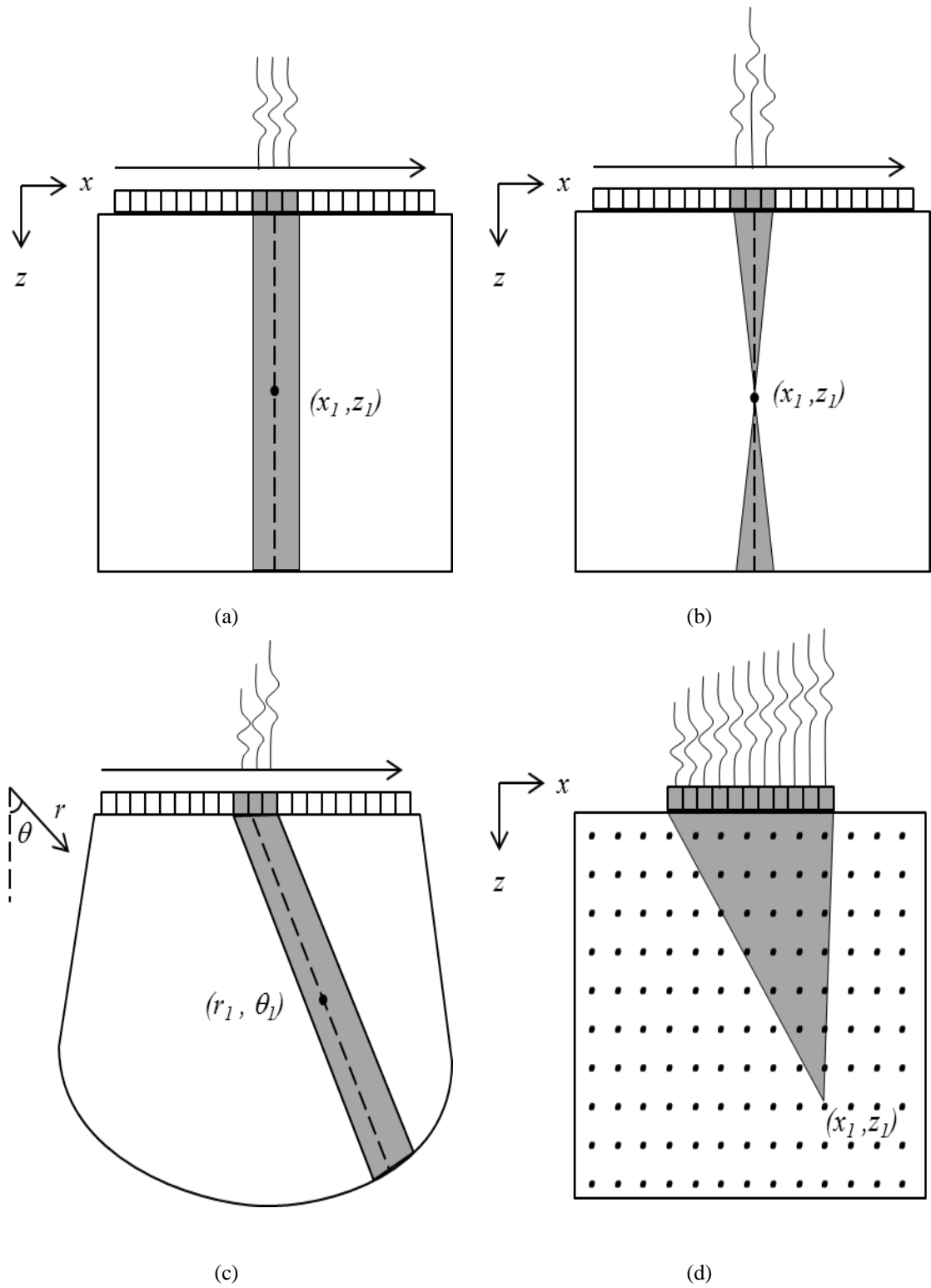
Fig. 2.3: Schematic diagram of: (a) plane B-scan, (b) focused B-scan, (c) sector B-scan, and (d) TFM. Shaded array elements constitute the active aperture of the phased array.

2.2.2.4   Total focusing method

TFM is an advanced imaging algorithm which can only be practically performed offline. It combines the full matrix of FMC data, i.e., it sums time-delayed A-scan traces from all the transmitter-receiver pairs, as illustrated in Fig. 2.3(d). In TFM, the imaging region meshes into a regular grid with a pre-defined resolution size and then the beam is synthetically focused at each node of the grid. The intensity at an arbitrary node (x_1, z_1) is given as

$$a(x_1, z_1)$$
$$= \sum_{rx=1}^{N} \sum_{tx=1}^{N} h_{rx,tx} \left(\frac{\sqrt{(x_{tx} - x_1)^2 + z_1^2} + \sqrt{(x_{rx} - x_1)^2 + z_1^2}}{c} \right) \qquad \text{Eq. 2.7}$$

where N is the number of array elements.

TFM is more computationally expensive than the other three previously described algorithms. Recently, an effort has been made to produce TFM images on the graphic processing unit (GPU) [34]. In this approach, the image intensity of each pixel is computed in parallel on a GPU device, consequently, the generation of TFM images is several orders of magnitude faster than the CPU-based approaches.

The TFM imaging algorithm has been extended for various applications. Vector TFM algorithm has the capability of defect characterisation since it can extract an angular scattering distribution of each scatterer [35]. Multi-mode TFM algorithm uses different reflections and mode conversions to improve the detection of angled defects whose reflections are outside the direct coverage of the array [36]. The autofocusing algorithm is exploited to enhance TFM imaging of components with complex surfaces [37].

2.2.2.5   Comparison

TFM algorithm performs better than the other three aforementioned conventional algorithms in terms of SNR and sensitivity to small defects [32, 38]. This is because TFM uses the maximum amount of available information for each imaging point so that the spatially uncorrelated grain noise can be suppressed to the largest extent, as compared to the other three algorithms. There exist other array imaging algorithms that can achieve better noise reduction than TFM. A detailed review of these algorithms will be given in Section 2.4.

25

TFM algorithm is also superior to the other three algorithms with regard to the spatial resolution that denotes the ability of an imaging system to resolve closely spaced flaws in the medium. Spatial resolution can be assessed by the point spread function (PSF) which describes the response of the imaging system to a point-like reflector. Holmes et al. used array performance indicator (API) as a quantitative measure of PSF and validated that TFM reduces API by 80% on the basis of plane B-scan [32]. Nevertheless, the spatial resolution of TFM is diffraction limited, known as Rayleigh limit [39]. Super-resolution techniques can be applied to enhance the spatial resolution beyond the Rayleigh limit. Time reversal with multiple signal classification (TR-MUSIC) is a widely used super-resolution technique and has been investigated to achieve ultrasonic super-resolution phased array imaging in [40, 41]. Fan et al. compared TR-MUSIC with TFM in terms of spatial resolution and robustness to noise and observed that TR-MUSIC produces significantly lower API than TFM at the low noise cases whilst TFM yields lower API at the high noise cases [39].

As illustrated in Eq. 2.3-Eq. 2.7, the time delays applied to different array element pairs are calculated using a constant ultrasound velocity c. However, as previously described, this approach leads to the phase aberration problem in the inspection of coarse-grained materials exhibiting elastical anisotropy. The review of methods developed to tackle phase aberration will be given in Section 2.3.

It should be noted that the images produced by any algorithms are generally absolute valued, normalised to the maximum value and then logarithmically compressed prior to being displayed on a computer screen. This is because the dynamic range of image intensity is usually very large and logarithmical compression can significantly reduce the dynamic range.

2.2.3 Crystallographic orientation

As previously mentioned, a crystal consists of atoms distributed in a repeating pattern in the three-dimensional space. Crystals can be classified into seven crystal systems according to their shape of atomic pattern or lattice. The seven systems include cubic, monoclinic, orthorhombic, rhombohedral, tetragonal, hexagonal, and triclinic [42].

Many coarse-grained metals employed in various applications in the nuclear and petrochemical industries have cubic crystal system.

The orientation of a crystal is defined as its coordinate system relative to a reference coordinate system. Typically, the sample coordinate system is usually selected as the reference coordinate system. There are several methods of representing crystallographic orientations [43]. Four commonly used methods are:

- (*hkl*)[*uvw*]. In crystallography, the orientation of a crystal plane is represented by Miller indices (*hkl*), which denotes that the plane intercepts with the *x*, *y* and *z* axes of the reference coordinate at *a/h, a/k* and *a/l*, respectively, where *a* is a constant. Directions in the crystal are referred to a set of coordinates [*uvw*] in the reference coordinate. The orientation of a crystal can be presented as a combination of the Miller indices (*hkl*) of the crystal plane parallel to the *x-y* plane and the coordinates [*uvw*] of the direction parallel to the *x* axis. Fig. 2.4(a) displays the crystallographic orientation (001)[110] as an example in the cubic crystal system in which the yellow cube is the crystal lattice and the blue rectangular cuboid is the sample.

- Axis-angle. The crystal coordinate system can become coincident with the reference coordinate system by a single rotation that is parameterised by a rotation axis and a rotation angle. It is a relatively efficient method of representing orientations.

- Rodrigues vector - this combines the two parameters of the Axis-angle representation by multiplying the rotation axis with a certain function of the rotation angle. It is more concise but difficult to interpret than the Axis-angle representation.

- Euler angle - this consists of three rotation angles required to make the crystal coordinate system coincide with the reference coordinate system. There are a few different definitions of Euler angle which differ in how the three rotations are conducted. Firstly, the rotations could be applied either by rotating the crystal coordinate system and fixing the reference coordinate system or by rotating the reference coordinate system and fixing the crystal coordinate system, which are named positive rotation and passive rotation, respectively. Secondly, the rotation could be applied by rotating around the fixed coordinate system (extrinsic rotation) or the rotating coordinate system (intrinsic rotation). Finally, there are six possible sequences of rotation axes – *zxz, xyx, yzy, zyz, xzx,* and *yxy*. The Bunge-passive

definition in which the rotation is passive, intrinsic and in *zxz* order is the most commonly used. Its rotation process is schematically drawn in Appendix A. The three Euler angles of the Bunge-pass definition are often expressed as (φ_1, φ, φ_2).

Due to the symmetry of crystal systems, equivalent crystal planes and directions exist. Planes equivalent to a plane (*hkl*) are denoted as {*hkl*} and directions equivalent to a direction [*uvw*] are denoted as <*uvw*> [43]. Fig. 2.4(b) shows three equivalent {110} planes of the cubic crystal system as an example. The ranges of the three Euler angles, φ_1, φ, and φ_2, are 0º~360º, 0º~180º, and 0º~360º. By applying symmetry, the ranges of φ, and φ_2 can both be reduced to 0º~90º. For the orientations falling out of the reduced range, their equivalent orientations inside the reduced range can be found by performing the two following transformations.

$$(\varphi_1+180º, 360º-\varphi, \varphi_2+180º) = (\varphi_1, \varphi, \varphi_2)$$

$$(\varphi_1+360º, \varphi+360º, \varphi_2+360º) = (\varphi_1, \varphi, \varphi_2)$$

Eq. 2.8

Similar symmetric properties apply to the Axis-angle and Rodrigues vector methods.

(a)

(b)
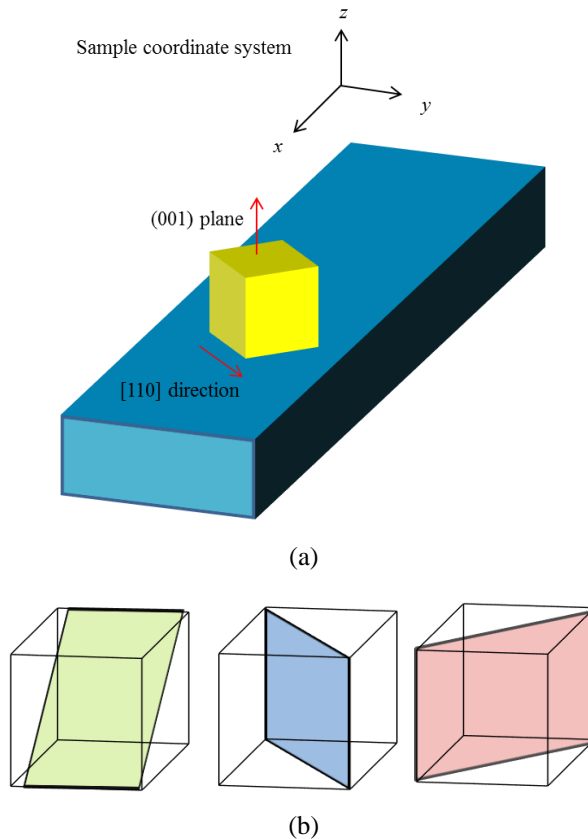
Fig. 2.4: (a) The crystallographic orientation (001)[110] in the cubic system; (b) three equivalent {110} planes in the cubic system.

28

2.2.4 Microstructural characterisation techniques

Several techniques are described in the literature that find application in the characterisation of polycrystalline microstructures. There exist two prevailing techniques, X-ray Diffraction (XRD) and Electron Backscatter Diffraction (EBSD), and one emerging technique, namely, Spatially Resolved Acoustic Spectroscopy (SRAS). The fundamentals of each technique will be introduced, followed by a comparison between EBSD and SRAS.

2.2.4.1   XRD

XRD is a technique that determines crystallographic characteristics based on the interference patterns of X-ray beams diffracted by crystals [44]. In this method, a (white) X-ray is incident on a single crystal surface at an angle. The atomic planes of a crystal reflect the incident beams of the X-ray and the reflected beams interfere with each other once they leave the surface to form diffraction patterns. This phenomenon is named X-ray diffraction. The interference between the reflected X-ray beams is governed by Bragg's law

$$2d_0 \sin \theta = n\lambda \qquad\qquad \text{Eq. 2.9}$$

where d_0 is the spacing between two atomic planes, θ is the angle between the incident beams and the lattice planes, λ is the wavelength of the incident beam, and n is an integer (1, 2, 3, etc.), as shown in Fig. 2.5. Constructive interference occurs at several wavelengths from the broad spectrum satisfying Bragg's law. Crystal orientations can be deduced from the analysis of the diffraction pattern using a Greninger chart [45].
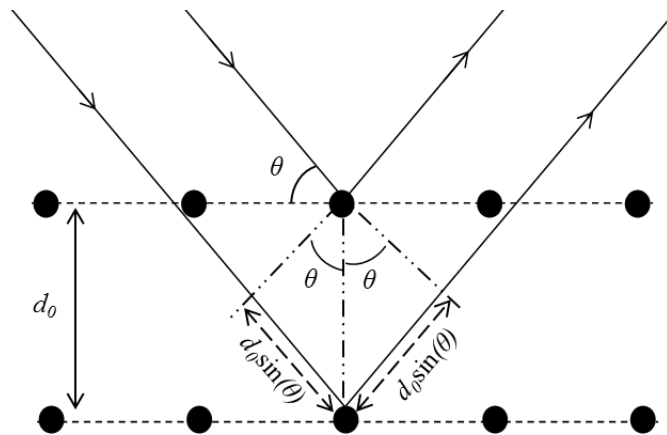
Fig. 2.5: Illustration of Bragg's diffraction

2.2.4.2   EBSD

EBSD is a well-established technique to determine the crystallographic characteristics of polycrystalline materials using scanning electron microscope (SEM) [43, 46]. The test sample is tilted with an angle of 70° to the horizontal and placed in an SEM chamber, and an electron beam is incident onto the sample surface. The atoms on the sample surface interact with the incident beam and scatter a fraction of the electrons. A phosphor screen is attached to the SEM chamber to capture the diffraction pattern formed by the scattered electrons. The interference between the scattered electrons also obeys Bragg's law due to the wave-particle duality of electrons. The scattered electrons satisfying Bragg's law produce characteristic lines called Kikuchi bands on the phosphor screen. The pattern of Kikuchi band is dependent on the orientation of the lattice planes onto which the electrons are incident. Then the Kikuchi bands undergo Hough transformation into points in the Hough space from which the orientation of the lattice planes represented by $(hkl)[uvw]$ is subsequently extracted. The $(hkl)[uvw]$ representations of crystallographic orientations are transformed into Euler angles in some cases.

EBSD scans the electron beam in a grid over the sample surface, and the crystallographic orientation is measured at each node of the grid. Then the misorientation angle, i.e., the minimum angular displacement between two neighbouring grains, is defined and used to reveal the position of the grain boundaries.

EBSD have several drawbacks. It is implemented over relatively small areas on a sample surface since the dimensions of SEM typically are in the order of 10 mm. Moreover, it is only tolerant to nanometre(nm)-scale surface roughness due to the limited free mean path of scattered electrons [47]. Consequently, samples must be accurately polished to obtain a highly reflective surface.

2.2.4.3   SRAS

SRAS is based on the spectroscopy technique and uses the acoustic characteristics of surface acoustic wave (SAW). A laser pulse is used to illuminate a region of the specimen surface and then gives rise to thermoelastic expansion and pressure in the region which induces the generation of SAW [48-50]. The SAW travels along the sample surface where a second laser acting as a detector is used to determine SAW

velocity. SRAS determines the orientation of a grain from the velocities of SAW measured in a number of directions.

There are two different methods of obtaining an SAW velocity: K-SRAS and F-SRAS. For the K-SRAS, a narrowband laser beam with a fixed modulation frequency f passes through a spatial light modulator whose fringe spacing can be changed, as illustrated in Fig. 2.6. When the fringe spacing period matches λ, the SAW will have the largest amplitude. Then the SAW velocity c is calculated as

$$c = \lambda f \qquad\qquad \text{Eq. 2.10}$$

For the F-SRAS, a wideband laser beam passes through a spatial light modulator whose fringe spacing are fixed, and the SAW velocity is calculated at the frequency with highest SAW amplitude.
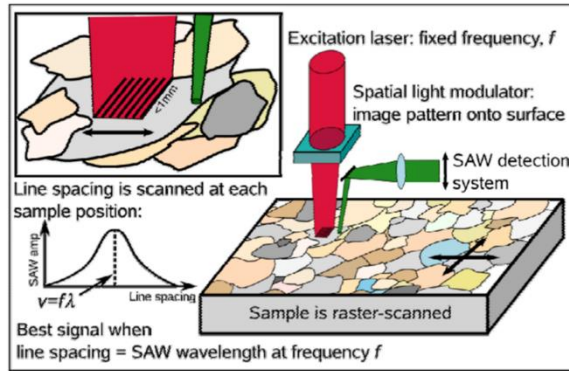
Fig. 2.6: Schematic diagram of K-SRAS, reproduced from [51].

By rotating the sample, SAW velocities at different directions are measured at a scanning location which in total are called as the measured velocity surface of the location. The crystallographic orientation of the scanning point is obtained by fitting the velocity surface to an SAW velocity model in which the velocity surface is calculated as a function of crystallographic orientation. Through an iterative search in the model, the orientation at which the corresponding calculated velocity surface most closely matches the measured velocity surface is deemed to be the orientation of the scanning location.

The SAW velocity model is calculated using the Christoffel equation with the prior information of the mass density and stiffness moduli of the material [42]. The Christoffel equation is

$$\rho c^2 \delta_{ik} - C_{ijkl} n_j n_l = 0 \qquad\qquad \text{Eq. 2.11}$$

where ρ is the density of the material, c is the sound velocity in the propagation direction specified by n_j and n_k, δ_{il} is the so-called Kronecker delta: $\delta_{ik} = 1$ if $i = k$; $\delta_{ik} = 0$ otherwise, C_{ijkl} is the stiffness tensor which is symmetric for a cubic crystal system

$$C_{ijkl} = C_{jikl} = C_{ijlk} = C_{jilk} \qquad\qquad \text{Eq. 2.12}$$

SRAS scans the laser over the sample surface to obtain microstructural characteristics of the whole sample surface. EBSD allows the step size to be in ten-nanometre scale, however, SRAS, as an emerging technique, can scan with the step size only in ten-micrometres scale. This is considered as one of the major limitations of the current SRAS technique. On the other hand, EBSD requires the surface roughness less than 10 nanometres and the sample size is limited by the SEM chamber. In contrast, SRAS can tolerate surface roughness on the scale of 100 nanometres and has no restriction on sample size. Some validation work of SRAS in determining crystallographic orientation will be presented in Chapter 3.

2.2.5 Modelling techniques

Modelling allows a wide range of virtual inspection scenarios to be carried out to develop, evaluate and optimise the methods for tackling the problems of phase aberration and backscattering noise in a time and cost-effective manner. To simulate the ultrasonic inspection of coarse-grained materials, the model should describe not only the ultrasonic wave propagation but also the interaction between the wave and the defects and grain boundaries in the materials. There are two major categories of modelling methods: (semi-) analytical methods and numerical methods.

Analytical models have a closed form solution to the elastodynamic equations used to describe the wave propagation and the interaction between wavefront and the defects and grain boundaries. That is, the solution can be expressed as an analytical function. Commonly used analytical modelling methods include multi-Gaussian beam method [52], Pencil method [53] and ray tracing model [54].

Analytical models are limited to simulating wave propagation in simple materials. For the complex coarse-grained materials of interest, analytical models no longer efficiently or even cannot simulate the wave propagation in the medium since each of the excessive grain boundaries present within the wave propagation path require a unique solution [55]. Therefore, simplifications are required in order that analytical models can provide an approximated solution to the wave propagation in a reasonable solution time. For instance, the interaction process between the interrogating wave and grain boundaries is simplified into a single parameter in [38]. Analytical models are also limited to simulating the interaction of the wavefront with regularly shaped defects. Kirchhoff approximation [56] and Born approximation [57] have been implemented into analytical models in order to efficiently and accurately simulate the interaction between the wavefront and irregularly shaped defects.

Common numerical methods include finite difference method, boundary element method, finite element method (FEM) [58]. FEM discretises the continuum field being analysed into a number of small non-overlapping sub-regions named elements. Each element can be separately assigned with elastic properties. The computation with respect to wave propagation and interaction with grain boundaries and defects is performed at the discrete connecting points called nodes. The element shape in a finite element (FE) model can be adjusted to fit different boundary conditions.

While FE models are inherently more computationally expensive than analytical models for simple materials, where the problem space encompasses complex coarse-grained materials exhibiting a multitude of grain boundaries, the computation workload for analytical models rapidly increases. However, the additional complexity does not present a significant computational overhead for FE models. This leads to FEM being a much more viable tool in modelling wave propagation in coarse-grained materials. Moreover, efforts have been made to accelerate the simulation of wave propagation in FE models by using GPU-based parallel computing techniques [59].

There are numerous commercial and proprietary FE modelling packages. PZFlex (Weidlinger Associates Inc., New York, USA) is used to conduct FE modelling studies introduced later in this Thesis. PZFlex code is a fast, large, explicit, time-domain solver that specialises in modelling wave propagation within the complex materials. It also

incorporates an implicit solver to model the behaviours of a transducer made of piezo materials.

Analytical modelling and FE modelling are commonly combined as hybrid modelling. For instance, Zhang et al. combined an analytical model for simulating backscattering grain noise and an FE model for describing the interaction between the interrogating wave and defects [56]. Recently, the French Alternative Energies and Atomic Energy Commission (CEA) coordinated the SIMPOSIUM project which aimed to provide a single and efficient hybrid simulation platform for NDE by linking the semi-analytical modelling package CIVA (Extende, Massy, France) with other FE simulation tools [60]. An example outcome of this project is that researchers at Imperial College developed a generic hybrid coupling method and applied it to link CIVA with their open-source GPU-driven FE code called Pogo [61].

2.3   Review of phase aberration correction methods

It has been explained in the Section 1.2.2.1 that the phase aberration problem in the inspection of coarse-grained materials arises since the wavefronts from different array elements propagate at different velocities due to the heterogeneity and anisotropy of the materials. The fundamental principle of phase aberration correction is to ensure the wavefronts from different array elements arrive at desired focal points at the same time and in phase to constructively produce a maximum in sound pressure. To achieve this, the time delays applied to array elements in the isotropic focal law should be modified to compensate for not only the geometric path length difference but also the phase shift as a result of directionally variant sound velocity. The modified focal law is usually referred to as an anisotropic focal law.

Many methods have been proposed in medical diagnostic imaging and ultrasound NDE to correct phase aberration. According to how anisotropic focal laws are generated, these methods can be generally classified into two main groups: data processing methods and model-based methods. Data processing methods generate anisotropic focal laws by correcting the elemental phase shifts via processing acquired data. Model-

based methods use the models of the materials under inspection to estimate the TOFs from array elements to focal points based on which anisotropic focal laws are generated. These two approaches will now be reviewed in turn.

2.3.1 Data processing methods

Many methods of correcting phase aberration through adaptively estimating time delay were proposed in the medical diagnostic sector. Flax and O'Donnell developed the nearest neighbour cross-correlation (NNCC) method which determines the phase shifts by a similarity (cross-correlation coefficient) measure between the signals of neighbouring array elements [62, 63]. Beardsley et al. applied NNCC for array self-focusing in NDE [64]. In the first iteration of NNCC, a signal segment of the first array element is used as the reference signal and the cross-correlation coefficients between the reference signal and a signal segment with a varying centre of the second array element are computed. The segment centre at which the highest cross-correlation coefficient is obtained is considered to have the correct arrival phase. In the second iteration, the phase-corrected signal segment of the second element is used as the reference signal to estimate the arrival phase of the third element. This process proceeds until the arrive phase of the last array element is obtained. Behar extended the NNCC technique by enriching the choice of the reference signal [20]. One such example is to use the sum of all previously phase-corrected signals as the reference signal. The beamsum (i.e., the sum of signals from all elements) can also be used as the reference signal to correct phase aberration assuming the phase errors of all elements are zero mean [65]. Other methods of estimating time delay include maximising mean speckle brightness in the region of interest [66] and minimising the sum of absolute differences between the signals of all array elements [67].

These adaptive time delay methods are effective and efficient to some cases in medical diagnostic imaging in which the phase aberration problem is induced by a thin aberrating layer close to the array surface. However, their results are observed to be disappointing in the case of the aberrators being distributed in the whole tissue volume [68]. This is because the temporal shape of a pulse is severely distorted by the volumetric aberrators via diffraction and multiple scattering. In such a case, the

methods based on estimating time delay typically fail to effectively correct phase aberration. For the same reason, these methods are also not effective in UT of coarse-grained materials with distributed inhomogeneity. Moreover, high backscattering grain noise may mask the flaw echoes which will induce errors in the similarity measure between the signals of array elements [69].

The time reversal mirror (TRM) technique was developed to correct phase aberration in inhomogeneous materials [70, 71]. In the process of TRM, the reflection signal received by a probe is recorded and then the probe retransmits the time-reversed version of the reflection signal. Compared to the adaptive time delay methods, the TRM method can refocus better since it not only corrects the phase shifts but also compensates the pulse distortions induced by the distributed inhomogeneity, however, at the expense of requiring programmable electronics for synthesising the time-reversed reflection signal for each array element. Iterative TRM process is typically required in the inspection of ultrasonically scattering materials such as titanium billet due to the strong grain noise interference [69].

DORT (French acronym for decomposition of the time reversal operator) method, as an extension of TRM, can avoid the iterative process by eliminating the grain noise interference and also allow the simultaneous phase aberration corrections of closely spaced flaws [69]. In this process, the scattering matrix is obtained from the phased array data and then the time-reversal matrix is computed as

$$T(\omega_c) = S^{*T}(\omega_c)S(\omega_c)$$
<div align="right">Eq. 2.13</div>

where ω_c is the centre frequency of the phased array, $S(\omega_c)$ is the scattering matrix and the superscript '$*T$' is the complex conjugate transpose operator of the matrix. Then the time-reversal matrix is eigenvalue decomposed. The number of significant eigenvalues is equal to the number of flaws or strong reflectors and larger eigenvalues correspond to the flaws with stronger reflectivity. The corresponding eigenvector of each significant eigenvalue indicates the phased array response to the corresponding flaw. Each eigenvector contains the amplitude and phase information that should be applied to the phased array in order to correct phase aberration at the corresponding flaw location. Grain scatterers typically have weaker reflectivity than the flaws so that they correspond to the insignificant eigenvalues. Since their corresponding eigenvectors are

not applied to the phased array, the interference of grain noise on phase aberration correction is avoided.

Besides, since DORT can separate the closely spaced flaws as illustrated above, it can also be applied to improve the spatial resolution of array imaging. Indeed, the super-resolution array imaging algorithm TR-MUSIC which has been mentioned in Section 2.2.2 is based on the DORT method.

2.3.2 Model-based methods

Many methods of overcoming phase aberration with the use of modelling techniques have been proposed. Most of them deal with austenitic stainless steel welds which are favoured for use as the components of pressure vessels and piping in the nuclear and petrochemical industries. In these methods, anisotropic focal laws are not calculated mathematically, instead, wave propagation in the material under inspection is simulated in the model of the material and the TOFs from array elements to focal points are measured in the model to instruct the generation of anisotropic focal laws. These methods differ in how the material model is obtained and TOFs are estimated.

The Ogilvy weld map is a well-recognised approximation to the microstructures of austenitic stainless steel welds [54]. The crystallographic orientations in the Ogilvy weld map are given as a function of the shape and dimensions of the weld. With the knowledge of the mass density and stiffness matrix of austenitic stainless steel, the sound velocity profile as a function of crystallographic orientation and sound incident angle can be calculated using the Christoffel equation. Connolly et al. employed this model to predict ray tracing of ultrasound waves within the stainless steel weld, such that TOFs from array element to a focal point were determined in simulations [72]. The ray tracing is estimated based on Fermat's principle of least time, stating that ray always takes the path between two points which costs the least time. Conventional ray-tracing algorithms typically follow an iterative trial-and-error procedure, hence, they can be computationally expensive. Two path-finding algorithms, Dijkstra and A* algorithms, have been proposed to rapidly find ray traces [73].

Although the Ogilvy weld map is widely used as the material model of austenitic steel weld materials, in reality, the microstructural characteristics of welds vary with the parameters of the fabrication process. Therefore, an accurate description of the microstructure of the weld is required in order to produce an accurate estimate of ray traces in the weld. Indeed, it is reported by Apfel et al. that too simplified structural descriptions of the weld give rise to incorrect results [74]. A number of methods have been developed to obtain the microstructural of the weld. Inverse models based on a genetic algorithm [75] and Monte Carlo Markov Chain [76] were created to estimate unknown microstructural anisotropy from experimentally acquired array data. The estimation was achieved by iteratively minimising the error between a forward model of welds and experimental array data. Researchers in EDF (Paris, France) developed the MINA model to describe the microstructural anisotropy of an austenitic steel multipass weld [77]. This model can produce a corresponding weld map with the input parameters such as the welding notebook, number of weld runs, etc.

More recently, TWI (Cambridge, UK) carried out considerable work to correct phase aberration and so to maximise the inspection sensitivity with the use of EBSD and the CIVA package [78-80]. In their approach, an austenitic steel weld was measured by EBSD scanning to obtain its crystallographic orientations represented with Euler angles. The crystallographic orientations were processed with a misorientation angle of 20° to reveal the positions of grain boundaries. Then the weld map with identified grain boundaries was processed to generate a 2D CAD drawing which was then read into CIVA to construct a material model of the weld. In addition, a 2 MHz linear phased array was also simulated coupled to the material model. The propagation of sound beams was simulated by the CIVA model where the TOFs from the array elements to focal points were determined in simulations. According to the TOFs, anisotropic focal laws which were adapted to the anisotropic properties of the weld were generated in simulations, following the criteria that the wavefronts from array elements must arrive at desired focal points at the same time and in phase to constructively produce a maximum in sound pressure. This approach for correction phase aberration is termed high-fidelity modelling in the Thesis, since EBSD can provide microstructural descriptions of welds with high fidelity and CIVA, as a well-recognised ultrasound modelling package, can accurately simulate ultrasound wave propagation in the model.

The preliminary semi-analytical model configured in CIVA was observed to be extremely computationally inefficient due to the excessive grain boundaries present in the model. To reduce the number of grain boundaries, the measured crystallographic orientations were processed to unify them to several dominant orientations (the orientations of columnar grains) and grain boundaries were redefined. Nevertheless, the time cost of wave simulation in the semi-analytical model was still considerable.

Harvey et al. extended the TWI work by constructing an FE model of the same weld in PZFlex which can obtain TOFs within a much shorter time period than the semi-analytical model [55]. This is because PZFlex code is specialised in simulating wave propagation in the complex medium, as previously stated.

2.4   Review of noise reduction methods

Historically, many methods have been developed in order to suppress grain noise and speckle observed in ultrasonic imaging applications in both ultrasonic diagnostic imaging in biomedicine and NDE. As per signals or images being processed prior to or after the formation of the final signals or images, existing methods can be classified into two groups: pre-processing or post-processing methods.

2.4.1   Pre-processing methods

Pre-processing methods attempt to reform the ultrasound field spatially and/or spectrally to eliminate or reduce grain noise and speckle. These methods involve modifications to signal acquisition and image formation. Examples of these methods include spatial compounding, frequency compounding, phase coherence imaging [81], TRM [69], etc. This section will review spatial and frequency compounding methods with the emphasis on frequency compounding since it forms the basis of the relevant research described in Chapter 4~5 of the Thesis.

2.4.1.1 Spatial compounding

Spatial compounding methods are based on spatial diversity which denotes the variation of received signals when a target region is insonified from different angles. Generally, grain noise and speckle patterns vary significantly in different insonification angles whilst flaw reflections are relatively coherent. By averaging signals or images acquired using slightly shifted transducer positions, noise reduction is attained. Advanced beamformers, such as TFM, inherently operate with spatial diversity [32]. TFM sums images acquired by different transmitter-receiver pairs of a phased array thus coherent reflections are enhanced.

Noise suppression by averaging signals or images is compromised if grain noise or speckle patterns are spatially correlated [82]. In addition to averaging, Wilhjelm et al. exploited other combination operators for spatial compounding, including median, geometric mean, etc. [83]. In recent work, Li et al. investigated the application of adaptive beamforming by weighting the per-element delayed data samples of the array where the weights are tuned according to local statistics [84]. This adaptive beamformer has the effect of decorrelating speckle noise acquired by different transmitter elements so it can produce an image with lower speckle intensity than TFM. Seo et al. proposed another advanced beamforming compounding technique called dual apodization with cross-correlation (DAX) for diagnostic imaging [85]. This technique measures the correlation between two images formed using two different apodized apertures. The measured correlation coefficient matrix is then multiplied with the image formed using the full aperture in a point-wise operation to generate the processed image. The authors also proposed the use of NNCC technique in conjunction with DAX to correct phase aberration in order to improve DAX's robustness [86].

2.4.1.2 Frequency compounding

Frequency compounding combines signals or images acquired at multiple frequencies. It determines if a received signal is reflected by a legitimate flaw or grain boundaries based on frequency diversity. Frequency diversity, analogous to frequency agility in the radar sector [87], states that the grain noise is frequency sensitive whilst the flaw echo is frequency insensitive. This is because grain noise indicates a multi-scattering event and is the mutual interference result of echoes from spatially unresolvable grain

scatterers. Since each individual scatterer has a different phase due to their randomness of dimension and spatial distribution, the interference of scatterers' echoes at different frequencies can be either constructive or destructive. On the contrary, a flaw echo indicates a sole-scattering event and it contains all the wavelengths comparable to or smaller than the flaw size. Therefore, flaw echoes are relatively more coherent than grain noise within an appropriate bandwidth. By combining signals or images acquired at different frequencies, only the coherent flaw echoes are retained and incoherent grain noise or speckle are reduced or eliminated.

It should be noted that frequency diversity neglects the multiple scattering effects between scatterers, which refers to the phenomenon wherein the ultrasound wave scattered from a grain scatter is re-scattered by neighbouring scatters [88]. That is, the amplitude of the re-scattered signal detected by the transducer is assumed to be negligible as compared to the scattered signal. Fortunately, the assumption is tenable for the majority of the regime of interest in NDE [38, 89].

Frequency compounding can be applied in transmission by employing multiple transducers or phased arrays with different central frequencies. However, it is best applied in reception by decomposing the signals received by a single transducer or array into sub-bands signals on condition that the received signals have a wide frequency band.

One representative method of frequency compounding is the split-spectrum processing (SSP) which is implemented by decomposing received wideband signals. It was introduced in the 1970s to improve SNR in NDT of coarse-grained materials [90]. It decomposes a wideband RF A-scan into a set of sub-band signals through a bank of bandpass filters and combines filter outputs with either linear algorithms such as averaging or nonlinear algorithms such as minimisation. SSP has been extensively used for the purpose of noise suppression due to its superior performance [81]. It was initially applied to reduce grain noise specifically for processing of individual A-scan traces but was subsequently extended to include the processing of each A-scan of array data with the aim of enhancing the contrast of medical images [91]. Li et al. applied the SSP algorithm to each column of a SAFT image, considering every image column as a synthetic A-scan [22].

The bandpass filtering step of SSP can be performed either in the time domain or in the frequency domain. Fig. 2.7 shows the flow chart of SSP of an A-scan signal with the bandpass filtering being performed in the frequency domain.
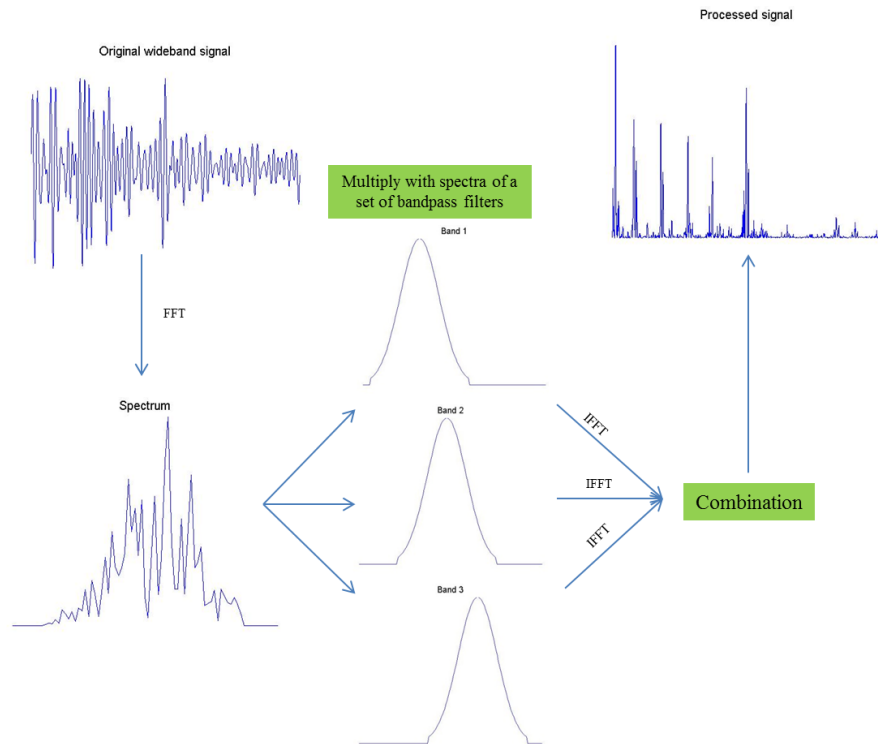
Fig. 2.7: Flow chart of SSP with a bank of three bandpass filters

SSP contains two set of parameters: the filter bank specifications and the combination algorithms. The filter specifications which have been studied in literature include the following five parameters:

- Total bandwidth

- The number of filters

- The bandwidth of each filter

- Overlap of filter pass-bands

- Filter type

In general, the total bandwidth is set to the bandwidth of the inspection probe. In some cases of inspecting coarse-grained materials, the upper limit of the bandwidth is selected lower than that of the transducer since signal energy at higher frequencies is attenuated by the grained structures [92]. The number of filters is generally chosen to

be smaller than 10 since it has been reported that SNR enhancement rate rapidly decreases when the filter number is greater than 10 [93]. Filters are usually designed with equal bandwidth and with their central frequencies equally spaced in the total bandwidth. Rodriguez et al. provide a multi-resolution design in which the bandwidth of each filter is proportional to the central frequency in order to prevent one band overwhelming others [94]. The filter overlap is usually selected as 0%~25% because an overlap less than 0% results in loss of frequency information whilst a large overlap negates the effect of SSP [93]. Finally, Gaussian type filters are commonly used because they provide the best joint time-frequency resolution [90].

The combination approaches which have been explored in the literature include the five algorithms formulated below. For notational convenience, these symbols are used in the equations: $A_i(n)$ is the output of ith band at the instant n; K is the number of bandpass filters; $Y(n)$ is the processed signal.

- *Mean (MEAN)*

$$Y(n) = \frac{\sum_{i=1}^{K} A_i(n)}{K}$$

Eq. 2.14

- *Minimisation (MIN)*

$$Y(n) = min(|A_1(n)|, |A_2(n)|, \cdots |A_K(n)|)$$

Eq. 2.15

- *Frequency multiplication (FM)*

$$Y(n) = \sqrt[K]{\left|\prod_{i=1}^{K} A_i(n)\right|}$$

Eq. 2.16

- *Polarity threshold (PT)*

$$Y(n) = C \cdot min(|A_1(n)|, |A_2(n)|, \cdots |A_K(n)|); \ \text{where } C$$
$$= 1 \text{ if all } A_i(n) > 0 \text{ or } < 0; \text{ otherwise}, C = 0$$

Eq. 2.17

- *Polarity threshold with scaling (PTS)*

$$Y(n) = \left|\frac{P - N}{K}\right| \cdot min(|A_1(n)|, |A_2(n)|, \cdots |A_K(n)|); \text{where } P$$
$$= \text{number of cases for } A_i(n) > 0, N = K - P.$$

Eq. 2.18

Amongst these five combination algorithms, MEAN, MIN and FM are based on the coherence of the magnitudes of the filter outputs. PT and PTS are based on the coherence of instantaneous polarities of the filter outputs. The two combination algorithms differ in the degree of stringent constraints on the polarity coherence of filter outputs. Other combination approaches include the phase deviation method in which the original signal is modulated by the standard deviation of the phases of filter outputs [95], and Wiener filtering (i.e., weighted MEAN with optimised weights) with the knowledge of the flaw and noise spectra [96].

Previous studies observed that SSP reduces noise at the expense of axial resolution due to the use of narrowband sub-band signals [97]. The loss of axial resolution denotes that the minimum distance in the axial direction between two temporally resolvable peaks in an A-scan signal or two spatially resolvable objects in a B-scan image is increased. Mulholland et al. attempted to increase the transducer bandwidth by attaching multiple matching layers in the front face of a transducer to improve the axial resolution [29]. Sanchez and Oelze proposed the use of the coded excitation and pulse compression technique called resolution enhancement compression (REC) in conjunction with SSP in order to enhance the bounds of the trade-off between the axial resolution and image contrast enhancement [98]. Dantas et al. proposed the use of a bank of wideband 2D directive filters each of which filters the 2D RF data in a given direction [99]. The filter outputs were combined by averaging. The results showed that speckle level is greatly reduced without apparent resolution loss.

Another drawback of SSP is that its performance is highly dependent on the selected filter specifications [81]. As a result, the practical implementation of SSP necessitates a troublesome interactive process of tuning filter specifications, usually following a trial-and-error procedure. Moreover, the performance of a tuned SSP system is very sensitive to the variations of the spectra information of flaw echoes and grain noise which results from the variations of material characteristics. Coarse-grained materials exhibit spatial fluctuation in the elastic properties which will give rise to significant variations in the spectra of grain noise. As a consequence, an SSP system with tuned filter specifications can reduce grain noise or speckle in some regions of the specimen but may not as effective in other regions.

In order to improve the robustness of SSP, efforts have been made to find methods capable of automatically tuning the filter specifications to adapt to different material characteristics. The total bandwidth in which SSP should be applied can be determined by locating the frequency range with the maximal group delay entropy which implies the highest SNR [100]. The optimal number of filters for the minimisation algorithms has been found in [101]. Although many efforts have been made, no fully successful method of automatically tuning the filter specifications have, to date, appeared in the literature.

Instead of tuning the filter specifications, efforts have also been made to explore other combination approaches which are insensitive to the variation of material characteristics for given filter specifications. Several pattern recognition techniques have been proposed as combination approaches of SSP to improve its robustness. These techniques include artificial neural network (ANN) [102, 103], support vector machine (SVM) [104], etc. Most of the pattern recognition methods firstly establish a statistical training process to train a system with a significant amount of known flaw echoes and grain noise. The training process allows the system to acquire the complete statistical properties of both flaw echoes and grain noise, the trained system is, therefore, insensitive to the variations of the spectra information of flaw echoes and grain noise which results from the variations of material characteristics. The trained system is then used to classify new inputs as either flaw reflections or grain noise.

2.4.2 Post-processing methods

Post-processing methods typically apply signal or image processing techniques to suppress noise after the final signal or image is formed and digitised. Examples of these methods include statistical analysis, deconvolution, adaptive filtering and so on [105].

In medical diagnostic imaging, ultrasonic scattering from tissue scatterers is fundamentally a statistical process. The probability distribution function (PDF) of the envelope amplitude of the backscattered signals by tissue was analysed to characterise tissue, offering parameters of the scatterers constituting the tissue, e.g., scatterer number and distribution. The tissue can be classified as malignant or benign with the

knowledge of the scatterer parameters [106-108]. Likewise, ultrasonic scattering from spatially unresolvable grain scatterers is also a statistical process in the regime of ultrasound NDE. For a large number of randomly distributed grain scatterers, the observed envelope is characterised by a Rayleigh PDF. If a flaw is present, the PDF of the observed envelope changes from the Rayleigh distribution into a post-Rayleigh distribution, often known as Rician distribution [107]. Hence, the PDF of the observed envelope can give an indication of the presence of flaws in materials.

An ultrasound image is a convolution result of the point spread function (PSF) of the array imaging system with the microstructure transfer function. The PSF of an imaging system is spatially variant and is determined by the transducer array configuration, excitation pulse and so forth. Deconvolution methods improve image contrast by reducing or eliminating the anisotropic effect of the PSF [109]. If the PSF is known, deconvolution approaches such as Wiener deconvolution can be applied to eliminate the anisotropic PSF effect. If the PSF is unknown, it is typically estimated in the cepstrum domain prior to performing deconvolution [110].

Adaptive filtering techniques smooth homogeneous regions whose statistics resemble to speckle statistics and do not smooth other regions so that speckle level is reduced and defect signals are preserved. These techniques differ in their filtering mechanism. Lee adopted the minimum mean square error as the cost function to design an adaptive filter whose output is based on the local mean and variance [111]. Chen et al. used an adaptive homogeneity threshold approach to adaptively adjust the homogeneous region size in order to avoid the distortion of defect edges [112]. The homogeneous regions are smoothed with an arithmetic mean filter and defect edges are processed with a nonlinear median filter. One drawback of the adaptive filtering methods is that they suppress speckle at the expense of blurred image and reduced spatial resolution.

Multiscale algorithms linearly decompose the final image into multiple scaled versions of the final image. Wavelet filtering is one example of such algorithms. The final image is processed with wavelet transformation in which the wavelet coefficients smaller than a pre-set threshold are regarded as noise and then removed and coefficients are kept otherwise. The processed coefficients are combined to form a processed image [113, 114].

2.5   Definition of improvement areas

Previous research with regard to high-fidelity modelling mainly employed EBSD for microstructural characterisation and analytical or semi-analytical modelling techniques for simulating wave propagation. However, the approach is limited in practical use. This is because EBSD can only scan small samples due to the limited size of SEM chamber and a considerable amount of time is required for sample preparation because of EBSD being tolerant to surface roughness only at the nanometre scale. Also, analytical modelling techniques have difficulty in coping with complex microstructure. It has been reported that CIVA takes 7.5 hours to simulate the wave propagation in a round-trip time in a 33.7 x 15.4 mm^2 austenitic steel weld [79]. In Chapter 3, the use of SRAS with no restriction to sample size and less surface preparation than EBSD and the PZFlex package as an efficient modelling platform will be explored, aiming to significantly enhance the practicability and operational efficiency of the high-fidelity modelling approach. In addition, most of the previous research pertaining to phase aberration correction focuses on austenitic steel weld materials with columnar-grained microstructure. Therefore, the complementary research for correcting the potential phase aberration problem in equiaxed-grained materials will be presented in Chapter 3.

The literature with respect to the combination of SSP with ANN has been reviewed in Section 2.4.1.2 - most of the publications adopted the MLP model of ANN. The MLP model typically needs an iterative training process to optimise its weights, as a consequence, it may become to an inefficient solution in some cases. Therefore, the investigation of combining SSP with other cost-effective ANN models such as RBF is prudent. In Chapter 4, the comparison work between the MLP model and the RBF model in terms of training time cost and effectiveness in SNR enhancement will be presented. Furthermore, in the majority of the prior art, it was assumed that the flaw locations were known and the flaw echoes for ANN training were readily accessible. However, in real cases of NDE, the knowledge of flaws is typically unavailable or very limited. Even if the flaw locations are known, the flaw echoes are commonly seriously corrupted by strong grain noise interference. Training an ANN with corrupted flaw echoes typically results in a significant classification error rate. For this reason, the performance of the MLP model and RBF model in the cases of no flaw information

available and flaw echoes being corrupted by grain noise will be also evaluated and compared in Chapter 4.

Statistical signal processing basically denotes the estimation or detection of deterministic signals from random noise using statistical techniques. It contains algorithms such as maximum likelihood estimation (MLE) and best linear unbiased estimator (BLUE) [115]. Ultrasonic backscattering at different frequencies can be considered as a stochastic process due to the random phases of the spatially unresolvable grain scatterers whilst flaw reflections can be considered as deterministic signals due to their coherence across different frequencies. Consequently, statistical signal processing algorithms can be applied as the combination algorithms of SSP to recover the coherent flaw reflections from noise-corrupted sub-band A-scan traces or speckle-corrupted sub-band B-scan images. The combination of SSP with statistical signal processing algorithms has been little considered in the literature. Hence, Chapter 5 will investigate the combination of SSP and the BLUE technique.

As described in Section 2.4.2, the PDF of the observed envelope can indicate the presence of a flaw. In most publications, the PDF of the envelope amplitude is obtained from a signal segment of an envelope-detected A-scan trace acquired by a monolithic probe. However, in this case, in order to attain enough envelope instances for a fair PDF representation, the signal segment is inevitably selected to be very long. Indeed, Narayanan et al. obtained the envelope PDF from a signal segment of equivalent 3.7 cm long [107]. This implies that the spatial resolution and so the accuracy of flaw positioning is greatly compromised. With the use of an N-element phased array and the FMC data acquisition approach, N^2 envelope instances are available at each point. In this case, a fair PDF representation is obtained without the drawback of compromised temporal resolution as long as the value of N is not too small. The use of phase array systems for the generation of PDF information will be investigated in Chapter 6.

To conclude, Chapter 3 is concentrated on addressing the phase aberration problem. Chapter 4~6 investigates novel signal and image processing algorithms for enhanced suppression of grain noise and speckle. More specifically, Chapter 4 and 5 are devoted to developing new combination algorithms for SSP; Chapter 6 focuses on array data processing.

2.6   Data acquisition

Prior to concluding the chapter, it is useful to describe at this point the experimental arrangements and material samples used in the Thesis. Fig. 2.8 gives a schematic diagram of the array data acquisition arrangement employed throughout the Thesis. The computer at the workstation sends a trigger command to a phased array controller (PAC) which then sends a pulse to excite the phased array according to the defined focal law. The array is placed on the surface of a test sample on which some water is applied to enhance the ultrasound energy transfer efficiency. After being stimulated, the array emits sound waves and captures the reflected echoes from the test sample which are then transferred back through PAC to the computer.

A commercially available 1D linear 128-element phased array (Vermon, Tours, France) was employed to acquire array data used in the Thesis. Details of the phased array are listed in Table 2.1. Two PACs were used to control the phased array in the Thesis. Fig. 2.9 shows the photos of the two PACs: the left one is DYNARAY (Zetec, Snoqualmie, USA); the right one is FlawInspecta (Diagnostic Sonar Ltd., Livingston, UK). DYNARAY is configured with 256 simultaneously active channels. It allows users to choose one sampling frequency from 25 MHz, 50 MHz and 100 MHz, with 100 MHz being selected in the Thesis. FlawInspecta is configured with 64 simultaneously active channels and so a multiplexing system is present to enable the 128-element phased array to be controlled by the FlawInspecta. It has a fixed sampling frequency of 40 MHz. The sampling frequencies for both PACs are sufficiently high as the phased array has a central frequency of 4.5 MHz. Both PACs sent a -40 volts negative square pulse having a time duration of 100 ns as the excitation pulse to the array. Array data were acquired in the FMC format and all of the B-scan images were created by post-processing the FMC data using the TFM algorithm in Matlab (The MathWorks Inc., Natick, USA).
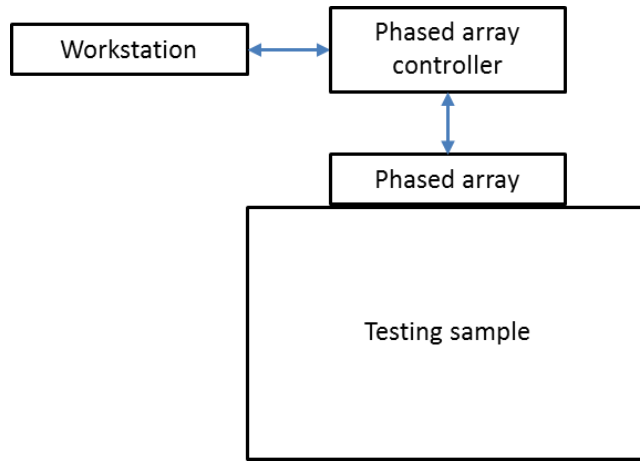
Fig. 2.8: Schematic diagram of experimental data acquisition arrangement

Table 2.1: Specifications of the phased array

Centre frequency (MHz)	4.5
Pitch size (mm)	0.7
Element number	128
-6 dB low cut-off frequency (MHz)	3.1
-6 dB high cut-off frequency (MHz)	6.0
Fractional bandwidth (-6 dB)	64%

(a)   (b)

Fig. 2.9: Two phased array controllers: (a) DYNARAY; (b) FlawInspecta.

Table 2.2 lists the six test pieces used in the Thesis. For brevity, these six samples are sometimes referred to as their numbers in the remainder of the Thesis.

Sample 1 is an 85 mm thick austenitic steel weld joining a 316L stainless steel plate with a 50D carbon steel plate. This sample is a typical dissimilar joint used as the safe-end weld of the pressurised water reactor (PWR) in the nuclear industry. This sample is provided by TWI and the same as the austenitic steel weld described in Section 2.3.2. Crystallographic orientations of a slice of the sample were obtained from the previous research projects in TWI which are used in the study of phase aberration correction in Chapter 3.

Sample 2 is a keystone-shaped Inconel (Nickel-Chromium based alloy) 617 alloy block provided by E.ON Technologies (Ratcliffe-on-Soar, UK). Inconel alloys are attractive construction material components in industries such as aerospace, power plants due to an exceptional combination of oxidation resistance and high-temperature modulus [116]. A slice of the sample was cut for the examinations of microstructural characterisation using EBSD and SRAS and the crystallographic orientation data is used in the analysis of phase aberration correction in Chapter 3.

Experiments were carried out on **Samples 3~6** detailed in Table 2.2 to acquire array data used in the analysis of noise reduction that will be presented in Chapters 4~6. The schematic diagrams of inspection geometry will be drawn in the following chapters.

Sample 3 is a flaw-free austenitic stainless steel block also provided by E.ON Technologies. Austenitic stainless steels are favoured for the use as the primary coolant piping of PWRs in nuclear power plants and piping and pressure vessels in the petrochemical industry due to their outstanding resistance to corrosion and oxidation as well as better plasticity and higher strength versus typical carbon steels [117]. Array data were acquired on the arc-shaped surface and so the backwall has a nominal thickness of 51 mm. The array data were analysed in Chapter 4 and 6 to reduce grain noise and speckle, respectively.

Sample 4 is a creep resistant ferritic steel block that is often used in the manufacture of power plant boilers. It is supplied by Doosan Babcock. It is 80 mm thick and has four 3-mm-diameter side-drilled holes (SDHs) at the depth of 20 mm, 40 mm, 60 mm and 75mm, respectively. All the four SDHs are 40 mm long inward. The array data of the

deeper three SDHs were acquired separately and were processed in Chapter 4 to reduce grain noise.
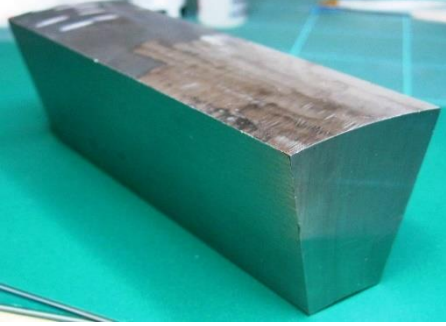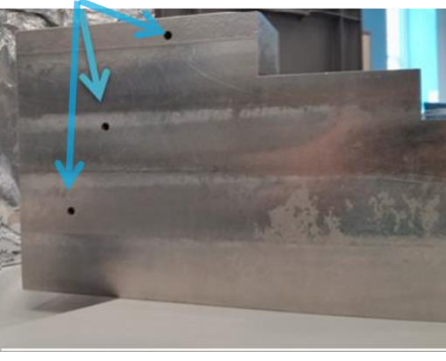
Sample 5 is a 160 mm thick Inconel 625 stepped wedge supplied by Siemens AG (Berlin, Germany). Its chemical compositions are slightly different from **Sample 2**. Three 5-mm-diameter SDHs are machined at the depth of 10 mm, 60 mm and 105 mm. Array data were acquired from the region covering the two deeper SDHs and were processed in Chapter 5 and 6.

Sample 6 is supplied by AMEC (Cheshire, UK) and is made up of two forged 316L austenitic stainless steel plates welded with steel 316L filler. The sample is 22 mm thick. It contains seven implanted flaws in various size and shape simulating cracks and lack of fusion. Array data of a tilted flaw implanted at the weld boundary were acquired. The data were processed in Chapter 5 and 6.

Samples 3~6 are composed of different materials and have different flaw type and size which allows the signal and image processing algorithms implemented in the Thesis to be evaluated under a wide range of inspection scenarios.

Table 2.2: Details of the six test pieces used in the Thesis.

Sample No.	Photo	Composition	Note
1	[118]	Austenitic steel weld joining a 316L stainless steel plate with a 50D carbon steel plate	A slice of the weldment was cut. The slice was polished and then examined by EBSD

2		Inconel 617 (~60% Ni, ~20% Cr, ~10% Co)	A slice of the sample was cut. The slice was polished and then examined by SRAS and EBSD.
3		Austenitic steel block (~18% Cr, ~8% Mn)	Cut from a larger in-service part. No flaws implanted.
4		Creep resistant ferritic steel block (~5% Cr, ~0.5% Mo)	A square block with four 3-mm-diameter SDHs.
5	SDHs	Inconel 625 (~60% Ni, ~20% Cr, ~10% Mo)	A very large sample with a size of 70*160*550 mm. Three SDHs were machined.
6		Austenitic steel weld plate	Seven flaws were implanted in the weldment.

CHAPTER 3. Phase aberration correction with high-fidelity modelling

3.1 Introduction

This high-fidelity modelling approach for phase aberration correction replicates practical inspection scenarios in virtual experiments within a suite of simulation tools. The actual TOFs from array elements to the focal point are predicted in the simulations to instruct the determination of anisotropic flaws. This approach contains four steps:

1) Microstructural characterisation

2) Data processing and model construction

3) Determination of the anisotropic focal law for the propagation path

4) Application of the anisotropic focal law in practical inspection

The first step is to obtain the crystallographic orientation using material characterisation techniques introduced in Chapter 2, EBSD and SRAS. In this chapter, the microstructural characterisation of two samples is discussed. The austenitic steel weld, i.e., **Sample 1** listed in Table 2.2, was examined by EBSD. The Inconel 617 alloy, i.e. **Sample 2** listed in Table 2.2, was examined by SRAS. Researchers at the University of Nottingham have conducted considerable validation work of SRAS in determining crystallographic orientation, however, most of the validation is limited to single-crystal materials [48] or single-crystal alloys [50]. No validation of the orientation data of the more commonly used polycrystalline materials like **Sample 2** has appeared, to date, in the literature. Therefore, five subsections of **Sample 2** were also examined by the well-recognised EBSD and the acquired orientation data will be used as benchmarks for validating the orientation data obtained by SRAS in Section 3.2.

The second step is to create models which precisely simulate, subject to some appropriate assumptions, the practical inspection scenario. In this chapter, the FE modelling package suite PZFlex is employed due to its efficiency in simulating wave propagation in complex materials. The crystallographic orientation data obtained from the first step must undergo some processing prior to FE model construction. This process aims to reduce the number of crystallographic orientations required to represent the material in the FE model whilst maintaining model fidelity. For example, the Inconel 617 sample has ~40,000 distinctive orientations which is unwieldy for computationally efficient FE modelling. This will be explored in more details in Section 3.3. It is noted that the raw EBSD data of the austenitic steel weld were measured by TWI and are kept confidential. However, the details of processing the orientation data are provided in the publication [79]. Moreover, the FE model created based on the processed orientation data by the Harvey et al. [55] is accessible. Therefore, a short representation of the orientation data processing for this austenitic steel weld will be given in Section 3.3 and the published FE model will be directly used for the analysis in next two steps. For the Inconel 617 sample, EBSD and SRAS datasets were generated in the course of the work presented in the Thesis by the Universities of Manchester and Nottingham, respectively. The measured SRAS data are then subject to the two proposed approaches to process the orientation data and then are used to construct FE models, this will be further described in Section 3.3.

The third step is to generate anisotropic focal laws based on the time reversal method. A new time reversal method is proposed. It inserts a pressure source at the focal point of the constructed FE model and records the TOFs of the wavefronts propagating from the focal point to the elements of the array. The TOFs data are then used to generate anisotropic focal law. The details regarding the generation of anisotropic focal law will be given in Section 3.4. The fourth step is to apply the anisotropic focal law produced in the third step into practical inspection. The execution of this step is not introduced in this chapter, but discussion will be provided in Section 3.5.

3.2   Microstructural characterisation

The first important parameter to establish for both EBSD and SRAS is the spatial scanning resolution which determines the cost in terms of expenses and time.

For the case of the austenitic steel weld, EBSD scanning of an area 8 mm^2 of the weld surface at a resolution size of 5 x 5 µm took nearly 12 hours whereas scanning with a resolution of 40 x 40 µm took only 12 minutes. In order to assist in defining the scanning resolution, the element size of the FE model is typically required to be approximate 1/15 of the wavelength for accurately simulating wave propagation and can be considered to be identical to the scanning resolution size. If a 1.5 MHz phased array is employed to inspect the weld, the generated longitudinal wavelength is approximate 4 mm. Since the scanning resolution size of 40 x 40 µm is smaller than the 1/15 of the wavelength, it is considered to be an appropriate spatial resolution to accurately simulate the wave propagation in the weld material at the proposed centre frequency of 1.5 MHz.

A slice was cut from the Inconel 617 alloy and polished for SRAS and EBSD scanning which shows in Fig. 3.1. SRAS measurement was conducted on the whole slice with a scanning resolution of 25 x 50 µm. The Inconel 617 alloy sample is thinner and less scattering than the austenitic steel weld, enabling the use of higher frequency than 1.5 MHz to inspect. If a 5 MHz phased array is employed, the generated longitudinal wavelength is approximate 1.2 mm. The scanning resolution of 25 x 50 µm is smaller than 1/15 of the wavelength in both spatial directions, it is therefore considered to be sufficient for accurately simulating wave propagation in the model.

SAW velocity maps were measured in 19 directions, from the top-bottom direction to the bottom-top direction with a step of 10°. Fig. 3.2 gives two examples of SAW velocity maps. Fig. 3.2(a) refers to the velocity variation when SAW propagates from top to bottom while Fig. 3.2(b) presents SAW propagating from left to right. The two figures are displayed with a velocity range from 2200 to 3100 m/s.

In order to validate the crystallographic orientation data obtained by SRAS, five overlapping subsections of the same Inconel 617 slice were also examined with EBSD with a scanning resolution of 10 x 10 µm. The location of the five subsections is

highlighted by a rectangular box in Fig. 3.2(a) and their total dimension is approximate 2.5 x 8 mm.
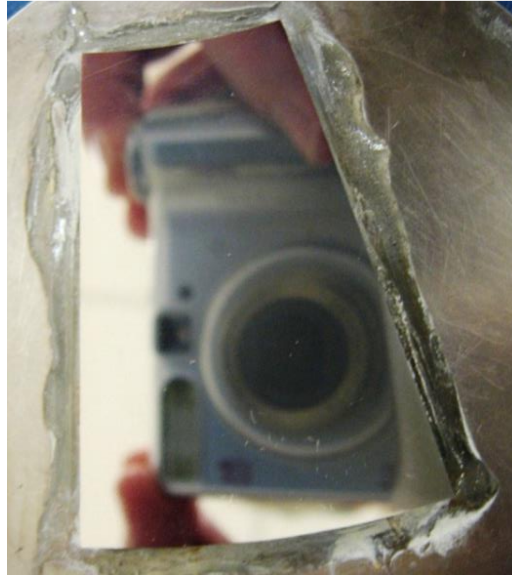
Fig. 3.1: Inconel 617 sample slice for SRAS and EBSD measurement

| (a) | (b) |
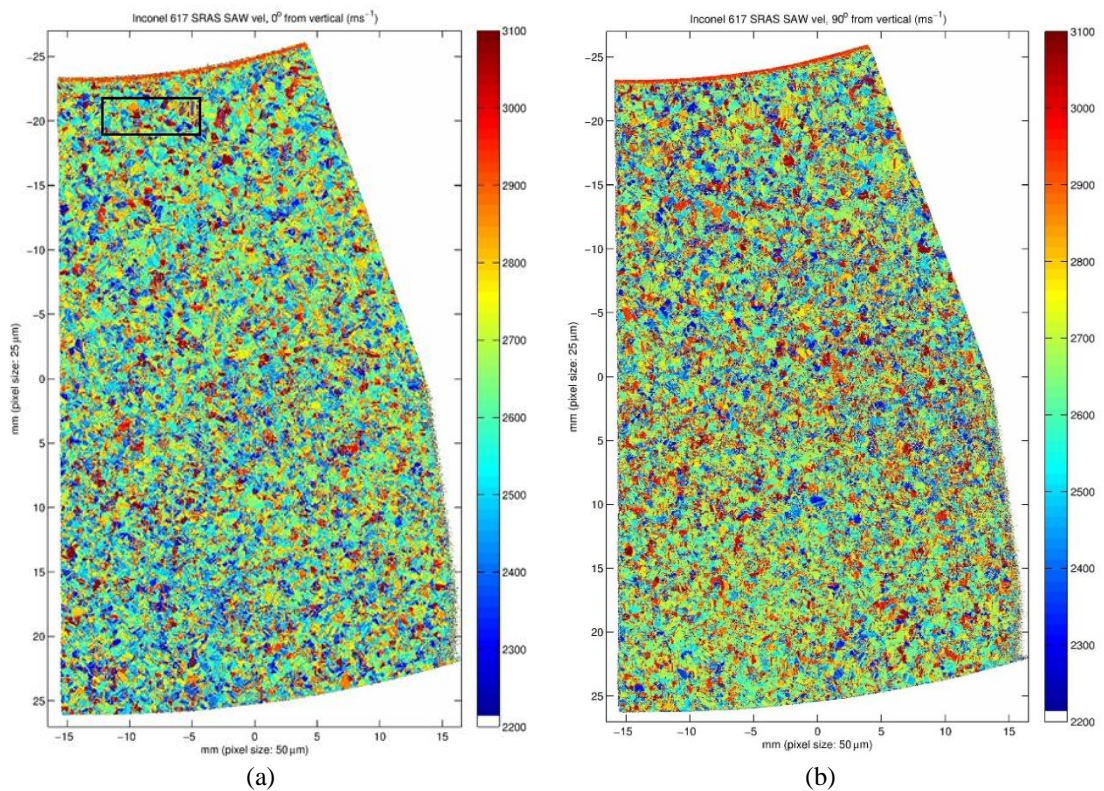
Fig. 3.2: Inconel 617 SAW velocity maps in the propagation direction: (a) from top to bottom and (b) from left to right.

Before validating the crystallographic orientation data obtained by SRAS technique, it would be interesting to compare the microstructure observed in the SAW velocity map with the counterparts observed in the EBSD orientation map. A key motivation for SRAS is to rapidly image material microstructure and thus to obtain an indication of grain orientation distribution using SAW velocity to differentiate crystallographic orientations [51].

Striking similarities between EBSD orientation image and SRAS velocity image for titanium alloys have been reported [51]. For the Inconel 617 sample described here, EBSD orientation maps and SRAS SAW velocity (propagating from top to bottom) maps for each of the five subsections is compared side-by-side in Fig. 3.3 in which the EBSD orientation maps are placed on the left side and SAW velocity maps are placed on the right side. In the figure, the EBSD orientation maps are displayed in the commonly used inverse pole figure (IPF)–colouring. An exhaustive description of IPF-colouring would require another section in this chapter so that the reader is referred to [43] for a full description. A certain colour corresponds to a certain orientation for the IPF orientation maps and a certain velocity for the SAW velocity maps. The colormap used for IPF displays is shown at the top of the left figure of Fig. 3.3(e) whilst the velocity dynamic range for SAW velocity displays is shown at the right side of the right figure of Fig. 3.3(e). Each subsection has an approximate dimension of 2.5 x 2 mm. The IPF map has a spatial resolution (i.e., the scanning resolution size) of 10 x 10 µm whilst the SAW velocity map has a spatial resolution of 25 x 50 µm.

The two maps for each subsection are generally in good agreement. The average grain size is observed with an equivalent diameter of ~250 µm for both EBSD and SRAS cases. However, quite a few grain boundaries are clearly depicted in the IPF maps but not as distinct in the SAW velocity maps. For instance, the grain boundary between the grain 1 and grain 2 of the second subsection as highlighted in Fig. 3.3(b) is identified by the IPF orientation map but not identified by the SAW velocity map. Two reasons responsible for these inconsistencies are discussed as follows. Firstly, the IPF maps have 12.5 times higher resolution than the velocity maps. In fact, as the velocity maps have a resolution size of 25 x 50 µm, they may be unable to recover the shape of grains whose equivalent diameter is lower than 100 µm. Secondly, it is possible that the

velocities of two neighbouring grains are coincidently similar when the SAW propagates from the top to bottom.

Fig. 3.4 shows the SAW velocity map of the second subsection in which the wave propagates at 10° deviation from the top-bottom direction. The boundary between the grain 1 and grain 2 is clearly observed for this SAW propagation direction. This illustrates the need of SAW velocities in more than one direction in order to describe the microstructure accurately.

(a)

(b)

(c)

(d)

(e)
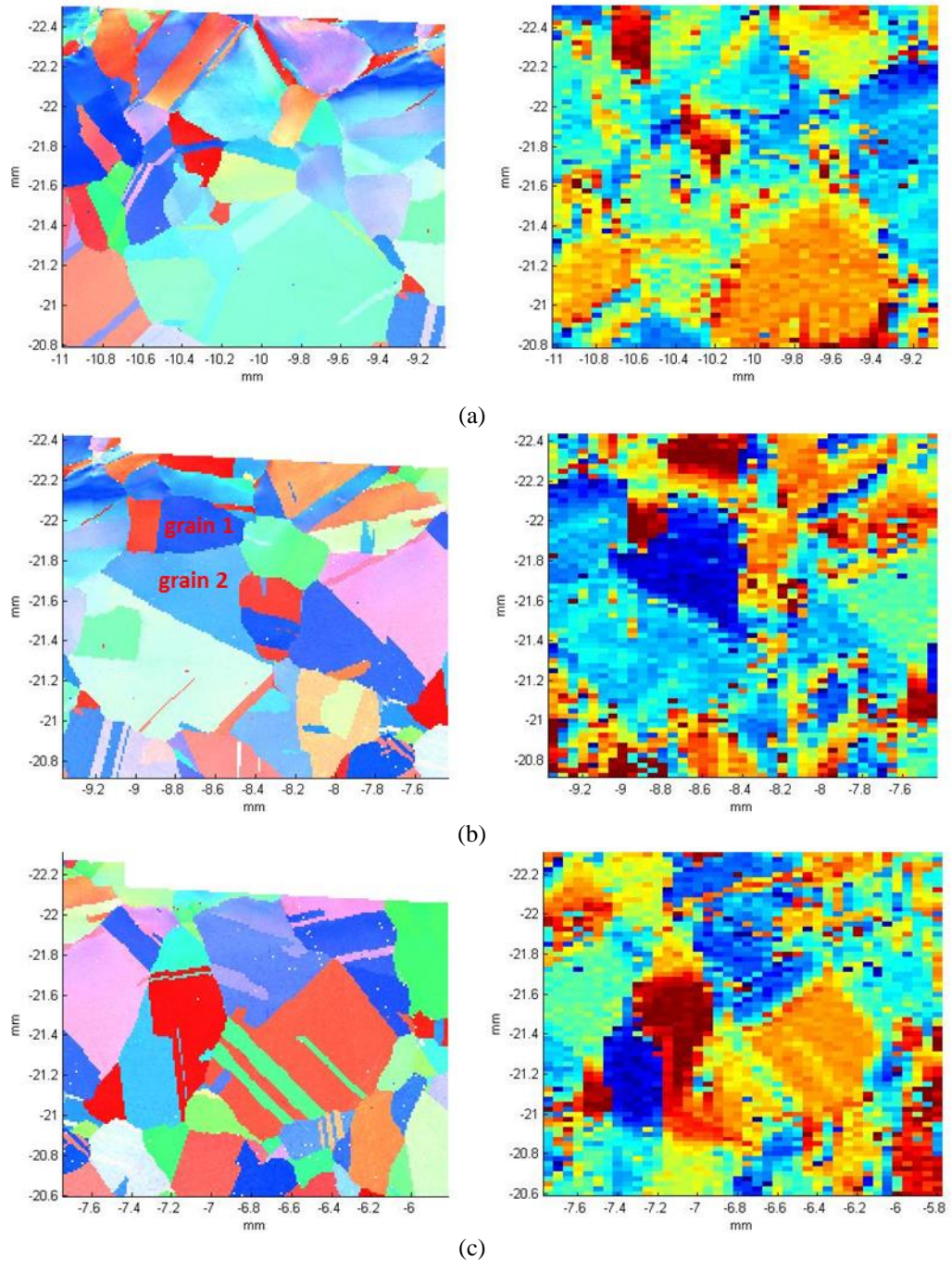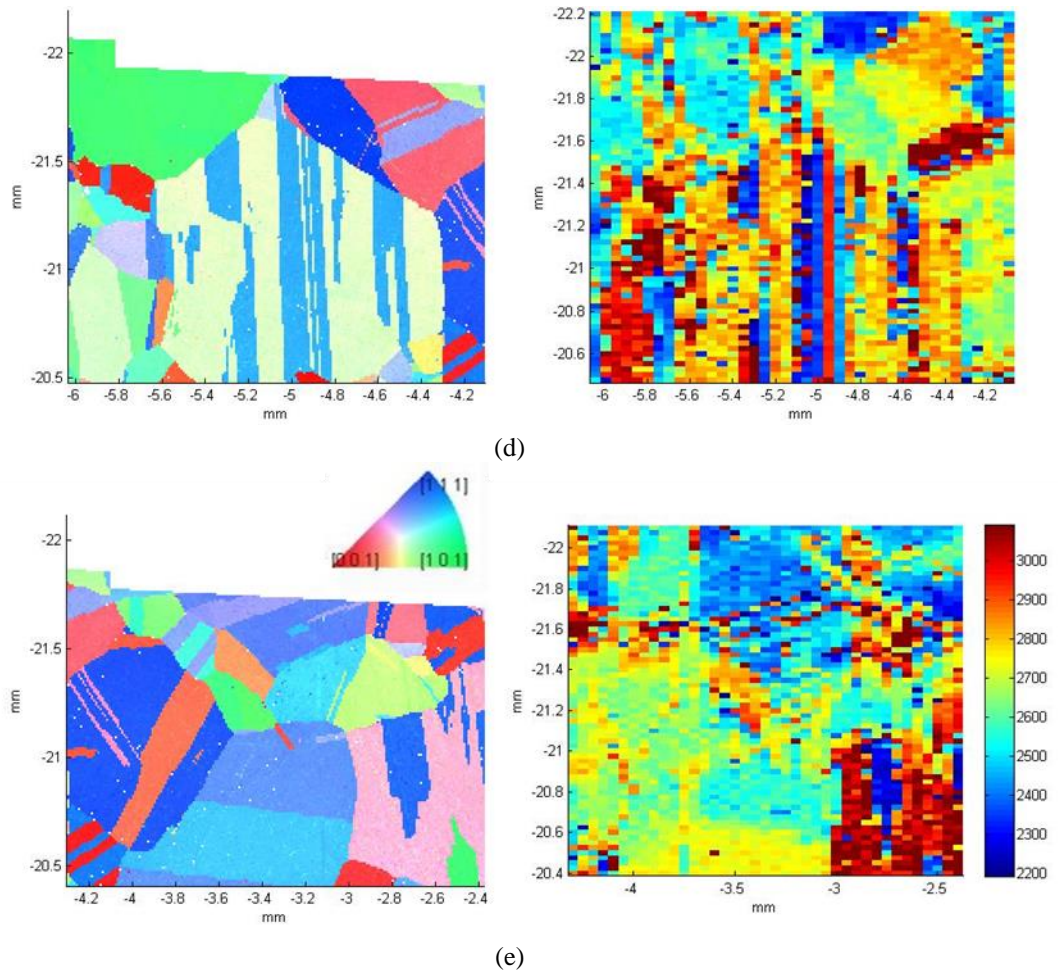
Fig. 3.3: Comparisons of EBSD IPF orientation maps (left) and SRAS SAW velocity maps measured from top to bottom (right) of the five subsections (a-e) of the sample slice.
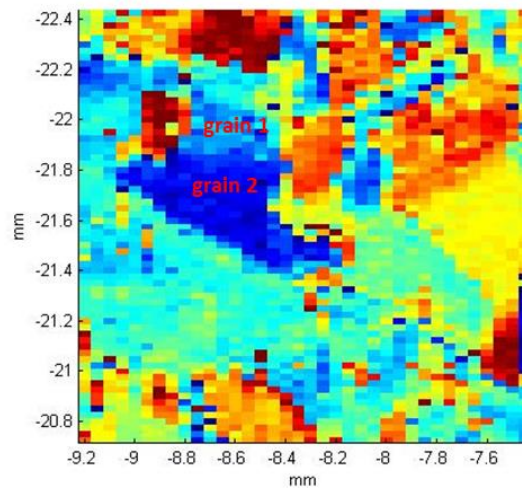
Fig. 3.4: SAW velocity map measured at 10-degree deviation from the top-bottom direction of the second subsection.

In SRAS, the SAW velocities measured at multiple directions are combined and processed by a so-called inversion method to obtain crystallographic orientation data [42]. In this inversion method, for each scanning point, the central-symmetric velocity surface (velocities of any two opposite directions are equal) is obtained from the measured SAW velocity maps at the first step. For the Inconel 617 sample, the central-symmetric velocity surface consisting of SAW velocities in 36 directions with 10° separation is obtained from the measured 19 SAW velocities. Then the velocity surface is fitted to an SAW velocity model, in which the velocity surface is calculated as a function of crystallographic orientation. Essentially, the fitting process calculates the cross-correlation coefficient between the measured velocity surface with every calculated velocity surface in the database of the SAW velocity model; the orientation corresponding to the calculated velocity surface with the best fit, i.e., the largest correlation coefficient, is considered to be the orientation of the scanning point.

To validate the SRAS technique in determining crystallographic orientation, Fig. 3.5 shows the comparison of IPF orientation map of the five subsections obtained by SRAS and the well-recognised EBSD technique. The five subsections are stitched and drawn as a whole for the EBSD in the figure. IPF orientation maps of EBSD and SRAS have a spatial resolution of 10 x 10 µm and 25 x 50 µm, respectively. It is observed that the EBSD result and SRAS result are in high agreement so that the orientation data provided by SRAS is proved to be valid. Therefore, the orientation data acquired by SRAS will be used to construct an FE model of the Inconel 617 sample. This will be discussed in the next section.
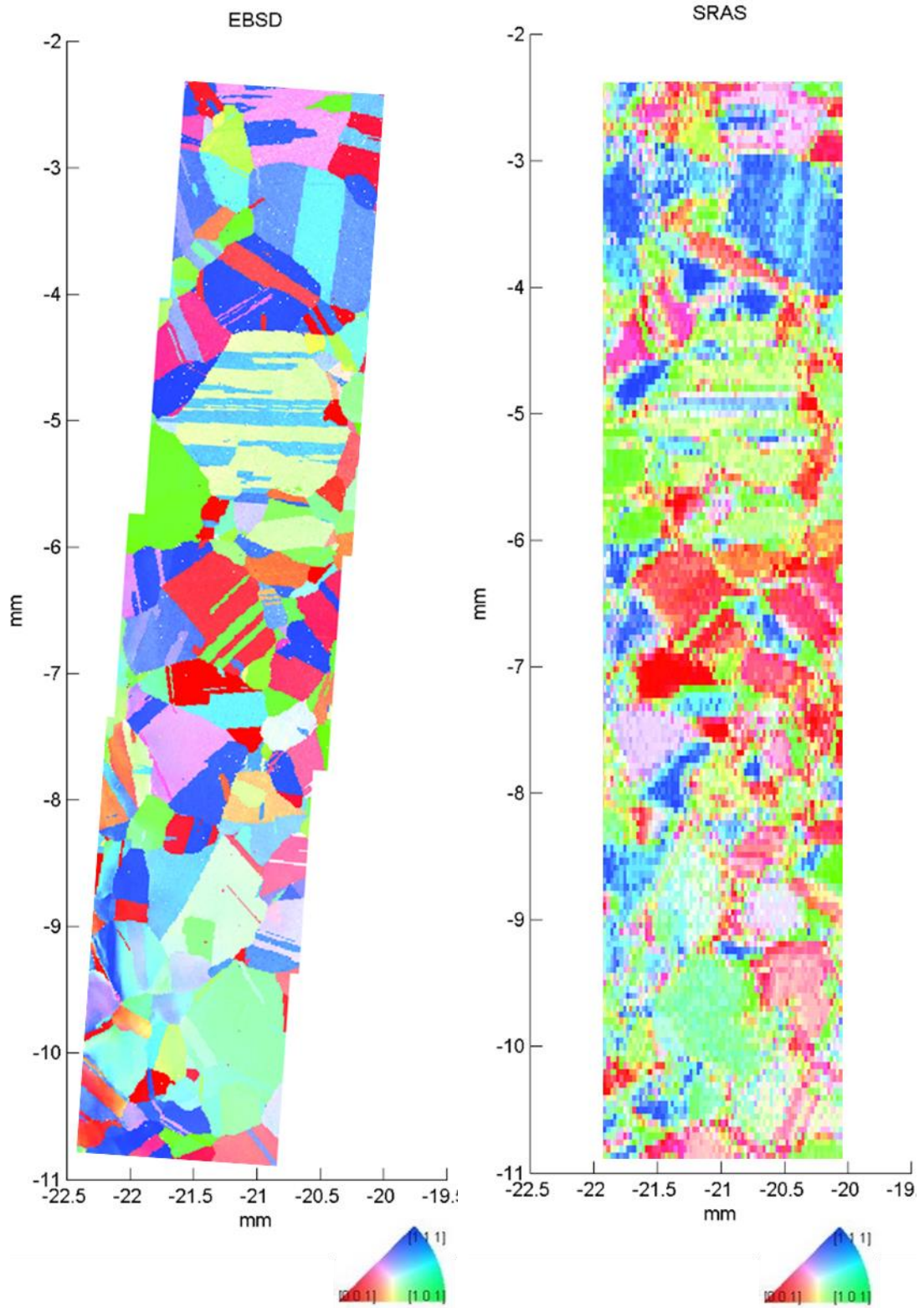
(a)   (b)

Fig. 3.5: Comparison of IPF orientation maps derived from: (a) EBSD and (b) SRAS.

3.3 FE model construction

3.3.1 FE modelling in PZFlex

FE modelling was performed in PZFlex due to its efficiency in modelling wave propagation in complex materials as compared with other FE simulation packages and analytical modelling techniques.

In PZFlex, each grain of the material can be defined using the density, the elastic moduli and a set of rotation angles that define the orientation of the grain in relation to the global axes of the model. It is assumed for both the austenitic steel weld and the Inconel 617 alloy that the stiffness moduli and density are the same for different grains such that anisotropy of the samples can be described using rotation angle to define the variation of grain orientations.

For the austenitic steel weld, the stiffness moduli are determined on a single crystal of a weld alloy of similar composition to the austenitic steel weld [79]. The cubic stiffness moduli are determined to be C_{11}=2.036e11 Pa, C_{44}=1.335e11 Pa, C_{12}=1.298e11 Pa. For the Inconel 617 alloy, the stiffness moduli are determined on an Inconel 600 single crystal which has quite similar composition to the Inconel 617. The stiffness moduli are determined to be C_{11}=2.346e11 Pa, C_{44}=1.262e11 Pa, C_{12}=1.454e11 Pa.

It is noted that the crystallographic orientation data acquired by both EBSD and SRAS are expressed in the form of Euler angles and all the three Euler angles are in the range of 0°~360°. Since both the austenitic steel weld and Inconel 617 samples have a cubic crystal system, the ranges of φ and $\varphi 2$ can be reduced to 0°~90° by applying Eq. 2.10. Since PZFlex requires the orientation expressed as three rotation angles about the global x, y and z-axes of the model, the step of one-to-one conversion from Euler angles to rotation angles is required.

3.3.2 FE modelling overhead

Both analytical modelling and FE modelling consist of two stages: the pre-processing, or model construction and model execution during the processing phase. As previously mentioned, FE modelling provides more rapid execution of simulating wave propagation in complex materials than analytical modelling, however, the computational requirement of model construction in FE modelling can be significant and contributes to the overall computational overhead when compared to analytical modelling. The amount of time expended in pre-processing the model can be considered as part of the modelling overhead, which in PZFlex is mainly determined by the number of distinctive crystallographic orientations that are defined within the model. In the current context, where the materials exhibit granular microstructure with large numbers of spatially variant crystallographic structure, pre-processing overhead could become significant. By way of example, Fig. 3.6 shows that the pre-processing overhead of the PZFlex platform increases with the number of distinctive orientations. It is observed that the construction of an FE model with 50,000 distinctive orientations in PZFlex requires an hour time of pre-processing whereas it takes only 20 seconds to construct a model with 500 distinctive orientations. Note that the pre-processing overhead is measured on a platform with an AMD (Advanced Micro Devices, Sunnyvale, USA) Opteron Processor 6128 running at 2 GHz with 16 GB of RAM.
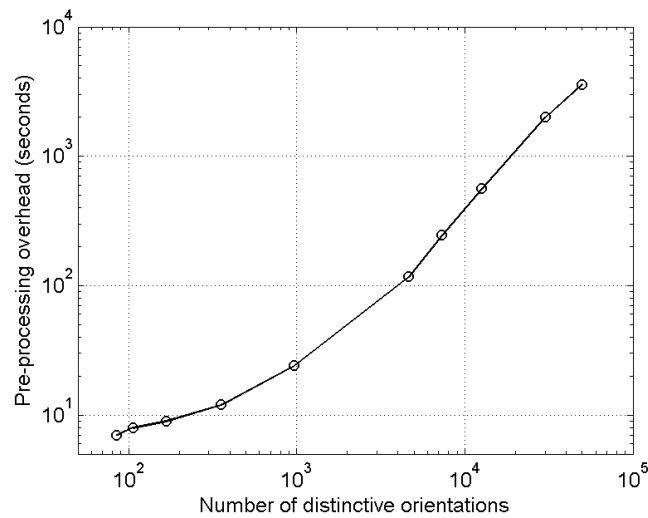
Fig. 3.6: The pre-processing overhead of PZFlex platform as a function of the number of distinctive orientations.

For both samples studied here, the number of distinctive crystallographic orientations acquired by EBSD and SRAS is significant due to the polycrystalline microstructure of the materials. For example, the SRAS data acquired for the Inconel 617 sample resulted in more than 40,000 distinctive orientations being identified. By considering the data presented in Fig. 3.6, construction of an FE model with 40,000 distinctive orientations will require ~40 minutes of pre-processing alone. This amount of pre-processing time is tremendous when compared to the ~2 minutes of processing time required to simulate the wave propagation in a round-trip path length of ~150 mm (125λ).

It is important to emphasise that the problem of significant pre-processing overhead is not unique to PZFlex. In fact, other FE modelling packages such as COMSOL Multiphysics (COMSOL Ltd., Cambridge, UK) typically takes even longer time than PZFlex to construct FE models of complex materials.

In order to decrease the pre-processing overhead, the crystallographic orientations should be processed to quantitatively reduce the number of distinctive orientations prior to constructing the FE model. However, it is essential that any reduction of pre-processing overhead is not at the expense of model fidelity.

The austenitic steel weld has an excessive number of grain boundaries for cost-effective analytical modelling, as described by Nageswaran et al. [79]. But several dominant orientations (<12) can be identified due to its columnar-grained microstructure which is a result of the partial melting between two weld beads where the grain growth is defined by the heat flow [78]. A processing method termed orientation unification was proposed to reduce the number of grain boundaries in which an angular spread of between 15° and 20° either side of the dominant orientation is set to be the dominant orientation. For FE simulations, the orientation unification processing can also be applied to significantly reduce the number of distinctive orientations to be as small as the number of dominant orientations. Consequently, the overhead arising from model pre-processing is trivial when compared to the processing phase of the FE model. Therefore, a cost-effective FE model of the austenitic steel weld can be readily established. Moreover, since the dominant orientations remain intact after processing, the fidelity of the FE model is guaranteed.

However, the processing of orientation data of the Inconel 617 alloy becomes an issue due to its equiaxed-grained microstructure. Fig. 3.7 shows the distribution of the orientation of the Inconel 617 sample measured by SRAS in Euler space, in which the measured orientation of each scanning location is drawn as a single point. Each subplot is displayed with 10° range of φ_2 and a full range of φ ($0°{\sim}360°$) and φ_1 ($0°{\sim}90°$). It is observed that the crystallographic orientations have an even distribution in the part of Euler space, indicating the randomness of the orientations of the grains. Since no dominant orientations can be identified, the straightforward orientation unification approach applied to the austenitic steel weld is not applicable to the Inconel 617 sample. Therefore, new approaches to process orientation data are required.
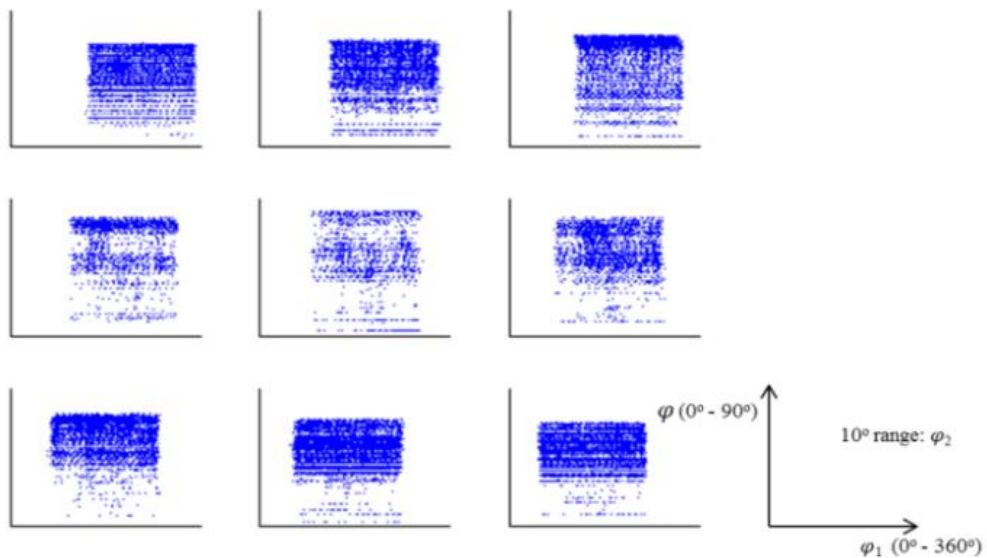
Fig. 3.7: Orientation distribution of the Inconel 617 sample expressed in Euler space

3.3.3 Orientation processing

One intuitive approach to address a large number of crystallographic orientations would be to quantise Euler space into a number of bins and then unify each bin by setting all of the orientations in the bin to be equal to the dominant orientation. Thus, the number of distinctive orientations is reduced to the number of bins within which at least one orientation falls. This method of processing orientations is termed Euler Binning (EB). However, it is possible that acquired orientations of a single grain are distributed into two or more bins; as a consequence, the grain is separated into two or more grains by

the EB processing. The effect of grain separation on model fidelity is discussed as follows.

The interaction of sound waves with the majority of metallic materials, including the Inconel 617 alloy sample described here, are generally dictated by Rayleigh scattering mechanism, which denotes that sound propagation wave is sensitive to the grains whose sizes are comparable to or larger than 1/10 of the wavelength (~120 μm for 5 MHz for the Inconel 617 alloy) and is insensitive to the grains of size less than 1/10 of the wavelength [79]. This then leads to the division of the overall microstructure into grains that affect the sound wave propagation, in the current context termed significant grains, and grains that do not satisfy the Rayleigh scattering criterion and therefore only marginally affect wave propagation, termed insignificant grains. It is, therefore, important that the process to reduce the number of distinctive orientations must ensure that any significant grains are not bifurcated. This is essential to maintain appropriate fidelity of the model with respect to wave propagation in the material of interest.

The inspection frequency and selected misorientation angle govern the distribution of significant grains that must be retained after orientation processing. Inspection frequency is selected based on several factors, including sample size, average grain size and so on. It determines the Rayleigh scatterer limit, that is, the 1/10 of the wavelength limit, as previously described. The misorientation angle, i.e., the minimum angular displacement between two neighbouring grains, is used to define the grain boundaries. The higher the misorientation angle, the smaller the number of grain boundaries and therefore the larger the averaged grain size in the modelling space. The misorientation angle is typically selected as 10°~20°. Here, it is selected as 10°.

After the determination of inspection frequency and misorientation angle, the significant grains are spatially indexed and then each significant grain is unified to the respective dominant orientation prior to binning Euler space and unifying each bin. This orientation processing method is termed Grain Unification with Euler Binning (GUEB). Four steps of the GUEB method are shown in Fig. 3.8. It is noted that the last two steps of GUEB method are the same as the EB method. Unlike the EB method, the GUEB method is able to prevent the separation of the significant grains such that model fidelity is guaranteed.
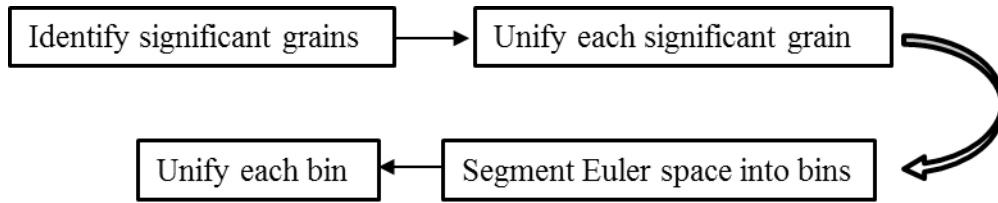
Fig. 3.8: Four steps of the GUEB method

The parameter to be established for a computationally cost-effective FE model of the sample being studied is the number of bins into which the Euler space is quantised. The quantisation level of Euler space directly governs the number of distinctive orientations which determines the amount of pre-processing overhead, as depicted in Fig. 3.6. As the number of bins decreases, the pre-processing overhead will decrease due to the reduced number of distinctive orientations, but the size of the bin (with a unit of degree/Euler phase) in Euler space will increase so that the step of bin unification will introduce larger error in terms of Euler angles, which deteriorates the model fidelity. Conversely, quantising Euler space into more bins introduces smaller error in Euler angles meanwhile increases the pre-processing overhead. Therefore, a trade-off between pre-processing overhead and model fidelity is identified. In the following, this trade-off as a function of the bin size in Euler space is studied for both EB and GUEB methods, in order to create an FE model of the Inconel 617 sample which balances the competing metrics of pre-processing overhead and model fidelity.

To quantify the model fidelity, a number of metrics can be considered to assess the interrelationship of the original SRAS dataset and the datasets that result from the EB and GUEB processes. The first metric would be to quantify the degree of intactness of significant grains. This is achieved by considering the cross-correlation coefficient between the original binary material map of SRAS dataset and the binary material map resulting from orientation processing. To illustrate the concept of the binary material map, Fig. 3.9 (a) and (b) show the schematic plots of the distributions of the original and the processed significant grains respectively in which the coloured components are the significant grains and the white background is for insignificant grains; Fig. 3.9 (c) and (d) show the corresponding binary material maps in which the significant grains are plotted in red (value 1) and the insignificant grains are plotted in blue (value 0). The cross-correlation coefficient C between the two binary material maps is formulated as

$$C = \frac{\sum_{x=1}^{m} \sum_{y=1}^{n} (B_0(x,y) - \overline{B_0})(B_p(x,y) - \overline{B_p})}{\sqrt{\left(\sum_{x=1}^{m} \sum_{y=1}^{n} (B_0(x,y) - \overline{B_0})^2\right)\left(\sum_{x=1}^{m} \sum_{y=1}^{n} (B_p(x,y) - \overline{B_p})^2\right)}} \qquad \text{Eq. 3.1}$$

where m and n are the numbers of elements in the lateral and axial directions on the binary map, respectively; B_o and B_p are the values of the original and processed binary map, respectively. $\overline{B_0}$ and $\overline{B_p}$ are the averaged values of the two binary maps. It is obvious that the higher cross-correlation coefficient indicates that more significant grains are retained after orientation processing.
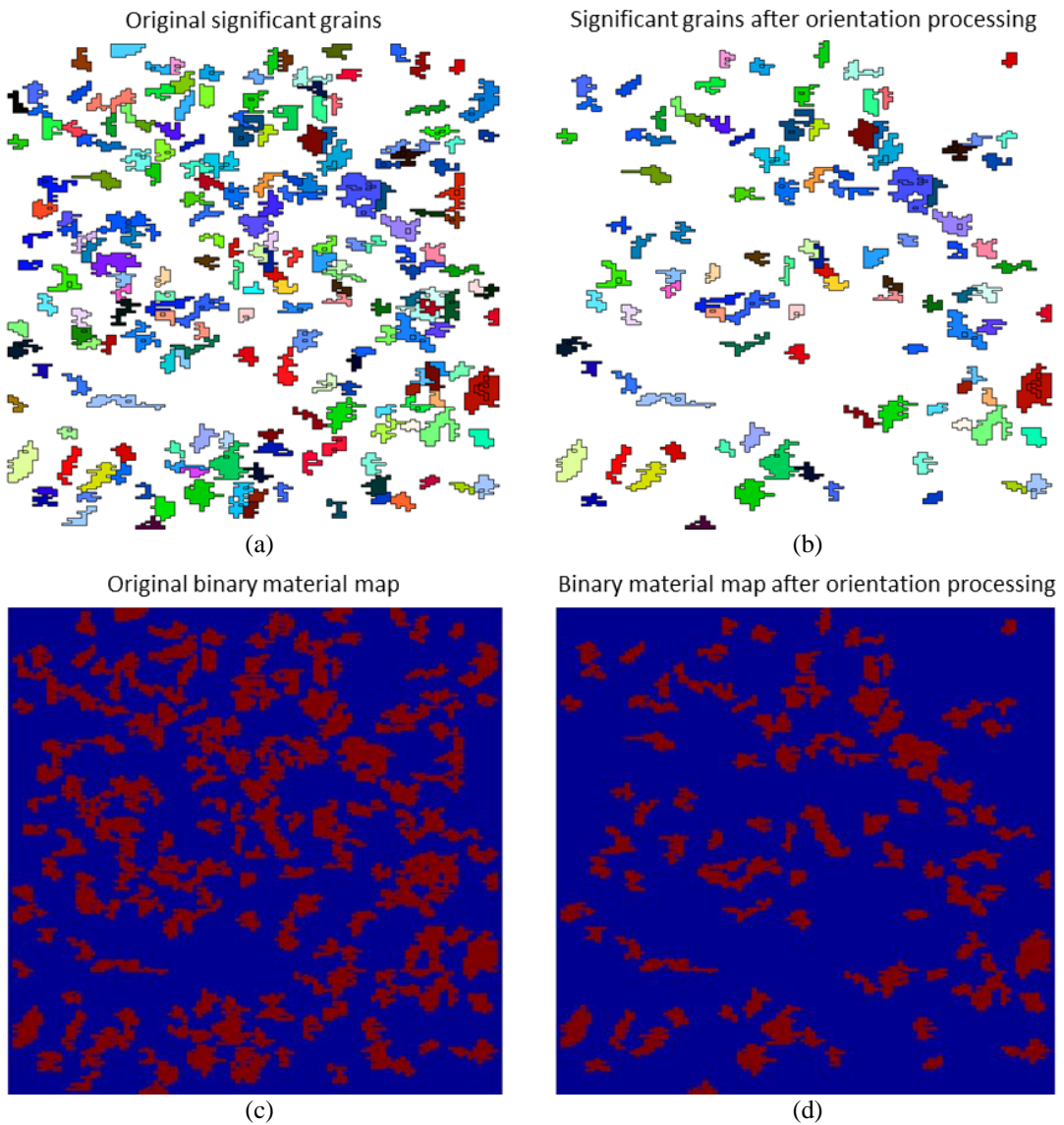
Fig. 3.9: Schematic plot of: (a)-(b) the distributions of the original and processed significant grains; (c)-(d) the two respective corresponding binary material maps.

The second metric considers the root-mean-square error (*RMSE*) of the Euler angles of the elements of the significant grains introduced by bin unification. It is formulated as

$$RMSE = \sqrt{\frac{\sum_{i=1}^{N}\sum_{k=1}^{3}(E_0(i,k) - E_p(i,k))^2}{3*N}}$$

Eq. 3.2

where *N* is the number of the elements of the significant grains; E_o and E_p are the original Euler angles and the processed ones, respectively.

By considering *RMSE* and *C*, a cost function *T*, relating the model pre-processing time, *Time,* to these two metrics can be written

$$T = \frac{RMSE * Time}{C}$$

Eq. 3.3

The *T* has a unit of degree*second and represents the trade-off between pre-processing overhead and model fidelity. The trade-off will be optimised when the *T* reaches its minimum. Fig. 3.10 shows how the *T* changes with the size of the bin for both the EB and GUEB processing approaches. The GUEB approach consistently yields lower *T* values than EB approach. This is explained by that the GUEB approach performs better in preserving significant grains than the EB approach. Particularly, *T* value of EB is around 47% higher than the GUEB counterpart at the bin size of 15 degrees per Euler phase. *T* is observed to reach the minimum value at the bin size of 15 degrees per Euler phase for both EB and GUEB approaches. In this case, for the GUEB approach, the *RMSE* of the Euler angles of significant grains is approximately 4 degrees per Euler phase and the pre-processing overhead is measured as only 12 seconds. This amount of pre-processing overhead is trivial when compared to the ~2 minutes of processing time required to simulate the wave propagation in a round-trip path length of ~150 mm (125λ). Therefore, the overall modelling overhead now is ~2.2 minutes. This is contrast to the ~42 minutes (the sum of 40 minutes of pre-processing and 2 minutes processing) of modelling overhead with no orientation processing applied. This indicates that the orientation processing significantly reduces the computational overhead by ~20 times for the Inconel 617 sample whilst maintaining model fidelity.
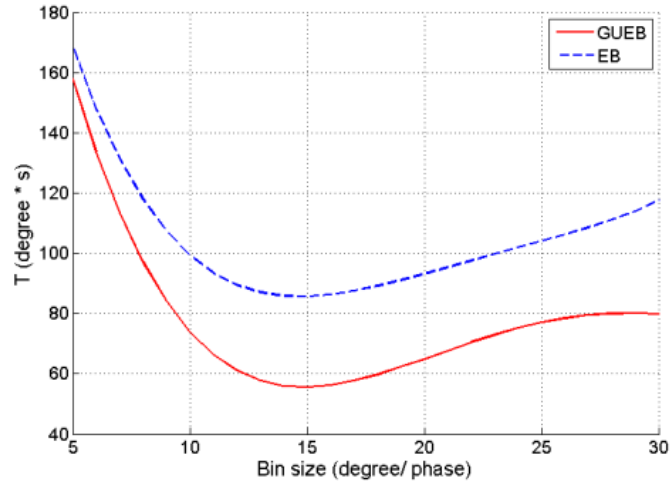
Fig. 3.10: The trade-off between pre-processing overhead and model fidelity as a function of the bin size.

Fig. 3.11 displays the distribution of significant grains within the original material map in (a), within the material map processed by EB in (b), and within the material map processed by GUEB in (c), when the Euler space is quantised at the bin size of 15 degrees per Euler phase. In all figures, the red region surrounding the keystone shaped sample is the background; the irregular and coloured components are significant grains and each colour presents a unique orientation; the white background is for insignificant grains which are not plotted individually. A large loss of significant grains is readily discerned in the EB processing result and the value of *C* (defined in Eq. 3.1) is calculated as approximately 0.62. By contrast, the GUEB approach almost retains all the significant grains and *C* is calculated as approximately 0.95.

Therefore, the orientation data of the Inconel 617 sample is processed by GUEB with the bin size of 15° per Euler phase and misorientation angle of 10° and are then used to construct an FE model for later investigation of anisotropic focal law. The existing FE model of the austenitic steel weld constructed by the Harvey et al. [55] is also used for later investigation of anisotropic focal law.

Distribution of original significant grains

(a)

Distribution of significant grains after EB processing

(b)

Distribution of significant grains after GUEB processing

(c)
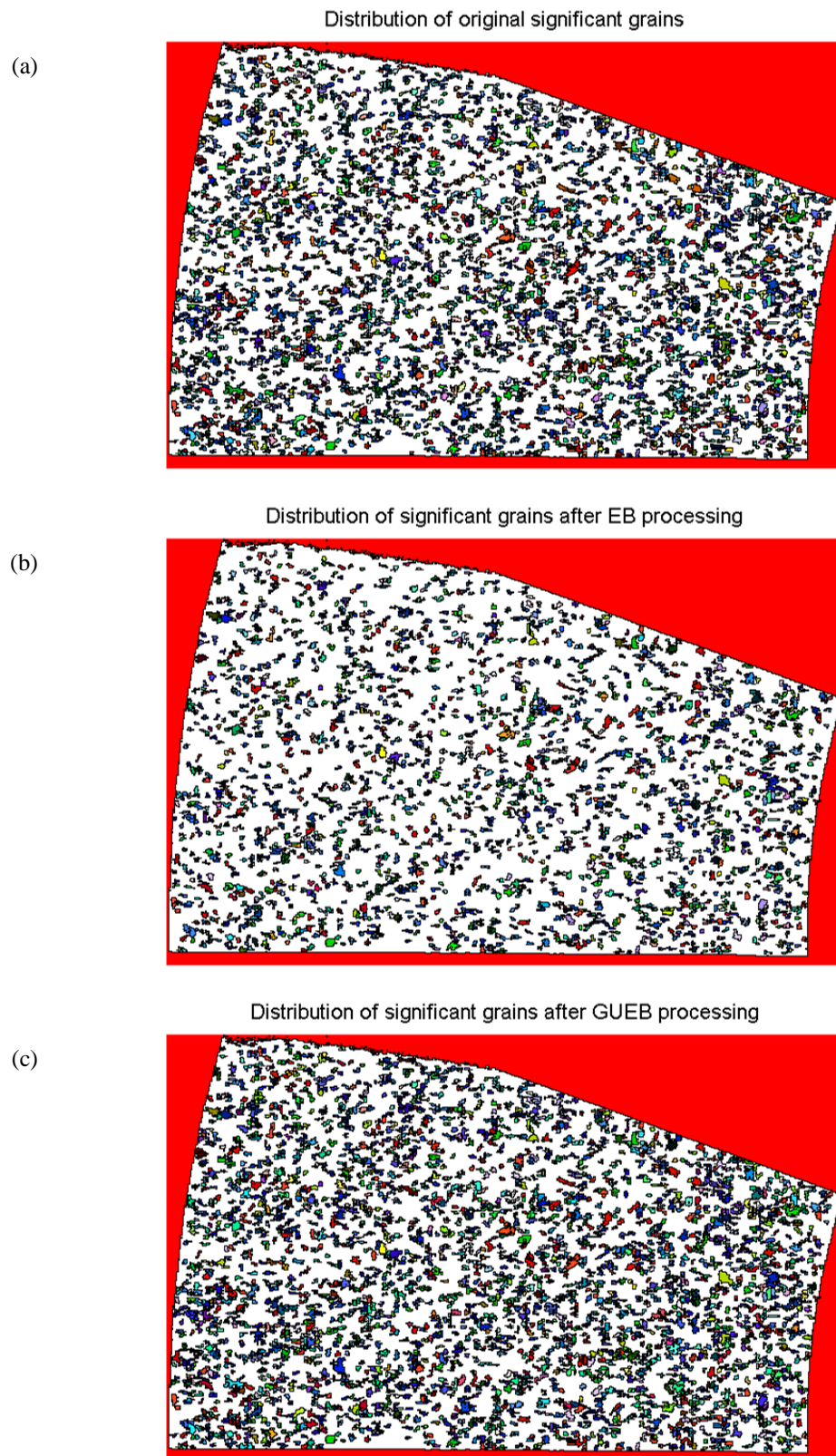
Fig. 3.11: Distribution of the significant grains in the Inconel 617 sample in the cases of: (a) original data; (b) after EB processing; (c) after GUEB processing.

3.4   Determination of anisotropic focal law

3.4.1   Time reversal techniques

In the process of a common TRM technique [70, 71], the reflection signal received by a probe is recorded and then the probe retransmits the reversed version of the reflection signal. In the application of time reversal method for generating anisotropic focal laws, array elements typically only record the arrival time of the reflection signal by a target at the element locations instead of the whole reflection signal, as with [64]. Then the time delay sequences applied to array elements in the isotropic focal law are modified according to the reversal of the recorded arrival time to generate the anisotropic focal law. The anisotropic focal law compensates for both the geometric path length difference and the phase shift to each element of the phased array, thus, can provide a tight focus at the target.

To enable the online implementation of time reversal method during the inspection, the arrival time of echoes from the defect of interest at array elements, in other words, the locations of defect echoes in the signals captured by array elements, must be easily identified. For simple materials, the echoes from a defect are readily identifiable in the captured signals due to the overwhelming amplitude of defect echoes over grain noise; the time reversal method can, therefore, be easily implemented online during inspection to achieve tight focus at the defect. Unfortunately, it is usually not the case for inspecting coarse-grained materials. Instead, the defect echoes are usually obscured by the high level of backscattered noise thus their arrival time at element locations are unidentifiable.

Nageswaran et al. in TWI used the high-fidelity model of the austenitic steel weld to estimate the arrival time of the reflected signal by a SDH target at the element locations [79]. The model was constructed in CIVA platform and only resolved the interaction of the interrogating ultrasound with the SDH target, i.e., the interactions of the ultrasound with grain boundaries were not evaluated, such that no backscattered noise signals were predicted and so the arrival time is readily identified. In the model, an element-by-element pulse-echo time reversal approach was applied to determine the

elemental arrival time of the SDH echoes [79]. As schematically plotted in Fig. 3.12 (a), in this approach a phased array was simulated and positioned above the sample and the pulse-echo response (with only SDH echoes due to no prediction of backscattered noise) of each element was recorded in turn from which the arrival time was obtained.

Here another time reversal method is investigated which is schematically plotted in Fig. 3.12 (b). In this method, an omnidirectional pressure load is applied at the target focal point in the simulation, and then the arrival time of the pressure load at each element location is measured. The target focal point is active, i.e., emitting sound energy itself, in this time reversal method, which is contrary to the aforementioned element-by-element pulse-echo based approach having a passive target focal point – in the current context, the former method is termed active time reversal and the latter is termed passive time reversal. The active approach needs the simulation to run only a single-trip time instead of multiple round-trip times required by the passive time reversal approach – this significantly reduces the time in the model of determining the arrival time of all array elements.

(a)   (b)
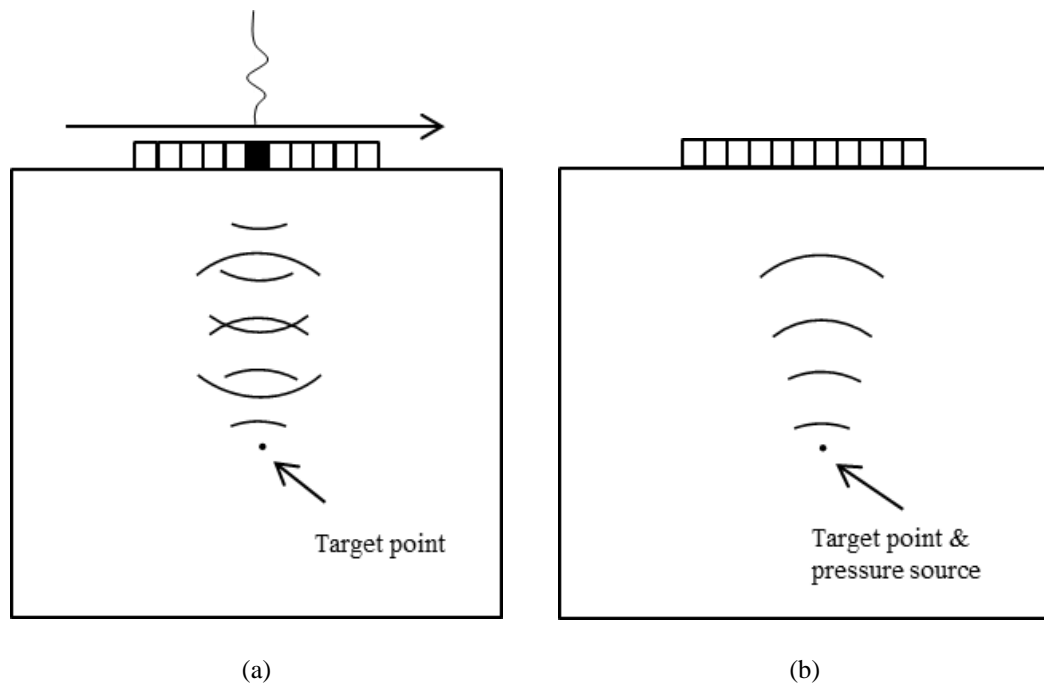
Fig. 3.12: Schematic diagram of the: (a) passive time reversal method and (b) active time reversal method

3.4.2 Anisotropic focal law analysis

In order to determine the anisotropic focal law, the simulation of wave propagation using the active time reversal method (referred to as time reversal simulation for brevity for the reminder of the Thesis) is conducted within the FE model of the Inconel 617 sample constructed in Section 3.3 and the FE model of the austenitic steel weld constructed by the Harvey et al. [55]. The details for the two samples are sequentially given as follows.

3.4.2.1   Inconel 617 case

In order to simulate the practical inspection scenario, a 5 MHz linear phased array with a pitch size of 0.7 mm and 32 elements is also constructed in the model, placed on the top of the sample. The simulated array is configured to exhibit a comparable impulse response and corresponding bandwidth to the Vermon array described in Table 2.1. Each array element can be stimulated individually which allows the application of any focal laws. The model geometry is shown in Fig. 3.13(a), where the yellow background is set as water; the green block at the top is the backing layer of the array; the ceramic-and-polymer layer of the array is sandwiched between the backing layer and the material map; different colours in the material map represent different crystallographic orientations.

In order to reveal the phase aberration induced by the complex microstructure, another model with isotropic Inconel 617 material is constructed. The model geometry for the isotropic case is shown in Fig. 3.13(b). The definition of isotropic materials requires the density ρ, longitudinal velocity V_L and shear velocity V_S to be specified. The two velocities are related to the elastic constants of the isotropic material:

$$V_L = \sqrt{\frac{E(1 - \mu)}{\rho(1 + \mu)(1 - 2\mu)}} \qquad\qquad \text{Eq. 3.4}$$

$$V_S = \sqrt{\frac{E}{2\rho(1 + \mu)}} \qquad\qquad \text{Eq. 3.5}$$

where E is the young's modulus and μ is the Poisson's ratio. For this Inconel 617 material, the two velocities are 5870 m/s and 3089 m/s for V_L and V_S, respectively.

Time reversal simulation is conducted within both the isotropic and anisotropic models. The differences in the arrival time at the element locations between the isotropic and anisotropic models are considered to be the elemental phase shifts. The details are given as follows.

(a) (b)
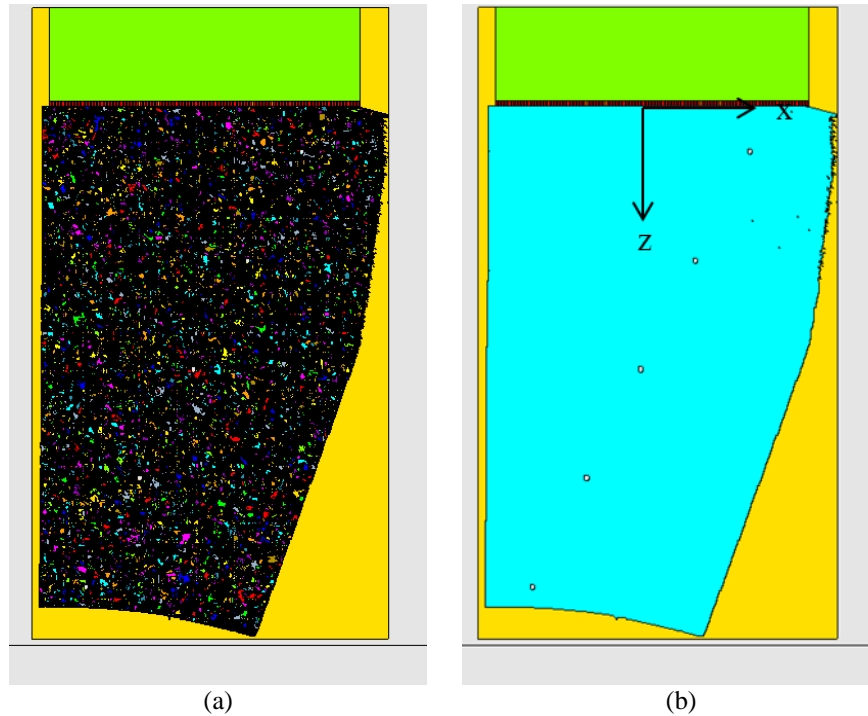
Fig. 3.13: The FE model of the Inconel 617sample for the: (a) anisotropic case and (b) isotropic case.

As shown in Fig. 3.13, five SDHs with a diameter of 0.5 mm (approximate 0.4λ) are inserted in both the models in order to investigate the phase aberration at various depths and positions. The locations of the five SDHs are listed in Table 3.1. The coordinate frame is set with its origin at the intermediate point of the array, shown in Fig. 3.13(b). For simplicity purpose, these five SDHs are named as SDH1~5 according to their depths. Amongst the five SDHs, SDH5 has the largest distance to the array so that it is deemed to exhibit the most severe phase aberration thus is chosen to conduct the time reversal simulation. An omnidirectional 5 MHz pressure load with Blackman-Harris window shape is applied at the SDH5. The time domain response of each array element is recorded.

SDH No.	1	2	3	4	5
(x, z) in mm	(10, 5)	(5, 15)	(0, 25)	(-5, 35)	(-10, 45)

Fig. 3.14 compares the time domain response of the 16th element in the array for the isotropic and anisotropic cases. It is observed that the signal amplitude in the anisotropic case is much smaller than the isotropic case, indicating strong attenuation induced by the complex microstructure. It should be explained that the pressure load emanating from the SDH5 is reflected by the two side walls of the material which is captured by array elements, resulting in the signal of a considerable high magnitude after the first reception of pressure for the isotropic case.
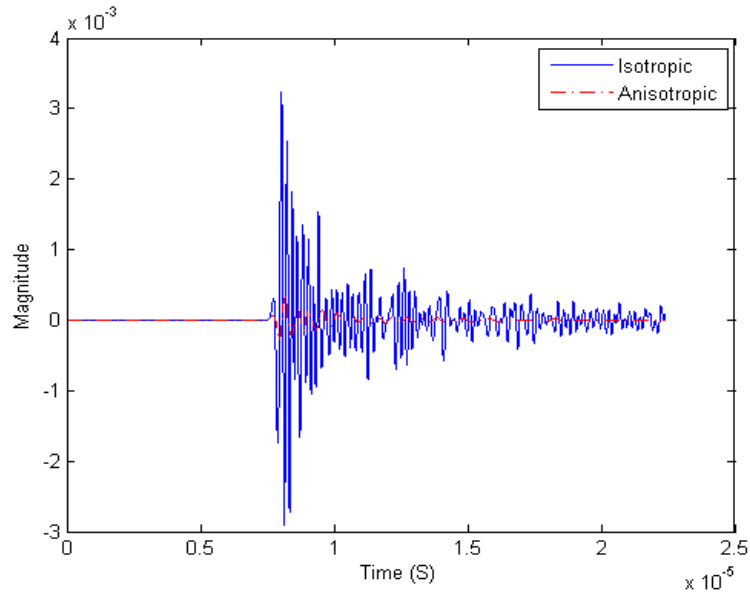
Fig. 3.14: Time response of the 16th array element in the model of the Inconel 617 sample.

The exact value of arrival time is obtained from the time domain response for each array element using zero-crossing detection – the corresponding time of the first sampling point at which the received signal has a different sign from the next neighbouring sampling point in time sequence is denoted as the arrival time.

Fig. 3.15(a) compares the arrival time on an element-wise basis for a pressure load applied at SDH5 for the isotropic and anisotropic material models. The phase aberration

induced by microstructure is manifested in that arrival time of the anisotropic and isotropic cases are different. Specifically, the arrival time at the first 12 array elements in the anisotropic case are slightly larger than that in the isotropic case while arrival time at other elements in the anisotropic case are slightly smaller than their isotropic counterparts. The difference in arrival time between the two cases is calculated as a phase shift, which can give a direct indication of the severity of phase aberration. The calculated phase shifts are also depicted in Fig. 3.15(a). The phase shifts are found to have a range of -0.66π~0.47π radians. Such a low variability of phase shift could be explained by that although the propagating wavefronts encounter grains exhibiting a range of sound velocities arising from the variation of grain orientation, the contributions from the velocity variations are statistically neutralised since a large number of grains exist within the propagation path of the wavefront and their crystallographic orientations are random. Therefore, the sound velocity exhibits no or an insignificant degree of direction dependence. The other four SDHs are expected to have an even lower variability of phase shift than the SDH5 due to their smaller distances to the array.

From Fig. 3.15(a) since the variability of the phase shift as a function of array element position is minimal, it is, therefore, reasonable to expect that performing array imaging using isotropic focal laws will result in acceptable focusing quality in such a sample. This will be discussed in more detail.

Fig. 3.15 (b) compares the signal amplitudes of all the 32 array elements between the isotropic case and anisotropic case. For both cases, the amplitude profiles have similar shape; the highest amplitude occurs at the sixth element which has the shortest distance to SDH5 and the amplitudes diminish gradually towards the outermost elements of the array. It is observed from the figure that the amplitude differences between two cases are in the order of -20 dB. Such strong attenuation for the anisotropic material is attributed to the larger number of grain boundaries within the propagation paths between the source and receiver positions. Therefore, for the case of the Inconel 617 sample being inspected with a 5 MHz phased array, the attenuation problem is more prominent than phase aberration.

(a)   (b)
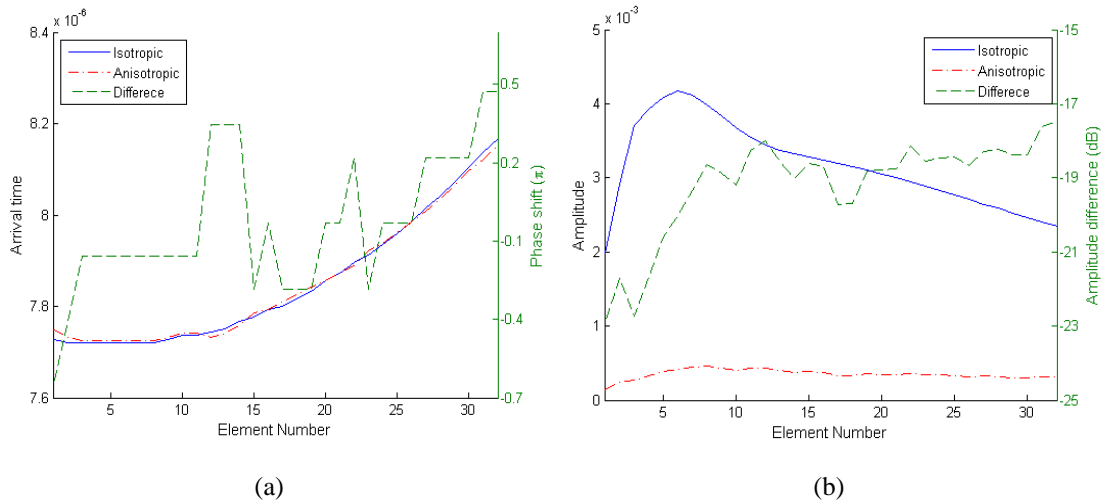
Fig. 3.15: FE model derived comparison of the isotropic and anisotropic cases of the Inconel 617 sample in terms of: (a) arrival time and (b) signal amplitude.

To visualise the focusing quality using the isotropic focal laws, the two FE models are employed to collect two FMC datasets. The acquired data are then used to construct TFM images using isotropic focal laws for both the anisotropic and isotropic cases with a velocity of 5870 m/s. The two TFM image are shown in Fig. 3.16 with a dynamic range of 40 dB. Reflections from side walls are responsible for the noise at the region near to the array in Fig. 3.16(a) for the isotropic case; whilst grain scattering are responsible for the speckle noise in Fig. 3.16(b). The isotropic focal law is found to perform well for the anisotropic material since all the five SDHs are well-focused. This verifies the previous deduction that the phase aberration is inconsequential for the equiaxed-grained Inconel 617 material. However, it is readily observed that the image of the anisotropic material case has worse spatial resolution than the isotropic counterparts and the amplitudes of SDH3~5 on the image are lower than the isotropic counterparts. This is attributed to the low-pass filtering effect of the anisotropic material resulting from the frequency-dependent attenuation.

(a)   (b)
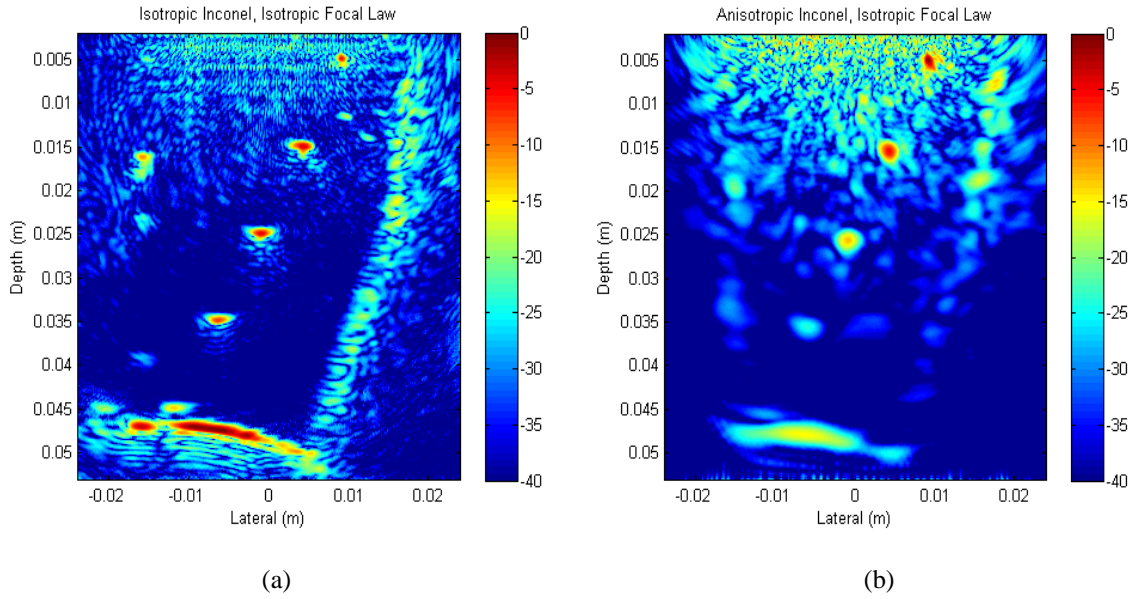
Fig. 3.16: FE model derived TFM images of the Inconel 617 sample for the: (a) isotropic case and (b) anisotropic case. 40 dB display range applied.

3.4.2.2   Austenitic steel weld case

For the austenitic steel weld case, a 1.5 MHz linear phased array with a pitch size of 2 mm and 32 elements is constructed in the model, placed on the top of the sample. The model geometry is shown in Fig. 3.17(a). In order to reveal the phase aberration induced by the complex microstructure, another model with isotropic weld and the same array is constructed, shown in Fig. 3.17(b). Using Eq. 3.4 and Eq. 3.5, the longitudinal velocity and shear velocity are calculated as 5750 m/s for and 3127 m/s, respectively. Similar to the Inconel 617 case, five SDHs with a diameter of 2 mm (0.67λ) are inserted in both the models in order to investigate phase aberration at various depths and positions. The coordinates of the five SDHs are listed in Table 3.2. Again, the coordinate frame is set with its origin at the intermediate point of the array, and for simplicity purpose, these five SDHs are named as SDH1~5 according to their depths. The time reversal simulation is conducted on SDH3 at the first step of the analysis. An omnidirectional 1.5 MHz pressure load with Blackman-Harris window shape is applied at the SDH3. The time domain response of each array element is recorded.
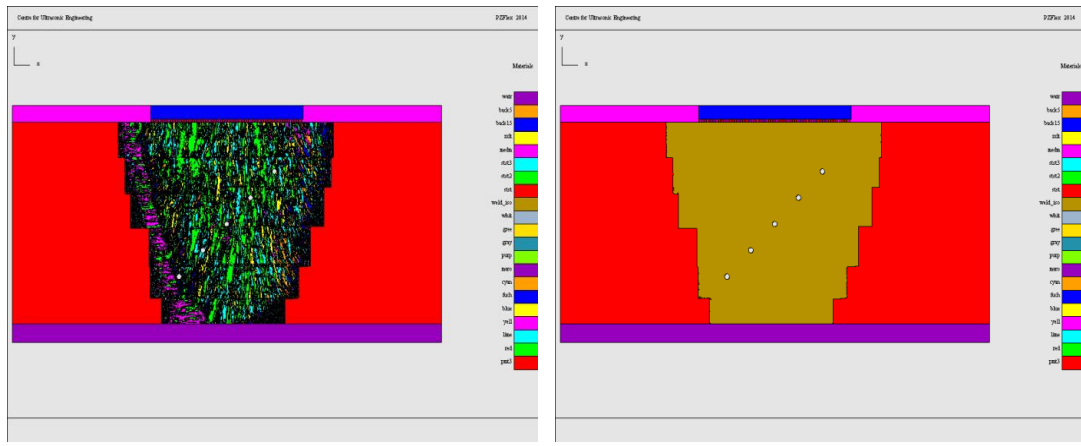
(a)   (b)

Fig. 3.17: The FE model of the austenitic steel weld for the: (a) anisotropic case and (b) isotropic case.

Table 3.2: Coordinates of the five SDHs inserted in the two austenitic steel weld models

SDH No.	1	2	3	4	5
(x, z) in mm	(20, 20)	(10, 30)	(0, 40)	(-10, 50)	(-20, 60)

Fig. 3.18 compares the time domain response of the 16th element in the array for the isotropic and anisotropic cases. As with the Inconel sample, the signal amplitude in the anisotropic case is found to be much smaller than that in isotropic case, indicating strong attenuation induced by the complex microstructure. It is also evident that the propagation of the wavefront is affected by the anisotropic microstructure, resulting in the arrival time being later than that observed in the isotropic case.
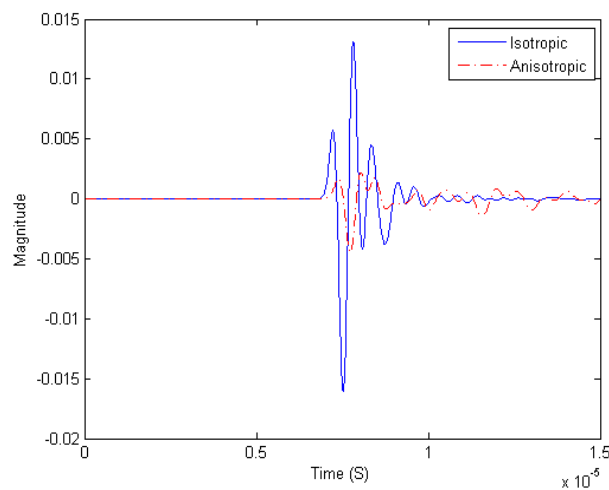
Fig. 3.18: Time response of the 16th array element in the model of the austenitic steel weld.

81

Fig. 3.19(a) compares the arrival time on an element-wise basis for a pressure load applied at SDH3 for the isotropic and anisotropic material models. Again, these arrival time are obtained using zero-crossing detection. The phase aberration induced by the complex microstructure is revealed by that the arrival time at the 12th~27th elements in the anisotropic case are larger than the isotropic case whilst arrival time at other elements are smaller. The phase shift between the isotropic case and the anisotropic case is calculated and plotted in Fig. 3.19(a) to give an indication of the severity of phase aberration. The phase shifts are found to have a range of -2.6π~5.3π radians which is much larger than that of the Inconel 617 sample. Such a high variability of phase shift could be explained by that the columnar-grained microstructure of the austenitic steel weld renders the large elemental variability of sound velocity.

From Fig. 3.19(a) since the variability of the phase shift as a function of array element position is significant, it is, therefore, reasonable to expect that the isotropic focal law will not be appropriate in this case and the determination of an anisotropic focal law is desirable. This will be described in more detail.

Fig. 3.19(b) compares the signal amplitudes of all the 32 array elements between the isotropic case and anisotropic case. The amplitude profile in the anisotropic case is observed to be very different from the profile in the isotropic case; the highest amplitude for the anisotropic material occurs at the sixth element instead of the middle element which is nearest to the SDH3. The amplitude differences between the two cases are in the range of -17~3 dB. The significant variability of amplitude differences indicates the attenuation within the anisotropic weld material is directionally dependent arising due to the columnar-grained microstructure of the austenitic steel weld.

(a)   (b)
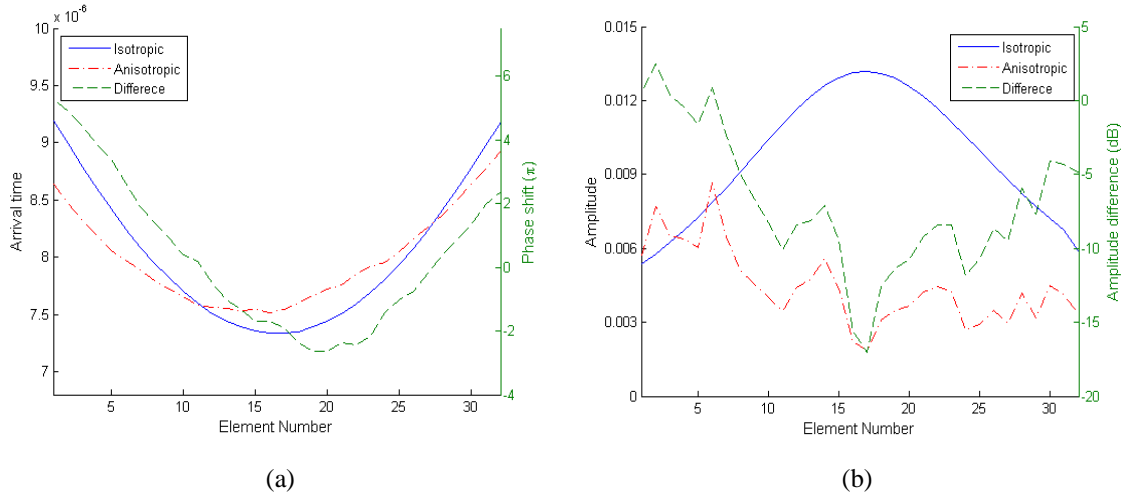
Fig. 3.19: FE model derived comparison of the isotropic and anisotropic cases of the austenitic steel weld in terms of: (a) arrival time and (b) signal amplitude.

To visualise the focusing quality using isotropic focal laws, the two models are employed to collect two FMC datasets. The acquired data which are then used to construct TFM images using isotropic focal laws for both the anisotropic and isotropic cases with a velocity of 5750 m/s. The two images are shown in Fig. 3.20(a)-(b) with 40 dB dynamic range. It is observed in Fig. 3.20(b) that SDH1 and SDH2 are well focused, and SDH3 is poorly focused and its location is shifted, whereas the SDH4 and SDH5 are completely unfocused. This is as expected since the deeper SDHs suffer more severe phase aberration due to the longer sound propagation path. Therefore, anisotropic focal laws are required to restore focusing quality at SDH3~5.

The corresponding time of the phase shifts drawn as the green dash line in Fig. 3.19(a) is subtracted from the isotropic focal law required for normal TFM. The subtraction result is the anisotropic focal law which is used along with the FMC data to construct the TFM image shown in Fig. 3.20(c). For brevity, this anisotropic focal law generated by conducting time reversal simulation at SDH3 are named anisotropic focal law-SDH3 and other anisotropic focal laws are named in the same manner. It is clearly observed in Fig. 3.20(c) that with the use of anisotropic focal law-SDH3 the SDH3 is restored to the isotropic case in terms of position and sizing. SDH4 is also restored to the isotropic case in sizing but its location is shifted by around 3 mm in the *z* direction and 2 mm in the *x* direction. The focusing of SDH5 is seen to be slightly enhanced but still very poor and its location is greatly shifted. This means the anisotropic focal law-SDH3 is only

suitable for removal or alleviation of phase aberration problem for the vicinity region of SDH3. In order to restore the SDH4 and SDH5, the time reversal simulation is required at their locations to generate anisotropic focal law-SDH4 and anisotropic focal law-SDH5. The TFM images using anisotropic focal law-SDH4 and anisotropic focal law-SDH5 are shown in Fig. 3.20(d) and (e), respectively.

To quantify the effect of the application of the anisotropic focal law on improving focusing (i.e., sizing), the Array Performance Index (API) is defined as [32]

$$\text{API} = \frac{Area_{-6dB}}{\lambda^2} \qquad\qquad \text{Eq. 3.6}$$

where $Area_{-6dB}$ is the area within which the intensity is greater than -6dB of the maximum value in a defined region on the TFM image, λ is the wavelength. For each SDH, the defined region is a 10 x 10 mm square centred at the centre of the SDH on images. The maximum value within each region is also recorded as an indicator of the inspection sensitivity and defect detectability. In addition, positions of the SDHs on the images are also recorded to evaluate the effectiveness of the anisotropic focal law on restoring defect positions.

(a)

(b)

(c)

(d)

(e)
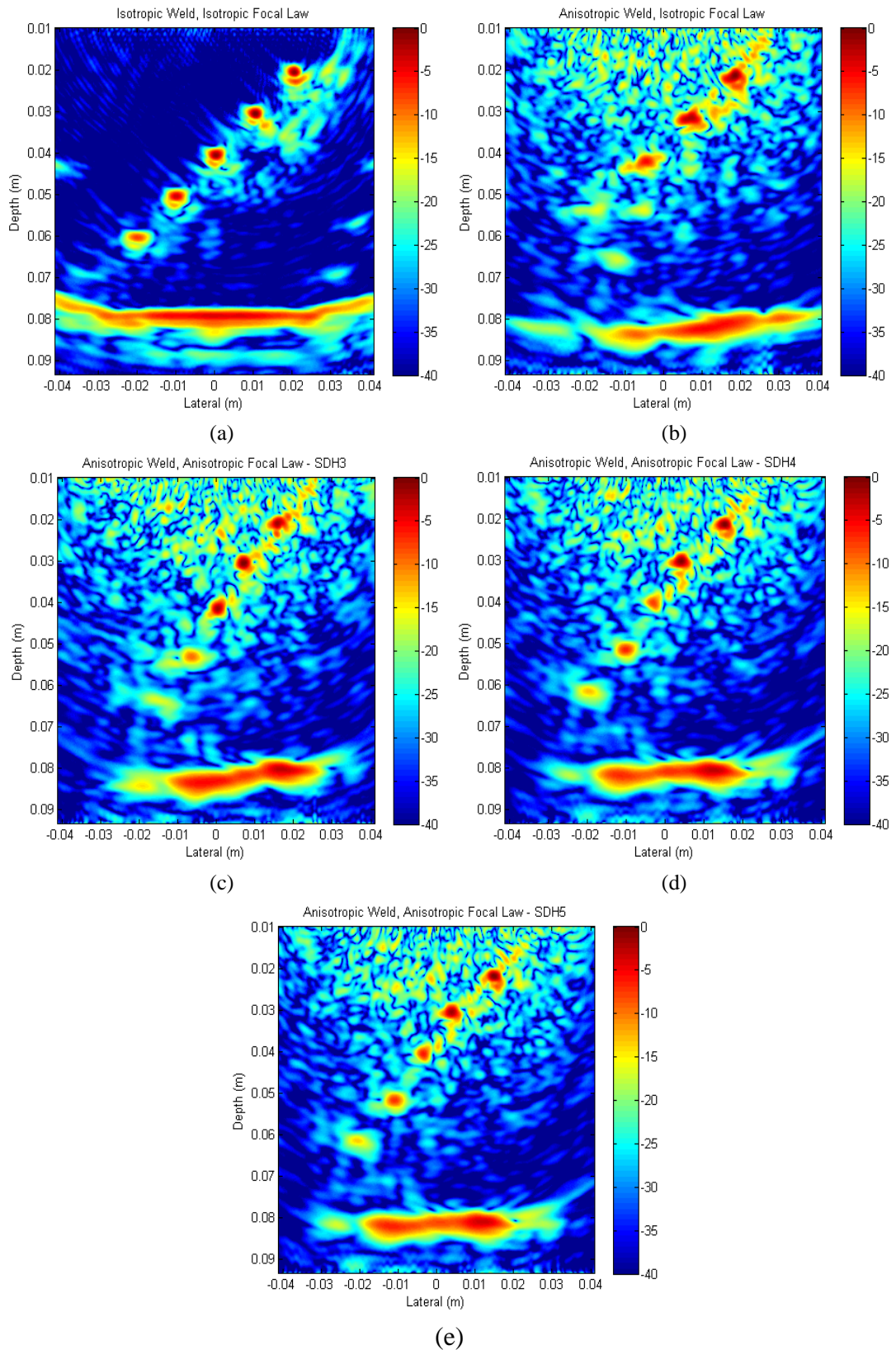
Fig. 3.20: FE model derived TFM images of the austenitic steel weld for the (a) isotropic case; (b) anisotropic case with isotropic focal law; (c-f) anisotropic case with anisotropic focal laws-SDH3~5

The three metrics, i.e., inspection sensitivity, API, and the defect locations, at various cases of materials and focal laws for SDH3~5 are listed in Table 3.3. For each SDH, the three metrics in the case of the isotropic weld with isotropic focal law applied are used as benchmark values for examining the performance of an anisotropic focal law on correcting phase aberration in the anisotropic weld. It is seen from the table that the three metrics for each SDH in the case of the anisotropic weld with the anisotropic focal law of the SDH applied are close to the benchmark values. However, some discrepancies between the two cases are found. For example, for SDH5, the image of the anisotropic weld generated with anisotropic focal law-SDH5 has the sensitivity 9 dB lower, API 0.58 higher than the benchmark values. Also, the location is shifted by 1.3 mm in the z direction. The reasons for discrepancies are given as follows. Attenuation is responsible for the reduced inspection sensitivity; the grain scattering effect of the weld distorts and widens the beam wavefront, the API value is, therefore, larger than the benchmark one; the grain scattering can redirect the beam so that the location of SDH5 is slightly shifted.

An interesting finding in Fig. 3.20(d) and (e) is that all the SDHs are well focused, though some of them are shifted by some distances. To exploit the effectiveness of the anisotropic focal law-SDH5 in improving focusing at SDH4, the three metrics at SDH4 on Fig. 3.20(e) (i.e., the TFM image with the anisotropic focal law-SDH5 applied) are measured and listed in Table 3.3. They are found very close to the values measured at SDH4 on Fig. 3.20(d) (i.e., the TFM image with the anisotropic focal law-SDH4 applied). The three metrics at SDH3 on Fig. 3.20(e) are also measured and listed in Table 3.3 in order to exploit the effectiveness of the anisotropic focal law-SDH5 in improving focusing at SDH3. They are observed to be similar to the values measured at SDH3 on Fig. 3.20(c) (i.e., the TFM image with the anisotropic focal law-SDH3 applied), except the position of SDH3. This would suggest that anisotropic focal laws generated for restoring deeper objects are somewhat applicable to the restoration of nearer objects. The explanation for this is that the anisotropic focal laws for restoring deeper objects correct the phase shifts by a large extent such that the phase shifts for nearer objects may also be corrected.

Table 3.3: Quantitative analysis of the effectiveness of anisotropic focal laws on improving inspection sensitivity, focusing and positioning.

SDH No.	Material	Focal law	Sensitivity (max amplitude in dB)	Sizing (API)	Positioning ((x, z) in mm)
3	Isotropic	Isotropic	-14.03	0.40	(0, 40)
	Anisotropic	Isotropic	-22.74	0.70	(-4.5,42)
	Anisotropic	Anisotropic-SDH3	-18.94	0.43	(0, 40.8)
	Anisotropic	Anisotropic-SDH5	-22.39	0.50	(-3.2,40.5)
4	Isotropic	Isotropic	-16.53	0.49	(-10, 50)
	Anisotropic	Isotropic	-33.44	1.94	(-17.3,53.5)
	Anisotropic	Anisotropic-SDH4	-23.20	0.61	(-10, 51)
	Anisotropic	Anisotropic-SDH5	-23.41	0.63	(-11,51.7)
5	Isotropic	Isotropic	-20.76	0.66	(-20, 60)
	Anisotropic	Isotropic	N/A	N/A	N/A
	Anisotropic	Anisotropic-SDH5	-29.80	1.14	(-20, 61.3)

3.5 Discussions

It has been shown that the orientation map of the Inconel 617 sample obtained by SRAS is in agreement with the one obtained by EBSD. This means that the ability of SRAS to determine the crystallographic orientation of complex polycrystalline materials is validated and it is qualified as an alternative of ESBD. EBSD requires the surface roughness less than 10 nanometres and the sample size is often limited by the size of

SEM - typically in the order of 10 mm. On the other hand, SRAS can tolerate surface roughness on the scale of 100 nanometres, has no restriction on sample size, and is completely non-destructive. The use of SRAS can significantly enhance the practical applicability of the high-fidelity modelling approach, opening the possibility of the application of the approach to a wider range of components.

The time cost is another important factor to consider. Table 3.4 shows that it costs 60 milliseconds to obtain the orientation of a scanning point of the Inconel 617 sample using EBSD, including acquisition and processing. SRAS technique costs 4 milliseconds to acquire an SAW velocity for a scanning point of the Inconel 617 sample. The SAW velocities are measured in 19 directions so that the total acquisition time for a scanning point is 76 milliseconds. The processing time of SRAS for each point, i.e., derivation of the orientation from the SAW velocities, is 500 milliseconds using a computer with a 4-core processor. That is, for scanning the same material at the same step size, the time cost of SRAS is approximately ten times of that of EBSD. It is admitted that this is the major disadvantage of the current SRAS technique over EBSD, however, it is believed that the processing time and so the total time cost can be significantly reduced by applying more computing resources or advanced parallel computing techniques.

Table 3.4: Comparison of scanning resolution and time cost of ESBD and SRAS on examining the Inconel 617 sample

Techniques	EBSD	SRAS
Pixel size (μm)	10 x 10	25 x 50
Acquisition time (ms)/point	60	4
Processing time (ms) /point		500

As the last step of the proposed high-fidelity modelling approach, a matrix of location-dependent anisotropic focal laws generated within simulations can be programmed into a PAC and are applied in the practical inspection. PAC is programmed to choose a programmed anisotropic focal law which is generated at a location nearest to the desired focal location. Such an approach is effective since an anisotropic focal law can improve

beam focusing not only at the position where the time reversal simulation is performed but also at its vicinity region, as illustrated in Section 3.4.2.2.

For both samples described above, only a slice of the material sample was examined by EBSD and/or SRAS and its orientation data is input into a 2D FE model to determine the anisotropic focal laws. The microstructure is assumed to be uniform along the third direction (the welding direction for the austenitic weld). Hence, the applicability of the anisotropic focal laws generated in the simulation in improving the beam focusing at other regions of the material is uncertain. Fortunately, results in [78] illustrate that the crystallographic orientation distribution is consistent and the dominant orientations are conserved along the welding direction for the austenitic steel weld materials. Therefore, it is suggested that the high-fidelity modelling may be done on a few representative samples and the generated anisotropic focal laws may be generic for the materials manufactured in a similar way [78].

It is worth noting that the high-fidelity modelling approach typically requires much higher cost in terms of expenses and time to implement than other phase aberration correction methods, therefore, it is only applicable to materials in safety critical components such as the safe-end weld of the PWR in the nuclear industry [79].

3.6   Conclusions and future work

The high-fidelity modelling approach for correcting the phase aberration problem induced by the complex microstructures has been presented. The approach replicates the practical inspection within FE simulations. The crystallographic orientations data obtained through material characterisation techniques are processed to construct a cost-effective FE model with high fidelity. Two methodologies of processing orientation data are presented in order to establish computationally efficient FE models of coarse-grained materials. It is observed that the GUEB methodology can remarkably reduce the computational overhead of the FE model of the Inconel 617 sample by 20 times whilst maintaining model fidelity. The FE models are then employed to establish anisotropic focal law based on a proposed time reversal technique.

Previous approaches with regard to the high-fidelity modelling approach mainly employ EBSD and analytical modelling which have been found to be impractical and inefficient. In this chapter, SRAS and FE modelling are proposed to replace EBSD and analytical modelling, respectively. SRAS has been validated as an accurate technique for microstructural characterisation. It has no restriction on sample size and needs less surface preparation than EBSD, thus can significantly enhance the practicability of the high-fidelity modelling approach. The computationally efficient FE simulation platform PZFlex in conjunction with the proposed time reversal technique provide a reliable and rapid solution of the establishment of anisotropic focal laws in the simulation, thus can remarkably improve the operational efficiency of the high-fidelity modelling approach.

Through simulation studies, the Inconel 617 sample, with equiaxed-grained microstructure, is found to be macroscopically elastically isotropic so that the phase aberration problem is on a negligible scale. However, targets at depths over 30 mm are unfocused for the austenitic steel weld which exhibits columnar-grained microstructure. It is observed that the anisotropic focal law generated via the proposed time reversal technique is effective at restoring focusing quality. More importantly, an anisotropic focal law is found to be able to improve the focusing not only at the location of the target at which the time reversal simulation is conducted but also for the nearby region. Additionally, an anisotropic focal law for restoring the focusing at deeper targets are found to be able to improve the focusing at nearer targets by a more or less scale.

Future work consists of three aspects.

For FE models of the both samples, the anisotropy is described only with the variation of crystallographic orientations and the stiffness moduli are assumed constants. In fact, the compositional variation of coarse-grained anisotropic materials has an influence on the stiffness moduli of single crystals. In the ideal case, both the variations of orientations and stiffness moduli should be considered. However, determination of the stiffness moduli of all scanning points is a rather onerous and non-trivial task. Therefore, it is worth investigating the impact of compositional variation on the stiffness moduli. If it is proved the impact is negligible, the assumption of constant

90

elastic moduli is justified. Otherwise, the stiffness moduli have to be determined point-by-point. The investigation is considered as one aspect of future work.

The misorientation angle determines the distribution of grains, consequently determines the backscattering level in simulations. The angle is empirically set to 10 degrees; however, the value is subject to modification due to the backscattering level measured in experiments. This is considered to be another aspect of future work.

The last aspect of future work is to validate the FE models by applying the anisotropic focal laws generated within simulations into practical inspections.

CHAPTER 4. Enhanced   split-spectrum processing with artificial neural network

4.1   Introduction

Frequency diversity forms the theoretical basis of the techniques for grain noise suppression which are evaluated or developed in this chapter and the subsequent Chapter 5. This chapter is arranged as follows. Firstly, an analytical model of the grain scattering process, as a combination of the two existing models described in [38, 94], is introduced. Subsequently, the prevalent frequency diversity based Split Spectrum Processing (SSP) technique for grain noise suppression is evaluated and its combination with artificial neural network (ANN) techniques is proposed to increase its robustness and performance. The focus will be on comparing the performance of two common ANN models used in conjunction with SSP. This chapter concludes with a set of recommendations of which model to choose in various cases.

4.2   Analytical modelling of the backscattering

For both the development and evaluation of signal processing methods, it is prudent to begin with data arising from models of the physical scenario rather than experiment. Once validated, the models allow a wide range of virtual experiments to be undertaken to assess the performance of a signal processing algorithm in various cases of material characteristics and transducer configurations in a time and cost-effective manner. In contrast, such an approach from an experimental standpoint would very quickly become unwieldy.

In this section, a frequency domain based analytical model of the grain scattering process is introduced. Under some adequate assumptions and approximations, this analytical model can become computationally efficient. The theory and formulation of the analytical model are described as follows.

Ultrasonic scattering occurs where there exists an acoustic impedance mismatch at the boundary between adjacent grains. The backscattering amplitude from a grained material is dependent on the transducer configurations, grain size, the extent of impedance mismatch and grain distribution in the volume. Creation of a material backscattering model including all of these factors is rather complicated and somewhat challenging. For the purpose of simplicity, the single scattering assumption is adopted that the grain size and extent of impedance mismatch can be combined as a single parameter, ρ_s, representing the scattering amplitude of an individual grain scatterer [38]. Moreover, the single scattering assumption dictates that the backscattered grain noise can be simply modelled as the superposition of scattering signals from each individual grain scatters embedded in a homogeneous material, that is, the multiple scattering effects between spatially unresolved scatters are neglected. The single scattering assumption is valid only if the wave propagation distance is small and the backscattered signal from each grain is weak relative to the flaw reflectivity. Fortunately, the majority of the scattering regimes in NDE fall within this regime [89].

Importantly, the employment of the single scattering assumption enables the scattering of each individual grain scatterers to be simulated in parallel. Therefore, the backscattered signals in a grained material can be rapidly simulated with the use of advanced parallel computing techniques.

The other two assumptions made in the analytical model are that:

- Each grain scatterer is an omnidirectional scatterer regardless of incident angle

- All grain scatterers have the same reflectivity

Consider a 2D slice of a load medium coupled to a 1D ultrasonic phased array, as shown in Fig. 4.1. A Cartesian coordinate system is employed, where x and z represent locations in the lateral and axial directions, respectively. Fig. 4.1 depicts the ultrasound wave path from a transmitter element tx at $(x_{tx}, 0)$ to the scatterer i at (x_i, z_i) and the

return path to a receiver element rx at $(x_{rx}, 0)$. In the time domain, the received signal $h_{tr}(t)$ for any pair of tx and rx, can be analytically expressed as

$$h_{tr}(t) = \sum_{i=1}^{M} \rho_{si} e^{-\alpha_t d_{i,tr}} p\left(t - \frac{d_{i,tr}}{c}\right) \qquad \text{Eq. 4.1}$$

where ρ_{si} is the scattering amplitude of the scatterer i, α_t is the attenuation coefficient, $d_{i,tr}$ is the propagation distance from the tx to the scatter and to the rx, $d_{i,tr} = \sqrt{(x_{tx} - x_i)^2 + z_i^2} + \sqrt{(x_{rx} - x_i)^2 + z_i^2}$, $p(t)$ is the emitted pulse, M is the number of grain scatters and c is the wave propagation velocity in the material.

Eq. 4.1 gives a quite simple expression of backscattering but ignores the fact, which is of particular importance for the frequency analysis, that the scattering amplitude of grain scatterers and attenuation coefficient are both frequency-dependent. Therefore, a frequency domain approach to modelling backscattering is proposed here.
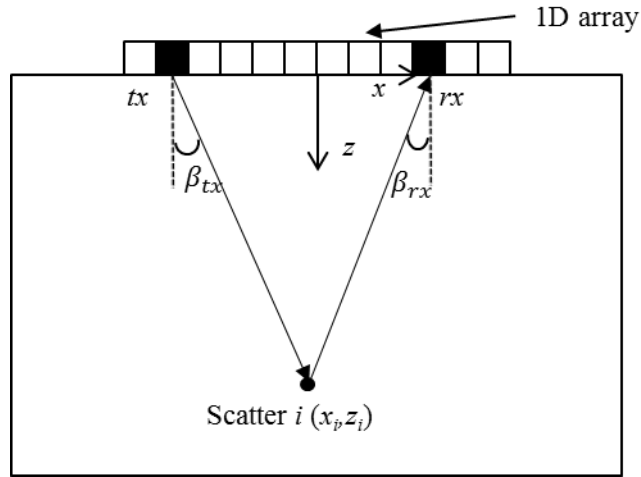
Fig. 4.1: Schematic diagram for the derivation of the analytical model of backscattering

The scattering amplitude by the scatterer i as a function of frequency can be written as

$$\rho_{si}(\omega) = k \frac{\omega^2}{d_{i,tr}} \qquad \text{Eq. 4.2}$$

where k is a characteristic constant of the material determined by the scatterer's reflectivity and geometry and ω is the angular frequency. It is seen in Eq. 4.2 that the

scattering amplitude is proportional to the frequency squared and inversely proportional to the propagation distance.

Based on Eq. 4.2, Gustafsson and Stepinski have conducted detailed mathematical derivation and provided an approximation of the attenuation effect H_{si}^{att} as [119]

$$H_{si}^{att}(\omega) = e^{-\alpha d_{i,tr}\omega^4} \qquad \text{Eq. 4.3}$$

where α is the material attenuation coefficient and its value depends on the composition of the grain scatterers. It is seen in Eq. 4.3 that the attenuation is proportional to fourth power of frequency, indicating that the grained material can be considered as a low-pass filter whose characteristics are determined by the material composition and the wave propagation distance.

By multiplying Eq. 4.2 with Eq. 4.3, the frequency response of the grain scatterer is obtained which can be expressed as

$$H_{si}(\omega) = k\frac{\omega^2}{d_{i,tr}}e^{-\alpha d_{i,tr}\omega^4}e^{-j\omega d_{i,tr}/c} \qquad \text{Eq. 4.4}$$

where the last exponential term denotes the phase shift determined by the wave propagation distance and velocity.

The frequency response of a flaw is considered to be different to that of grain scatterers. A flaw reflects all of the wavelengths comparable to or smaller than its size. Therefore, the reflectivity of a flaw is regarded as invariant within a wide frequency range. By modifying Eq. 4.4, the frequency response of the flaw can be given as

$$H_f(\omega) = \rho_f e^{-\alpha d_{f,tr}\omega^4}e^{-j\omega d_{f,tr}/c} \qquad \text{Eq. 4.5}$$

where ρ_f is the reflectivity of the flaw and $d_{f,tr}$ is the distance from the transmitter to the flaw to the receiver.

Regarding any element of the phased array, its impulse response in the frequency domain is usually modelled as a deterministic Gaussian envelope, $E(\omega)$. This frequency response has to be multiplied by two factors in order to include the effects of beam directivity and beam spread. Again considering the scatterer i, the beam directivity $P_{si}(\omega)$ at the scatterer location can be formulated as

$$P_{si}(\omega) = sinc\left(\frac{\omega e \sin(\beta_{tx})}{2c}\right) sinc\left(\frac{\omega e \sin(\beta_{rx})}{2c}\right) \qquad \text{Eq. 4.6}$$

where e is the array element width (assuming $e \ll$ the element length in the y direction), β_{tx} and β_{rx} are the angles between the z axis and the propagation path of transmitter and receiver, respectively, as shown in Fig. 4.1.

The beam spread effect reduces the transducer amplitude at the location of the scatterer i to $E_{si}(\omega)$ which is given as

$$E_{si}(\omega) = \frac{E_o(\omega)}{\sqrt{\sqrt{(x_{tx} - x_i)^2 + z_i^2}\sqrt{(x_{rx} - x_i)^2 + z_i^2}}} \qquad \text{Eq. 4.7}$$

where $E_o(\omega)$ is the signal amplitude at unity propagation distance.

For the flaw, the beam directivity function $P_f(\omega)$ and the beam spread function $E_f(\omega)$ are formulated as in Eq. 4.6 and Eq. 4.7, respectively.

Now consider the case of a flaw surrounded by M grain scatterers. In the frequency domain, the received spectrum of any tr can be expressed as

$$H_{tr}(\omega) = \sum_{i=1}^{M} P_{si}(\omega)E_{si}(\omega)H_{si}(\omega) + P_f(\omega)E_f(\omega)H_f(\omega) \qquad \text{Eq. 4.8}$$

The inverse Fourier transform of $H_{tr}(\omega)$ can be performed to obtain the time domain signal $h_{tr}(t)$.

4.3   Initial results of split spectrum processing

In order to evaluate the effectiveness of the existing combination algorithms for SSP, an A-scan signal was simulated using the above analytical model. In the model, a single-element transducer was simulated and its spectrum is modelled as a Gaussian window centred at 5 MHz with a fractional bandwidth of 60%. The material was modelled with the characteristic constant $k = 5 \times 10^{-18}$ and attenuation coefficient $\alpha = 5 \times 10^{-30}$ [94]. There were 6000 scatterers randomly distributed within a 10 x 120 mm structure ($c = 5000$ m/s), so the density of the scatterers is calculated as $5/\lambda^2$.

A single flaw was modelled with the reflectivity $\rho_f = 20$ and a distance of 100 mm to the transducer. It should be mentioned that the sampling points corresponding to the first 10 mm of propagation distance in the A-scan signal were zeroed prior to processing. This is to emulate the ring-down effect of the practical transducer leading a dead-zone immediately in front of the transducer. Note that the modelling was performed in Matlab and the code template for the modelling is given in Appendix B.

The derived time domain signal is shown in Fig. 4.2(a). The spectral magnitudes of the flaw echo and the counterpart of the pulse emitted by the transducer are compared in Fig. 4.2(b). Also, the spectral magnitudes of a grain noise segment extracted from the A-scan signal are obtained by Fourier transform and also plotted in Fig. 4.2(b). It is observed that the spectral magnitude of the flaw echo exhibits a similar shape to that of the emitted pulse and has a downward shift due to the effect of frequency-dependent attenuation. This is in contrast to the grain noise, which tends to emphasise the upper part of the spectrum of the emitted pulse, as the net effect of the frequency-dependent attenuation and grain scattering. The spectral difference between flaw echo and grain noise illustrates the authenticity of frequency diversity phenomenon.

(a)　　　　　　　　　　　　　　　(b)
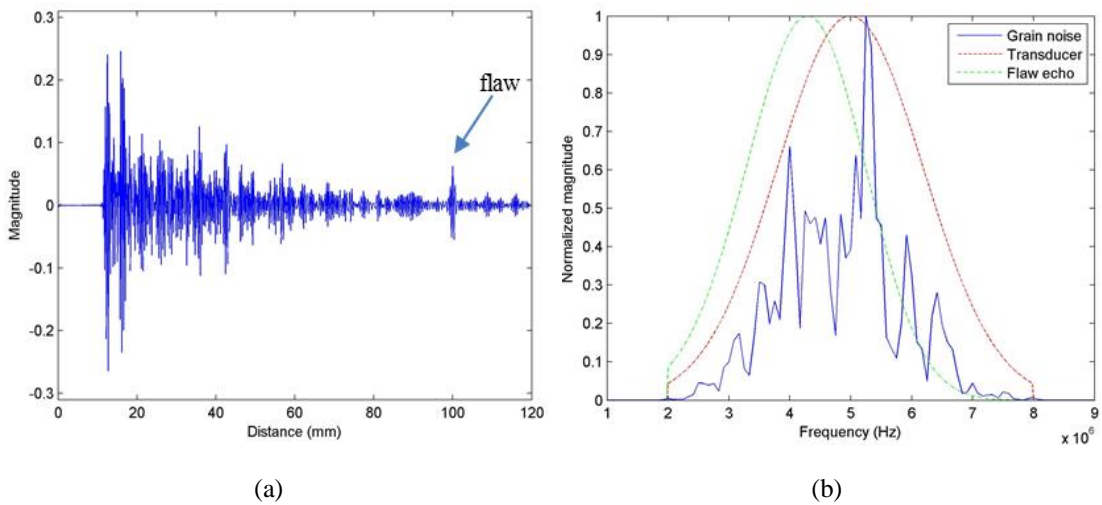
Fig. 4.2: (a) a simulated A-scan signal; (b) spectra comparison.

The simulated A-scan signal was partitioned by 10 equal-bandwidth bandpass Gaussian filters with 25% overlap of each other (total bandwidth is selected as 2~8 MHz) to generate sub-band signals. See Appendix C for the code template of generating sub-band signals. The sub-band signals are then combined using the five previously

described algorithms formulated as Eq. 2.14~Eq. 2.18. The original A-scan signal and the processed results are shown in Fig. 4.3(a). To exemplify the sensitivity of the five combination algorithms to the variation of material characteristics, another A-scan signal was simulated using the same modelling parameters after modifying the spatial distribution of the grain scatterers. This A-scan signal and its processed results by SSP using the same filter bank are shown in Fig. 4.3(b).

The results obtained by MEAN, MIN and FM algorithms show very poor SNR improvement irrespective of the grain distribution. PT algorithm provides considerable SNR enhancement but also introduces several artefacts in Fig. 4.3(a), moreover, the flaw indication at the depth of 100 mm is removed in Fig. 4.3(b). The PTS algorithm retains the flaw echo but gives poor SNR improvement in both cases. Therefore, none of the five combination algorithms is effective in improving SNR meanwhile robust to the variation of material characteristics. In fact, the SNR improvement obtained by the five combination algorithms is highly dependent on the selected parameters of the filter bank and the suitable parameters of the filter bank are typically different for different material characteristics. The sensitivity of the five combination algorithms to the material characteristics necessitates a troublesome interactive tuning process of the filter bank parameters, usually following a trial-and-error procedure. Furthermore, the parameters of the filter bank may require retuning when the material characteristics vary.

Therefore, it is clear that scope exists for an alternative combination algorithm that can effectively improve SNR and is insensitive to the variation of material characteristics. This can be achieved by ANN techniques which demand a training stage. An ANN adapts itself to the selected filter bank and the characteristics of training data after the training. If sufficient training data comprising the variability of material characteristics are used, the trained ANN is insensitive to the variation of material characteristics, therefore, neither tuning nor retuning filter bank parameters is required. Full analysis and evaluation of ANN technique used in conjunction with SSP are given in the next section.

(a)   (b)
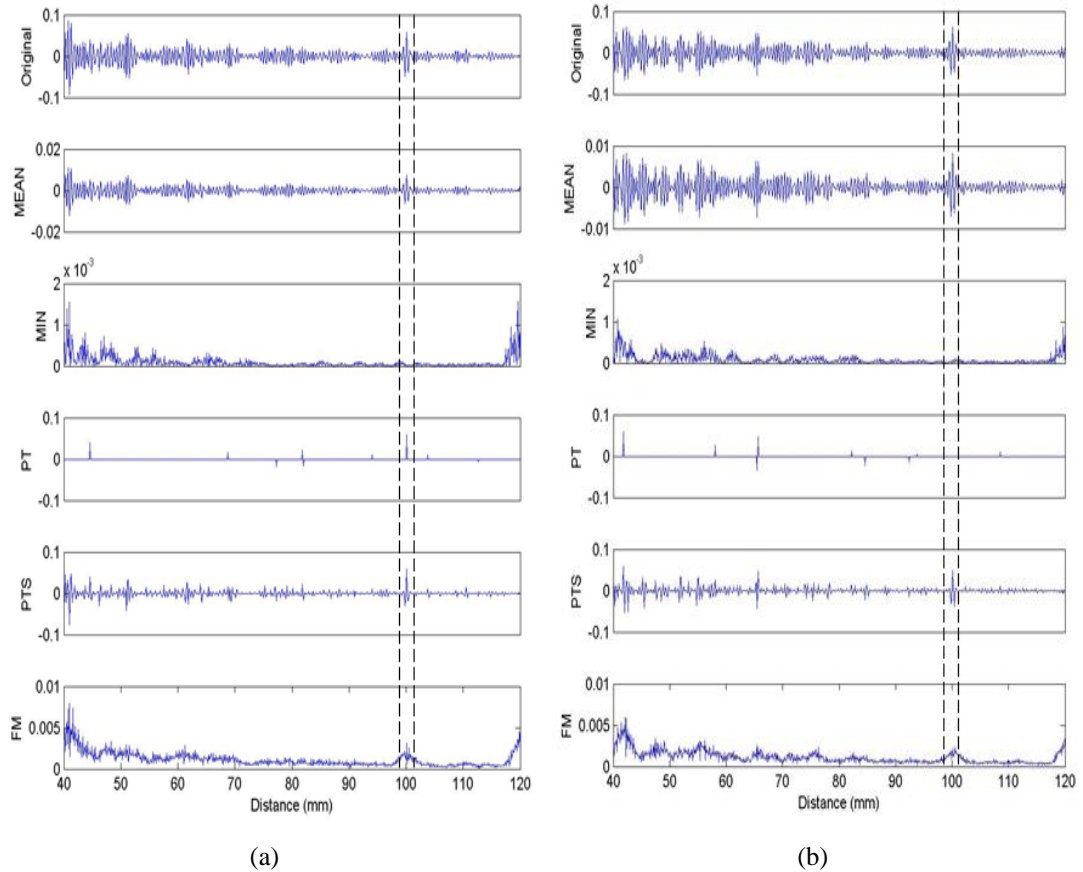
*Fig. 4.3: Conventional SSP processed results of two different realisations of grain distribution,
displayed as (a) and (b), respectively.*

4.4   Combining SSP with artificial neural network

4.4.1 Introduction of artificial neural network

ANN is a branch of pattern recognition discipline that focuses on the recognition of underlying trends and regularities of input data. Pattern recognition techniques are generally categorised into supervised learning and unsupervised learning according to their learning styles. Supervised learning requires a set of prior-known training data with each instance being labelled with the desired output. A network which has undergone sufficient and appropriate supervised training gains the ability to give solutions to unknown input data. On the other hand, unsupervised learning attempts to identify the main features of the training data without labelled outputs. A network which has undergone unsupervised training determines the output of new input data

based on the similarity measure between the main features of the new inputs with the counterparts of the training data.

Inspired by the information processing mechanisms in the biological nervous system, an ANN is usually designed as a parallel computational system with many interconnected processing elements (called neurons). The computational system provides a set of nonlinear algorithms for mapping the input datasets into hyperspaces and performing classification in the hyperspaces. This computational paradigm allows an ANN to learn the complex nonlinear relationship between input and output and thus adapt itself to the training data.

There are two basic neural network models forming the basis for many ANN applications, known as the multilayer perceptron (MLP) and the radial basis function (RBF). These two models belong to a general model class referred to as feedforward network model. Previous work of combining SSP with ANN techniques mostly used MLP model [102, 103]. However, MLP model has several intrinsic limitations which can cause the ANN sometimes to be a burden rather than a benefit [120]. One important limitation is the time cost of the training process. This is because, as what will be described subsequently, MLP model requires an iterative training process to optimise the network weights. Moreover, MLP is more like a 'black box' inside which the data representations and the activations of hidden neurons are difficult to interpret and understand.

In contrast, RBF model typically exhibits a reduced training time and has a much simpler architecture. In spite of exhibiting clear benefits, the combination of SSP and RBF model has received little attention in the literature and, therefore, is carried out in this chapter. In the subsequent analysis, the workflow of the approach of combining SSP with the two ANN models are firstly described and then their performances in terms of training time cost and effectiveness in SNR enhancement are compared. It is noted that all of the training and evaluation of ANN models were conducted in Matlab.

4.4.2 Methodology of combining SSP with ANN

Fig. 4.4 plots the flow chart of ANN techniques used in conjunction with SSP. The process consists of five steps described as follows:

1) The RF A-scan traces are partitioned into K sub-bands A-scan traces by a bank of bandpass filters.

2) A small portion of the sub-band signals consisting of flaw echoes and grain noise are selected as the training data. The desired outputs of flaw echoes and grain noise are labelled as 1 and 0, respectively.

3) The training data are used to train the ANN. The ANN recursively adjusts its parameters and evolves the decision boundary during the training until the termination conditions are met.

4) All the sub-band signals are processed by the trained ANN. The trained ANN classifies each instance of the sub-band signals using the developed decision boundary and produces a coefficient within the range of 0~1 indicating the possibility of a legitimate flaw signal.

5) The coefficients are multiplied pointwise with the RF A-scan traces to obtained the processed A-scan traces.

The detailed training processes for the MLP model and RBF model along with their network architectures are detailed as follows. Appendix D shows a template code for combining MLP and RBF with SSP.
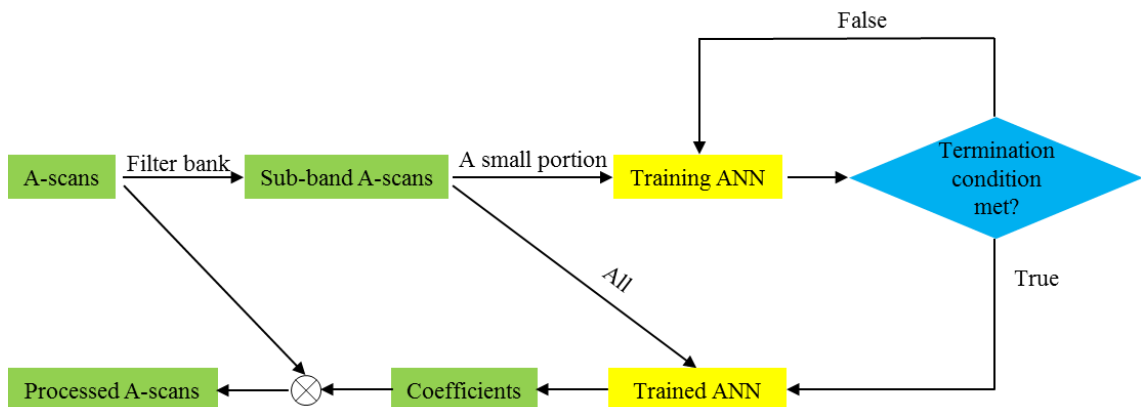
Fig. 4.4: Flow chart of ANN used in conjunction with SSP

4.4.2.1   Training process of MLP model

Fig. 4.5 (a) shows the typical architecture of an MLP model. It is composed of an input layer with K inputs, a hidden layer consisting of N neurons and an output layer with a single neuron. As previously defined, $A_i(n)$ and $Y(n)$ are the output of the ith band and the output of the ANN at the instant n, respectively. The weights between the input layer and the hidden layer, $W_{ih,}$ and the weights between the hidden layer and the output layer, W_{ho}, are randomly initialised as, usually between -1 and 1. All of neurons in the hidden layer and the output layer use a sigmoid function as their activation functions. The purpose of training a MLP network is to minimise the mean square error (MSE) between $Y(n)$ and the target output $T(n)$ by adjusting the two set of weights iteratively using the back propagation (BP) algorithm. In addition, the bias of each hidden neuron b_h and the bias of the output neuron b are also optimised. The system is trained to behave as a binary classifier, that is, $Y(n)$ is forced to be 1 for flaw echo input and is forced to be 0 for grain noise input. The training process is described below:

For each instance n of the training sub-band signals, steps 1 and 2 are undertaken.

1) Feedforward: the input signals are fed into the network. They are multiplied with weights W_{ih} and then the products are summed. The result is used as the input of neurons in the hidden layer which have an activation function of

$$f(x) = 1/(1 + exp(-x))$$ Eq. 4.9

Hence, the output of the neurons in the hidden layer can be expressed as

$$S_h = 1 \bigg/ \left(1 + exp\left(-\left(b_h + \sum_{i=1}^{K} A_i W_{ih}\right)\right)\right), h$$ Eq. 4.10
$$= 1,2, \dots, N$$

The outputs of hidden neurons are multiplied with weights W_{ho} and then the products are summed. The output of the neuron in the output layer whose activation function is also Eq. 4.9 is calculated as

$$Y = 1 \bigg/ \left(1 + exp\left(-(b + \sum_{h=1}^{N} S_h W_{ho})\right)\right)$$ Eq. 4.11

2) Weights updating: the error gradient E is calculated at the output layer

$$E = T - Y \qquad \text{Eq. 4.12}$$

Then E is propagated backwards through the network. So the changes of the two set of weights are calculated as

$$\delta_{w_{ho}} = EY(1 - Y)S_h \qquad \text{Eq. 4.13}$$

$$\delta_{w_{ih}} = \delta w_{ho}S_h(1 - S_h)A_i \qquad \text{Eq. 4.14}$$

The weights are updated with a pre-set learning rate μ and a pre-set momentum η

$$W_{ih}(\text{new}) = \eta W_{ih}(\text{old}) + \mu\delta_{w_{ih}} \qquad \text{Eq. 4.15}$$

$$W_{ho}(\text{new}) = \eta W_{hp}(\text{old}) + \mu\delta_{w_{ho}} \qquad \text{Eq. 4.16}$$

3) Error checking: after all of the time instants have gone through step 2 and 3, the MSE is calculated as

$$\text{MSE} = \frac{1}{L}\sum_{n=1}^{L} (Y(n) - T(n))^2 \qquad \text{Eq. 4.17}$$

where L is the number of training instances.

The three steps are iteratively performed until the MSE value becomes lower than the preset error tolerance (TOL) or the maximum number of allowable iterations (epoch) is met.
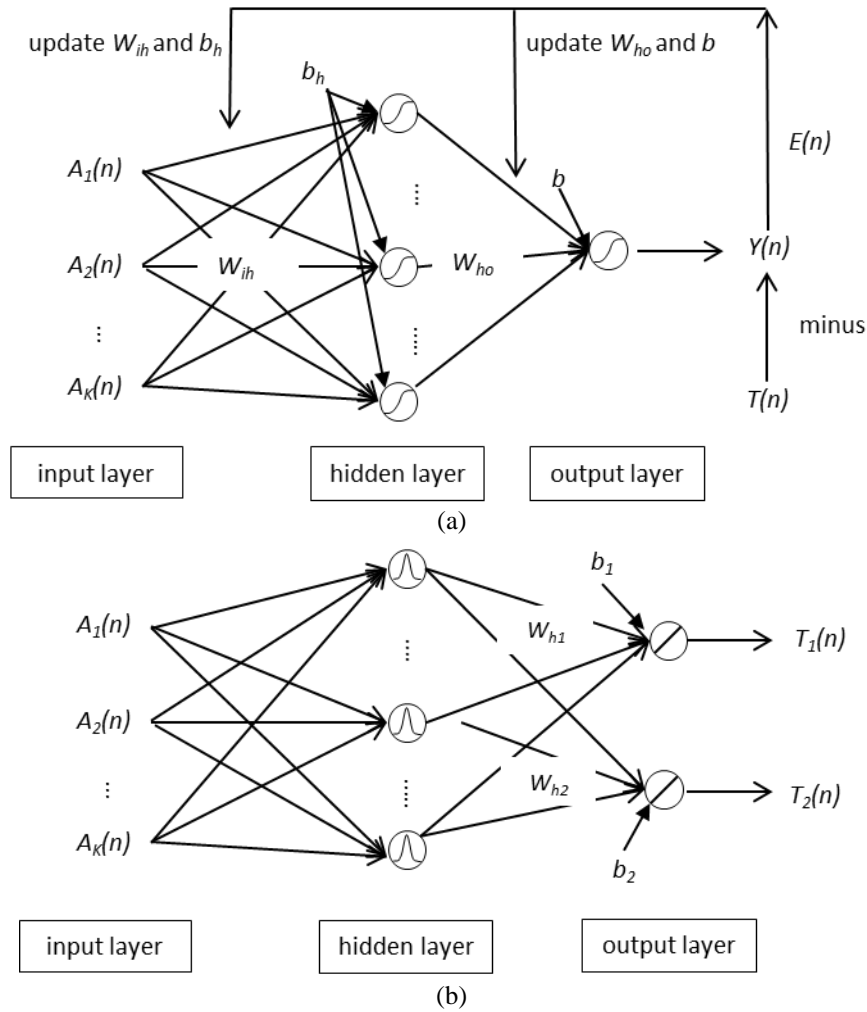
Fig. 4.5: Schematic plot of the architecture and training process of the: (a) multilayer perceptron model and (b) radial basis function model.

4.4.2.2 Training process of RBF model

Fig. 4.5(b) shows the typical architecture of an RBF model, consisting of an input layer, a hidden layer, and an output layer with two neurons. The N neurons in the hidden layer usually use the Gaussian function as their activation function. The two neurons in the output layer use a linear activation function. The RBF model is based on an intuitive idea that input sub-band signals at a time instant can be approximated as the linear combination of a set of prototype vectors which are termed basis functions. Parameters of each basis function consist of a K x 1 centre and its width. Basis function centres are initialised heuristically – usually using the first N K x 1 training instances. The purposes of training this network model are to optimise the basis function of each hidden neuron and also to obtain the set of hidden-output weights and biases. In the training process,

T_1 and T_2 are set as 1 and 0 for flaw echo input, respectively; they are set as 0 and 1 for grain noise input, respectively. The training process is described below:

1) Basis functions optimisation: the basis functions are optimised using the *k*-means clustering method, which firstly clusters the *L* training instances into *N* ($\leq L$) sets ($\mathbf{S} = \{S_1, S_2,..., S_N\}$), subsequently, minimises the sum of square $\delta_{S_h}(h=1,2,...,N)$ within each set S_h.

$$\delta_{S_h} = \sum_{A \in S_h} \sum_{i=1}^{K} \left(A_i - \mu_h(i)\right)^2, h = 1,2,...,N \qquad \text{Eq. 4.18}$$

where μ_h is the centre of the basis function of the *h*th neuron in the hidden layer. The μ_h is iteratively updated until it does not change from the last iteration or the epoch is met. Then the width σ_h of the basis function is set as equal to δ_{S_h}. In fact, the value of μ_h is very close to mean value of the training instances in the set S_h and σ_h is very close to the sum of variances of the training instances in the set S_h.

2) Hidden layer computation: after all basis functions are determined, the Euclidean distance between each training instances and each basis function is calculated and processed by a Gaussian function. So the output S_{nh} at the neuron *h* in hidden layer for the training instance *n* (*n=1,2,...,L*) is calculated as

$$S_{nh} = \exp\left(-\sqrt{\sum_{i=1}^{K}\left(A_i(n) - \mu_h(i)\right)^2}\Big/\sigma_h\right) \qquad \text{Eq. 4.19}$$

3) Weights calculation: the *N* x 1 weights vector $\mathbf{W}$ between the hidden layer and each neuron in the output layer are calculated separately. As both neurons in the output layer use a linear transfer function as their activation function, the transformation is formulated as

$$\mathbf{SW} = \mathbf{T} \qquad \text{Eq. 4.20}$$

where $\mathbf{S}$ is the *L* x *N* output matrix of the hidden layer and $\mathbf{T}$ is the *L* x 1 vector of desired outputs. The weights vector $\mathbf{W}$ can be easily solved by using the Moore-Penrose pseudoinverse

$$\mathbf{W} = (\mathbf{S}^T\mathbf{S})^{-1}\mathbf{S}^T\mathbf{T} \qquad \text{Eq. 4.21}$$

where the superscript '*T*' is the transpose operator.

It is important to note that RBF model produces two coefficients, T_1 and T_2, by two respective neurons in the output layer. For a new input instance of sub-band signals to the trained RBF model, the below calculation

$$C = \frac{T_1}{T_1 + T_2}$$
Eq. 4.22

is carried out to obtain a single coefficient C indicating the possibility of a legitimate flaw indication.

The RBF model does not need an iterative training, thus is much faster than the MLP model.

4.4.3 Generalisation comparisons

4.4.3.1 Introduction of generalisation

It is important to note that the focus of this chapter is the comparison of the performance of MLP model with RBF model used in conjunction with SSP. The performance of a trained ANN is determined not by its performance on the training set but that whether the network performs well on unseen datasets which do not form part of the training set. This is called the generalisation ability of an ANN system [120]. A trained system with good generalisation ability truly 'learns to behave' from the training samples rather than simply memorising the training samples.

Generally speaking, there are two types of generalisation: interpolation and extrapolation. They apply to different distances between the characteristics of the training set and the characteristics of the test set. Interpolation applies to the cases in which the test set are close to the centres of the training set, and reside inside the subspace spanned by the training samples. Extrapolation applies to the cases in which the test set is far away from the centres of the training set. A trained network with good interpolation ability has an insight into the underlying trends in the training set whilst a network with good extrapolation ability is able to 'see' beyond the training set, allowing some degree of deviation of the characteristics of the test set from that of the training set.

Interpolation ability of a trained network is mainly determined by the ratio of the number of training samples, L, to the number of neurons N in the hidden layer [121]. Fig. 4.6 depicts a schematic of the MSE, as defined in Eq. 4.17, of a training set and a test set each as a function of L, for a network with a certain value of N. The interpolation ability of the trained network can be determined by considering the MSE of the test set. As indicated in Fig. 4.6, if too few training samples are used to train the network, the training MSE will be small but MSE of the test set will be very large, i.e., the interpolation ability of the trained network is very poor. This problem occurs since the number of training samples is too less to contain the complete characteristics of the data. As shown in Fig. 4.6, the interpolation ability of the trained network increases with L until the optimal number of training samples $\bar{L}$ is reached. The training set generally contains noise and outliers. Therefore, if more than $\bar{L}$ training samples are used, the excessive noise and outliers in the training set, would typically result in an increase in training MSE and a larger test MSE. The value of $\bar{L}$ is typically dependent on the architecture of the employed network model and the contents of the training set and test sets [120].
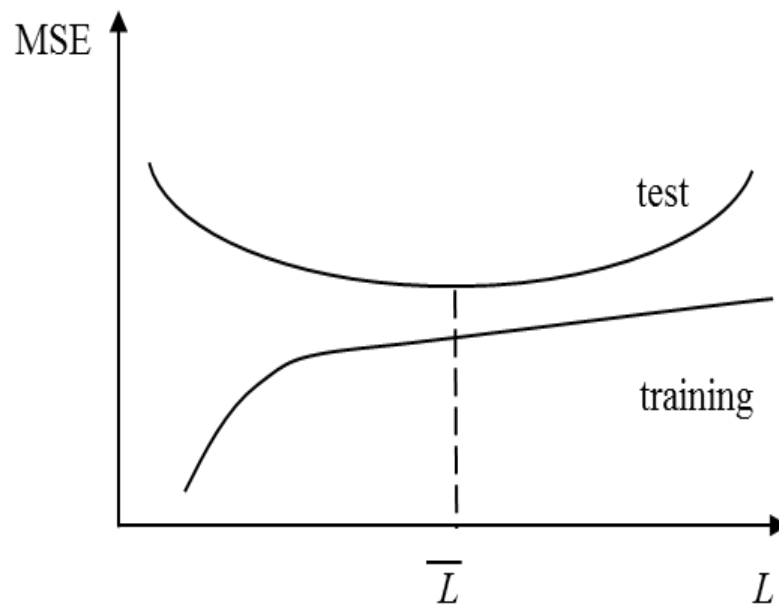
Fig. 4.6: Schematic plot of the MSE of the training and test as a function of the number of training samples.

The interpolation ability of a trained network is often reliable as long as the network is trained sufficiently and appropriately whereas the extrapolation ability of a trained network is notoriously unreliable. This is because the network has fitted itself to the training set after training; therefore, its performance in extrapolating to a new dataset whose characteristics are significantly different from the counterparts of the training set is quite unpredictable. For the case of combining SSP with ANN techniques, the trained network is required to have good interpolation ability and sometimes also have good extrapolation ability. The reason is given as follows.

When SSP is combined with an ANN, the training samples of grain noise are usually easily accessible. Typically, a large number of grain noise instances at various depths are selected as the training samples to ensure the training set encompasses the entire range of spectral characteristics of grain noise. In contrast, the selection of training samples of flaw echoes is subject to their availability. If the locations of flaws are known, the echoes of these flaws are of course selected as the training samples. In such cases, the generalisation of a trained network is determined by its interpolation ability.

However, in most practical inspections, no prior knowledge of flaws can be given. In such cases, backwall signals can be used as an alternative training set of flaw echoes since they are easy to locate in sub-band signals. Then the trained network is used to find the possible flaws. In this case, the backwall can be considered as a deepest semi-infinite flaw. However, the spectral characteristics of flaws echoes deviate from that of backwall due to the frequency-dependent attenuation effect in the propagation channel - the larger the distance between the flaw and backwall, the greater the deviation of spectral characteristics. The difference in spectral characteristics between flaw echoes and backwall signals, therefore, places the demand of extrapolation ability of an ANN. In such cases, the generalisation of a trained network is mainly determined by its extrapolation ability.

4.4.3.2   Methods

The interpolation and extrapolation ability of the two ANN models are sequentially investigated in the next two sections. In the section of investigating interpolation ability, the echoes of a known defect are used in training the two ANN models and the A-scan traces are processed by the two trained models. The resultant SNR improvements with

respect to the known defect are measured as an indication of the interpolation ability of the two ANN models. In the section of investigating extrapolation ability, the echoes of the backwall are used in training the two ANN models and the A-scan traces are processed by the two trained models. The resultant SNR improvements with respect to the defects in the materials are measured as an indication of the extrapolation ability of the two ANN models. For both sections, the SNR improvements obtained by the two ANN models are investigated for a range of number of training samples of grain noise. Note that the number of training samples of grain noise is expressed as the number of the wavelengths corresponding to the central frequency of the employed filter bank.

In addition to assessing the interpolation and extrapolation ability of the MLP and RBF models for ANN implementation, the training time costs of the two ANN models are also compared. The training time cost plays a significant role in the practical implementation of an ANN, especially when real-time signal processing is required. Therefore, it is also considered as an important indicator of the overall performance of the two ANN models. It is noted that the training time costs were measured on a platform with an AMD (Sunnyvale, USA) Opteron Processor 6128 running at 2 GHz with 16 GB of RAM.

Both simulated and experimentally acquired data are used in the assessment of the performance of the two ANN models. For the simulation analysis in the next two sections, all of the A-scan traces were simulated using exactly the same modelling parameters described in Section 4.3 which were employed to generate the A-scan shown in Fig. 4.2(a). However, in order to generate sufficiently challenging data for testing the two ANN models, the spatial distribution of the grain scatterers within the model was randomised for each of the A-scan traces.

Experimental FMC data acquired from **Sample 3** and **Sample 4** were processed to further analyse the interpolation and extrapolation performances of two ANN models, respectively. The inspection geometries for the two samples are schematically drawn in Fig. 4.7. Recall that **Sample 3** is an arc-shaped flaw-free austenitic steel block with a nominal thickness of 51 mm. Considering its arc-shaped surface, the inspection phased array was positioned to allow its 16th element just above the vertex of the surface, as illustrated in Fig. 4.7(a). FMC data were acquired using the first 32 elements

of the array in which the element-wise pulse-echo A-scan traces were extracted for the interpolation analysis of the two ANN models. Recall that **Sample 4** is an 80 mm thick ferritic steel block with four 3-mm-diameter through SDHs at different depths. Three FMC datasets corresponding to the three SDHs at the depths of 40 mm, 60 mm and 75 mm were acquired separately. To avoid the mutual interference between the three SDHs, the array was placed on the sample surface with its aperture perpendicular to the plane of the paper, as illustrated in Fig. 4.7(b). 32 A-scan traces of pulse-echo mode were extracted from each FMC dataset for the extrapolation analysis of the two ANN models.

For all of the simulation and experimental analysis, each A-scan was firstly normalised to its absolute maximum and then was partitioned by 10 equal-bandwidth bandpass Gaussian filters with 25% overlap, and the total bandwidth is selected as 2~8 MHz for 5 MHz array transducers. Refer to Appendix C for the code of generating sub-band signals. The sub-band signals were then fed into two ANN models. For both ANN models, the number of neurons in the hidden layer was taken from [103] and set as 10. TOL=0.002, μ=1.5, η=0.7 were set for MLP. The epoch value was set as 1000 and 100 for MLP and RBF models, respectively. Besides, each of the A-scan traces displayed in the next two sections was normalised to its own absolute maximum.

(a)   (b)
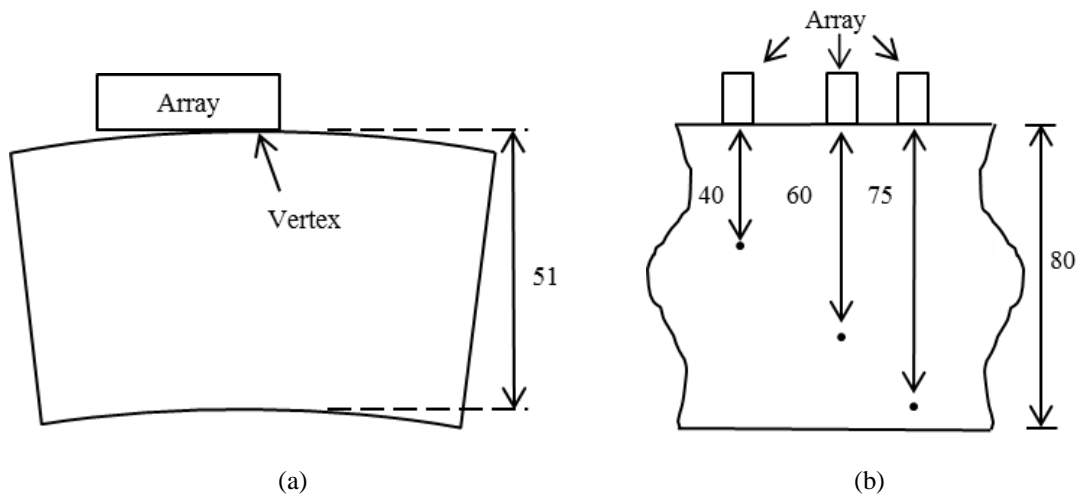
Fig. 4.7: Schematic plots of the array and sample geometry labelled in millimetres for experiments on the: (a) austenitic steel block; (b) ferritic steel block.

110

4.4.3.3   Interpolation comparison

Interpolation abilities of the two ANN models are manifested as their capacities to improve SNR of a known flaw when the echoes of the known flaw are used as the training dataset for the flaw echoes. In this section, simulated and experimentally acquired data are sequentially analysed to assess the interpolation ability of the two ANN models.

Recall that the density of the grain scatterers is selected as $5/\lambda^2$ in the simulated model of backscattering. It is illustrated in [29] that at least 15 realisations of grain scatterer distribution are required to yield a converged SNR for this density of grains. Therefore, 50 A-scan traces were simulated for different random realisations of grain scatterer locations, in each case a flaw located at a fixed position of (0, 100) mm was also simulated in the model. The SNR values of all the 50 simulated A-scans are averaged to obtain a converged SNR. Fig. 4.8(a) shows the 50 stacked original A-scan traces from the simulation with a dynamic range of -1~1. Note that the A-scan traces express signal amplitude as a function of axial distance instead of TOF in order to facilitate the subsequent analysis.

The training dataset for the flaw echoes was created by windowing the flaw echo response in the first simulated A-scan, a 3λ window around the centre of the flaw echo (100 mm deep) was used. The training dataset for the grain noise was created by windowing the grain noise signals also in the first simulated A-scan, a window with its centre at the depth of 70mm and size varying from 2λ to 30λ, with a step of 2λ, was used. Both MLP and RBF models were trained using this training set and all the 50 A-scan traces are processed using the trained MLP and RBF models.

For the purpose of comparison, Fig. 4.8(b) displays the processed results using the same filter bank as the one employed for ANN analysis and the previously described PTS combination algorithm. It is clear from Fig. 4.8(b) although the PTS algorithm serves to suppress the grain noise, in some instances the flaws are not detected, indicating the sensitivity of PTS to the variation of material characteristics. Fig. 4.8(c)-(d) show the processed results by MLP and RBF, respectively – in each case 10λ sample of length grain noise was used in training the network. Fig. 4.8(e)-(f) show the processed results by MLP and RBF, respectively – in each case 30λ sample of length grain noise was

111

used in training the network. From a qualitative point of view, it is clear from Fig. 4.8 that the RBF model obtains better noise suppression than MLP in the case where 10λ of noise training samples was employed and MLP model is slightly superior in the case of 30λ. Both models yield better noise suppression when more noise training samples are used and their performances are superior to the conventional PTS combination approach in terms of both noise suppression and robustness to the variation of material characteristics.

Fig. 4.8: Simulated A-scan traces with a flaw at 100mm: (a) original; (b) processed by PTS; (c)-(d) processed by MLP and RBF trained with 10λ of noise training samples; (e)-(f) processed by MLP and RBF trained with 30λ of noise training samples.

The generalisation ability of a trained ANN can be quantified by considering the SNR of the processed signal when compared to the original SNR. This can be realised by calculating the SNR gain (SNRG) which is defined as the quotient of output SNR (SNR_{out}) and input SNR (SNR_{in}) [94]

$$SNRG = \frac{SNR_{out}}{SNR_{in}} \qquad \text{Eq. 4.23}$$

where

$$SNR_{in} = \frac{\frac{1}{p}\sum_{D-p/2}^{D+p/2} A^2(n)}{\frac{1}{M-p}\left(\sum_{1}^{D-p/2-1} A^2(n) + \sum_{D+p/2+1}^{M} A^2(n)\right)} \qquad \text{Eq. 4.24}$$

where D is the flaw location, p is the pulse length, M is the total number of sampling points in an A-scan signal and A is the A-scan signal. An equivalent definition holds for SNR_{out}. For the case of interpolation analysis using simulation here, D is the centre of the simulated flaw at the depth of 100 mm whilst p is the window size for the extraction of the training set of flaw echoes and is equal to 3λ. SNRG can be considered a synthetic indicator of POD and PFA. The higher the value of SNRG, the higher the classification rate achieved by a trained ANN.

In order to assess the interpolation ability of the two models in simulation, the average SNRG value of all the 50 A-scan traces and the training time, as a function of the number of grain noise training samples, are compared in Fig. 4.9. For both models, the average SNRG value exhibits a general trend of increase as the increase of the number of noise training samples. This implies that optimal number of training samples $\bar{L}$ is larger than 30λ for both models in the simulation analysis. RBF is found to have higher SNRG than MLP when the number of noise training samples is less than 17λ. Particularly, the SNRG value obtained MLP is observed to be even lower than 1 in the cases of 2λ and 4λ of noise training samples. The SNRG of MLP exceeds that of RBF when the number of noise training samples is greater than 17λ. This would suggest that RBF has a superior interpolation performance when less training samples are used whereas MLP interpolates better after sufficient training.

As indicated in Fig. 4.9(b), the computation costs of training the two ANN models have a general trend of increase with the increase of the number of noise training samples. It

114

is important to note that the time cost is natural logarithm transformed to reduce its dynamic range. Interestingly, the training time cost of the MLP model is found to be 20~50 times higher than that of the RBF model. This is attributed to the iterative training process of the MLP network. It is worth noting that for MLP the network weights are randomly initialised so that sometimes it takes a longer time for the MSE of the training set to become lower than the TOL. This explains the fluctuation of time cost of the MLP network.

<p align="center">(a)   (b)</p>
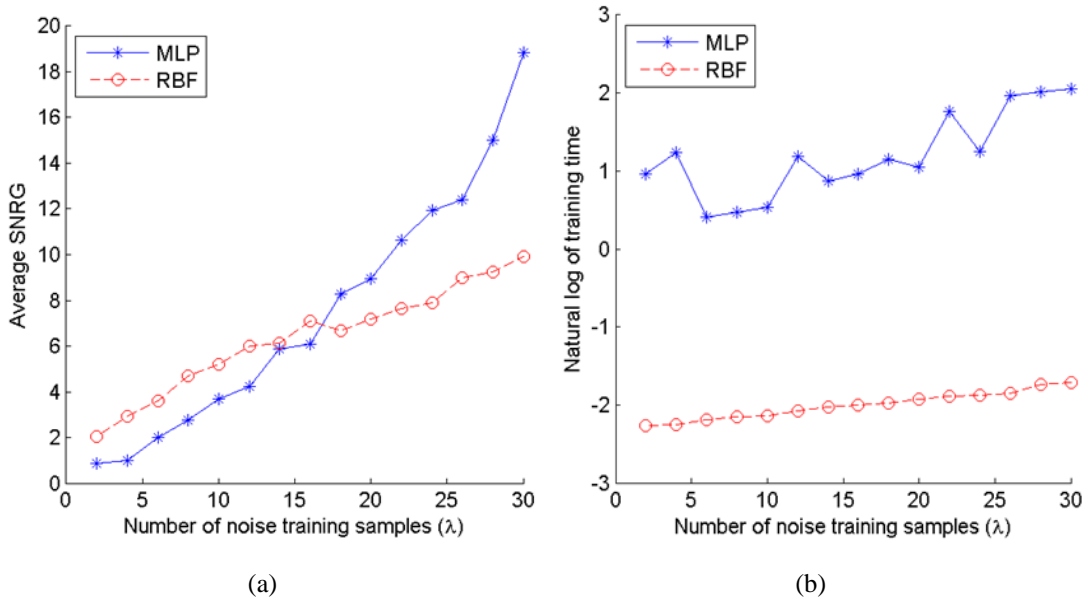
Fig. 4.9: (a) Average SNRG and (b) natural log of training time varying with the number of noise training samples for simulated data

Further analysis was undertaken by using experimental FMC data acquired from the austenitic steel block. 32 A-scan traces of pulse-echo mode were extracted from the FMC dataset for processing. Similar to the preceding simulation analysis, the training dataset were extracted from the first A-scan trace. The training dataset consists of the backwall echoes within the 3λ window around the centre of the backwall (~51 mm deep) and grain noise samples within the window centred at a depth of 35 mm, varying in size from 2λ to 30λ with a step of 2λ. Both MLP and RBF models were trained using this training set and all the 32 A-scan traces are processed using the trained MLP and RBF models.

Fig. 4.10(a) shows the 32 stacked original A-scan traces from experimental acquisition with a dynamic range of -1~1. Results processed using SSP based on PTS are shown in

Fig. 4.10(b) and found that the grain noise is suppressed to a certain extent but the backwall indications are weaker than their counterparts in the original unprocessed data. Fig. 4.10(c)-(d) show the processed results by MLP and RBF, respectively - in each case 8λ sample of length grain noise was used in training the network. Fig. 4.10(e)-(f) show the processed results by the MLP model and the RBF model, respectively – in each case 22λ sample of length grain noise was used in training the network. From a qualitative point of view, it is clear from Fig. 4.10 that the RBF is slightly superior to MLP in terms of noise suppression in the case of 8λ of noise training samples and MLP is better in the case of 22λ. Both models yield much better noise suppression when more training samples of grain noise are used and outperform the conventional PTS combination approach in terms of both noise suppression and robustness to the variation of material characteristics.

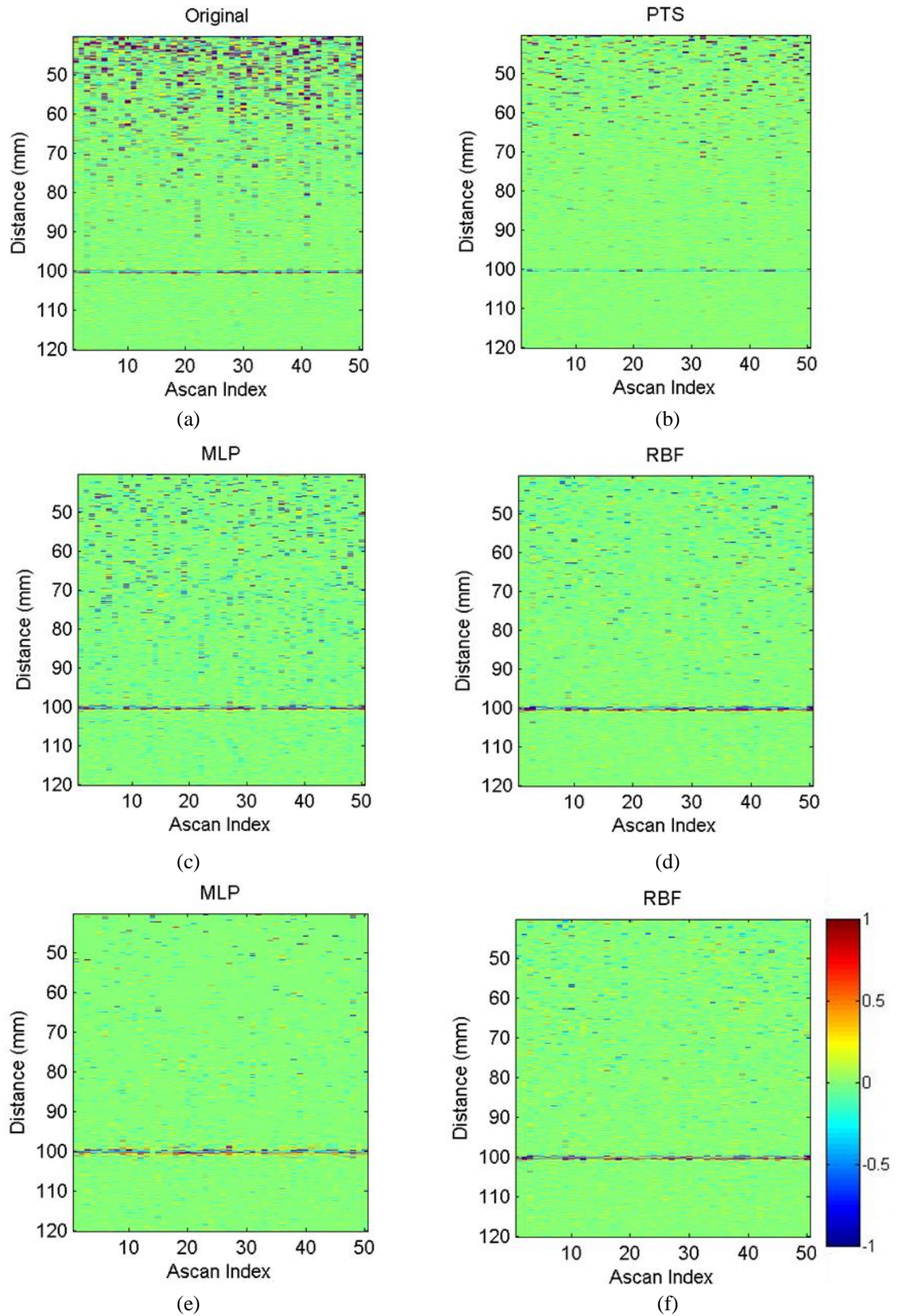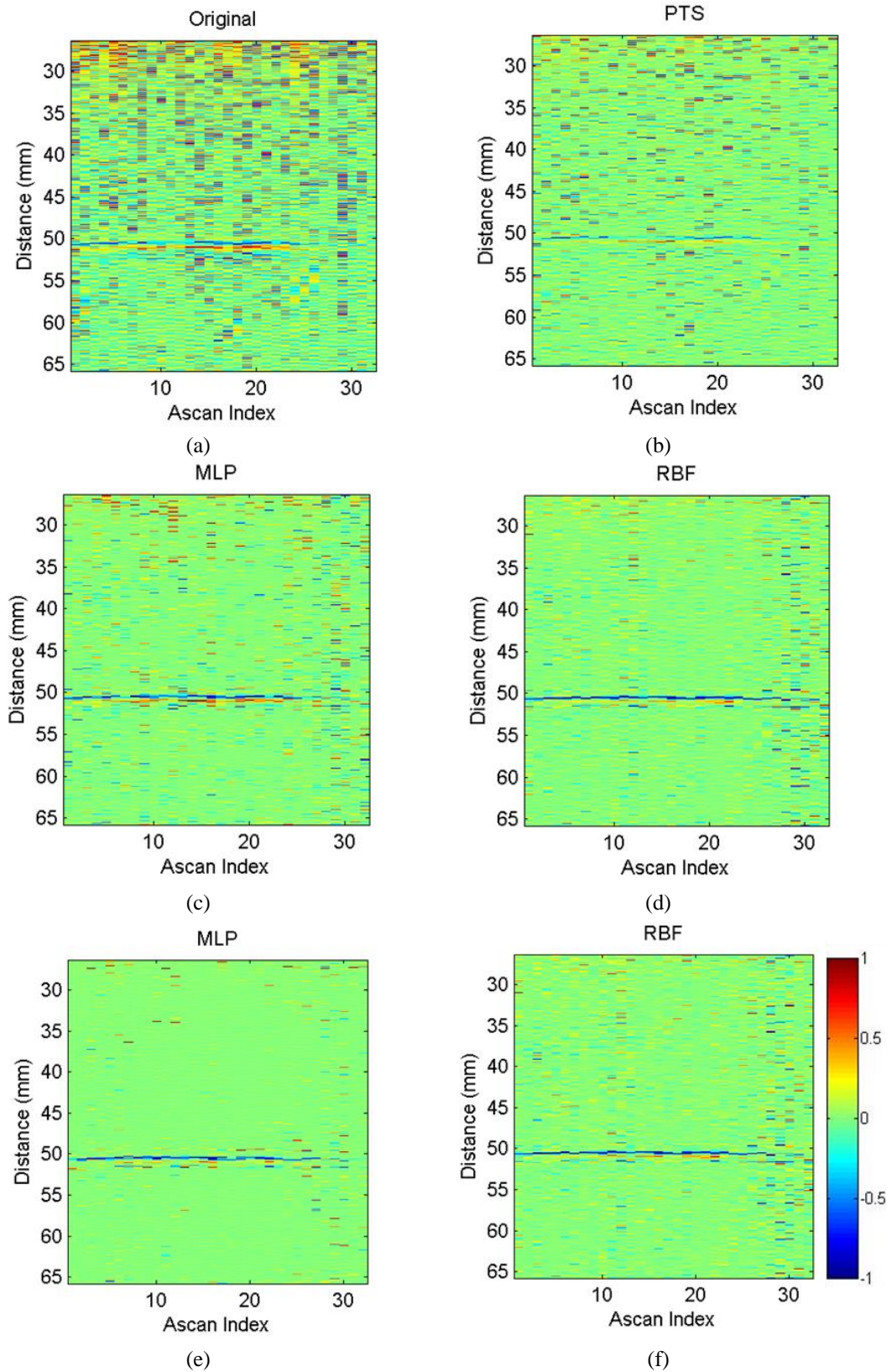*Fig. 4.10: Experimental A-scan traces from the austenitic steel block: (a) original; (b) processed by PTS; (c)-(d) processed by MLP and RBF with 8λ of noise training samples; (e)-(f) processed by MLP and RBF with 22λ of noise training samples.*

117

In order to quantify the interpolation ability of the two ANN models to the data acquired from the austenitic steel block, the average SNRG values of all the 32 A-scan traces and training time costs, as a function of the number of noise training samples, of the two models are compared in Fig. 4.11. Similar to the ANN processing of simulated data, RBF performs better than MLP in terms of interpolation when less than 18λ of noise training samples are used and MLP is a superior model to RBF after sufficient training; and the training of RBF costs much less time than MLP.

(a)   (b)
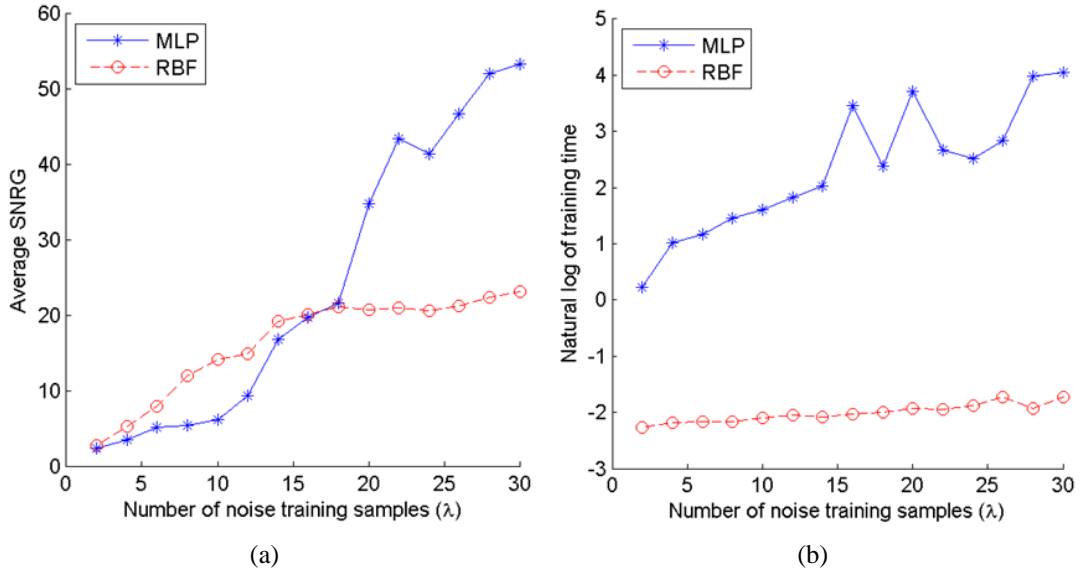
Fig. 4.11: (a) Average SNRG and (b) natural log of training time varying with the number of noise training samples for the experimentally acquired data from the austenitic steel block

While it is encouraging that the good agreement exists between the experimental and simulation results, there are some discrepancies. Firstly, the average SNRG values of experimental results were found to be consistently larger than those of simulation results for any size of the training set. This is attributed to the fact that the difference between the grain noise and flaw echoes in terms of their spectral characteristics in experiments is larger than the counterpart observed in simulation, arising since the simulation approach implements a similar formalism to represent the frequency responses of the grain scattering and flaw reflections, as indicated by Eq. 4.4 and Eq. 4.5. Secondly, the average SNRG value for RBF model monotonically increases with the number of noise training samples in simulations whereas the growth rate of the average SNRG value for MLP model quickly asymptotes after 16λ in experimental results. This suggests that the optimal number of training samples $\bar{L}$ for the

experimental analysis may be between16λ and 30λ. This discrepancy arises since, as previously stated, the value of $\bar{L}$ varies for different contents of training set and test set.

4.4.3.4   Extrapolation comparison

Extrapolation abilities of the two networks models are manifested as their capacities to improve SNR of flaws within the material when the backwall echoes are used as the substitutive training samples of flaw echoes. In this section, simulated and experimentally acquired data are sequentially analysed to assess the extrapolation ability of the two ANN models.

In order to study the extrapolation ability of the two ANN models in simulation, another flaw (also $\rho_f = 20$) was simulated with its distance to the backwall varying from 10 mm to 55 mm, with an incremental step of 5 mm, in addition to the flaw at 100 mm depth which is now treated as the backwall in the extrapolation analysis. For each case of flaw location, 30 A-scan traces were simulated for different random realisations of grain scatterer locations.

The ANN training and signal processing were performed separately for different cases of flaw location. That is, for each case of flaw location, the training dataset were extracted from the first A-scan trace, consisting of the backwall echoes within the 3λ window around the centre of the backwall (100 mm deep) and grain noise samples within the window centred at a depth of 70 mm, varying in size from 2λ to 30λ with a step of 2λ, and both MLP and RBF models were trained using this training set and all the 30 A-scan traces are then processed using the trained MLP and RBF models.

See Appendix B, C and D for the signal simulation, the generation of sub-band signals and ANN analysis, respectively.

Fig. 4.12 depicts the extrapolation results of the simulations, displaying the results within the depth range of 40~95 mm. Fig. 4.12(a) shows the 30 stacked original A-scan traces from the simulation with a dynamic range of -0.6~0.6 in which the flaw and the backwall are separated by 15 mm. Fig. 4.12(b)-(c) display the processed results by MLP model and RBF model, respectively – in each case 26λ sample of length grain noise was used in training the network. From a qualitative point of view, it is observed that both models retain the flaw echoes at the depth of 85 mm and grain noise level is lower

in the MLP results. Fig. 4.12(d)-(i) display the original and processed results for the cases of the flaw and backwall being separated by 30 mm and 45 mm – in both cases 26λ sample of length grain noise was used in training the two ANN models. As with the case of the flaw and backwall being separated by 15 mm, MLP model obtains better noise suppression than RBF model for the cases of 30 mm and 45 mm.

It would be interesting to note that in this case of the flaw and backwall being separated by 30 mm, the trained MLP model fails to detect the flaw at 70 mm depth in a number of A-scan traces whilst the trained RBF model effectively retains all the flaw echoes. This arises since in this case the flaw location (70 mm deep) coincides with the central location of the window for the extraction of the grain noise training samples so that the selected noise training samples are corrupted by the flaw echoes. The outperformance of RBF model against MLP model indicates that RBF model is more tolerant to the corrupted training set.
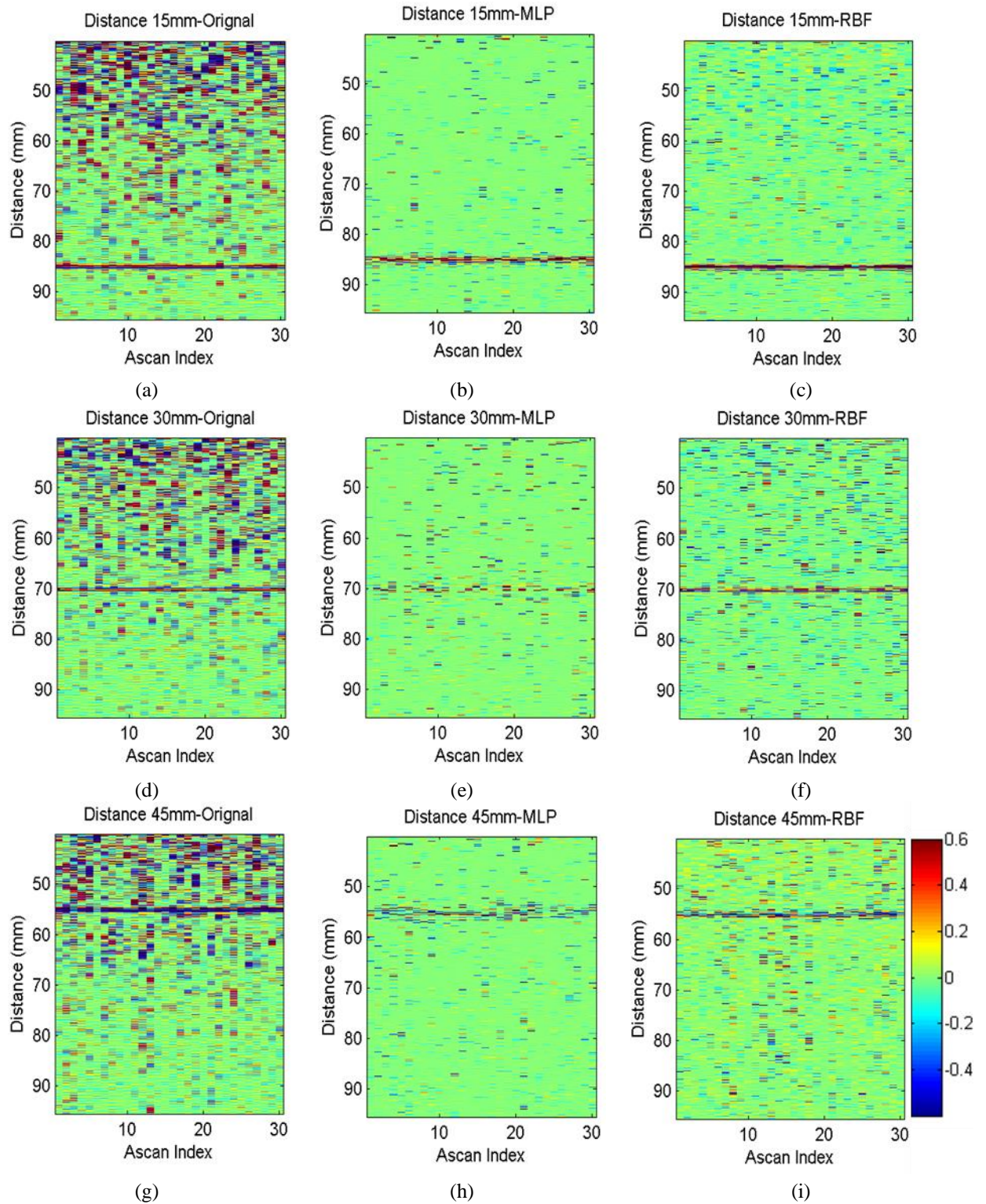
Fig. 4.12: The original simulated A-scan traces with the backwall at 100mm and the processed results by MLP model and RBF model for the case of the flaw and backwall being separated by: (a)-(c) 15mm; (d)-(f) 30mm; (g)-(i) 45mm.

121

In order to quantify the extrapolation ability of the two models in simulation, the average SNRG values of all 30 A-scan traces, as a function of the flaw-backwall distance and the number of noise training samples, obtained by the two ANN models are compared in Fig. 4.13(a)-(b). It should be noted that the backwall signals were excluded when calculating SNRG. The average SNRG values are observed to generally increase when more noise training samples are employed for both models. The average SNRG value generally increases as the distance between the flaw and backwall decreases. This is attributed to the fact that the spectral characteristics of a flaw closer to the backwall are more similar to those of the backwall signals which were used as the training data. It is observed that MLP model constantly yields higher average SNRG values than RBF model except the case of the distance between the flaw and backwall being 30 mm. This exception arises since the flaw location coincides with the central location of the window for the extraction of grain noise training samples, resulting in corrupted training data, as has been explained above. The outperformance of MLP model against RBF model suggests that the MLP network has a better extrapolation ability which allows the spectral characteristics of the testing flaw echoes to exhibit a larger degree of deviation from those of the training flaw echoes.

The computation costs of training, as a function of the flaw-backwall distance and the number of noise training samples, of the two models are displayed in Fig. 4.13(c)-(d) with different dynamic ranges. Similar to the above interpolation analysis, RBF is found to be more computationally efficient than MLP. It is interesting to note that the time costs for the case of the flaw and backwall being separated by 30 mm are greater than the other cases for both models. This occurs since the iterations tend to exhaust during training when the training samples of grain noise are corrupted by flaw echoes.
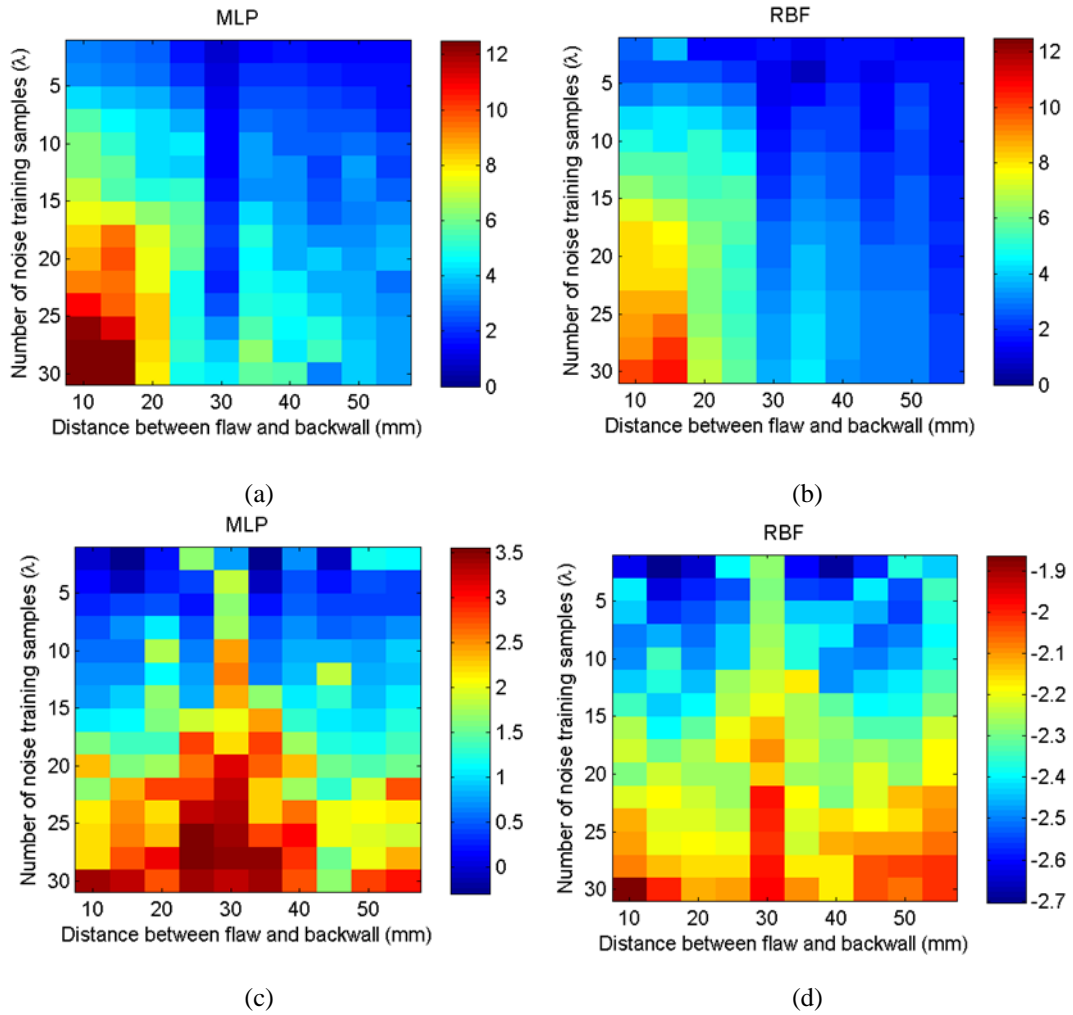
Fig. 4.13: (a)-(b) Average SNRG and (c)-(d) natural log of training time varying with the distance between the simulated flaw and backwall and the number of noise training samples.

Experimental exemplifications were undertaken via three FMC datasets acquired from the ferritic steel block corresponding to three deeper SDHs. 32 A-scan traces of pulse-echo mode were extracted from each FMC dataset for processing.

Same with the preceding simulation analysis for extrapolation, the ANN training and signal processing were performed separately for the three SDHs. For each SDH, the training data were extracted from the first A-scan trace, consisting of the backwall echoes within the 3λ window around the centre of the backwall (80 mm deep) and grain noise samples within the window varying in size from 2λ to 30λ with a step of 2λ. However, unlike to the preceding simulation analysis for extrapolation, the central locations of the window for the extraction of grain noise training samples were set as 52 mm for the two SDHs at the depths of 40 mm and 75 mm whilst the central location

of the window was set to 42 mm for the 60 mm deep SDH, in order to avoid the training samples of grain noise being corrupted by the flaw echoes.

Fig. 4.14(a) shows the 32 stacked original A-scan traces from the simulation with a dynamic range of -0.3~0.3 in which the flaw and backwall are separated by 5 mm. Fig. 5.14(b)-(c) display the processed results by MLP model and RBF model, respectively – in each case, 26λ of grain noise samples was used in training the network. From a qualitative point of view, it is observed that both models retain the flaw echoes at the depth of 75 mm in most A-scan traces and yield considerable grain noise reduction whilst the grain noise level in the RBF results are more significant than the MLP results. Fig. 4.14(d)-(i) display the original and processed results for the cases of the flaw and backwall being separated by 20 mm and 40 mm – in both cases 26λ of grain noise samples was used in training the two ANN models. For both cases, MLP model obtains better noise suppression than RBF model.

The average SNRG values of all 32 A-scan traces and the training time costs, as a function of the number of noise training samples, of the two models for the three SDHs are compared in Fig. 4.15. Again, the backwall signals at 80 mm deep were excluded when calculating SNRG. It is observed that MLP model constantly yields higher average SNRG values than RBF model. These experimental results are highly consistent with the simulation results. Same with the above interpolation analysis, the average SNRG values of experimental results for the extrapolation analysis are found to be larger than those observed when processing simulated data. Again, this discrepancy occurs since the difference of spectral characteristics between grain noise and flaw echoes in experiments are larger than the counterparts in simulations, arising since the simulation approach implements a similar formalism to represent both grain scattering and the flaw reflections.

(a)

(b)

(c)

(d)

(e)

(f)

(g)

(h)

(i)
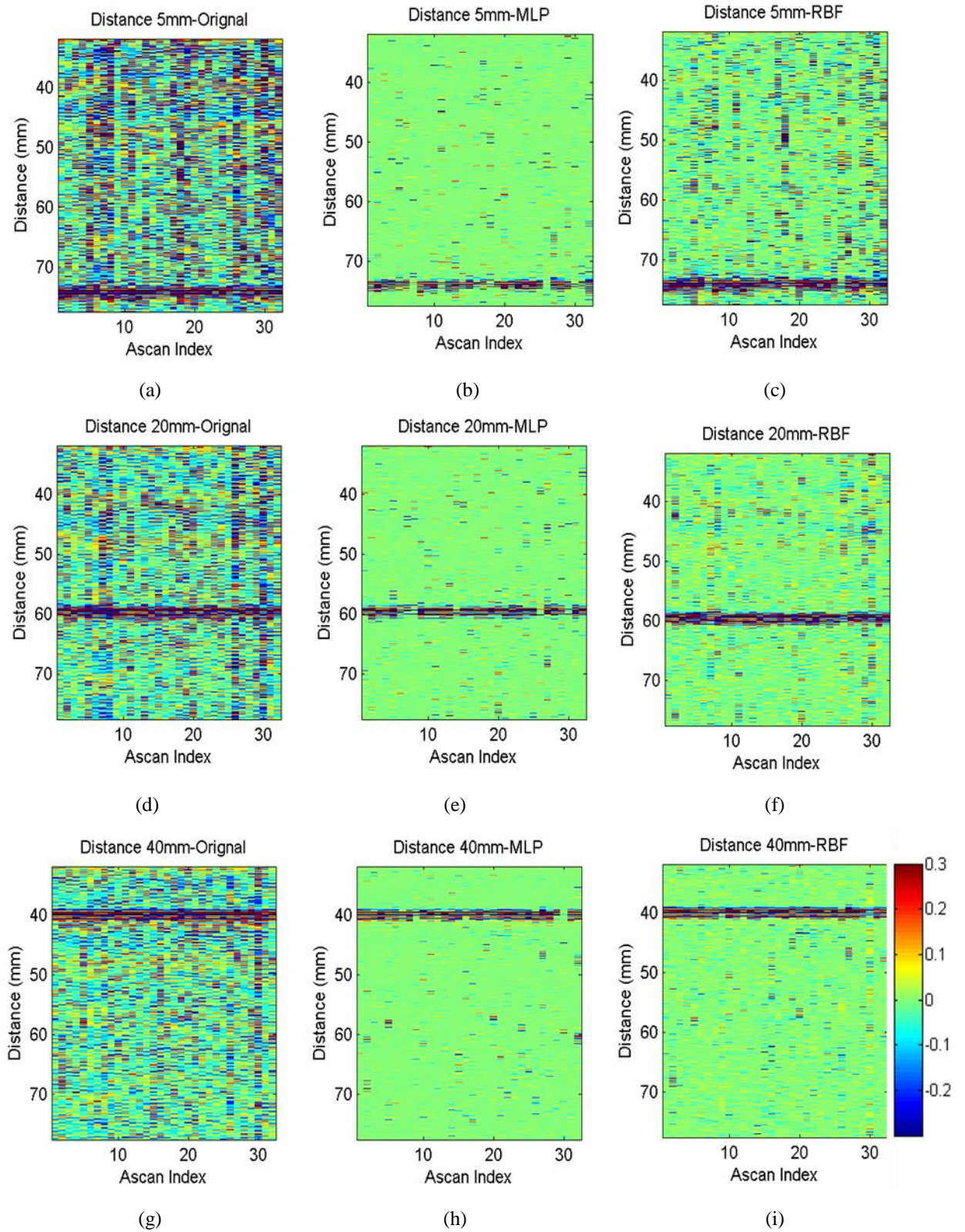
Fig. 4.14: The original A-scan traces experimentally acquired from the ferritic steel block (backwall at 80 mm depth) and the processed results by MLP model and RBF model in the case of the flaw and backwall being separated by: (a)-(c) 5mm; (d)-(f) 20mm; (g)-(i) 40mm.

125
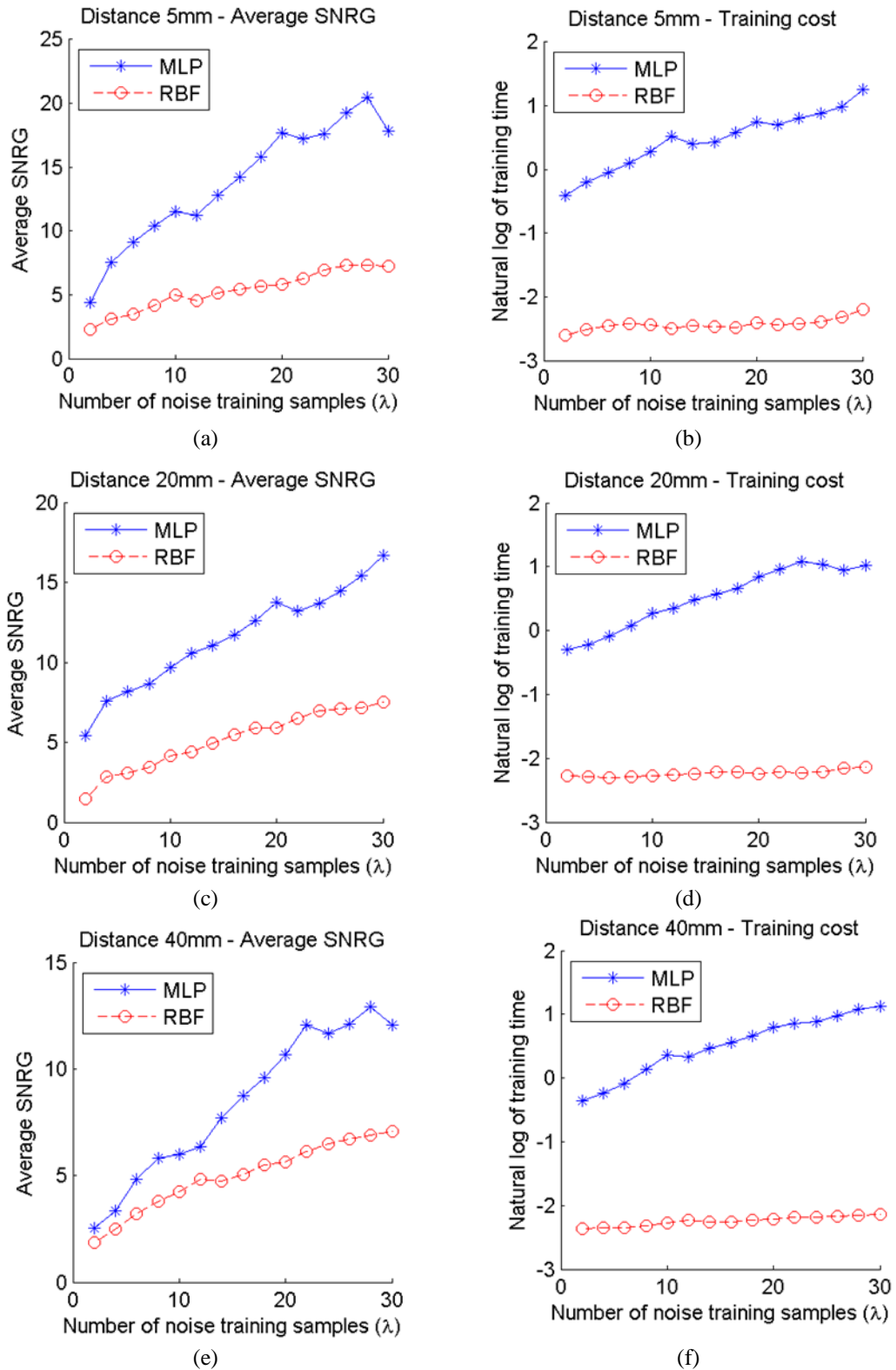
Fig. 4.15: Average SNRG and natural log of training time varying with the number of noise training samples for the experimentally acquired data from the ferritic steel block in the case of the flaw and backwall being separated by: (a)-(b) 5mm; (c)-(d) 20mm; (e)-(f) 40mm.

126

4.4.3.5   Discussion

The MLP network and RBF network operate with different classification mechanisms [122]. For both networks, inputs are mapped as hyperspatial points in a hyperspace in the hidden layer. For MLP, the separation of hyperspatial points is achieved by a hyperplane or hypersurface based on which the minimum training error can be obtained. For RBF, the hyperspatial points are clustered into hyperspheres each of which is defined by the activation function and basis functions. Fig. 4.16 shows the classification mechanisms in the simple two-dimensional case of hyperspace in which the flaw echoes and grain noise are plotted as two different colours. The MLP in Fig. 4.16(a) separates the flaw echoes and grain noise by an arbitrarily shaped line; while the RBF in Fig. 4.16(b) separates the cluster of flaw echo and the cluster of grain noise by ellipses.

Different classification mechanisms of the two models render the difference in their extrapolation performance. Because the receptive fields of the neurons in the hidden layer of RBF model are localised, the network outputs are decided by only a small portion of neurons and thus the decision boundary of RBF are defined locally. Hence, the inputs in the hyperspace which are far from the hypersphere of flaw echoes tend to yield low outputs. That is, the localised nature of receptive fields of RBF reduces its ability to 'see' beyond the training set. In contrast, the decision boundary of MLP is defined globally since the network outputs are jointly decided by all the neurons in the hidden layer and output layer. Thus, inputs in the hyperspace far from the sub-hyperspace spanned by the training samples of flaw echoes can possibly lead high outputs. This indicates that MLP has a better extrapolation ability than RBF which has been demonstrated by the above simulation and experimental analysis.

It is just the localised nature of the receptive fields of RBF that leads RBF to have better interpolation ability than MLP when less noise training samples are used. From a statistical perspective, the localised nature of receptive fields of RBF allows it to have a lower PFA and also a lower POD than MLP. When less grain noise samples are used in the training stage, the statistical variation of spectral characteristics of grain noise are not fully explored by the ANN, therefore, a grain noise signal is likely to trigger a false alarm in the testing stage. In this case, a model with a lower PFA triggers fewer false

alarms so that it has better interpolation performance. In contrast, when sufficient grain noise training samples are used, the ANN 'learns' from the entire range of spectral characteristics of grain noise, thus, the testing grain noise signals are less likely to trigger false alarms. On this occasion, a model with a higher PD possesses better interpolation performance. Therefore, the RBF network interpolates better with less training samples and MLP is superior after sufficient training.

(a)   (b)
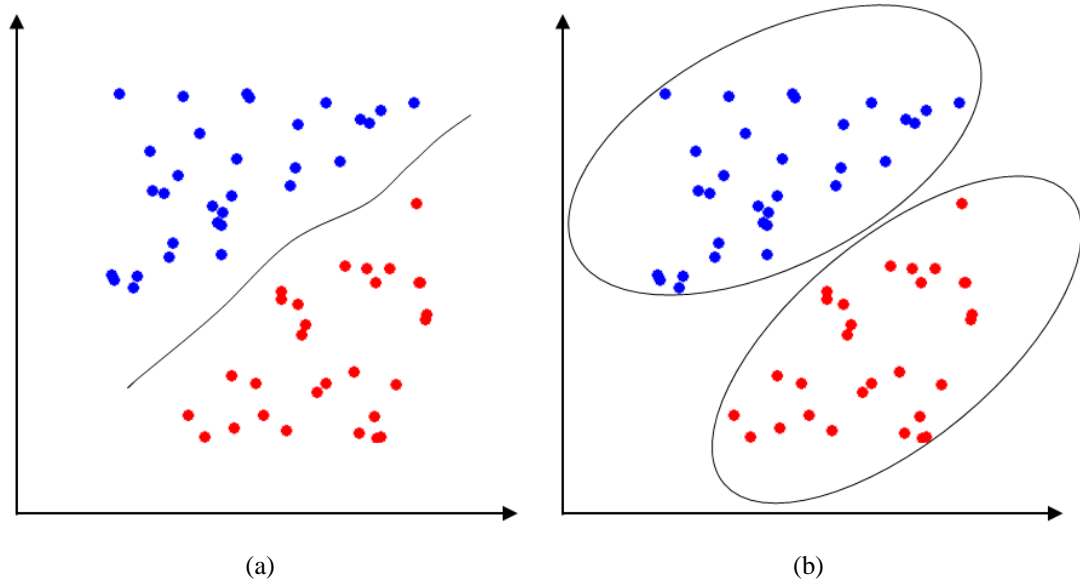
Fig. 4.16: Classification mechanisms of the: (a) MLP model and (b) RBF model

Different classification mechanisms of the two models also render their difference in the training cost. For a particular training sample, only a small portion of hidden neurons of RBF model are involved in processing the training sample. This leads to a decoupled two-stage training procedure in which the basis functions are optimised at the first stage and the weights of the hidden-output layer are subsequently determined at the second stage. Since the activation function of each output neuron in an RBF model is usually selected to a linear one, the weights of the hidden-output layer can be efficiently calculated using the Moore-Penrose pseudoinverse [123]. In contrast, all the neurons in the hidden layer of MLP network are involved for any training input samples. Besides, all the neurons in both hidden layer and output layer usually use nonlinear sigmoid functions as their activation functions. The resultant slow error back propagation greatly reduces the training speed.

In the above extrapolation analysis, the backwall signals are used as the alternative training set of flaw echoes. It is acknowledged that this approach is effective only if the backwall signals are prominent and not corrupted by grain noise. However, for some ultrasonically scattering and/or very thick specimens, the backwall signals may be very weak and severely corrupted by the scattering of neighbouring grains. In such cases, it is proposed that the attenuation coefficient is firstly measured from a specimen of similar material composition and then used to estimate the spectral characteristics of the backwall signals.

4.5   Conclusion and future work

In this chapter, an analytical model of grain backscattering is first described which enables the simulation of backscattering data captured by a phased array. Then some initial results are presented to exemplify the sensitivity of conventional combination algorithms of SSP to the variation of material characteristics. The ANN techniques are proposed to be used as the combination algorithms of SSP to increase its robustness and effectiveness in improving SNR. With sufficient and appropriate training, an ANN can discover the frequency components mapped in a hyperspace at which the statistically significant differences between the flaw echoes and grain noise exist. Therefore, a trained ANN is insensitive to the variation of the spectral characteristics of grain noise.

The performances in terms of SNR enhancement and computational efficiency of the well-known MLP model and RBF model used in conjunction with SSP have been compared in various cases through simulation and experimental analysis. The comparison results are described as follows. When the echoes of a known flaw are used as the training set, RBF is superior if the training data of grain noise is expensive or rare whilst MLP is proposed to use if sufficient training data of grain noise are accessible. However, the flaw information is inaccessible or unknown in an industrial context. In order to implement the ANN techniques in industrial applications, backwall echoes can be used as an alternative training set of flaw echoes and then the trained network is used to detect unknown possible flaws. The comparison results show that MLP model outperforms RBF model in most cases but RBF model performs better if

the training set of grain noise coincidently is corrupted by the echoes of the flaw to be detected. When the training cost is of significant importance to signal processing, for instance, when real-time signal processing is required, RBF is no doubt much more superior to MLP.

Future work consists of two aspects. Although the simulation results are generally consistent with experimental results, some discrepancies still exist, arising since the simulation approach implements a similar formalism to represent the frequency characteristics of grain scattering and the flaw reflections. Therefore, in future work, the factor of spatial correlation (i.e., the multiple scattering effects) as a function of frequency between neighbouring grain scatterers will be added into the current analytical model. Additional work is also required to assess the interpolation and extrapolation abilities of the two ANN models for other types of flaws, such as cracks and slots.

CHAPTER 5. Enhanced split-spectrum processing with best linear unbiased estimator

5.1 Introduction

In the preceding chapter, ANN techniques are combined with SSP to suppress grain noise in the scope of A-scan signal processing. This chapter will introduce a statistical signal processing algorithm used in conjunction with SSP to reduce speckle by combining B-scan images acquired at multiple frequencies.

When delay-and-sum beamforming techniques are applied to a set of A-scan traces to construct a B-scan image, the grain noise in the A-scan traces aggregates to form speckle on the B-scan image. Speckle can be considered as an accumulation result of the imaging system's response to spatially unresolvable grain scatterers within a volume range which is often known as resolution cell [11]. It is often with a granular pattern and not closely linked to actual object structure. The speckle granularity is typically equal to the size of the resolution cell. The speckle pattern is undesirable since it degrades image contrast and decreases flaw detectability.

There are two approaches to suppressing speckle: reducing speckle intensity and reducing speckle contrast. The next chapter will focus on the reduction of speckle intensity. In this chapter, the attention is restricted to reducing speckle contrast with SSP.

When SSP is used to process array data, each A-scan of the array data is decomposed into several sub-band signals. An image is constructed in each sub-band and the sub-

band images are combined. In order to quantify the performance of various combination methods of SSP on the reduction of speckle contrast, the Speckle Index (SI) is defined as [114]

$$\text{SI} = \left| \frac{\mu_s}{\sigma_s} \right| \qquad \text{Eq. 5.1}$$

where the μ_s and σ_s are the mean and standard deviation of the pixel values of a speckle region of interest (ROI), respectively. The higher values of SI indicate a reduced speckle contrast, leading to an improvement in image contrast and flaw detectability. At the extreme case of SI being infinity, the speckle becomes to a constant background noise which can be easily removed by changing the dynamic range of the image.

The simplest method of combining sub-band images is to average them. By averaging K white speckle, where the patterns are statistically identical and independent, μ_s remains unchanged and the σ_s is reduced by a factor of $\sqrt{K}$, the SI is consequently improved by a factor of $\sqrt{K}$. However, for K coloured speckle, where the patterns are statistically unequal and correlated, the averaging approach yields improvements in SI of less than $\sqrt{K}$ [81]. For coarse-grained materials, different speckle variances are observed on the sub-band images. Frequency-dependent phenomena such as attenuation and element directivity are responsible for this difference. The dissimilarity of the speckle variances between sub-band images, which is termed variance dissimilarity for brevity, is dependent on the spectral distance of sub-bands and the distance of ROI to inspection probe. The speckle correlation is proportional to the overlap of frequency sub-bands. Reducing the overlap between sub-bands can decrease the speckle correlation but also increase the variance dissimilarity. Increasing the overlap between sub-bands can reduce the variance dissimilarity but also increase the speckle correlation. The averaging approach therefore yields poor reduction of the contrast of coloured speckle at various overlapping conditions.

It is clear that scope exists for an alternative combining approach for SSP that can effectively reduce the contrast of coloured speckle. This can be achieved by pre-whitening the coloured speckle patterns by statistically equalising and decorrelating the speckle prior to averaging. In this chapter, such a combination approach is proposed to coherently reduce speckle contrast in ultrasonic imaging of coarse-grained material. In

this method, images acquired at different frequencies are adaptively combined in a pixel-wise manner using a statistical estimator named Best Linear Unbiased Estimator (BLUE) where the combination weights are adaptively tuned based on local statistics [115]. The local statistics are extracted from the corresponding local neighbourhoods of corresponding pixels on the sub-band images. This combination process statistically equalises and decorrelates speckle patterns on the sub-band images prior to averaging them with weights, achieving a considerable reduction of speckle contrast whilst maintain axial resolution.

This chapter is arranged as follows. Firstly, the underpinning theory of BLUE is introduced. Then the simulation and experiments arrangements are described. Subsequently, the pre-whitening effect of BLUE is validated in simulation and the comparison of BLUE with conventional combination methods of SSP in terms of image contrast enhancement is given for experimentally acquired data. The potential improvement to image contrast attained by the BLUE method is studied by considering the filter overlap and segment length when extracting the local statistics. Conclusion and suggestions for future work are given in the end.

5.2   Theory

Consider a 2D geometry with Cartesian coordinates shown in Fig. 5.1, where x and z represent locations in the lateral and axial direction, respectively. When an object with reflectivity distribution $r(x, z)$ is interrogated by an imaging system with point spread function (PSF) $p(x, z)$, the detected image envelope can be expressed as

$$a(x,z) = \left| \int_{x-W/2}^{x+W/2} \int_{z-L/2}^{z+L/2} r(x',z')p(x',z')dz'dx' + \eta(x,z) \right| \quad \text{Eq. 5.2}$$

where '| |' is the absolute operator and $\eta(x, z)$ is additive white Gaussian noise arising from the transduction system and electronic circuit; W and L represent the width and length of the resolution cell respectively within which the scatterers have a contribution to the object's echo. The contribution from scatterers outside the resolution cell is assumed to be negligible.

Assuming that the scatterers in the resolution cell are randomly distributed and elastically isotropic, the PSF of an imaging system with TFM beamformer at, for example, the point (x_a, z_a) shown in Fig. 5.1, is

$$p(x_a, z_a)$$

$$= \sum_{tx=1}^{N} \sum_{rx=1}^{N} \left(\frac{1}{\pi} \int_0^\infty A_0(w) B(\alpha_{tx}, \beta_{rx}, w) e^{-jw\tau_{tx,rx,x_a,z_a}} e^{jwt} \, dw \right) \Big|_{t=0} \qquad \text{Eq. 5.3}$$

where A_0 is the frequency spectrum of the signal emitted by array elements; $\tau_{tx,rx,x,z}$ is the time-of-flight from the emitter tx to the point of interest (x_a, z_a) and back to the receiver rx; B, which is a function of interrogating frequency, the incident angle α_{tx}, and the reflected angle β_{rx}, provides the effects of beam divergence and element directivity. Note that attenuation effect is ignored in this equation for brevity.
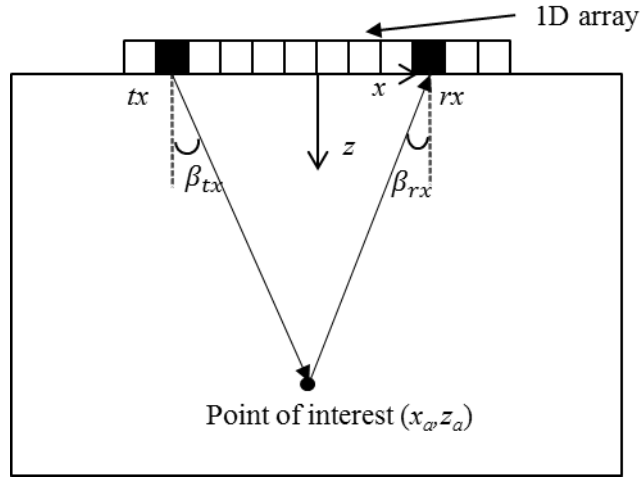
Fig. 5.1: Schematic diagram of an inspection with a phased array.

If the number of scatterers in the resolution cell is large, it is reasonable to assume the reflectivity function $r(x, z)$ is nearly constant over the resolution cell. Also assuming the additive noise $\eta(x, z)$ is insignificant, Eq. 5.2 can then be simplified into a speckle model [124]

$$a(x, z) \cong r(x, z) s(x, z) \qquad \text{Eq. 5.4}$$

where $s(x, z)$ represents the multiplicative speckle and is defined as the integral of the PSF of the imaging system

$$s(x,z) \triangleq \left| \int_{x-W/2}^{x+W/2} \int_{z-L/2}^{z+L/2} p(x',z')dz'dx' \right| \qquad \text{Eq. 5.5}$$

In SSP, an object is imaged at K shifted frequencies so that K speckle models can be obtained

$$a_i(x,z) = r_i(x,z)s_i(x,z) \quad i = 1,2,...,K \qquad \text{Eq. 5.6}$$

Since multiplicative noise is difficult to reduce as compared to additive noise, a homomorphic transform can be performed to convert the multiplicative speckle to an additive one. This homomorphic transformation can be achieved by logarithmic transformation. Then the K speckle models become to

$$log\, a_i(x,z) = log\, r_i(x,z) + log\, s_i(x,z) \quad i = 1,2,...,K \qquad \text{Eq. 5.7}$$

Assume that $log\, r_i(x,z)$ and the $log\, s_i(x,z)$ on average are identical at the K frequencies. By considering the speckle model as a generalised linear model, for each corresponding pixel (x,z), Eq. 5.7 can be re-written as

$$a^{log}[i] = DC + w[i] \quad i = 1,2,...,K \qquad \text{Eq. 5.8}$$

where DC is the coherent component to be estimated from the measured K x 1 vector $\boldsymbol{a}^{log}$ which is corrupted by a K x 1 noise vector $\boldsymbol{w}$. The $\boldsymbol{w}$ is zero mean and has a K x K local covariance matrix $\boldsymbol{Co}$ which is equal to the covariance matrix of the $log\, s_i(x,z)$. $\boldsymbol{Co}$ of the noise vector $\boldsymbol{w}$ is often unknown as it is the values of $\boldsymbol{a}^{log}$ that are typically available. However, the $\boldsymbol{Co}$ of $\boldsymbol{w}$ can be obtained from the measured $\boldsymbol{a}^{log}$ because $\boldsymbol{w}$ and $\boldsymbol{a}^{log}$ have the identical covariance matrix due to the DC being assumed to be identical in different sub-bands.

Therefore, the goal of reducing speckle variance is to yield an unbiased estimate of DC with reduced variance from the noise-corrupted $\boldsymbol{a}^{log}$. The unbiased estimate means that the estimated $\widehat{DC}$ is equal to the true DC value on the average and the reduced variance means the reduced root mean square error of the $\widehat{DC}$ from the true DC value. For simply averaging of the sub-band images, the variance of $\widehat{DC}$ on the resultant image is equal to the mean value of all entries of $\boldsymbol{Co}$.

$$\sigma_{\widehat{DC}}^2 = \sum_{i=1}^{K} \sum_{j=1}^{K} \frac{Co[i,j]}{K^2} \qquad \text{Eq. 5.9}$$

If $Co = \sigma^2 U$ where U is a K x K identity matrix, the $\widehat{DC}$ obtained by averaging the sub-band images has a variance of σ^2/K so that the SI is improved by $\sqrt{K}$. However, unequal variances and correlation between the speckle patterns on the sub-band images will result in $\sigma_{\widehat{DC}}^2$ larger than σ^2/K so that the SI improvement is less than $\sqrt{K}$.

In order to minimise the variance of $\widehat{DC}$, an estimator is required which is able to pre-whiten the speckle patterns, i.e., decorrelate and equalise the variances of the speckle patterns, prior to averaging sub-band images. The proposed BLUE is such an estimator which gives the estimation of DC as [115]

$$\widehat{DC} = \frac{I^T Co^{-1} a^{log}}{I^T Co^{-1} I} \qquad \text{Eq. 5.10}$$

where I is a K x 1 identity vector and the superscript 'T' denotes the matrix transpose. To explain the pre-whitening capability of BLUE, this equation is expanded as follows.

Since Co is a symmetric, positive definite matrix, Co^{-1} can be factored by Cholesky decomposition as

$$Co^{-1} = D^T D \qquad \text{Eq. 5.11}$$

where matrix D is a K x K invertible matrix. The matrix D acts as a whitening transformation when applied to a^{log}, since [115]

$$E\left[\left(Da^{log}\right)\left(Da^{log}\right)^T\right] = E[(Dw)(Dw)^T] = DCoD^T =$$
$$DD^{-1}D^{T^{-1}}D^T = I \qquad \text{Eq. 5.12}$$

where $E[\cdot]$ is the expectation operator. Therefore, the BLUE of DC can be expanded as

$$\widehat{DC} = \frac{I^T D^T}{I^T Co^{-1} I} Da^{log} = \sum_{i=1}^{K} d[i] a^{log'}[i] \qquad \text{Eq. 5.13}$$

where

$$a^{log'} = Da^{log} \qquad \text{Eq. 5.14}$$

is the pre-whitened speckle and $\boldsymbol{d} = \boldsymbol{I}^T\boldsymbol{D}^T/\boldsymbol{I}^T\boldsymbol{Co}^{-1}\boldsymbol{I}$ is the vector of pre-whitened weights. Since BLUE pre-whitens the speckle patterns, it is able to provide an estimation of DC with a variance [115]

$$\sigma_{\widehat{DC}}^2 = \frac{1}{\boldsymbol{I}^T\boldsymbol{Co}^{-1}\boldsymbol{I}} \qquad \text{Eq. 5.15}$$

This is in contrast to the simple averaging method which yields the larger $\sigma_{\widehat{DC}}^2$ (as formulated in Eq. 5.9) than BLUE for coloured speckle since the averaging method implicitly assumes that the speckle patterns on the sub-band images have the same variance and are uncorrelated. Because the $\widehat{DC}$ value at each pixel is used for display on a computer screen after normalisation, the minimum $\sigma_{\widehat{DC}}^2$ indicates a minimised speckle standard deviation and so minimised speckles contrast in the processed image.

$\boldsymbol{Co}$ is usually calculated over corresponding 2D windows of pixels centred at the pixel being estimated. For a window size of M x M, approximate $4M^2$ and $5M^2$ arithmetic operations are required to obtain each diagonal and off-diagonal entry of $\boldsymbol{Co}$, respectively. The computational cost can be reduced immediately with some approximations. Since PSF of the imaging system can be approximately separable as a product of lateral PSF and axial PSF, then $\boldsymbol{Co}$ is also separable [106],

$$Co[i,j] \cong Co_x[i,j]Co_z[i,j] \qquad i,j = 1,2,\dots,K \qquad \text{Eq. 5.16}$$

where $\boldsymbol{Co_x}$ and $\boldsymbol{Co_z}$ are the lateral and axial covariance matrices, respectively. $\boldsymbol{Co_x}$ and $\boldsymbol{Co_z}$ are obtained from the corresponding lateral 1 x M pixel segments and the corresponding axial M x 1 pixel segments, respectively. Note that the pixel segments are centred at corresponding pixel being estimated. With the PSF being separated, the number of arithmetic operations required to obtain each diagonal and off-diagonal entry of $\boldsymbol{Co}$ are significantly reduced to 8M and 10M, respectively.

The whole process of combining SSP with BLUE combination approach is depicted in Fig. 5.2 in which the final normalisation step means the BLUE results $\widehat{DC}$ of all pixels are subtracted by the maximum value of $\widehat{DC}$. It should be noted that M/2 pixels at all four edges of the images are not processed due to an insufficient number of adjacent pixels for the covariance matrix calculation, resulting in a reduced size of the imaging region after BLUE combination.

There are also other linear statistical estimators such as the maximum likelihood estimator. The justification of using BLUE is two-fold. First, most of the other estimators require complete knowledge of the probability density function (PDF) of speckle patterns whereas the logarithmic transform converts the Rayleigh PDF noise envelope into a PDF which is mathematically intractable to find. In contrast, BLUE only needs the first two moments of the speckle so that it has reduced computational complexity and is more suitable for practical implementation. Second, most of the other estimators are unbiased only under the condition of Gaussian noise. Conversely, BLUE holds its unbiasedness in both Gaussian and non-Gaussian noise environments [115].
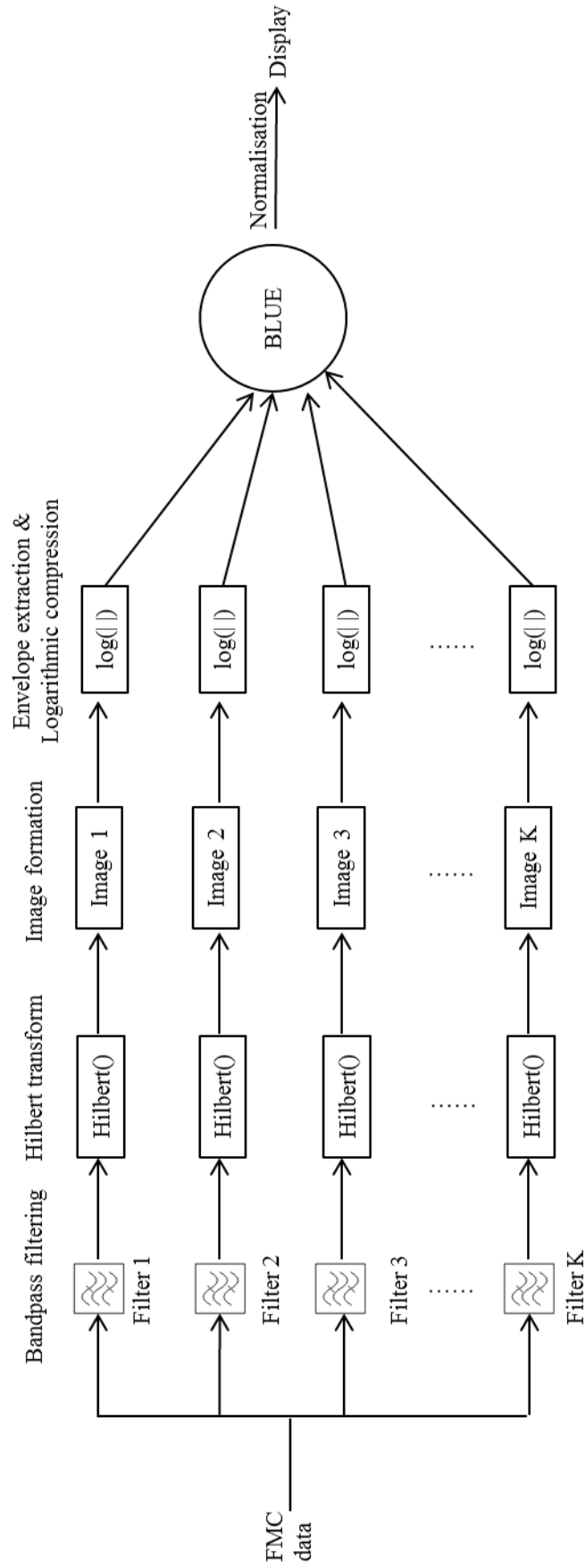
Fig. 5.2: Flow chart of combining SSP with the BLUE method

5.3   Methods

A 2D plain strain model was configured in the FE modelling suite PZFlex to illustrate the speckle pre-whitening capability of BLUE. In the model, for a 25 x 25 mm stainless steel structure (wavelength λ=1.158 mm at 5 MHz) with an element size of 50 x 50 μm, there were 8000 Brass elements randomly distributed within the volume acting as scatters (volume fraction 5%, 26.8 scatters/λ^2). A linear phased array whose parameters are listed in Table 5.1 was also simulated in the model, placed on the top of the steel structure. A 1.5-cycles Blackman-Harris windowed 5 MHz sinusoid pulse was used as the excitation signal. The model geometry and array position are shown in Fig. 5.3(a). FMC data were collected in PZFlex and then exported to Matlab for processing.

Table 5.1: Array parameters for simulation

Parameter	Value
Element number	32
Element pitch	0.7 mm
Central frequency	5 MHz
Bandwidth (-6dB)	3.5 ~ 6.5 MHz

Experiments were conducted on **Sample 5** and **Sample 6** whose details are given in Table 2.2. Recall that **Sample 5** is an Inconel 625 stepped wedge with three through thickness 5-mm-diameter SDHs and **Sample 6** is an austenitic steel weld plate with seven implanted flaws. The inspection geometry and flaws locations for the two samples are schematically drawn in Fig. 5.3(b)-(c). For the Inconel 625 sample, only the two SDHs at the depths of 60 mm and 105mm are considered in the Thesis. For the purpose of simplicity, the nearer SDH and the deeper SDH are named as SDH1 and SDH2, respectively. The Inconel sample is highly scattering and attenuative. Hence, its B-scan image suffers from strong speckle and the SDH2 is almost completely obscured by speckle. For the austenitic steel weld plate, the 45° tilted slot implanted at the weld boundary simulating the lack of fusion was inspected in experiments. The tilted slot is

6mm long in depth and its upper tip is at a depth of 14 mm. The austenitic steel weld plate is less scattering than the Inconel 625 sample but the sidelobe of backwall echo in the vicinity of the slot raises the difficulty of detecting the slot. These two samples have different scattering levels and flaw types, enabling the assessment of the robustness of the BLUE method. Again, all the data processing was conducted offline in Matlab.
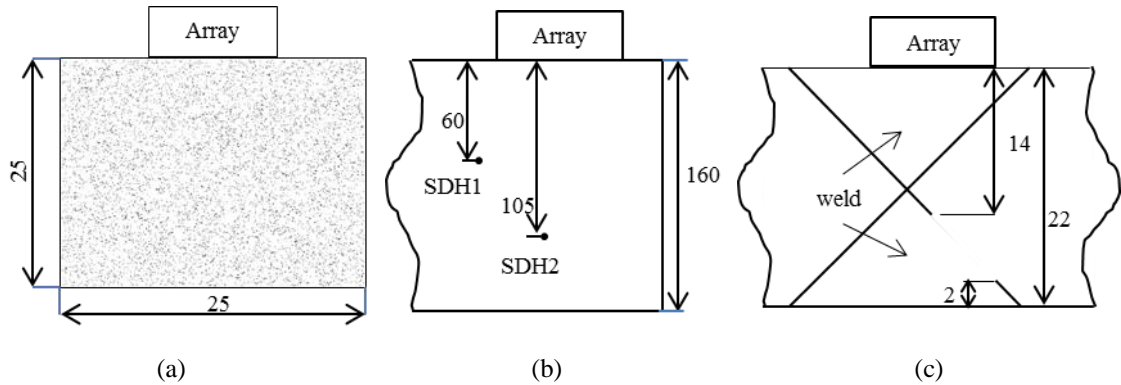
Fig. 5.3: Array and sample geometry labelled in millimetres for: (a) simulation, (b) experiment on the Inconel 625 sample, (c) experiment on the austenitic steel weld plate. Simulation has no flaw; the Inconel 625 sample has two SDHs at the depths of 60 and 105 mm, respectively; the austenitic steel weld plate has a 45º tilted slot with its upper tip at the depth of 14 mm.

For each case of the simulation and experiments analysis described in the next section, each A-scan of the collected FMC data underwent bandpass filtering by a bank of three bandpass filters and then Hilbert transform. All the filters in the filter bank were fourth-order infinite impulse response Butterworth filters. Then three TFM images were constructed which subsequently underwent envelope extraction, logarithmic transformation, combination, and normalisation prior to display. Three combination methods will be used and compared in next section: frequency multiplication (FM), mean (MEAN), and the proposed BLUE. The conventional FM and MEAN approaches yield the geometric mean and arithmetic mean of sub-band images. Their equivalent approaches in the scope of A-scan processing are formulated as Eq. 2.14 and Eq. 2.16, respectively. It should be noted that the MEAN approach is identical to the averaging approach mentioned in the two previous sections. Additionally, the FMC data filtered using a bandpass filter with a bandwidth equal to the total bandwidth of the three filters were used to construct a TFM image. This TFM image is served as the benchmark for comparison.

In the next section, for the simulation analysis, the SI values obtained by the three combination methods at various filter overlaps will be compared to demonstrate that BLUE approach yields the highest SI enhancement for the coloured speckle patterns. For experimental analysis, the improvements of image contrast obtained by the three methods will be compared. In addition, since the image contrast improvement achieved by the proposed BLUE method is a function of the filter overlap and the length of the pixel segment for the covariance matrix calculation, parametric studies of the effects of these two parameters on BLUE performance will be carried out to provide the optimal choices of these two parameters in various cases. Note that from this point onwards, this length of the pixel segment for the covariance matrix calculation will simply be referred to as the "segment length" and is expressed as the ultrasound wavelength corresponding to the central frequency of the aforementioned filter bank.

5.4 Results and discussion

5.4.1 Simulation result

In the simulation, the total bandwidth of the three filters was chosen as 3~7 MHz which is slightly wider than the pass band of the simulated array. The segment length for the BLUE approach was empirically selected as a length of 3λ (at 5 MHz). It should be noted that the SI values are measured on the resultant TFM images from BLUE combination before normalisation since the nonlinear normalisation operation would alter the SI values. All pixel values on each TFM image were used for SI calculation. Since BLUE operates under the condition of Co being positive definite, it is not applicable for 100% overlap which results in a singular matrix of Co. For this reason, the SI values were measured at the filter overlap varying from 0% to 90% in increment of 10%.

Fig. 5.4 plots the SI values varying with the filter overlap for FM, MEAN, and BLUE methods. The SI of the image obtained by applying a 3~7 MHz bandpass filtering has a benchmark value of 9.7 which is drawn on the far left of the axis. It is seen in the plot that the FM and MEAN approaches improve the SI to around $\sqrt{3}$ times of the

benchmark value at zero overlaps. This is because the speckle patterns on sub-band images are uncorrelated due to the complete separation of frequency bands and have identical variances as a result of insignificant frequency-dependent phenomena due to small simulated depth range. In other words, speckle on the sub-band images is white noise at zero overlaps. The SI values obtained by the two approaches approximately linearly decrease with overlap and are expected to be equal to the benchmark value at 100% overlap. The BLUE method also improves the SI by around $\sqrt{3}$ at zero overlaps. As the BLUE approach can pre-whiten speckle patterns, it consistently yields higher SI value than the other two approaches at other overlapping conditions.
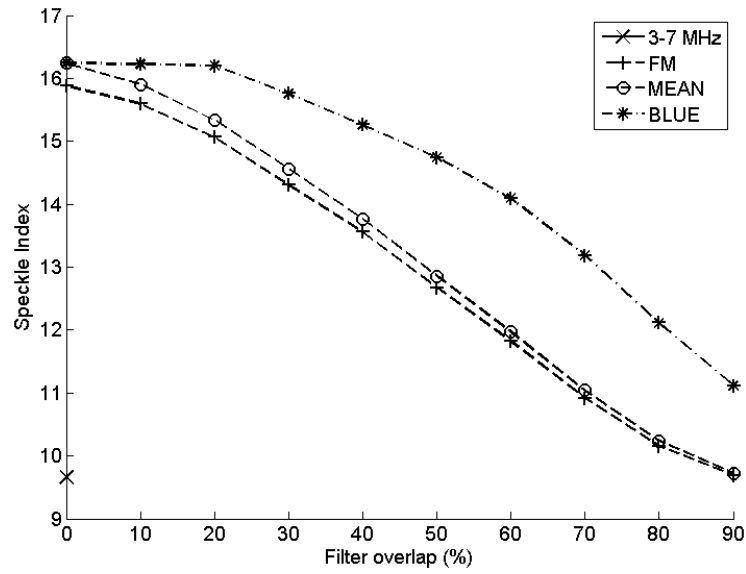
Fig. 5.4: Comparison of simulated SI obtained by three methods at various filter overlaps

To further validate the noise pre-whitening effect of the BLUE approach, the three axial beamplots on the three original sub-band images and the counterparts on the three pre-whitened sub-band images using 50% filter overlap are compared in Fig. 5.5. Note that the pre-whitened sub-band images are obtained by pixel-wise multiplying original sub-band images with the whitening matrix, as formulated in Eq. 5.14. As a 50% filter overlap was applied, the three filters have a central frequency of 4 MHz, 5 MHz, and 6 MHz, respectively. Each axial beamplot is labelled as its corresponding central frequency in Fig. 5.5. The axial beamplots were obtained from the middle column line of the sub-band images of the simulated material. It is observed that the three axial beamplots obtained from the three original sub-band images have similar magnitude

profiles indicating a high correlation between sub-band speckle patterns. This is in contrast to the three beamplots obtained from the pre-whitened case which show dissimilar profiles indicating uncorrelated sub-band speckle patterns.
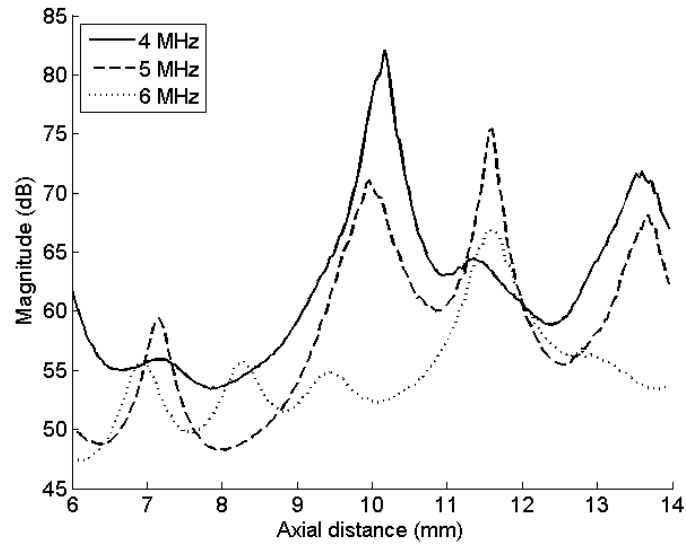
(a)
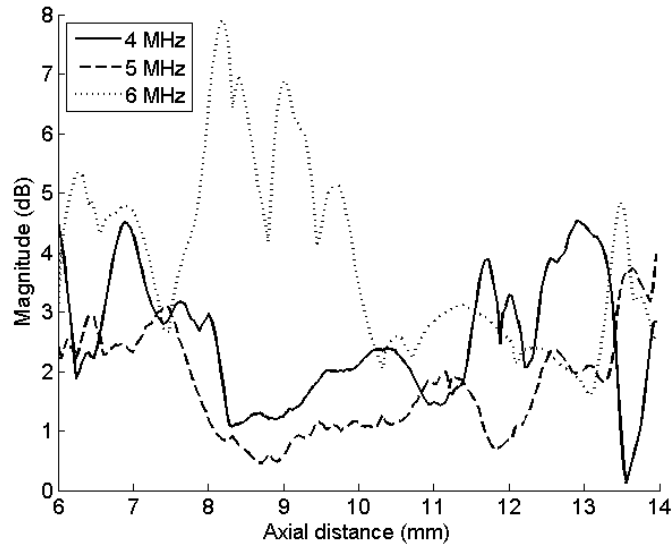
(b)

Fig. 5.5: Axial beamplots on: (a) original sub-band images and (b) pre-whitened sub-band images.

To quantitatively validate the pre-whitening effect of BLUE, all pixel values of the sub-band images are used to calculate the covariance matrix for both the original case and the pre-whitened case. Six unique entries of the covariance matrix for both cases are listed in Table 5.2 in which, for instance, σ_{13} is the covariance between the 4 MHz image

and the 6 MHz image. Variances of each sub-band images are very close for both cases. The covariance σ_{12} is around half of the variances as a result of 50% overlap for the original case whilst its value is reduced to -0.5 for the pre-whitened case. The reduced values of σ_{12}, σ_{13} and σ_{23} in the pre-whitened case prove that BLUE can pre-whiten coloured speckle patterns.

Table 5.2: Comparison of the covariance matrix of the speckle on the original and pre-whitened sub-band images

Sub-band images	Entries of covariance matrix					
	σ_{11}	σ_{12}	σ_{13}	σ_{22}	σ_{23}	σ_{33}
Original	33.1	16.2	3.03	32.7	11.5	30.2
Pre-whitened	7.6	-0.5	-0.3	7.7	0.22	6.9

5.4.2 Experimental evaluation - Inconel 625

In general, the frequency range for SSP is selected to be close to the pass band of the inspection transducer or array because of high ultrasound energy contained within this band. However, since the Inconel 625 sample is very thick and ultrasonically scattering, the sound energy contained in the upper part of the pass band is strongly attenuated at deep propagation ranges. The upper part of the pass band is, therefore, inappropriate for SSP.

To determine the appropriate frequency range for SSP, the frequency-dependent attenuation coefficient of this sample is obtained. The attenuation coefficient (with a unit of dB/cm) as a function of frequency can be obtained based on the difference between the spectral magnitudes of the first and the second backwall reflections. As the backwall reflections of the Inconel 625 sample are obscured by strong grain noise in the A-scan signals, the attenuation coefficient is measured from the experimentally acquired data of **Sample 2** (Inconel 617 sample) which has a similar composition to but much smaller size than the Inconel 625 sample.

The measured attenuation coefficient is multiplied by two times the thickness of the Inconel 625 sample to obtain the frequency-dependent attenuation of backwall signals of the Inconel 625 sample studied here which is drawn as Fig. 5.6. It is observed in the figure that the frequency band above 3 MHz exhibits severe amplitude loss and so is inappropriate for SSP. Therefore, the frequency range of 1~3 MHz was chosen as the total bandwidth of the three bandpass filters.
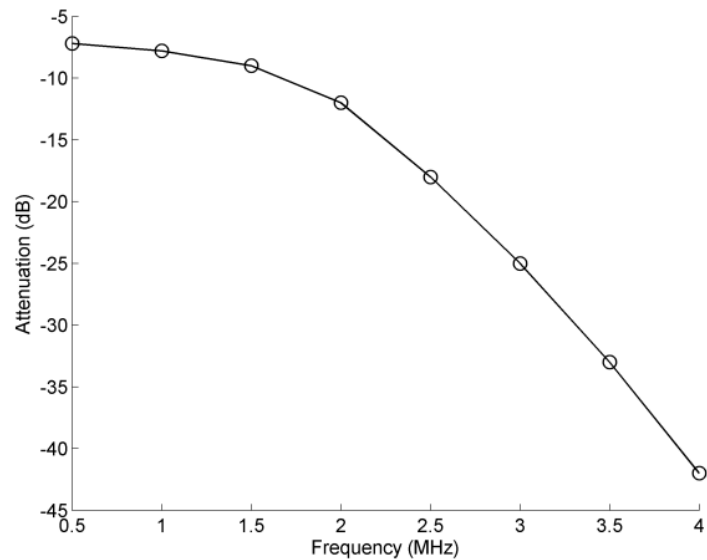
Fig. 5.6: Frequency-dependent attenuation of the backwall reflection of the Inconel sample.

A filter overlap of 50% was initially chosen for processing. In this case, the first filter and the third filter are just separated. The three filters have a central frequency of 1.5 MHz, 2 MHz, and 3 MHz, respectively and each filter has a -6dB bandwidth of 1 MHz. Fig. 5.7(a) shows the original TFM image without filtering applied in which the locations of SDH1 and SDH2 are highlighted. Fig. 5.7(b)-(d) show the three sub-band TFM images to be compounded. All the three sub-band images suffer from strong granular speckle. It is seen that the image acquired at 2.5 MHz has the highest spatial resolution due to the use of narrowest pulse. Meanwhile, the ultrasound wave suffers from the strongest attenuation, and the SDH2 is completely obscured by speckle. It should be emphasised that the image normalisation step is applied after the combination of sub-band images. Therefore, the three sub-band images to be combined as well as the original TFM image are displayed with a dynamic range of 70~130 dB.
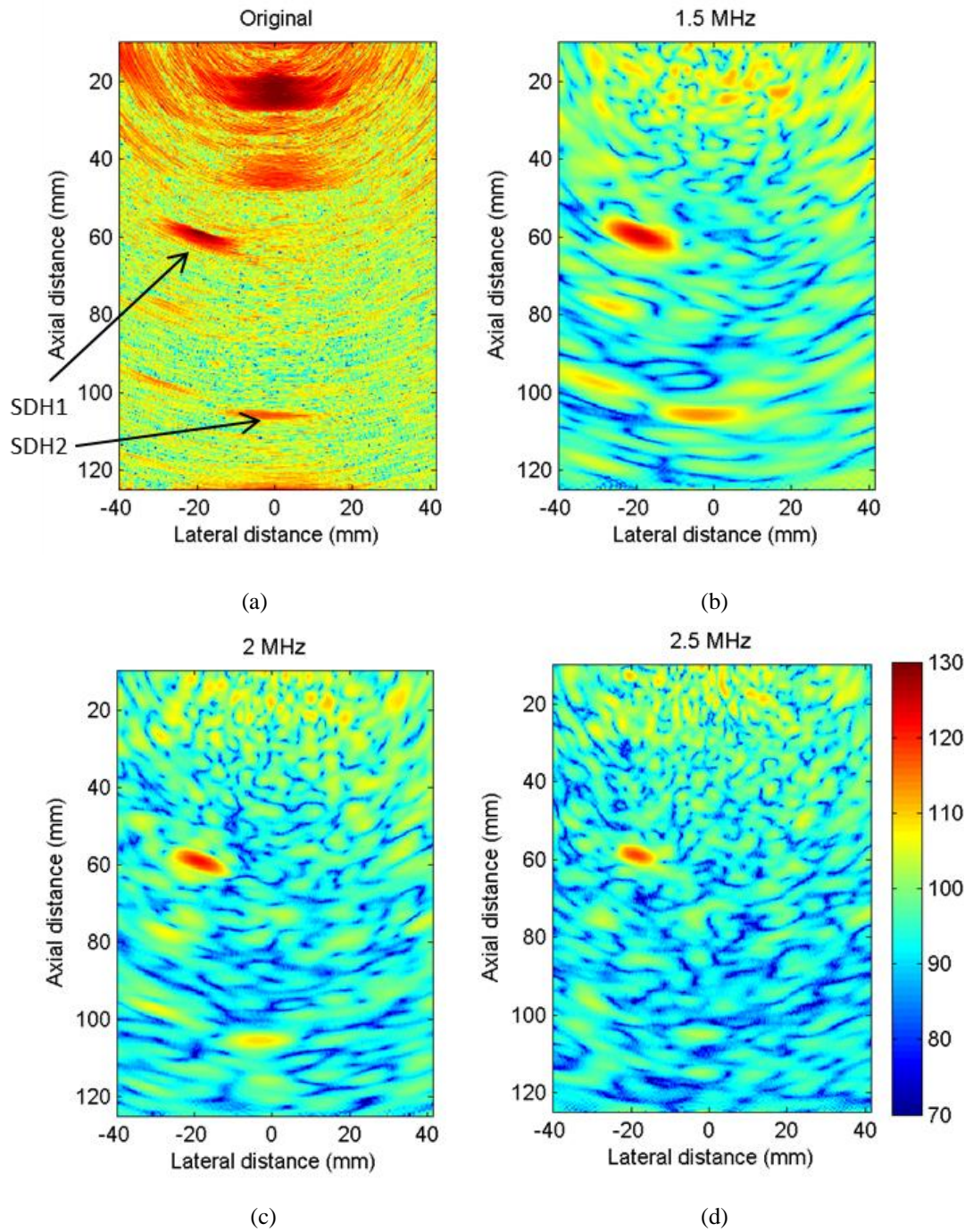
Fig. 5.7: TFM images of the Inconel625 sample filtered by: (a) no filtering; (b) 1.5 MHz (1~2 MHz);
(c) 2 MHz (1.5~2 MHz); (d) 2.5 MHz (2~3 MHz). (the format: central frequency (-6dB bandwidth)).

Fig. 5.8 (a) shows the benchmark TFM image constructed using the filtered FMC data by a bandpass filter with a -6 dB bandwidth of 1~3 MHz. Fig. 5.8(b)-(d) display the normalised resultant images of combining the three sub-band images, i.e., Fig. 5.7(b)-(d), using FM, MEAN, and BLUE, respectively. All the four images are displayed with

a dynamic range of -30~0 dB. A segment length of 4λ (at 2MHz) for BLUE was empirically chosen. The Matlab code for generating Fig. 5.8(d) is given in Appendix E.

(a)

(b)

(c)

(d)
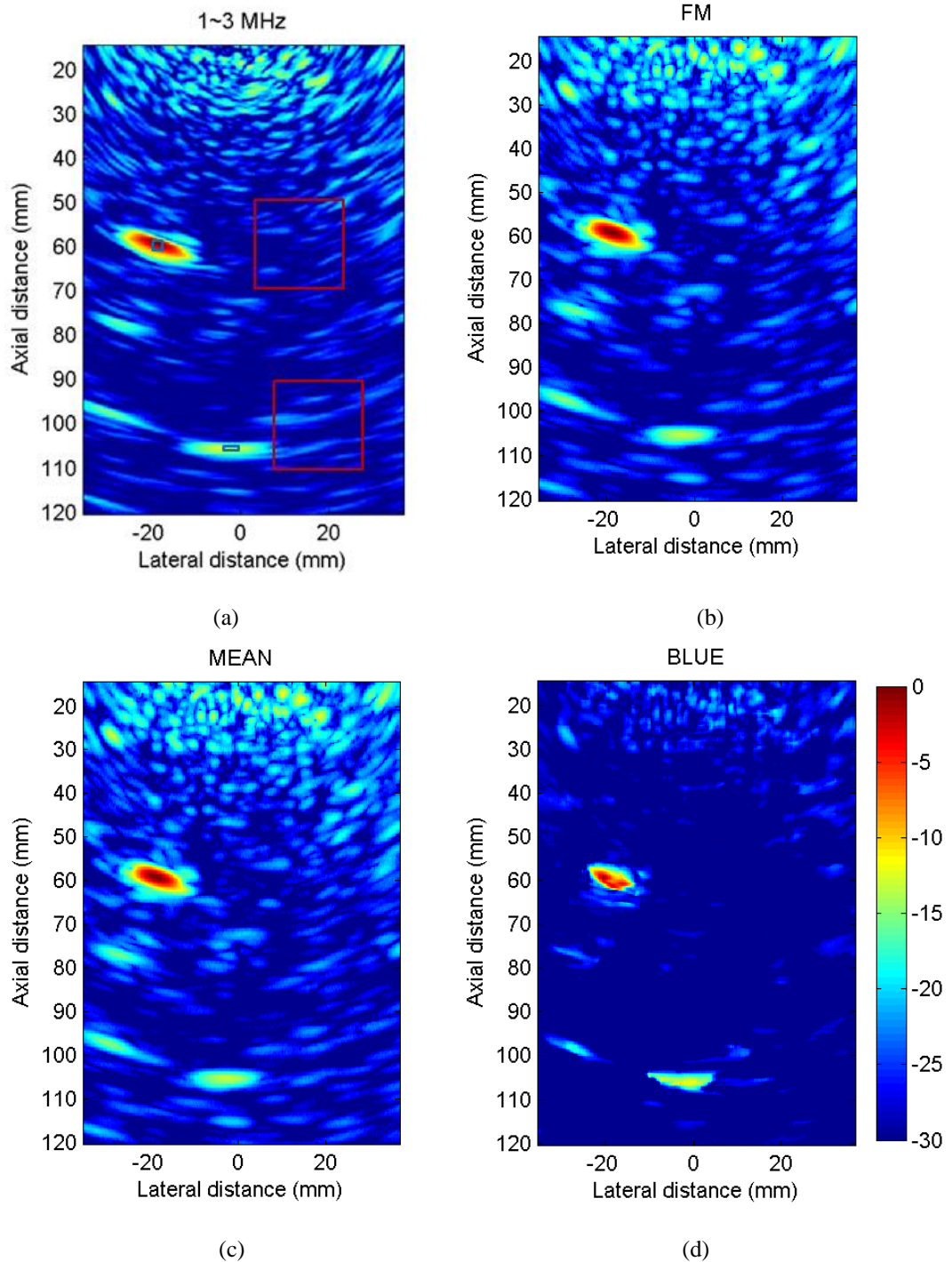
Fig. 5.8: Comparison of SSP results of the Inconel 625 sample using different combination approaches: (a) no combination, a bandpass filter (-6dB bandwidth of 1~3MHz) applied to FMC data; (b) FM; (c) MEAN; (d) BLUE. The blue and red boxes on (a) highlight the flaw and speckle regions for CNR calculation, respectively.

A qualitative observation gives that the FM and MEAN approaches obtain very limited enhancement in terms of image contrast and flaw visibility. Moreover, the speckle granularity on the FM and MEAN images is observed larger than that on the benchmark TFM image shown in Fig. 5.8(a). This is attributed to the use of narrowband sub-band images in the FM and MEAN approach. By contrast, the BLUE approach significantly improves image contrast and flaw visibility while spatial resolution is maintained, although the mainlobe of SDH1 is slightly distorted. Particularly, the SDH2 is much easier to discern, and its mainlobe has a slightly larger intensity in the BLUE result than the counterparts in the FM and MEAN results.

To quantify the image contrast and flaw detectability improved by SSP, the Contrast-to-Noise Ratio (CNR) is defined as

$$CNR = \frac{\mu_f - \mu_s}{\sigma_s} \qquad \text{Eq. 5.17}$$

where μ_f is the mean of pixel values in a flaw region, μ_s and σ_s are the same as defined in Eq. 5.1 for SI calculation. As shown in Fig. 5.8(a), for each SDH, the selected speckle region and flaw region for CNR calculation are highlighted by a red rectangle and a blue rectangle, respectively. The speckle regions are selected near to the corresponding SDHs and both have a size of 7λ x 7λ. The flaw regions are selected at the centre of corresponding SDHs and have a size of 0.7λ x 0.7λ and 0.3λ x 1.5λ for SDH1 and SDH2, respectively. It should be noted that the SI values were measured on the resultant images before normalisation as with the SI measurement in simulation whilst the CNRs so as the speckle level (μ_s) were measured on the normalised images indicating the true improvement of flaw detectability and image contrast.

Values of CNR and speckle level obtained by the three combination methods are listed in Table 5.3. Again, the values of CNR and speckle level of the image created by 1~3 MHz filtering serve as benchmark values. Each value within the parentheses in the CNR column is the CNR gain (CNRG), defined as the quotient of the CNR_c on the compounded image and the benchmark one CNR_b.

$$CNRG = \frac{CNR_c}{CNR_b} \qquad \text{Eq. 5.18}$$

It is seen in Table 5.3 that the BLUE approach yields higher CNRG than both FM and MEAN approaches for both SDHs. As explained in Section 5.2, the noise pre-whitening effect of BLUE enables it to obtain superior performance in improving image contrast than other two approaches. It would be interesting to note that the CNRG values of SDH2 are slightly smaller than the counterparts of SDH1 for any combination approaches. This is attributed to the fact that the speckle region near SDH2 has a larger degree of variance difference between sub-bands than SDH1 as a result of more prominent frequency-dependent phenomena at the deeper range. In addition, the speckle level yielded by BLUE is slightly lower than the benchmark one for both SDHs whereas the FM and MEAN approaches slightly increase speckle level. This is because BLUE weights the sub-band most heavily with the smallest variance which typically tends to be the sub-band with lowest speckle level [115].

Table 5.3: Comparisons of CNRG and speckle level obtained by different combination approaches for the two SDHs of the Inconel 625 sample.

Flaws	Approaches	CNR(CNRG)	Speckle level (dB)
SDH1	1~3 MHz	5.44	-31.48
	FM	8.09(1.47)	-28.81
	MEAN	8.24(1.50)	-28.74
	BLUE	10.26(1.86)	-33.63
SDH2	1~3 MHz	3.21	-28.82
	FM	4.49(1.40)	-29.15
	MEAN	4.58(1.43)	-28.97
	BLUE	5.67(1.77)	-31.93

Except image contrast, it is also useful to compare resultant axial resolution of the three combination methods. Axial resolution determines the ability of an imaging system to distinguish clustered targets in the axial direction. Fig. 5.9 shows the comparison of the axial beamplots on the four images of Fig. 5.8 in the range that corresponds to SDH1.

To quantify the axial resolution, the beamwidths are measured on the beamplots. The beamwidth is defined as the length of the axial range within which the beam magnitude

is greater than a certain dB from its maximum value. The beamwidths are measured for the case of -6 dB, -10 dB, -20 dB, and -30 dB on all the four beamplots and are listed in Table 5.4. For the FM approach and the MEAN approach, the beamwidths are consistently slightly larger than the benchmark ones which indicate deteriorated axial resolution. This is a consequence of the inevitable use of narrow individual sub-bands for SSP, as previously discussed in Section 2.4.1.2. On the contrary, the BLUE approach consistently reduces the beamwidths which means that BLUE improves the axial resolution. This is because the reduced axial resolution due to the use of narrow individual sub-bands for SSP is compensated by the speckle contrast reduction achieved by BLUE. The net effect is that BLUE yields better axial resolution than the benchmark one.
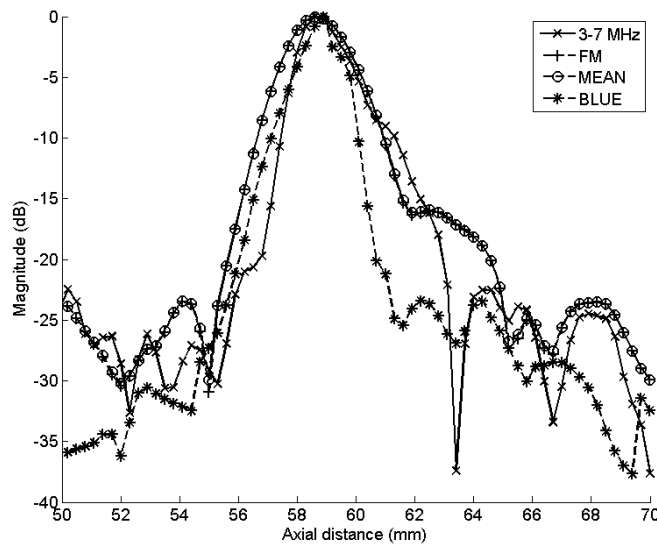
Fig. 5.9: Comparison of axial beam profiles centred at the SDH1 for the Inconel 625 sample.

Table 5.4: Comparisons of beamwidths for the SDH1 of the Inconel 625 sample. Note that beamwidth is measured in millimetres.

Approaches	-6dB	-10dB	-20dB	-30dB
1~3 MHz	3.2	5.2	8.4	22.8
FM	4.0	5.6	11.6	26.4
MEAN	4.0	5.6	11.6	26.8
BLUE	2.8	3.6	6.0	17.2

5.4.2.1 Parametric study

The CNRG obtained by BLUE is a function of the filter overlap and the segment length for the covariance matrix calculation. To give an indication of optimal values and value ranges of these two parameters, parametric studies of the effects of the two parameters on CNRG for both SDHs were carried out. The CNRGs were measured with the filter overlap varying from 0 to 90% in increment of 2.5% while the total bandwidth of the three bandpass filters was fixed at 1~3 MHz and with segment length varying from 1λ to 9λ in increment of 0.2λ. Fig. 5.10 presents the results of the parametric studies for both SDHs. It is easily discernible that the optimal values and value ranges of the two parameters are different for the two SDHs. The CNRG value of SDH1 as showed in Fig. 5.10(a), is particularly high at the filter overlap range of 0%~50% and segment length range of 2λ~4λ. The maximum CNRG occurs at 0% overlap and 3λ. For the SDH2, as shown in Fig. 5.10(b), significant CNRG is yielded at the filter overlap range of 0%~70% and segment length range of 4λ~6λ whilst the maximum CNRG occurs at 50% overlap and 6λ. The difference in optimal ranges of the filter overlap and segment length between the two SDHs are explained sequentially as follows.

(a)   (b)
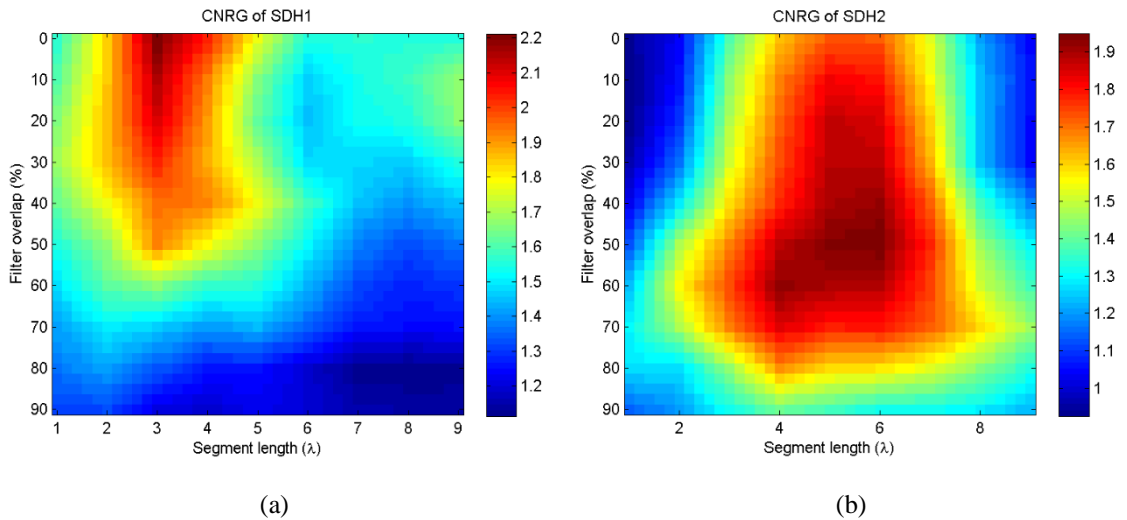
Fig. 5.10: CNRG as a function of the filter overlap and segment length for the covariance matrix calculation for the: (a) SDH1and (b) SDH2 of the Inconel 625 sample.

The optimal value and value range of the filter overlap which yields the highest CNRG is a result of mutual suppression of two competing factors: the speckle correlation and the speckle variance dissimilarity. The reduced overlap decreases the speckle

correlation meanwhile increases the speckle variances dissimilarity. The increased overlap reduces the variances dissimilarity meanwhile increases the speckle correlation. The optimal filter overlap is determined by the relative strength of the two competing factors. The strength of speckle correlation is proportional to filter overlap. The strength of variances dissimilarity is determined by the variability of frequency-dependent phenomena at difference sub-bands which is a function of the spectral distance between sub-bands and the distance of ROI to inspection probe.

Because the speckle region near to SDH1 is near to the inspection array and the spectral distance between sub-bands is small, the variability of frequency-dependent phenomena and so variances dissimilarity is insignificant. Therefore, though the strength of speckle correlation is zero and so is smaller than the strength of variance dissimilarity at zero overlaps, it rapidly surpasses the strength of variance dissimilarity as the filter overlap increases. Therefore, The CNRG of SDH1 has a general trend of decrease as the filter overlap increases which is in agreement with the monotonic decrease of SI with overlap increase obtained in simulation.

In contrast, the CNRG of SDH2 firstly increases and then decreases as the filter overlap increases. The peak CNRGs for all the cases of segment length fall in overlap range of 40%~60% for all instances of segment length. This is because the frequency-dependent phenomena are prominent at the speckle region near to SDH2 due to its far distance to the inspection array, as previously mentioned. As a result, the strength of variance dissimilarity is larger than the strength of speckle correlation in the overlap range of 0%~40%. Therefore, the CNRG increases as the filter overlap increases from 0% to 40%. As the strength of variance dissimilarity decreases with and the strength of speckle correlation increases with the rise of the filter overlap, the strengths of the two competing factors become approximately equal in the overlap range of 40%~60% and then the strength of speckle correlation dominates when the overlap is larger than 60%. Consequently, the value of CNRG reaches the peak at the filter overlap range of 40%~60% and decreases as the filter overlap increases from 60% to 100%.

The CNRG value firstly increases and then decreases as segment length increases for both SDHs. For SDH1, the available information would be insufficient to obtain an accurate representation of local variances and covariances if the segment length is

153

selected to be less than 1.5λ. When the segment length is larger than 4.5λ, the pixel segment for covariance matrix calculation at flaw region is dominated by speckle. As a result, the flaw signals are suppressed by BLUE along with speckle. The variation of CNRG of SDH2 with the segment length can be explained in the same fashion. Additionally, the optimal value of the segment length increase from 4λ for SDH1 to 6λ for SDH2 since the beam spread effect is more prominent at the deeper SDH2.

5.4.3 Experimental evaluation - austenitic steel weld plate

As previously mentioned, the sample is less scattering and much thinner than the Inconel sample, enabling the use of higher frequencies for SSP analysis. The total bandwidth of three bandpass filters was therefore selected as 3~7 MHz. The filter overlap and segment length are initially selected as 0% and 3λ (at 5 MHz), respectively. Fig. 5.11(a) shows the original TFM images without filtering and Fig. 5.11(b)-(d) show the three sub-band TFM images to be compounded. All the four images are displayed with a dynamic range of 70~120 dB. It should be noted that the ultrasound arrived at the two slot tips undergoes diffraction and some of the energy is captured by the array whereas the ultrasound arriving at the slot surface undergoes specular reflection with a large angle thus cannot be captured by the array. In addition, energy diffracted by the lower tip is overwhelmed by backwall echoes. For these reasons, only the upper tip of the tilted slot can be observed on images and is seen to locate at the depth of 14 mm. Unlike the Inconel sample, there are two contributors to image noise interference: speckle at the right side of the slot and sidelobes of backwall echo at the left side of the slot. The sidelobes of backwall echo near to the slot are prominent since the slot is very near to the sample backwall.

Fig. 5.12(a) shows the benchmark TFM image created using the filtered FMC data by a bandpass filter with a -6 dB bandwidth of 3~7 MHz. Fig. 5.12(b)-(d) compare the results using different combination approaches. All the four images are displayed with a dynamic range of -35~0 dB. In line with the previous Inconel sample, an observation gives that the FM and MEAN approaches yield very limited enhancement in terms of image contrast and flaw visibility. By contrast, the BLUE approach significantly improves image contrast and flaw visibility.
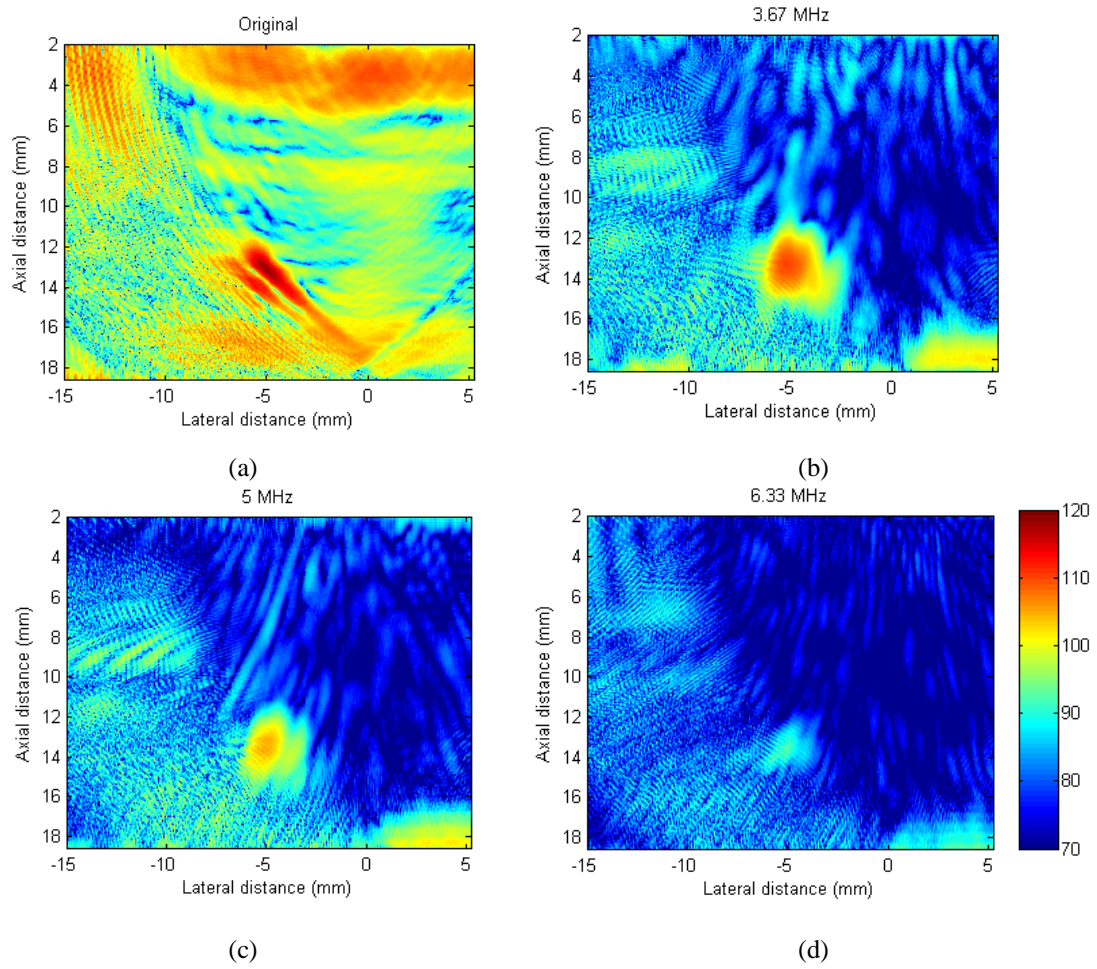
Fig. 5.11: TFM images of the austenitic steel weld plate filtered by: (a) no filtering; (b) 3.67 MHz (3~4.33 MHz); (c) 5 MHz (4.33~5.67 MHz); (d) 6.33 MHz (5.67~7 MHz). (the format: central frequency (-6dB bandwidth)).

Values of CNR and speckle level are calculated using a flaw region of $\lambda \times \lambda$ size labelled by a blue rectangle and a speckle region of $8\lambda \times 5\lambda$ size labelled by a red rectangle shown in Fig. 5.12(a). Again, the CNR obtained by 3~7 MHz filtering serves as benchmark CNR for CNRG calculation. These values are listed in Table 5.5. Both FM and MEAN approaches yield much lower CNRG than the BLUE approach. In addition, the speckle level obtained by BLUE combination is over -10 dB lower than the benchmark value. Again, this is attributed to the fact that BLUE weights the sub-band most heavily with the smallest variance which is the sub-band with a central frequency of 6.33 MHz in this case.

155

(a)

(b)

(c)

(d)
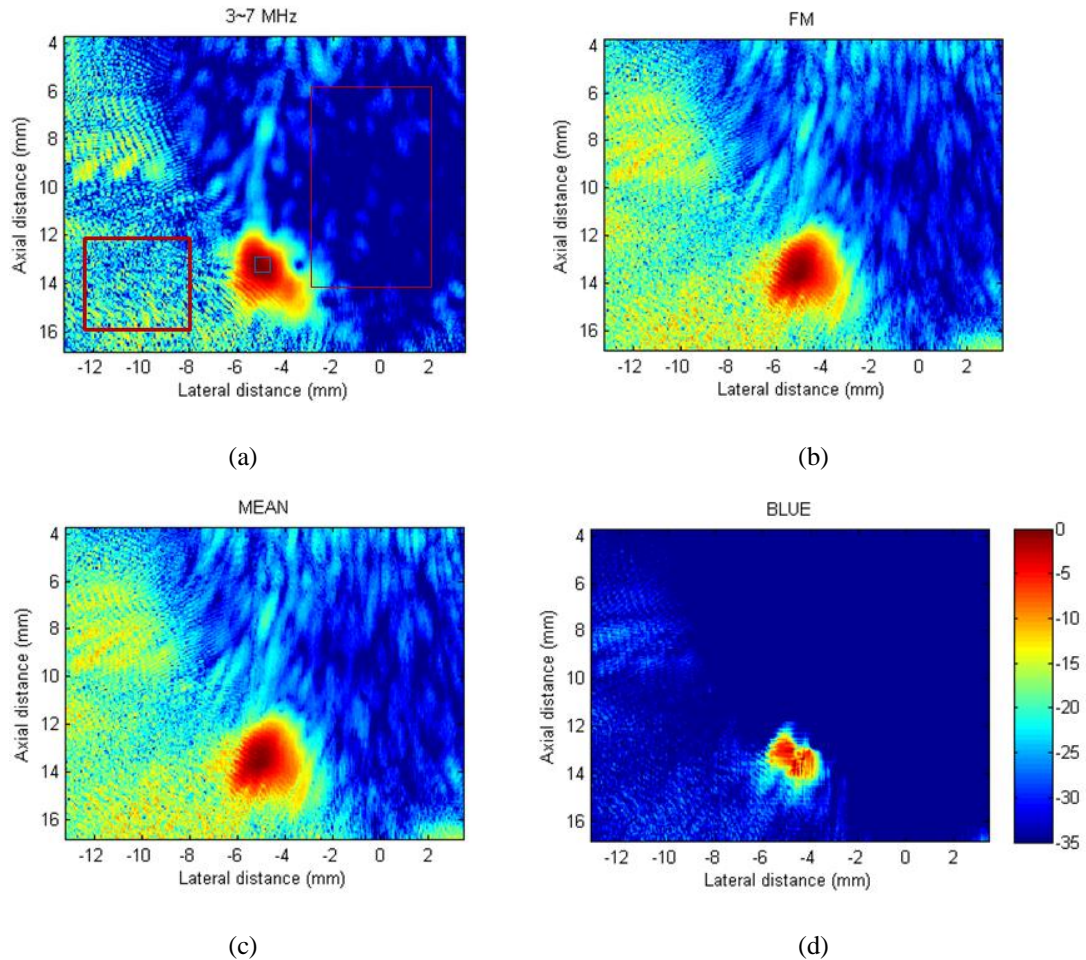
Fig. 5.12: Comparison of SSP results of the austenitic steel weld plate using different combination approaches: (a) no combination, a bandpass filter (-6dB bandwidth of 4~7MHz) applied to FMC data; (b) FM; (c) MEAN; (d) BLUE. The blue and red boxes on (a) highlight the flaw and speckle regions for CNR calculation, respectively; the bold red box encloses the region at where the sidelobe is measured.

It is interesting to mention that the sidelobes level of backwall echoes is also reduced in the BLUE result. Insonifying the backwall with different frequencies give similar mainlobe patterns and different sidelobe patterns. In fact, the sidelobe at low frequency is a stretched version of the sidelobe at high frequency. Therefore, similar to speckle, sidelobes on sub-bands images are partially correlated. Consequently, the BLUE method is also able to suppress sidelobes. Averaged sidelobe level of an area highlighted by a bold red rectangle shown in Fig. 5.12(a) are measured as -23.20 dB, -20.18 dB, -20.17 dB, and −29.95 dB for 3~7 MHz filtering, FM, MEAN, and BLUE, respectively.

Table 5.5: Comparisons of CNR improvement and speckle level obtained by different combination approaches for the slot of the austenitic steel weld plate.

Approaches	CNR(CNRG)	Speckle level (dB)
3~7 MHz	6.01	-37.41
FM	7.75(1.29)	-31.36
MEAN	7.94(1.32)	-31.40
BLUE	11.09(1.85)	-49.82

5.4.3.1 Parametric study

Again, a parametric study was carried out by measuring CNRG in the cases of the segment length varying from 0.5λ to 5λ in increment of 0.15λ and the filter overlap varying from 0 to 90% in increment of 2.5% while the total bandwidth of three bandpass filters was fixed at 3~7 MHz. Fig. 5.13 shows the CNRG as a function of the filter overlap and segment length. It is seen that CNRG is significant at the filter overlap range of 0%~40% and the segment length range of 2λ~4λ. The optimal ranges for the two parameters are similar to those of the SDH1 of the above Inconel sample. CNRG is observed to decrease monotonically with filter overlap. This would imply that the strength of variance dissimilarity is consistently overwhelmed by the strength of speckle correlation as the filter overlap increases.
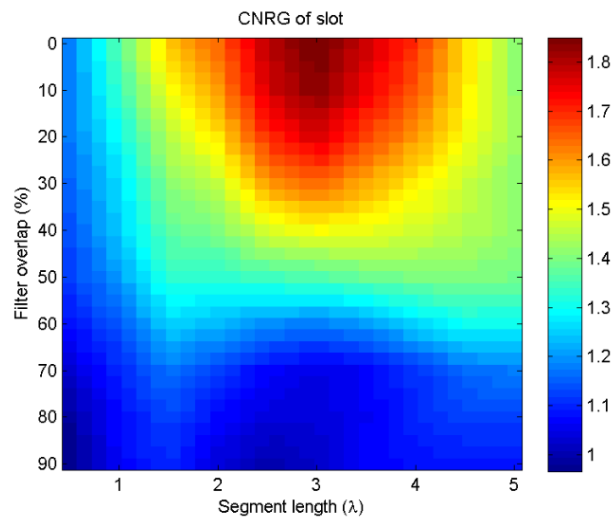
Fig. 5.13: CNRG as a function of the filter overlap and segment length for covariance matrix calculation for the slot of the austenitic steel weld plate.

5.4.4 Discussion

It is worth noting that by simply reducing the display dynamic range the flaw indications on the bandpass filtered images, i.e., Fig. 5.8(a) and Fig. 5.12(a), can also be greatly improved. The justification of conducting processing using BLUE is two-fold. Firstly, the adjustment of the display range is a subjective process. It is typically in the case that the display range is initially set as a relatively large value to keep all the important information and then gradually reduced to remove speckle; the reduction process stops until all the speckle is removed or before the indications of weaker flaws are removed. The reduction process is completely subject since one has to know the locations of the flaws to determine when the reduction process should stop. However, no flaw information is typically available in an industrial context. Compounding sub-band images using BLUE can reduce the speckle level thus shorten or even eliminate the reduction process, improving the objectiveness in defect detection. Secondly, BLUE compounding can greatly reduce the variation of speckle intensity, therefore, it can remove spurious flaw indications and so prevent unnecessary repairs.

The optimal value range of the filter overlap obtained by the above parametric studies may be not applicable to other materials. Therefore, the extra analysis is provided below to give a generalisable indication of this optimal value range for a variety of materials.

As previously mentioned, this optimal value range is determined by the relative strength of variance dissimilarity to speckle correlation which can be quantified as the ratio of the two competing factors (RDC)

$$\text{RDC} = \frac{\sigma_{Co(i,i)}}{\mu_{Co(i,j)}}, i = 1,2,\dots,K; \; i \neq j \qquad \text{Eq. 5.19}$$

where $\sigma_{Co(i,i)}$ is the standard deviation of the variances of speckle on sub-band images as a representation of variance dissimilarity and $\mu_{Co(i,j)}$ is the mean value of the covariances of speckle on sub-band images as a representation of speckle correlation.

If the RDC value is significant, the increase of the filter overlap will raise the CNRG value meanwhile, of course, reduce the value of RDC. As the overlap increases, CNRG will reach its highest value when RDC is reduced to a critical value. CNRG will decrease as the overlap increases if RDC is lower than the critical value.

Hence, a question arises: what is the critical value of RDC? The results of the above four parametric studies can be analysed to derive the critical value of RDC. RDC varying with the filter overlap for all four cases are plotted in Fig. 5.14. For the simulation, SDH1 of the Inconel 625 sample, and the slot of the austenitic steel weld plate, CNRG consistently decreases as the filter overlap increases. This implies that their RDC values are consistently lower than the critical value as the filter overlap varies. For the SDH2 of the Inconel 625 sample, CNRG increases when the filter overlap increases from 0% to 40% and reaches its highest value at the overlap range of 40%~60%. This implies that RDC value is approximately equal to the critical value which occurs in the filter overlap ranges of 40%~60%. Therefore, it can be inferred from Fig. 5.14 that the critical value of RDC is around 3.

To conclude, if the RDC value is greater than 3, both CNRG and the axial resolution are enhanced as the filter overlap increases until the RDC value is reduced to be equal to 3. For the case of RDC lower than 3, CNRG is improved at the price of the axial resolution as the filter overlap decreases whilst the axial resolution is improved at the price of CNRG as the filter overlap increases.
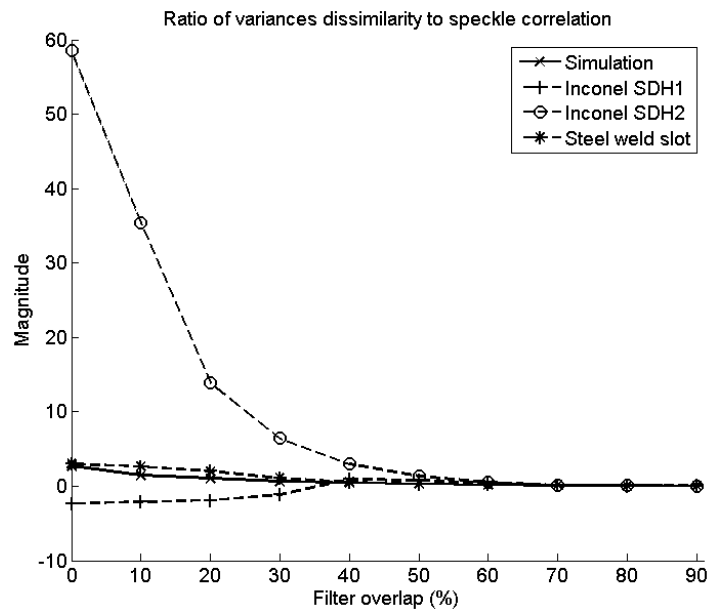
Fig. 5.14: Ratio of variance dissimilarity to speckle correlation as a function of the filter overlap for all four cases.

5.5   Conclusion and future work

In this chapter, the use of the BLUE algorithm as a combination method of SSP has been presented. BLUE linearly combines the sub-band images with weights which are adaptively tuned based on local statistics. It has the effect of pre-whitening, i.e., decorrelating and equalising the variances, the speckle patterns acquired at different frequencies. This enables the effective reduction of speckle contrast thus improvement of image contrast and flaw detectability. The pre-whitening effect of BLUE has been validated with FE simulation. Experimental results of the application of BLUE to data acquired from an Inconel sample with two SDHs and an austenitic steel weld plate with a tilted slot have been presented. An average of ~80% image contrast enhancement is observed for combining three sub-band images of the two samples. It has been demonstrated in experimental results that BLUE offers superior enhancement in terms of image contrast and flaw detectability to conventional combination approaches of SSP. Parametric studies of the effects of the filter overlap and length of pixel segment for covariance matrix calculation on image contrast improvement have been carried out to give an indication of optimal value ranges of these two parameters. Experimental result on the austenitic steel weld plate shows that the BLUE algorithm is also capable of lowering sidelobe levels. It is worth noting that though only the TFM imaging algorithm is used in this chapter, the proposed BLUE method is also applicable to other array imaging algorithms.

One drawback of the current BLUE approach is that it results in distortion to the mainlobe of legitimate flaws. This problem arises because when combining the pixels of the flaw mainlobe on sub-band images, the pixel segments for the covariance matrix calculation are occasionally dominated by speckle even though the segment is short, allowing the flaw mainlobe to be suppressed by BLUE along with speckle. Another approach to obtaining the covariance matrix in the scope of A-scan processing is worth investigation, in order to minimise the speckle disturbance to the covariance matrix of flaw signals. In this approach, the signal segment obtained from the A-scan of each transmitter-receiver of a phased array is bandpass filtered by a filter bank whose outputs are used to calculate the covariance matrix; then the covariance matrices of all transmitter-receiver pairs are averaged to obtain a single covariance matrix for the use

by BLUE. Alternatively, it is also worth applying signal or image processing algorithms to sub-band images to suppress the speckle level prior to combination these images. This would reduce the speckle disturbance to the covariance matrix of flaw signals.

Also in the future work, it would be prudent to consider parametric studies based upon varying sample dimensions, grain structure, and flaw characteristics to provide optimal choices of the filter overlap and segment length for covariance matrix for a broad range of inspection conditions.

Another aspect of future work is to further exploit the optimal number of filters. Theoretically, enhancement of image contrast increases with filter number at the price of axial resolution and computation cost. The trade-off between image contrast and axial resolution is worth further investigation to give the optimal filter number. Certainly, the determination of optimal filter number is subject to computation capacity.

CHAPTER 6. Distribution dissimilarity imaging for speckle reduction

6.1 Introduction

In this chapter, a new algorithm termed Distribution Dissimilarity Imaging (DDI) operating with phased array systems is proposed for the purpose of speckle reduction.

It has been described in Section 2.4.2 that the PDF of time-domain envelope signals can give an indication of the presence of a flaw. Typically, the envelope of the backscattered echoes from an ensemble of randomly distributed grain scatterers is characterised by a Rayleigh PDF. The envelope PDF changes from the Rayleigh distribution into a post-Rayleigh distribution, often known as Rician distribution, when a flaw is present.

Conventionally, the envelope PDF is generated from an envelope-detected A-scan trace acquired by a monolithic probe [107]. Such a way of generating envelope PDF typically leads to significant loss of axial resolution, since a large number of envelope instances are required to obtain a fair PDF representation.

If an N-element phased array and the FMC data acquisition approach are employed, N^2 envelope instances are available for each spatial point of the imaging area. In this case, a fair PDF representation can be obtained without the drawback of compromised axial resolution as long as the value of N is not too small. However, this PDF may no longer follow a Rayleigh distribution when only scatterers exist and also may no longer follow a Rician distribution if a flaw is present. This arises since the pulse amplitudes arriving at a spatial point are different for different array elements due to the element-dependent effects (e.g., beam divergence, element directivity and attenuation) [28], resulting in

nonlinear changes to the PDF of the envelope. If these element-dependent properties are known, their impact on the envelope PDF can be eliminated by deconvolution [109]. However, it is often the case in an industrial context that the details of these element-dependent properties are not available.

In this proposed DDI algorithm, the element-dependent properties are eliminated by normalisation and the PDFs of a few frequency components (FCs) instead of time-domain envelope signals are generated from FMC data and used for analysis. The DDI algorithm measures the dissimilarity between the PDFs of the magnitudes of FCs and corresponding reference Rayleigh PDFs whose parameters are obtained by the maximum likelihood estimation (MLE) technique. This dissimilarity reveals the possibility of a legitimate flaw indication.

This chapter is arranged as follows. The process and the theoretical basis of the DDI algorithm will be given in the next section. Then the simulation and experimental arrangements are described. Subsequently, the simulation and experimental results are shown to complement the theory of DDI and to showcase the superior performance of DDI on speckle reduction, respectively.

6.2   Theory

The DDI algorithm consists of three processing phases: the generation of the PDFs of a few FCs and the corresponding reference Rayleigh PDFs; the assessment of the dissimilarity between the two PDFs for each FC; the multiplication of the averaged dissimilarity coefficient with the beamformer output to obtain final processed image. The three phases are described sequentially as follows.

6.2.1   PDF generation

To generate the PDFs of FCs and corresponding reference Rayleigh PDFs, for each focal point of the imaging area, the following four steps are sequentially performed:

1)   For each A-scan in an FMC dataset acquired by an N-element array, the data sample corresponding to the focal point is positioned and a segment of data

samples centred at the positioned data sample is extracted. The length of the data segments is pre-defined. Fig. 6.1 shows the schematic diagram of extracting N^2 data segments from FMC data where the extracted data segments are shaded by yellow colour.

2) Each data segment is divided by its Euclidean norm to eliminate the aforementioned element-dependent effects. Each normalised data segment then undergoes Discrete Fourier Transform to produce an array of discrete FCs. K FCs with high ultrasound energy are selected for the use in the next step.

3) For each of the K FCs, there are N^2 instances which are sorted into L bins equally spaced between the minimum and maximum values of the instances, and the discrete PDF of the FC, $\boldsymbol{P_s}$, is generated by

$$P_s(i) = \frac{count(i)}{N^2}, i = 1,2,\ldots L \qquad \text{Eq. 6.1}$$

where the $count(i)$ is the number of instances falling in the ith bin and the sum of the elements of $\boldsymbol{count}$ is N^2.

4) For each of the K FCs, a reference discrete Rayleigh PDF $\boldsymbol{P_r}$ is also generated. Firstly, the scale parameter σ of the Rayleigh PDF is estimated by MLE from the N^2 instances of the FC

$$\sigma = \sqrt{\frac{\sum_{tx=1}^{N} \sum_{rx=1}^{N} A_{tx,rx}^2}{2N^2}} \qquad \text{Eq. 6.2}$$

where $A_{tx,rx}$ is the magnitude of the FC of a certain transmitter-receiver pair that is obtained in the second step. Then the equivalent $\boldsymbol{count}$ for $\boldsymbol{P_r}$ is calculated at the centres $\boldsymbol{C}$ of the aforementioned equally spaced L bins using the estimated σ

$$count(i) = \frac{C(i)}{\sigma^2} e^{-C(i)^2/2\sigma^2}, i = 1,2,\ldots L \qquad \text{Eq. 6.3}$$

Finally, $\boldsymbol{P_r}$ is computed as

$$P_r(i) = \frac{count(i)}{\sum_{i=1}^{L} count(i)}, i = 1,2,\ldots L \qquad \text{Eq. 6.4}$$
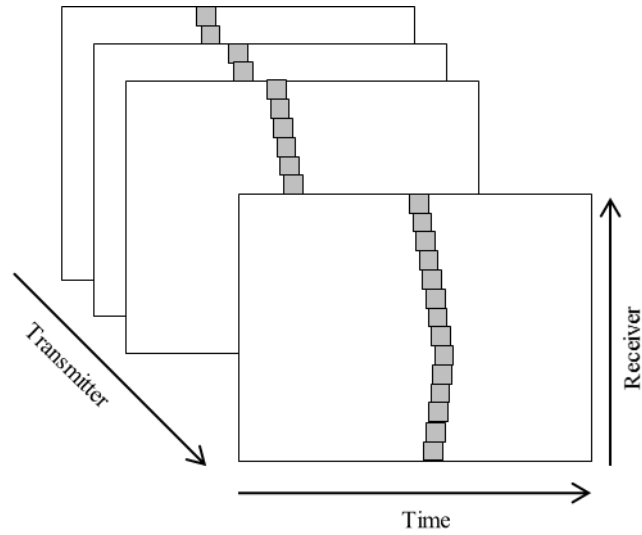
Fig. 6.1: Schematic diagram of data segments extraction from FMC data

Prior to introducing the second processing phase of the DDI approach, some mathematical analysis is given as follows in order to prove that the PDF of the magnitude of an FC can give an indication of the presence of a flaw from a theoretical perspective.

With the element-dependent effects being removed, the complex backscattered signal by a single scatterer *i* as a function of frequency can be formulated as

$$H_i(\omega) = G_i(\omega)e^{-j\omega t_i} \qquad \text{Eq. 6.5}$$

where $G_i(\omega)$ accounts for the reflectivity of the scatterer *i*; t_i is the TOF from the transmitter to the scatterer *i* then back to the receiver. By applying the single scattering assumption as described in Section 4.2, the backscattered signal detected by an array element is the superposition of backscattered signals from each individual grain scatterer in the resolution cell. Therefore, the detected complex frequency component A_c for a frequency ω_0 is formulated as

$$A_c = \sum_{i=1}^{M} H_i(\omega_0) = \sum_{i=1}^{M} G_i \cos(\varphi_i) + j * \sum_{i=1}^{M} G_i \sin(\varphi_i) = A_{real} + j * A_{imag} \qquad \text{Eq. 6.6}$$

where φ_i are the phase of scatterer *i*; *M* is the number of grain scatterers in the resolution cell; A_{real} and A_{imag} are the real and imaginary parts of the complex amplitude, respectively. The magnitude of A_c is calculated as

165

$$A = \sqrt{A_{real}^2 + A_{imag}^2} \qquad \text{Eq. 6.7}$$

If the scatterers are randomly distributed in the resolution cell, the phasor A_c is considered as a random walk in the complex plane. For the Rayleigh scattering regime where the grain diameter size is much smaller than wavelength [125], it can be assumed that a large number of scatterers are randomly distributed in the resolution cell, therefore, the Central Limit Theorem can be applied to the phasor A_c [107]. That is, the A_{real} and A_{imag} can be considered as Gaussian random variables with zero mean and equal standard deviation σ. Therefore, the magnitude of the frequency component, A, follows a Rayleigh distribution.

When a flaw exists and is surrounded by M scatterers in the resolution cell, a constant strong phasor with magnitude A_r is added in the complex plane. This has the effect of altering the Rayleigh PDF of the frequency component into a Rician PDF which is defined as

$$P(A) = \frac{A}{\sigma^2} e^{-(A^2 + A_r^2)/2\sigma^2} I_0\left(\frac{AA_r}{\sigma^2}\right) \qquad \text{Eq. 6.8}$$

where $I_0\left(\frac{AA_r}{\sigma^2}\right)$ is the modified Bessel function of the first kind with zero order.

Therefore, the changes of PDF of the magnitude of a frequency component can give an indication of the presence of a flaw.

6.2.2 Dissimilarity assessment

Many methods of measuring the statistical distance between two statistical objects can be used to compute the dissimilarity coefficient between the PDFs of FCs and the reference Rayleigh PDFs, i.e., $\boldsymbol{P_s}$ and $\boldsymbol{P_r}$. These methods include Euclidean distance, Chebychev distance, etc. [126]. The correlation and Spearman methods are exploited in the DDI algorithm since the dissimilarity coefficient produced by them increases smoothly with the increase of the degree of the deviation between the two PDFs. The two methods of utilising the correlation and Spearman methods are termed DDI-C and DDI-S, respectively. DDI-C is formulated as

$$\text{DDI– C} = 1 - \frac{(P_s - \bar{P}_s)(P_r - \bar{P}_r)'}{\sqrt{(P_s - \bar{P}_s)(P_s - \bar{P}_s)'}\ \sqrt{(P_r - \bar{P}_r)(P_r - \bar{P}_r)'}} \qquad \text{Eq. 6.9}$$

where the $\bar{P}_s$ and $\bar{P}_r$ are the mean values of P_s and P_r, respectively.

DDI-S is formulated as

$$\text{DDI– S} = 1 - \frac{(R_s - \bar{R}_s)(R_r - \bar{R}_r)'}{\sqrt{(R_s - \bar{R}_s)(R_s - \bar{R}_s)'}\ \sqrt{(R_r - \bar{R}_r)(R_r - \bar{R}_r)'}} \qquad \text{Eq. 6.10}$$

where the 1 x L R_s and the 1 x L R_r are the vectors of the rank orders of the P_s and P_r, respectively. $\bar{R}_s$ and $\bar{R}_r$ are the mean values of the rank orders and are both equal to $(1+L)/2$.

Both methods produce the dissimilarity coefficient within the range 0~1. The dissimilarity coefficient of the two PDFs is measured at each of the K selected FCs. Finally, the dissimilarity coefficients obtained from the K FCs are averaged to produce a final dissimilarity coefficient C at each focal point.

6.2.3 Coefficients multiplication

The coefficient matrix $C(x, z)$ obtained from the previous phase is then used to weight the beamformer output $a(x, z)$ to obtain the processed image

$$y(x, z) = a(x, z) \cdot C(x, z) \qquad \text{Eq. 6.11}$$

The focal points at the speckle region where the frequency components follow a Rayleigh distribution have much smaller coefficients than the flaw region, thus the intensity of the speckle region in the processed image is greatly reduced and the flaw region is conserved.

6.3 Methods

A model of describing grain scattering in a resolution cell was created using the analytical backscattering model described in Section 4.2, in order to evaluate the PDF characteristics of backscattered signals by this cell. The material was modelled with the

characteristic constant $k = 5 \times 10^{-18}$ and attenuation coefficient $\alpha = 5 \times 10^{-30}$. The sound propagation velocity in the material, c, was set as 5000 m/s. A 5 MHz 32-element array with a -6dB bandwidth of 3 MHz and 0.63 mm element pitch was simulated (λ=1 mm), with its intermediate point at the origin of a coordinate system. The array and the resolution cell, as well as the Cartesian coordinate system, are depicted in Fig. 6.2. The centre of the resolution cell is located at (0, R_F) where R_F =1.5D, in which D is the lateral length of the array (=20.16 mm). The resolution cell width W is the width of the mainlobe and can be calculated as $W \approx 2\lambda R_F /D$ (=3 mm) [81]. Its length H is the pulse length and can be calculated as $H \approx 2c/bw$ (=3.3 mm), where bw is the array bandwidth (3 MHz) [81]. There were 200 scatterers randomly distributed within the resolution cell, so the density of scatterers is calculated as $20/\lambda^2$. Additionally, another identical model except the introduction of a flaw (reflectivity $\rho_f = 1$) at the centre of the resolution cell was also created. For both models, a set of FMC data was simulated and used for later analysis.
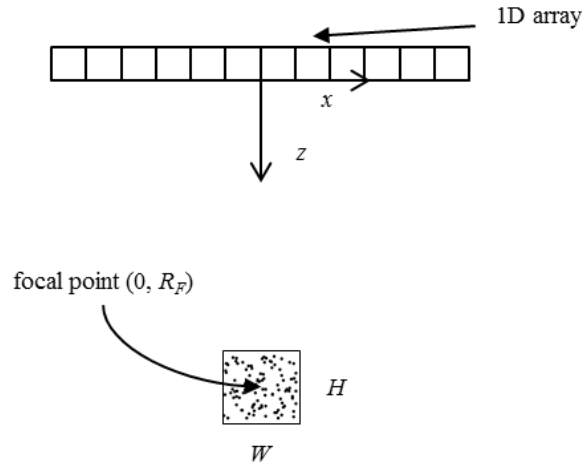
Fig. 6.2: Schematic diagram of an array and a resolution cell with randomly distributed scatters.

An FMC dataset of **Sample 3** which has been used for ANN analysis, as described in Chapter 4, also are used for DDI analysis here. Recall that **Sample 3** is an arc-shaped flaw-free austenitic steel block with a nominal thickness of 51 mm. The inspection geometry for the sample is schematically drawn in Fig. 4.7(a). The two FMC datasets of **Sample 5** and **Sample 6** which have been used for BLUE analysis, as described in Chapter 5, are again used in this chapter for DDI analysis. Recall that **Sample 5** is an

Inconel 625 stepped wedge with three through thickness 5-mm-diameter SDHs and the FMC dataset was acquired from the region covering the two deeper SDHs; **Sample 6** is a two-portion-welded forged austenitic steel weld plate with seven implanted and the FMC dataset was required from the 45° tilted slot implanted at the weld boundary simulating the lack of fusion. The inspection geometries for the two samples are schematically drawn in Fig. 5.3(b)-(c).

For all the simulation and experimental analysis, the length of data segments is set to be equal to the ratio of the sampling frequency to 1 MHz. Hence, the discrete FCs are separated by 1 MHz. Discrete (L=30) PDFs are obtained at three FCs (K=3) at each focal point for dissimilarity assessment. The three FCs for the analysis of the simulation and the **Sample 6** are selected as 4, 5, 6 MHz. However, the three FCs are chosen as the 1, 2, 3 MHz for the **Sample 3** and **Sample 5** since the sound energy contained in the upper part of the pass band is strongly attenuated in these two samples, as described in Chapter 5. It should be noted that eight realisations of scatterers distribution were generated in the simulation and the eight generated PDFs are averaged to obtain a converged PDF representation for each FC.

6.4   Results and discussion

6.4.1 Simulation result

Fig. 6.3(a) plots the observed PDF of the 5 MHz frequency component and the calculated reference Rayleigh PDF, which are generated from the simulated model with scatterers only. The two distributions are observed to have very similar profiles. In this situation, low-valued dissimilarity coefficients are produced, namely: DDI-C=0.05, DDI-S=0.04. Fig. 6.3(b) plots the observed PDF of the 5 MHz frequency component and the calculated reference Rayleigh PDF, which are generated from the model with scatterers and one flaw located at the resolution cell centre. The observed PDF is seen to change significantly from the reference Rayleigh PDF. This distribution is often called as post-Rayleigh distribution or Rician distribution. This situation produces high-valued dissimilarity coefficients, namely: DDI-C=0.9, DDI-S=0.96.

(a)

(b)
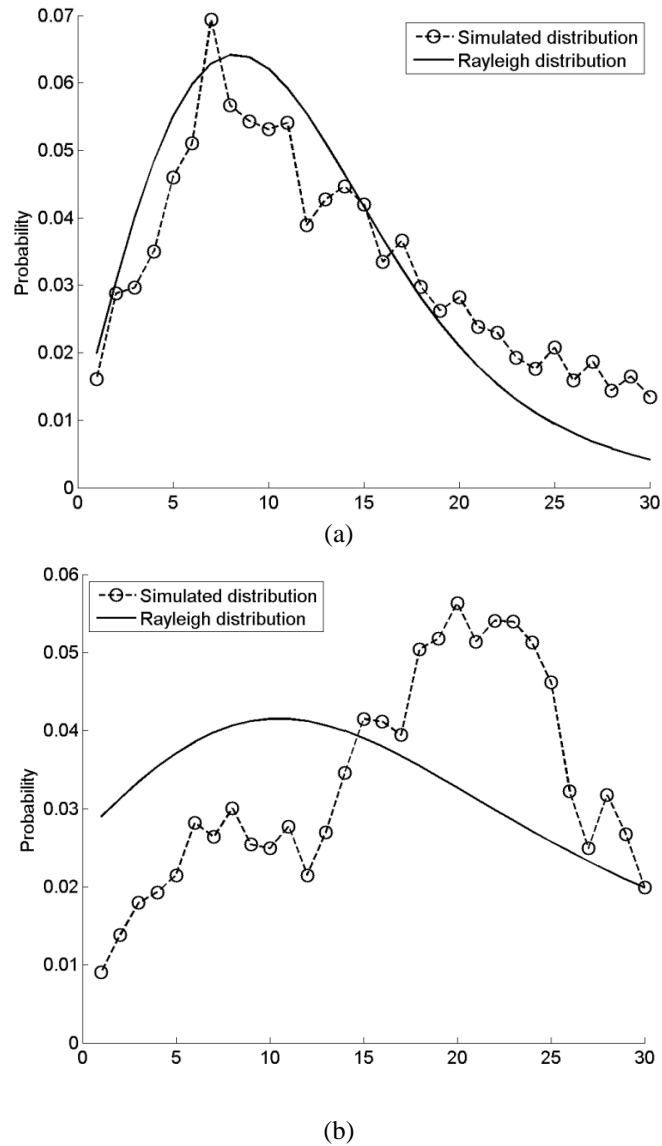
Fig. 6.3: Comparisons of the simulated PDF of the 5 MHz frequency components and the reference Rayleigh PDF: (a) with scatterers only; (b) with scatters and a flaw.

6.4.2 Experimental evaluation - austenitic steel block

The FMC data acquired from the austenitic steel block were processed in order to compare the performance of the two DDI approaches with the standard TFM algorithm. Fig. 6.4 shows the original TFM image and the two processed images by DDI-C and DDI-S with a dynamic range of -45~0 dB. The backwall indication is observed at the depth of 51 mm. The DDI-C approach is found to outperform the DDI-S method in terms of speckle suppression. However, the sidelobe of backwall reflection is evident

on the DDI-C processed image. The speckle level in each case is compared by considering the pixel magnitudes of each image in a region enclosed by the black rectangle, as plotted in Fig. 6.4(a). The speckle level of the TFM image, the DDI-C and DDI-S processed images are -19.48 dB, -44.81 dB and -41.14 dB, respectively.

(a)

(b)

(c)
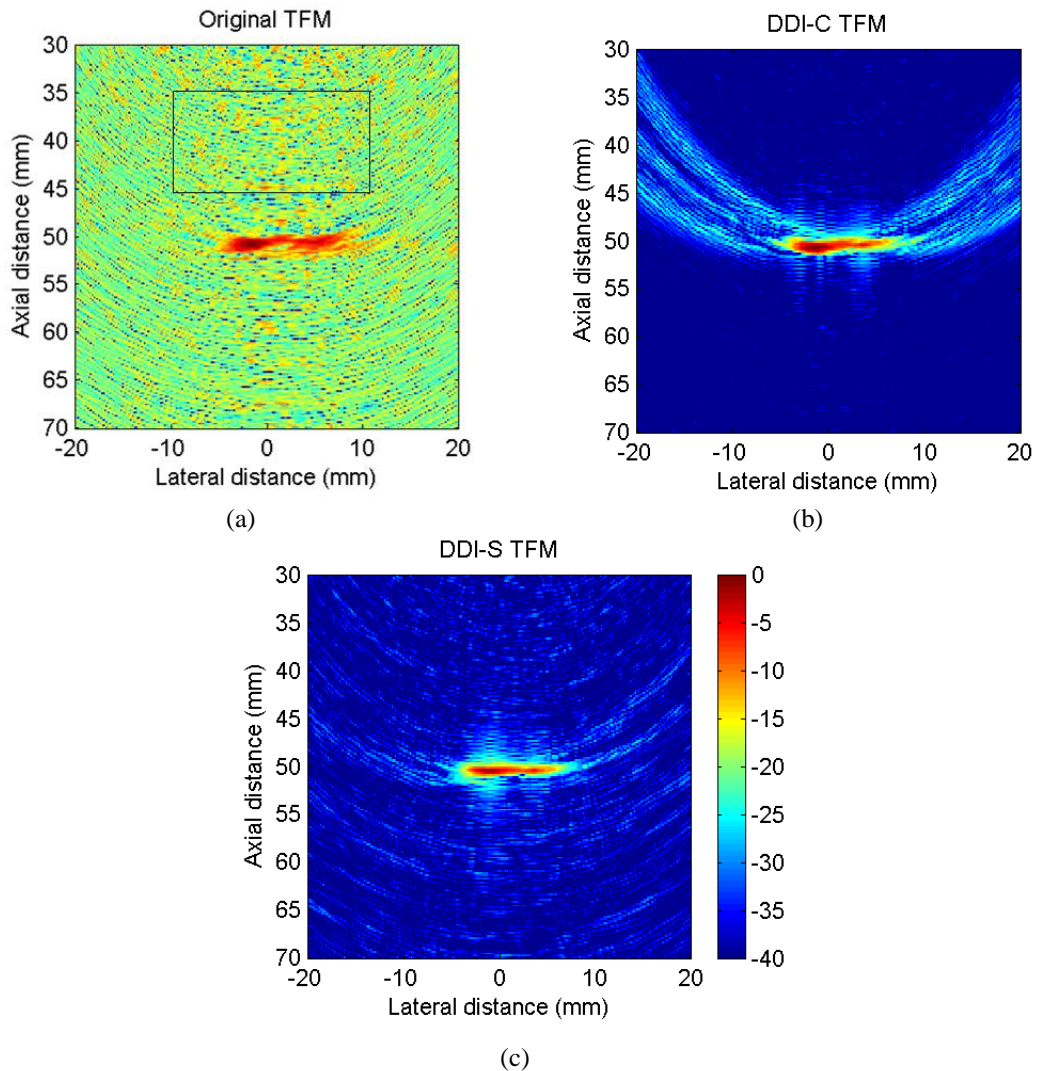
Fig. 6.4: TFM images of the austenitic steel block: (a) original; (b) processed by DDI-C; (c) processed by DDI-S. The black box encloses the region at where the speckle level is measured.

6.4.3 Experimental evaluation - Inconel 625

The process described in the preceding section was repeated for the Inconel 625 sample. Fig. 6.5 shows the original TFM image and the two processed images of the Inconel 625 sample with a dynamic range of -30~0 dB. Considerable speckle reduction is

observed on both processed images. The two SDHs located at 60 mm and 105 mm remain on both processed images, although the intensity of the deeper SDH is reduced in comparison with the original TFM image. As before, the speckle levels are measured at the area confined by the white rectangle plotted in Fig. 6.5(a). The speckle levels are -28.66 dB, -36.38, and -36.56 dB for the original TFM image, the DDI-C and DDI-S processed images, respectively. Appendix F provides the Matlab code for generating the coefficients of both DDI-C and DDI-S.
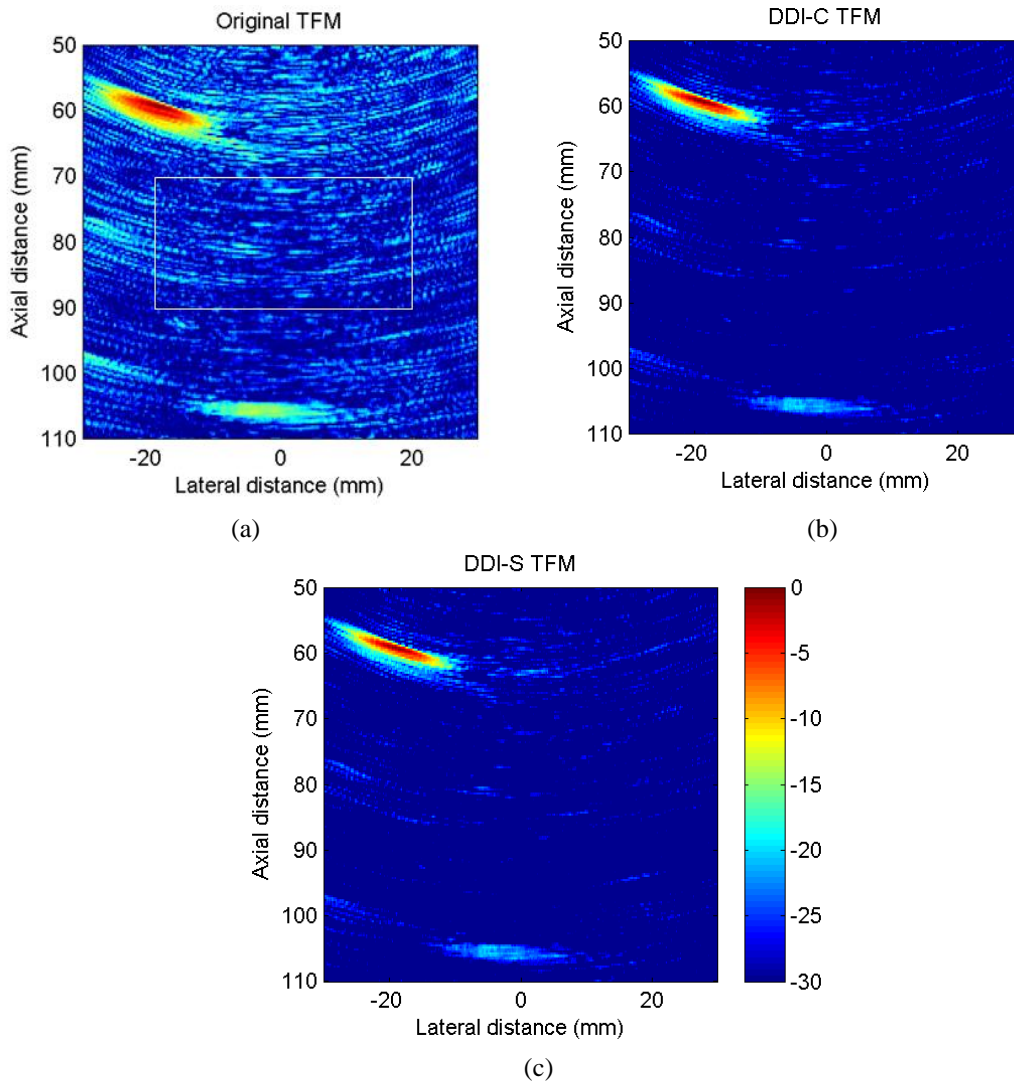
Fig. 6.5: TFM images of the Inconel 625 sample: (a) original; (b) processed by DDI-C; (c) processed by DDI-S. The white box encloses the region at where the speckle level is measured.

6.4.4 Experimental evaluation - austenitic steel weld plate

The process described in the two preceding sections was repeated for the austenitic steel weld plate. Fig. 6.6 shows the original TFM image and the two processed images of the austenitic steel weld plate with a dynamic range of -35~0 dB. Speckle is greatly suppressed on both processed images and the DDI-S approach is observed to offer slightly better speckle reduction. As before, the speckle levels are measured in the region bounded by the black rectangle, as plotted in Fig. 6.6(a). The speckle levels are -22.14 dB, -38.09, and -39.82 dB for the original TFM image, the DDI-C and DDI-S processed images, respectively.

(a) (b)

(c)
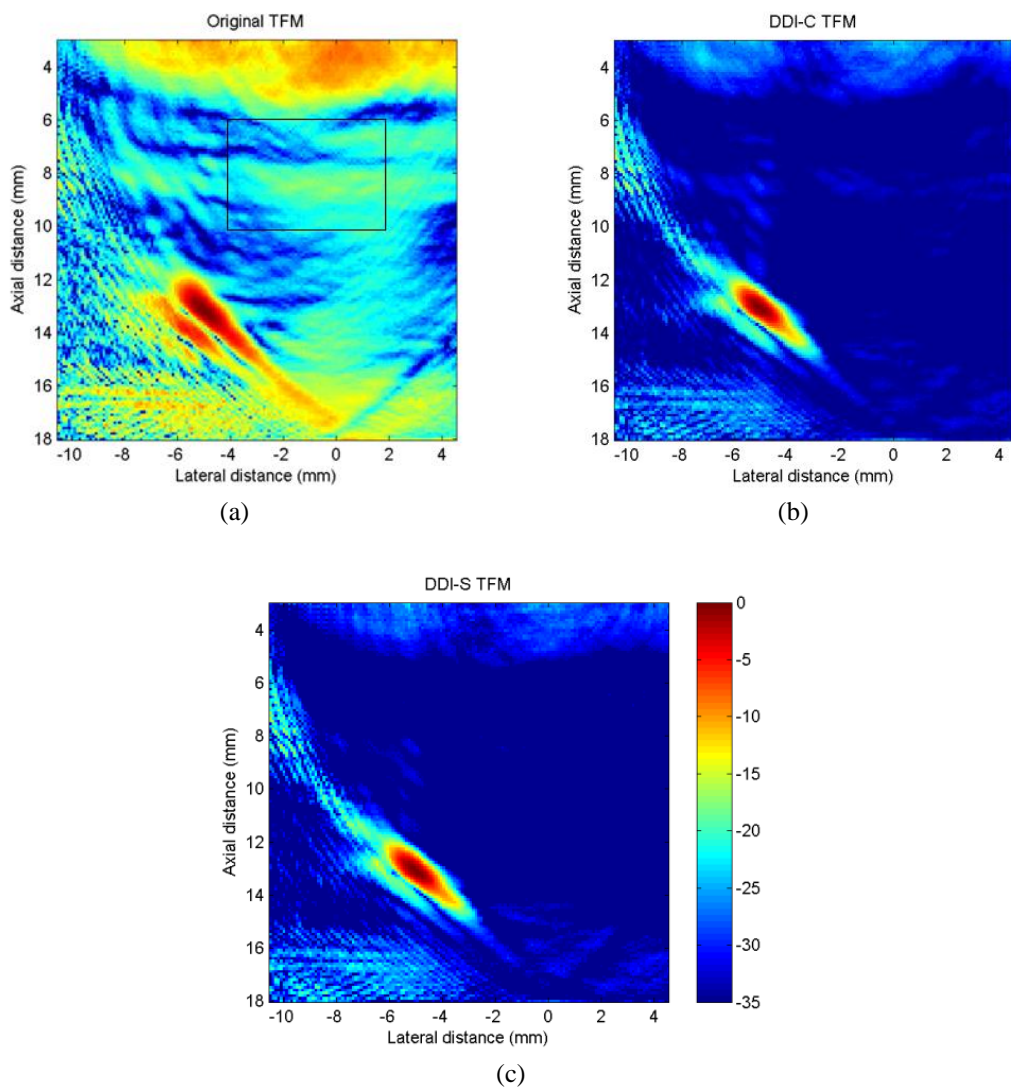
Fig. 6.6: TFM images of the austenitic steel weld plate: (a) original; (b) processed by DDI-C; (c) processed by DDI-S. The black box encloses the region at where the speckle level is measured.

6.4.5 Discussion

It is acknowledged that the flaw indications on the original images, i.e., Fig. 6.4(a), Fig. 6.5(a) and Fig. 6.6(a), can also be greatly improved by simply reducing the display dynamic range. However, as previously explained in Section 5.4.4, since the DDI methods can significantly reduce the speckle level, the objectiveness in defect detection is greatly improved.

It is worth noting that the DDI approach assumes Rayleigh scattering regime which dictates grain diameter size is much smaller than the wavelength. If grain diameter size is comparable to or even larger than the wavelength, the scattering may extend beyond Rayleigh regime and enter the stochastic and geometric regimes [125]. In these cases, the number of the scatterers in the resolution cell may be not enough for the Central Limit Theorem to be applied, so that the DDI approach may be ineffective for speckle reduction. Therefore, a low frequency should be used in the inspection of materials with large grain size to enable the DDI approach to reduce speckle level.

6.5 Conclusion and future work

A novel algorithm for speckle suppression of ultrasound images, named as Distribution Dissimilarity Image (DDI), is introduced in this chapter. The algorithm operates based on the fact that the magnitudes of frequency components for regions with a flaw and regions with grain scatterers only are different in a statistical sense. The method has been exemplified by considering simulated array data from a resolution cell and experimentally acquired data from three different samples. It is observed in the experimental analysis that the speckle level is reduced by an average of 15 dB. The proposed DDI algorithm is found to provide excellent speckle suppression irrespective of the sample microstructure, proving the robustness of the DDI algorithm and highlighting its potential for application to various materials.

Future work consists of two aspects. The dissimilarity coefficients obtained from different FCs are simply averaged in this chapter. Other sophisticated techniques for combining the dissimilarity coefficients such as the BLUE method introduced in Chapter 5 are worth further investigation, in order to obtain even better speckle

reduction. The other aspect of future work is related to the length of data segments. In this chapter, the length is selected to lead to FCs having a resolution of 1 MHz. With the use of longer data segment, the better frequency resolution is obtained, and thus dissimilarity assessment can be performed in more FCs. However, in this case, the spatial correlation of neighbouring focal points rises which results in spatial resolution loss and target edge blurring. Therefore, additional work is needed to find the optimal trade-off between the amount of extractable spectral information and spatial resolution.

CHAPTER 7. Conclusion and future work

The extensive use of coarse-grained materials in many industrial applications demands highly accurate and reliable NDE measurements. The Thesis investigates two challenging problems faced in ultrasonic NDE of coarse-grained materials, i.e., phase aberration and backscattering noise. The two problems arise due to the heterogeneous microstructures and elastically anisotropic properties often exhibited by such materials.

In Chapter 1, a general overview of NDE techniques is given with emphasis on ultrasound inspection. The problems faced by ultrasound inspection of coarse-grained materials are described.

In Chapter 2, some background knowledge relevant to the research topics of the Thesis is firstly introduced for the purpose of providing some key information and terminology. Existing methods for phase aberration correction and the reduction of grain noise and speckle are reviewed. This is followed by the definition of the potential improvement areas and general descriptions of Chapter 3~6. The experimental arrangement of data acquisition and the specifications of test pieces used in the Thesis are described in the end.

In Chapter 3, a high-fidelity modelling approach is explored in order to investigate potential methodologies for the correction of the phase aberration problem. The modelling approach replicates practical ultrasound inspection in a versatile simulation environment. Microstructural characterisation techniques such as EBSD and SRAS are used to acquire the crystallographic orientation data of a material which are then input into a platform to construct a model of the material. Wave propagation in the material is simulated and TOFs between the array elements and the targets are determined in the model. The time delay sequences in the isotropic focal law are modified according to the determined TOFs to generate anisotropic focal laws which can overcome the phase

176

aberration problem. In Chapter 3, validation of the emerging SRAS technique is presented. The combination of SRAS and the computationally efficient FE simulation platform PZFlex is investigated, in order to remarkably improve the practical applicability and operational efficiency of the high-fidelity modelling approach. Two methodologies for processing orientation data are presented in order to establish computationally efficient finite element models of coarse-grained materials. The FE models are then employed to establish anisotropic focal law based on time reversal techniques. Future work consists of three aspects. Firstly, the spatial variation of stiffness moduli of the material sample will be exploited in order to construct an FE model of the material with higher fidelity. Second, different misorientation angles will be attempted to study its effect on the model fidelity. Finally, the anisotropic focal laws generated using high-fidelity modelling will be applied in practical inspections in order to assess the accuracy of the anisotropic focal laws thus to access the fidelity of the FE models.

In Chapter 4, an analytical model of backscattering is implemented which enables the simulation of backscattering data captured by a phased array. Some initial results are presented in order to illustrate that conventional combination algorithms of SSP are either ineffective in reducing grain noise or sensitive to the variation of material characteristics. The use of ANN techniques as the combination algorithms of SSP has been investigated for the purpose of improving the performance and robustness of SSP. The MLP model and RBF model of ANN are compared in various cases through simulation and experimental analysis in terms of SNR enhancement and computational efficiency when used in conjunction with SSP. It has been observed that when the echoes of a known flaw are used as the training set, MLP is better if sufficient training data of grain noise are accessible whilst RBF is superior if the training data of grain noise is expensive or rare. MLP model outperforms RBF model when the network is trained with backwall echoes and employed to detect unknown flaws. RBF model performs better when the training samples are corrupted. When the training cost is of significant importance to signal processing, for instance, real-time signal processing is required, RBF is undoubtedly the better choice. Future work consists of two aspects. Firstly, the factor of spatial correlation as a function of frequency between neighbouring grain scatterers will be added into the current analytical model of backscattering, in

order to improve the accuracy of the model. Second, the MLP and RBF models will be compared in the inspection of a wide range of flaw types.

In Chapter 5, the use of the BLUE algorithm as a combination method of the SSP technique is investigated. BLUE combines sub-band images with weights which are adaptively tuned based on local statistics. It has the effect of pre-whitening the speckle patterns in sub-band images, i.e., decorrelating and equalising the speckle. This enables effective reduction of speckle contrast whilst maintaining spatial resolution. The pre-whitening effect of BLUE is validated with FE simulation. The methodology is exemplified using experimental data from two samples; namely an Inconel 625 sample and an austenitic steel weld plate. The images generated using BLUE showcase superior enhancement in terms of image contrast and flaw detectability as compared to conventional combination approaches. Parametric studies of the effects of the filter overlap and length of pixel segment for covariance matrix calculation on image contrast improvement have been carried out to give an indication of optimal value ranges of these two parameters. Experimental result on the austenitic steel weld plate shows that the BLUE can also reduce the intensity of sidelobe. Future work consists of three aspects. Firstly, the current approach to obtaining covariance matrix from sub-band images results in distortion to the mainlobe of legitimate flaws, other approaches to obtaining covariance without the drawback of distorting the mainlobe of flaws are therefore worth further investigation. Secondly, the optimal number of filters will be exploited. Finally, parametric studies will be carried out in the inspection of a wide range of materials and flaw characteristics, in order to provide optimal values of the two variables of the BLUE method for a broad range of inspection conditions.

In Chapter 6, a novel algorithm, named as Distribution Dissimilarity Image (DDI), is introduced in order to suppress speckle in ultrasound images. The algorithm is based on the fact that the magnitude of frequency components at a region with a flaw and a region with grain scatterers only are different in a statistical sense. Experimental analysis of three coarse-grained samples has been presented. It is found that the proposed DDI algorithm can significantly suppress speckle level for all the three samples which highlights its potential for application to other coarse-grained materials. Future work consists of two aspects. Firstly, the combination of DDI and other

sophisticated combination algorithms such as BLUE will be investigated in order to future suppress speckle level and improve image contrast. Secondly, the trade-off between the amount of extractable spectral information and spatial resolution will be exploited.

Additionally, since the BLUE and DDI algorithms both operate in a pixel-wise manner, the implementation of advanced parallel computing techniques is considered as another aspect of future work in order to enable the processing of each pixel to be executed in parallel. This will significantly reduce the computational time required by the two algorithms.

Appendix

A. Definition of Bunge-passive Euler Angles

The figure below shows the three rotations of the Bunge-passive Euler angles. (x, y, z) is the reference coordinate system and (x_0, y_0, z_0) is the crystal coordinate system.

(a)   (b)

(c)
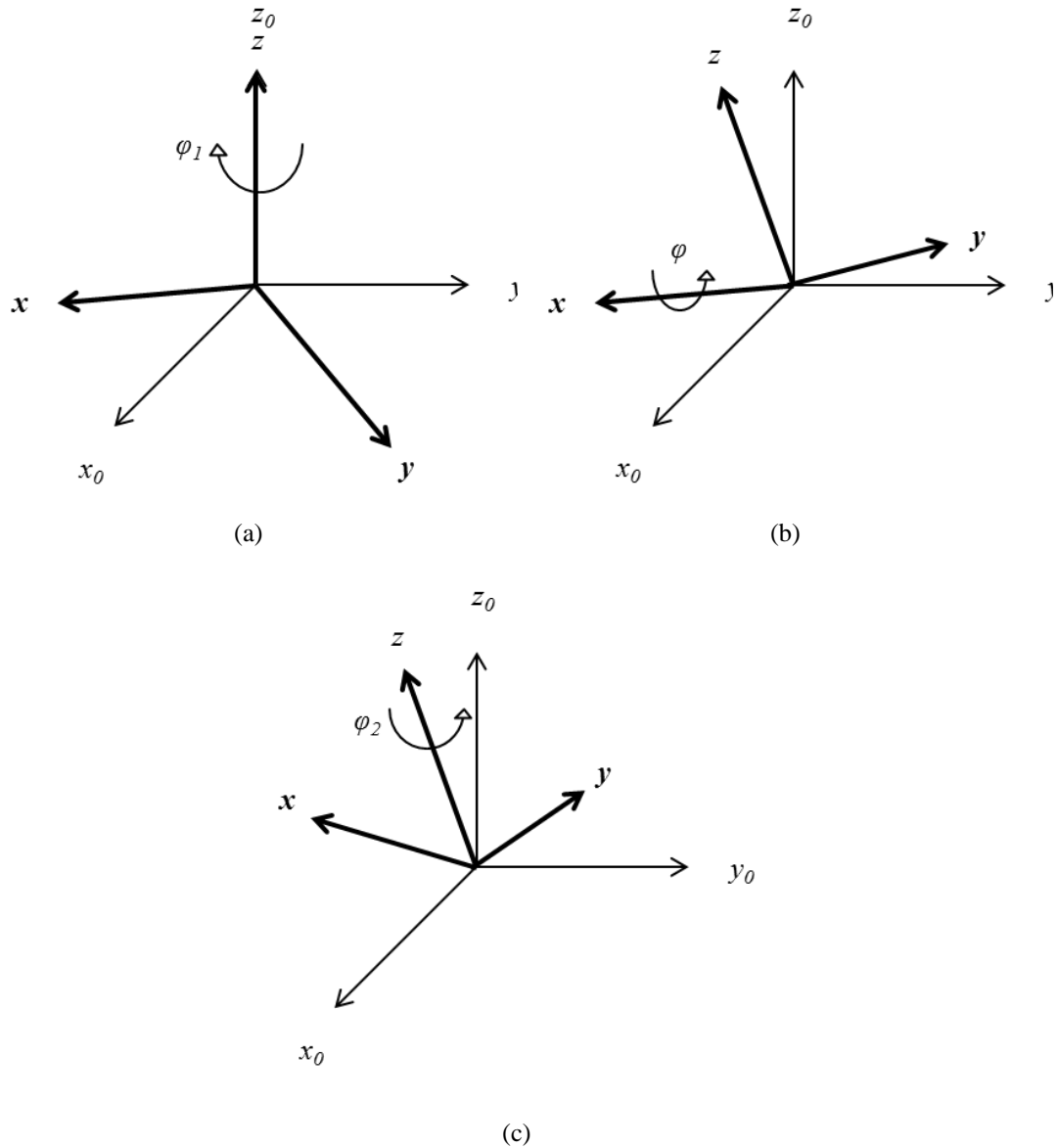
Fig. A.1: Definition of the Bunge-passive Euler angles: (a) Rotate around z axis by φ_1; (b) Rotate around new x axis by φ; (c) Rotate around new z axis by φ_2

B. Matlab Code for the analytical model of the backscattering

```matlab
clear all; clc; close all;
 %% parameters
atten=5e-30; % atteunation coefficient
ModelZRange=0.12; % model range in z direction
ModelXRange=0.01; % model range in x direction

fs=25e6;% sampling frequency
C=5000; % wave speed m/s
fc=5e6; % central frequency
fil_low=3.5e6; % lower pass band of tranducer
fil_high=6.5e6; % upper pass band of tranducer

AscanLength=round(2*ModelZRange/C*fs);
if mod(AscanLength,2)
    AscanLength=AscanLength+1;
end

ElementCount=64; % element number
ElementPitch=0.63e-3; % element pitch
ElementWidth=0.53e-3; % element width
ElementLocation=[-ElementCount/2+0.5:1:ElementCount...
    /2-0.5]*ElementPitch;

wavelength=C/fc; % wavelength
binSize=fs/AscanLength; % frequency bin

%% transducer spectrum
passband=fil_high-fil_low;
win_halflength=round(passband/binSize);
stopbandBinNo=round(fil_low/binSize-win_halflength/2);
if stopbandBinNo <=0
    stopbandBinNo=1;
end
tran_spec=[zeros(stopbandBinNo,1);gausswin(2*win_halflength);...
    zeros(AscanLength/2+1-2*win_halflength-stopbandBinNo,1)];

%% scatterers' reflectivity and flaw locations
ScatterNo=6000; % number of grain scatterers
ScatterRefle_nomial=5e-18; % reflectivity of scatters
ScatterRefle=normrnd(1,0,[ScatterNo,1])*ScatterRefle_nomial;
% randomise scatters' reflectivity a bit

FlawRefle=[20,20]; % reflectivity of flaws, between 10-20 is appropriate
FlawLocations=0.045:0.005:0.09; % locations of simulated flaws

%% Data generation
AscanHub=zeros(length(FlawLocations),30,AscanLength);
for iter=1:length(FlawLocations)
    FlawCoord(1,:)=[0,0.10];  % location of the simulated backwall
    FlawCoord(2,:)=[0,FlawLocations(iter)];
    % location of the simulated flaw in this iteration
    for iter1=1:size(AscanHub,2)
        ScatterXcoord=rand(ScatterNo,1)*ModelXRange-ModelXRange/2;
        ScatterZcoord=rand(ScatterNo,1)*ModelZRange*0.9...
            +ModelZRange*0.1;
        Spectra=zeros(AscanLength/2+1,1);

        i=32; j=32; %here only simulate signals of the 32th array element
        %% scatterers
        for k=1:length(ScatterRefle); % number of scatters
```

```
            d1=sqrt((ScatterXcoord(k)-ElementLocation(i))^2+...
                ScatterZcoord(k)^2);  %transmitting to scatter
            d2=sqrt((ScatterXcoord(k)-ElementLocation(j))^2+...
                ScatterZcoord(k)^2);  %receiving distance
            dist=d1+d2;
            % element directivity
            tx_direc=sinc(pi*ElementWidth*...
                sin(acos(ScatterZcoord(k)/d1))/wavelength);
            rx_direc=sinc(pi*ElementWidth*...
                sin(acos(ScatterZcoord(k)/d2))/wavelength);
            %beam divergence factor
            Green=1/(sqrt(d1*d2));
            para=tx_direc*rx_direc*Green;

            Spectrum=zeros(AscanLength/2+1,1);
            for binNo=1:AscanLength/2+1
                omiga=2*pi*(binNo-1)*binSize; %angular frequency
                Spectrum(binNo)=ScatterRefle(k)/dist*omiga^2*...
                 exp(-atten*dist*(omiga)^4).*exp(-1i*omiga*dist/C);
            end

            Spectrum=para*Spectrum;
            Spectra=Spectra+Spectrum;
        end

        %% flaw
        for kk=1:size(FlawCoord,1)
            d1=sqrt((FlawCoord(kk,1)-ElementLocation(i))^2+...
                FlawCoord(kk,2)^2);  %transmitting to scatter
            d2=sqrt((FlawCoord(kk,1)-ElementLocation(j))^2+...
                FlawCoord(kk,2)^2);  %receiving distance
            dist=d1+d2;
            % element directivity
            tx_direc=sinc(pi*ElementWidth*...
                sin(acos(FlawCoord(kk,1)/d1))/(wavelength));
            rx_direc=sinc(pi*ElementWidth*...
                sin(acos(FlawCoord(kk,1)/d2))/(wavelength));
            %beam divergence factor
            Green=1/(sqrt(d1*d2));
            para=tx_direc*rx_direc*Green;

            Spectrum=zeros(AscanLength/2+1,1);
            for binNo=1:AscanLength/2+1
                omiga=2*pi*(binNo-1)*binSize; %angular frequency
                Spectrum(binNo)=FlawRefle(kk)*...
                 exp(-atten*dist*(omiga)^4).*exp(-1i*omiga*dist/C);
            end

            SpectrumFlaw=para*Spectrum;
            Spectra=Spectra+SpectrumFlaw;
        end
        %% tranducer effect and signals
        Spectra_win=Spectra.*tran_spec;
        Spectra_win1=[Spectra_win(1);2*Spectra_win(2:AscanLength/2);...
            Spectra_win(AscanLength/2+1);...
            zeros(AscanLength-(AscanLength/2+1),1)];
        Ascan=real(ifft(Spectra_win1));
        AscanHub(iter,iter1,:)=Ascan;
    end
end
% The 'AscanHub' is the simulated data. 'parfor' function can be used in
% the outmost loop to enable parallel simulations

save('30Ascans_flaws.mat','AscanHub');
```

C. Matlab code for generating sub-band signals

```
clear all; close all

load('30Ascans_flaws.mat');
tstart=401;%1st 400 points are not analysed
tend=size(AscanHub,3);

% filter bank desgin
fstart=2e6; % lower band of the filter bank
fend=8e6; % upper band of the filter bank
overlap=0.25; % overlap of filters
filterNo=10; % number of filters
bw=(fend-fstart)/(1+(filterNo-1)*(1-overlap));
incre=bw*(1-overlap);

% initialise memory
AscanHub1=zeros(size(AscanHub,1),size(AscanHub,2),tend-tstart+1);
subsethub=zeros(size(AscanHub,1),size(AscanHub,2),tend-tstart+1,filterNo);
fs=25e6;% Sampling frequency
C=5000; % velocity in m/s

for i=1:size(AscanHub,1)
    for j=1:size(AscanHub,2)
        Ascan=squeeze(AscanHub(i,j,:));

        Ascan=Ascan(tstart:tend);
        Ascan=Ascan/max(abs(Ascan)); % normalise each A-scan
        AscanHub1(i,j,:)=Ascan;
        AscanLength=length(Ascan);
        spectrum=fft(Ascan);
        binSize=fs/AscanLength;

        for iter=1:filterNo
            fc1=fstart+(iter-1)*incre;
            fc2=fc1+bw;
            passband=fc2-fc1;
            win_halflength=round(passband/binSize);
            stopbandBinNo=round(fc1/binSize-win_halflength/2);
            filter_halfspectrum=[zeros(stopbandBinNo,1);...
                gausswin(2*win_halflength);...
                zeros(AscanLength/2+1-2*...
                win_halflength-stopbandBinNo,1)];
            filter_spectrum=[filter_halfspectrum;...
                flipud(filter_halfspectrum(2:end-1))];
            temp=ifft(filter_spectrum.*spectrum);
            subset(:,iter)=temp/max(abs(temp));
            % equalize each sub-band - optional
        end

        subsethub(i,j,:,:)=subset;
    end
end

AscanHub1=squeeze(AscanHub1);
subsethub=squeeze(subsethub);
distance=1e3*[tstart:1:tend]/fs*C/2;

save('30Ascans_flaws_subsethub.mat','subsethub','distance')
save('30Ascans_flaws_normalized.mat','AscanHub1')
```

D.Matlab code for ANN analysis

```matlab
clear all; clc; close all
load('30Ascans_flaws_subsethub.mat')
load('30Ascans_flaws_normalized.mat');
AscanHub=AscanHub1; clear AscanHub1;

%% Notes
% An open source Matlab code was used to build and evaluate RBF model.
% The source code can be downloaded from
% https://chrisjmccormick.wordpress.com/2013/08/16/rbf-network-matlab-code/
% Version 1.0 is used in the Thesis.
% Add the paths of the two folders in the downloaded file like below.
addpath('kMeans'); addpath('RBFN');

% An open source Matlab code was used to enable the 'Tic' and 'Toc' commands
% to work with 'parfor' command. Namely, timing can be performed in parallel
% in the different parallel threads.
% The source code can be downloaded from
% http://www.mathworks.com/matlabcentral/fileexchange/27472-partictoc
% Add the path of the folder in the downloaded file like below.
addpath('parTicToc');

%%

fs=25e6; % sampling frequency
C=5e6; % central frequency
wl=fs/C; %number of sampling points corresponding to one wavelength
waveNo=1:15;
TrainLength=waveNo*wl;

% locations of backwall and the flaws
FlawLoc=[50:50:500]; % the locations of flaws
BackwallLoc=600; % centre of the backwall signal
BackFlawLength=15; % number of sampling points for the signals of the

Ascan4Train=1:1;

RBF_time=zeros(length(TrainLength),length(Ascan4Train)...
    ,size(AscanHub,1));
SNRG_RBF=zeros(length(TrainLength),length(Ascan4Train)...
    ,size(AscanHub,1),size(AscanHub,2));
MLP_time=zeros(length(TrainLength),length(Ascan4Train)...
    ,size(AscanHub,1));
SNRG_MLP=zeros(length(TrainLength),length(Ascan4Train)...
    ,size(AscanHub,1),size(AscanHub,2));

%% RBF

p1=Par(length(TrainLength));

parfor Index=1:length(TrainLength)
    RBF_time_temp=zeros(length(Ascan4Train),size(AscanHub,1));
    MLP_time_temp=zeros(length(Ascan4Train),size(AscanHub,1));
    SNRG_RBF_temp=zeros(length(Ascan4Train),size(AscanHub,1)...
        ,size(AscanHub,2));
    SNRG_MLP_temp=zeros(length(Ascan4Train),size(AscanHub,1)...
        ,size(AscanHub,2));

    %% RBF
    for Ascan4TrainID=1:length(Ascan4Train)
        for FlawID=1:size(AscanHub,1)
```

```
            td=squeeze(subsethub(FlawID,Ascan4Train(Ascan4TrainID)...
                ,BackwallLoc-BackFlawLength:BackwallLoc+BackFlawLength,:));
            tn=squeeze(subsethub(FlawID,Ascan4Train(Ascan4TrainID),...
                300-TrainLength(Index):300+TrainLength(Index),:));
            % centre of noise training samples is at 70 mm

            %normalisation before training
            for i=1:size(td,1)
                td(i,:)=td(i,:)/max(abs(td(i,:)));
            end
            for i=1:size(tn,1)
                tn(i,:)=tn(i,:)/max(abs(tn(i,:)));
            end

            X=[td;tn];
            y=[ones(size(td,1),1); 2*ones(size(tn,1),1)];
            % Desired training values
            %% training
            Par.tic;
            [Centers, betas, Theta] = trainRBFN(X, y, 10, false);
            p1(Index)=Par.toc;
            RBF_time_temp(Ascan4TrainID,FlawID)=...
                p1(Index).ItStop-p1(Index).ItStart;
            %% meansure SNRG
            for AscanID=1:size(AscanHub,2)
                Ascan=squeeze(AscanHub(FlawID,AscanID,:));
                Ori_SNR=mean(Ascan(FlawLoc(FlawID)-BackFlawLength:...
                    FlawLoc(FlawID)+BackFlawLength).^2)...
                    /mean(Ascan([1:FlawLoc(FlawID)-BackFlawLength,...
                FlawLoc(FlawID)+BackFlawLength:BackwallLoc-BackFlawLength...
                    ,BackwallLoc+BackFlawLength:end]).^2);

                te=squeeze(subsethub(FlawID,AscanID,:,:));

                for i=1:size(te,1)
                    te(i,:)=te(i,:)/max(abs(te(i,:)));
                end

                scores=zeros(2,size(te,1));
                coeff=zeros(size(te,1),1);
                for i = 1 : size(te,1)
                    scores(:,i)=evaluateRBFN(Centers,betas,Theta,te(i,:));
                    coeff(i)=scores(1,i)./sum(scores(:,i));
                end
                Ascan_p=coeff.*Ascan;

                RBF_SNR=mean(Ascan_p(FlawLoc(FlawID)-BackFlawLength:...
                    FlawLoc(FlawID)+BackFlawLength).^2)...
                    /mean(Ascan_p([1:FlawLoc(FlawID)-BackFlawLength,...
                FlawLoc(FlawID)+BackFlawLength:BackwallLoc-BackFlawLength...
                    ,BackwallLoc+BackFlawLength:end]).^2);
                SNRG_RBF_temp(Ascan4TrainID,FlawID,AscanID)=RBF_SNR/Ori_SNR;
            end
        end
end

%% MLP
for Ascan4TrainID=1:length(Ascan4Train)
    for FlawID=1:size(AscanHub,1)

        td=squeeze(subsethub(FlawID,Ascan4Train(Ascan4TrainID),...
            BackwallLoc-BackFlawLength:BackwallLoc+BackFlawLength,:));
        tn=squeeze(subsethub(FlawID,Ascan4Train(Ascan4TrainID),...
            300-TrainLength(Index):300+TrainLength(Index),:));
```

```matlab
%normalisation before training
for i=1:size(td,1)
    td(i,:)=td(i,:)/max(abs(td(i,:)));
end
for i=1:size(tn,1)
    tn(i,:)=tn(i,:)/max(abs(tn(i,:)));
end

tr=[td;tn]';
Dtr = [ones(1,size(td,1)), zeros(1,size(tn,1))];
% Desired training values
%% training
eta= 1.5; % Learning rate
alpha = 0.7; % Momentum
tol= 0.002; % Error tolerance
epochs = 1000;      % number of iterations
Q = size(tr,2); % Total segment number for training
n = size(tr,1); q = 10; p = 1; % Architecture
Wih= 2 * rand(n+1,q) -1;% Input-hidden weight matrix
Whj= 2 * rand(q+1,p) -1; % Hidden-output weight matrix
DeltaWih= zeros(n+1,q); % Weight change matrices
DeltaWhj= zeros(q+1,p);
DeltaWihOld= zeros(n+1,q);
DeltaWhjOld= zeros(q+1,p);
Si= [ones(1,Q); tr]; % Input signals
deltaH= zeros(1,q+1);% Error-slope product at hidden
errormean =1;
Par.tic;
for  itr =1:epochs
    if errormean<=tol
        break
    else
        error=zeros(Q,1);
        for k = 1:Q
            Zh= Si(:,k)' * Wih;% Hidden activations
            Sh= [1 1./(1 + exp(-Zh))];% Hidden signals
            Yj= Sh* Whj;% Output activations
            Sy= 1./(1 + exp(-Yj));% Output signals
            Ek= Dtr(k) -Sy;% Error vector
            deltaO= Ek* Sy.* (1 -Sy);
            % derivative of siglog function
            DeltaWhj = deltaO* Sh';% Delta W:hidden-output
            deltaH(2:end)=deltaO*Whj(2:end)'.*...
                Sh(2:end).*(1-Sh(2:end));
            for kk = 1:n+1 % Delta W:input-hidden
                DeltaWih(kk,:) = deltaH(2:end) * Si(kk,k);
            end % Update weights
            Wih= Wih+ eta* DeltaWih+ alpha * DeltaWihOld;
            Whj= Whj+ eta* DeltaWhj+ alpha * DeltaWhjOld;
            DeltaWihOld= DeltaWih; DeltaWhjOld= DeltaWhj;
            % Store changes
            error(k)= Ek^2; % Compute error
        end
        errormean=mean(error);
    end
end
p1(Index)=Par.toc;

MLP_time_temp(Ascan4TrainID,FlawID)=p1(Index).ItStop...
    -p1(Index).ItStart;

for AscanID=1:size(AscanHub,2)
    Ascan=squeeze(AscanHub(FlawID,AscanID,:));
    Ori_SNR=mean(Ascan(FlawLoc(FlawID)-BackFlawLength:...
```

186

```
                        FlawLoc(FlawID)+BackFlawLength).^2)...
                        /mean(Ascan([1:FlawLoc(FlawID)-BackFlawLength,...
                    FlawLoc(FlawID)+BackFlawLength:BackwallLoc-BackFlawLength...
                        ,BackwallLoc+BackFlawLength:end]).^2);

                    te=squeeze(subsethub(FlawID,AscanID,:,:));

                    for i=1:size(te,1)
                        te(i,:)=te(i,:)/max(abs(te(i,:)));
                    end

                    te=te';

                    Ti= [ones(1, size(te,2)); te]; % Input signals
                    To=zeros(size(te,2),1);
                    for k=1:size(te,2);
                        Zh= Ti(:,k)' * Wih;% Hidden activations
                        Sh= [1 1./(1 + exp(-Zh))];% Hidden signals
                        Yj= Sh* Whj;% Output activations
                        Sy= 1./(1 + exp(-Yj));% Output signals
                        To(k)=Sy;
                    end
                    Ascan_p1=To.*Ascan;

                    MLP_SNR=mean(Ascan_p1(FlawLoc(FlawID)-BackFlawLength:...
                        FlawLoc(FlawID)+BackFlawLength).^2)...
                        /mean(Ascan_p1([1:FlawLoc(FlawID)-BackFlawLength,...
                    FlawLoc(FlawID)+BackFlawLength:BackwallLoc-BackFlawLength...
                        ,BackwallLoc+BackFlawLength:end]).^2);
                    SNRG_MLP_temp(Ascan4TrainID,FlawID,AscanID)=MLP_SNR/Ori_SNR;
                end
            end
        end

    RBF_time(Index,:,:)=RBF_time_temp;
    SNRG_RBF(Index,:,:,:)=SNRG_RBF_temp;
    MLP_time(Index,:,:)=MLP_time_temp;
    SNRG_MLP(Index,:,:,:)=SNRG_MLP_temp;
end

save('30AscansFlawVarAnalysis.mat','MLP_time','SNRG_MLP','RBF_time','SNRG_RBF');
```

E. Matlab code for BLUE algorithm

```
clear all; close all

filename ='Inconel625_FMC.mat';
data = load(filename); %'data' contains FMC data, sampling frequency,
FMC acquisition start time, Array element locations
tstep = 1/data.FMCSamplingRate;
centre_time = data.FMCTimeStart;
velocity = 5859;
caxis_range = 30;
tx_idx = 1e3*data.ProbeElementLocations(2,:);


res=0.2; %resolution 0.2 mm
imageWidth = 80; %mm
xPoints=round(imageWidth/res);
imageDepthStart=10; %mm
imageDepthEnd=120;
yPoints=round((imageDepthEnd-imageDepthStart)/res);
```

```matlab
x = linspace(-imageWidth/2,imageWidth/2,xPoints);
y = linspace(imageDepthStart,imageDepthEnd,yPoints);

overlap = 0.5;
AF=3; % number of frequency bands
bw=2e6/(AF-2*overlap); % total bandwidth/(number of band-2*overlap)
fs1=1e6; fs2=fs1+bw;
figure;
TFM=zeros(AF+2,yPoints,xPoints);
% 1st for filtered TFM; 2nd for original TFM; 3rd-5st for subband images
for i=1:AF+2;
    FMC=data.FMC;
    if i==1;
        h = design.bandpass('N,F3dB1,F3dB2',4,1e6,3e6,data.FMCSamplingRate);
        fil = design(h, 'butter');
        for  j=1:size(FMC,2);
           subset=flipud(filter(fil,flipud(filter(fil,squeeze(FMC(:,j))))));
            FMC(:,j) = hilbert(subset);
        end
    elseif i==2;
        for  j=1:size(FMC,2);
            FMC(:,j) = hilbert(FMC(:,j));
        end
    else
        h=fdesign.bandpass('N,F3dB1,F3dB2',4,fs1,fs2,data.FMCSamplingRate);
        fil=design(h, 'butter');
        for  j=1:size(FMC,2);
           subset=flipud(filter(fil,flipud(filter(fil,squeeze(FMC(:,j))))));
            FMC(:,j) = hilbert(subset);
        end
        fs1=fs1+bw*(1-overlap);
        fs2=fs2+bw*(1-overlap);
    end

    [dTFM,~]=Partial_TFM(FMC,x,y,xPoints,yPoints,tstep,centre_time,tx_idx,…
    velocity);
    TFM(i,:,:) = 20*log10(abs(squeeze(sum(dTFM))));
end

%% BLUE
temp=squeeze(TFM(3:end,:,:));
k =size(temp,1); % AF
wavelength=round(velocity/2e6/res*1e3); % velocity/total bw/pixel size
N = round((4*wavelength)/2); %4 wavelengths of segment length for BLUE
c=zeros(size(temp,2),size(temp,3));

s=ones(1,k)';
for i=1+N:size(temp,2)-N;
    for j=1+N:size(temp,3)-N;
        input=squeeze(temp(:,i,j));
        C1=cov(squeeze(temp(:,i-N:i+N,j))');
        C2=cov(squeeze(temp(:,i,j-N:j+N-2))');
        C=C1.*C2;
        c(i,j)=(s'*C^-1*input)/sum(sum(C^-1));
    end
end

x=x(N+1:end-N);
y=y(N+1:end-N);
DC=c(1+N:end-N,1+N:end-N);
DC_final=DC-max(DC(:));

% 'DC_final' is the processed result by BLUE
```

Partial_TFM.m

```matlab
function [ dTFM, Sampling ] = Partial_TFM(FMC,x,y,xPoints,yPoints,tstep,…
centre_time, source_x_positions, velocity)
n_transducers = length(source_x_positions);
dTFM = zeros(n_transducers,yPoints,xPoints);
i=1;
[X, Y] = meshgrid(x,y);
figure;
for tx=1:n_transducers
    for rx=1:n_transducers;
        distanceTX = sqrt((X-source_x_positions(tx)).^2 + Y.^2);
        distanceRX = sqrt((X-source_x_positions(rx)).^2 + Y.^2);
        delay = (distanceTX + distanceRX)*1e-3 / velocity - centre_time;
        trace_idx = min(max(round(delay./tstep),1),length(FMC));
        dTFM(tx,:,:)=squeeze(dTFM(tx,:,:))+ reshape((FMC(trace_idx,i)),…
        yPoints,xPoints);
        Sampling(tx,rx,:,:) = trace_idx;

        i=i+1;
    end
    imagesc(x,y,abs(squeeze(dTFM(tx,:,:)))); colorbar; axis image
    drawnow;
    disp('Generating TFM image.');
    end
end
```

F. Matlab code for DDI algorithm

```matlab
clear all; close all
filename ='Inconel625_FMC.mat';
data = load(filename); %'data' contains FMC data, sampling frequency,
%FMC acquisition start time, Array element locations
tstep = 1/data.FMCSamplingRate; centre_time = data.FMCTimeStart;
FMCSamplingRate= data.FMCSamplingRate;
velocity = 5859;
tx_idx = 1e3*data.ProbeElementLocations(2,:);
FMC=data.FMC;

res=0.2; %resolution 0.2 mm
imageWidth = 80; %mm
xPoints=round(imageWidth/res);
imageDepthStart=10; %mm
imageDepthEnd=120;
yPoints=round((imageDepthEnd-imageDepthStart)/res);
x = linspace(-imageWidth/2,imageWidth/2,xPoints);
y = linspace(imageDepthStart,imageDepthEnd,yPoints);

AF=3; % number of frequency bands
NoElement=sqrt(size(FMC,2));

[dTFM,Sampling]=Partial_TFM(FMC,x,y,xPoints,yPoints,tstep,centre_time,…
tx_idx, velocity); % 'Partial_TFM' function is provided in the last page

SegLength=round(FMCSamplingRate/1e6/2);
Sampling=reshape(Sampling, NoElement^2,yPoints,xPoints);
Sampling(Sampling<SegLength)=SegLength;
Dissimi=zeros(AF,2,yPoints,xPoints);

parfor i=1:yPoints;
    Dissimi_temp=zeros(AF,2,xPoints);
```

```
    seg=zeros(SegLength*2,NoElement^2);
    for j=1:xPoints;
        for ii=1:NoElement^2
            temp=FMC(Sampling(ii,i,j)-SegLength+1:Sampling(ii,i,j)…
            +SegLength,ii);
            temp=temp/norm(temp);
            seg(:,ii)=temp;
        end

        a=abs(fft(seg.*repmat(hamming(size(seg,1)),[1 NoElement^2])));
        a=a(2:1+AF,:); % only first AF frequency components are used

        for ii=1:size(a,1)

            a_bin=linspace(min(a(ii,:)),max(a(ii,:)),30);
            a_binsize=a_bin(2)-a_bin(1);
            b=hist(a(ii,:),a_bin);

            mle_Rayl = sqrt(sum(a(ii,:).^2)/(2*numel(a(ii,:))));
            % maximum likelihood estimation for a Rayleigh parameter
            ref = raylpdf(a_bin+a_binsize/2,mle_Rayl);
            Dissimi_temp(ii,:,j)=[pdist([b;ref],'correlation'); ...
                pdist([b;ref],'spearman')];
        end
    end
    Dissimi(:,:,i,:)=Dissimi_temp;
end
Coe_xcorr=squeeze(mean(Dissimi(:,1,:,:),1));
% coefficients for correlation method
Coe_spearman=squeeze(mean(Dissimi(:,2,:,:),1));
% coefficients for spearman method
```

References

[1]   M. A. Drewry and G. A. Georgiou, "A review of NDT techniques for wind turbines," *Insight,* vol. 49, pp. 137-141, Mar. 2007.

[2]   I. G. Scott and C. M. Scala, "A review of non-destructive testing of composite materials," *NDT International,* vol. 15, pp. 75–86, Apr. 1982.

[3]   V. Deutsch, "History of NDT-Instrumentation," in *15th WCNDT*, Roma, 2000.

[4]   W. C. Röntgen, "On a new kind of rays," *Science,* vol. 3, pp. 227-231, Feb. 1896.

[5]   R. Hanke, T. Fuchs, and N. Uhlmann, "X-ray based methods for non-destructive testing and material characterization," in *9th International Workshop on Radiation Imaging Detectors*, 2007, pp. 14–18.

[6]   R. D. Adams and P. Cawley, "A review of defect types and nondestructive testing techniques for composites and bonded joints," *NDT International,* vol. 21, no. 4, pp. 208-222, Aug. 1988.

[7]   J. J. C. Newman, "A Nonlinear Fracture Mechanics Approach to the Growth of Small Cracks," in *National Aeronautics and Space Administration Hampton VA Langley Research Center*, Apr. 1983.

[8]   K. Goebbels, "State of the art and short term development tendencies in nondestructive surface defect detection and evaluation," in *12th World Conference on Non-Destructive Testing*, Amsterdam, The Netherlands, 1989, pp. 3-8.

[9]   B. A. Auld and J. C. Moulder, "Review of Advances in Quantitative Eddy Current Nondestructive Evaluation," *Journal of Nondestructive Evaluation,* vol. 18, pp. 3-36, Mar. 1999.

[10]   D. C. Jiles, "Review of magnetic methods for nondestructive evaluation," *NDT International,* vol. 21, pp. 311-319, Oct. 1988.

[11]   A. J. Healey and S. Leeman, "Speckle reduction methods in ultrasound pulse-echo imaging," in *International Conference on Acoustic Sensing and Imaging*, 1993, pp. 68-76.

[12]   K. G. Prabhakaran, B. S. Wong, and Y. Y. Teng, "Time of flight diffraction - an alternate non-destructive testing procedure to replace traditional methods," *NDT.net,* vol. 10, May 2005.

[13]   B. W. Drinkwater and P. D. Wilcox, "Ultrasonic arrays for non-destructive evaluation: A review," *NDT&E International,* vol. 39, pp. 525–541, Oct. 2006.

[14]   *A Brief History of Phased Array Testing*. Available: http://www.olympus-ims.com/vi/ndt-tutorials/intro/breif-history/

[15]   U. Schnars and R. Henrich, "Applications of NDT methods on composite structures in the aerospace industry," in *Conference on damage in composite materials*, Stuttgart, Germany, 2006.

[16]   A. M. Stansfield, "Practical problems of data collection and interpretation for large scale automated ultrasonic inspections," in *IEE Colloquium on Advanced Techniques for Collection and Interpretation of NDT Data*, London, 1994, pp. 1-3.

[17] R. V. Booler, R. C. Owen, and R. K. Chapman, "Case study of qualification of remote automated ultrasonic," in *Proceedings of the Joint EC OECD IAEA Specialists Meeting*, 1997.

[18] *NDT Course Material*. Available: https://www.nde-ed.org/EducationResources/CommunityCollege/Materials/Structure/solidification.htm

[19] A. K. Bhargava and C. P. Sharma, *Mechanical Behaviour and Testing of Materials*: PHI Learning, 2011.

[20] V. Behar, "Techniques for phase correction in coherent ultrasound imaging systems," *Ultrasonics,* vol. 39, pp. 603-10, Aug. 2002.

[21] J. Camacho and C. Fritsch, "Phase coherence imaging of grained materials," *IEEE Trans Ultrason Ferroelectr Freq Control,* vol. 58, pp. 1006-1015, May 2011.

[22] Y. Li, V. L. Newhouse, and P. M. Shankar, "Speckle reduction in ultrasonic SAFT images in the coarse grained material through split spectrum processing," in *Review of Progress in Quantitative Nondestructive Evaluation*, 1989, pp. 727-734.

[23] K. Goebbels, "Structure Analysis by Scattered Ultrasonic Radiation," *Research Techniques in Nondestructive Testing*, vol. IV, pp. 87-157, 1980.

[24] A. Gachagan, G. Harvey, R. L. O'Leary, and J. W. Mackersie, "Investigating the influence of the constituent materials on the performance of periodic piezoelectric composite arrays," in *33rd Annual Review of Progress in Quantitative Nondestructive Evaluation*, 2007, pp. 759-766.

[25] W. A. Smith and B. A. Auld, "Modeling 1-3 composite piezoelectrics: thickness-mode oscillations," *IEEE Trans Ultrason Ferroelectr Freq Control,* vol. 38, pp. 40-7, Jan. 1991.

[26] G. Hayward and J. A. Hossack, "Unidimensional modeling of 1-3 composite transducers," *The Journal of Acoustical Society of America,* vol. 88, pp. 599-608, 1990.

[27] R. L. O'Leary, G. Hayward, and V. Murray, "Finite element technique for the assessment of 3-1 and "super 1-3" connectivity piezoelectric composite transducers," *IEEE Trans Ultrason Ferroelectr Freq Control,* vol. 54, pp. 2024-2035, Oct. 2007.

[28] *Introduction to Phased Array Ultrasonic Technology Applications.* Available: http://www.olympus-ims.com

[29] A. J. Mulholland, N. Ramadas, R. L. O'Leary, A. C. S. Parr, G. Hayward, A. Troge*, et al.*, "Enhancing the performance of piezoelectric ultrasound transducers by the use of multiple matching layers," *IMA Journal of Applied Mathematics,* vol. 73, pp. 936-949, Dec. 2008.

[30] A. Trogé, R. L. O'Leary, G. Hayward, R. A. Pethrick, and A. J. Mullholland, "Properties of photocured epoxy resin materials for application in piezoelectric ultrasonic transducer matching layers," *Journal of Acoustical Society of America,* vol. 128, Nov. 2010.

[31] S. N. Ramadas, R. L. O'Leary, A. J. Mulholland, G. Hayward, A. R. MacKintosh, A. Troge*, et al.*, "Tapered transmission line technique based graded matching layer for thickness mode piezoelectric transducers," in *IEEE International Ultrasonics Symposium (IUS)*, Rome, 2009, pp. 1695-1698.

[32] C. Holmes, D. B. W., and W. P.D., "Post-processing of the full matrix of ultrasonic transmit-receive array data for non-destructive evaluation," *NDT & E International,* vol. 38, pp. 701-711, Dec. 2005.

[33] F. W. Kremkau, *Diagnostic Ultrasound: Principles and Instruments.*: WB Saunders Company, 2002.

[34] J. Dziewierz, T. Lardner, and A. Gachagan, "A design methodology for 2D sparse NDE arrays using an efficient implementation of refracted-ray TFM," in *IEEE International Ultrasonics Symposium (IUS)*, Prague, 2013, pp. 136-138.

[35] P. D. Wilcox, C. Holmes, and B. W. Drinkwater, "Advanced Reflector Characterization with Ultrasonic Phased Arrays in NDE Applications," *IEEE Trans Ultrason Ferroelectr Freq Control,* vol. 54, pp. 1541-1550, Aug. 2007.

[36] J. Zhang, B. W. Drinkwater, P. D. Wilcox, and A. J. Hunter, "Defect detection using ultrasonic arrays: The multi-mode total focusing method," *NDT&E International,* vol. 43, pp. 123–133, Mar. 2010.

[37] J. Zhang, B. W. Drinkwater, and P. D. Wilcox, "Efficient immersion imaging of components with nonplanar surfaces," *IEEE Trans Ultrason Ferroelectr Freq Control,* vol. 61, pp. 1284-1295, Jan. 2014.

[38] J. Zhang, B. W. Drinkwater, and P. D. Wilcox, "Comparison of ultrasonic array imaging algorithms for nondestructive evaluation," *IEEE Trans Ultrason Ferroelectr Freq Control,* vol. 60, pp. 1732-1745, Aug. 2013.

[39] C. Fan, M. Caleapb, M. Pan, and B. W. Drinkwater, "A comparison between ultrasonic array beamforming and super resolution imaging algorithms for non-destructive evaluation ," *Ultrasonics,* vol. 54, pp. 1842-1850, Sep. 2014.

[40] F. K. Gruber, E. A. Marengo, and A. J. Devaney, "Time-reversal imaging with multiple signal classifications considering multiple scattering between the targets," *Journal of Acoustical Society of America,* vol. 115, pp. 3024-3027, Jun. 2004.

[41] S. K. Lehman and A. J. Devaney, "Transmission mode time-reversal super-resolution imaging," *Journal of Acoustical Society of America,* vol. 113, pp. 2742-2753, 2003.

[42] W. Li, "Laser ultrasonic method for determination of crystallographic orientation of large grain metals by spatially resolved acoustic spectroscopy (SRAS)," PhD thesis, Univeristy of Nottingham, 2012.

[43] V. Randle and O. Engler, *Introduction to Texture Analysis: Macrotexture, Microtexture and Orientation Mapping*: CRC Press, 2007.

[44] H. P. Klug and L. E. Alexander, *X-Ray Diffraction Procedures: For Polycrystalline and Amorphous Materials, 2nd Edition*: Wiley-VCH, 1974.

[45] A. B. Greilinger, "A Back-Reflection Laue Method for determining Crystal Orientation : Zeitschrift fur Kristallographie - Crystalline Materials," *Zeitschrift fur Kristallographie - Crystalline Materials,* vol. 91, pp. 424-432, Dec. 1935.

[46] O. C. Wells, "Comparison of different models for the generation of electron backscattering patterns in the scanning electron microscope," *Scanning,* vol. 21, pp. 368-371, 1999.

[47] G. L. Wynick and C. J. Boehlert, "Electron backscattered diffraction characterization technique for analysis of a Ti2AlNb intermetallic alloy," *Journal of Microscopy,* vol. 219, pp. 115-121, Sep. 2005.

[48] W. Li, S. D. Sharples, R. J. Smith, M. Clark, and M. G. Somekh, "Determination of crystallographic orientation of large grain metals with surface acoustic waves," *Journal of Acoustical Society of America,* vol. 132, pp. 738-45, Aug.2012.

[49] R. J. Smith, W. Li, J. Coulson, M. Clark, S. M. G., and S. D. Sharples, "Spatially resolved acoustic spectroscopy for rapid imaging of material microstructure and grain orientation," *Measurement Science and Technology,* vol. 25, 2014.

[50] W. Li, J. Coulson, J. W. Aveson, R. J. Smith, M. Clark, M. G. Somekh*, et al.*, "Orientation characterisation of aerospace materials by spatially resolved acoustic spectroscopy - IOPscience," *Journal of Physics: Conference Series,* vol. 520, 2014.

[51] S. D. Sharples, M. Clark, W. Li, and M. G. Somekh, "Rapid imaging of microstructure using spatially resolved acoustic spectroscopy," in *1st International Symposium on Laser Ultrasonics: Science, Technology and Applications* Montreal, Canada, 2008.

[52] M. Spies, "Modeling of transducer fields in inhomogeneous anisotropic materials using Gaussian beam superposition," *NDT & E International,* vol. 33, pp. 155–162, Apr.2000.

[53] N. Gengembre, "Pencil method for ultrasonic beam computation," in *WCU*, Paris, 2003, pp. 1533-1536.

[54] J. A. Ogilvy, "Ultrasonic beam profiles and beam propagation in an austenitic weld using a theoretical ray tracing model," *Ultrasonics,* vol. 24, pp. 337–347, Nov. 1986.

[55] A. T. G. Harvey, C. Carpentier, P. Reynolds, "Finite Element Analysis of Ultrasonic Phased Array Inspections on Anisotropic Welds," in *Review of Progress in Quantitative Nondestructive Evaluation*, 2011, pp. 827-834.

[56] J. Zhang, B. W. Drinkwater, and P. D. Wilcox, "Defect characterization using an ultrasonic array to measure the scattering coefficient matrix," *IEEE Trans Ultrason Ferroelectr Freq Control,* vol. 55, pp. 2254-2265, 2008.

[57] K. M. M. Tant, A. J. Mulholland, and A. Gachagan, "A model-based approach to crack sizing with ultrasonic arrays," *IEEE Trans Ultrason Ferroelectr Freq Control,* vol. 62, pp. 915-926, May 2015.

[58] J. C. Aldrin, "Overview of Mathematical Modeling in Nondestructive Evaluation (NDE)," *Nondestructive Testing Information Analysis Center,* Austin, 2002.

[59] W. Choi, E. Skelton, M. J. Lowe, and R. V. Craster, "Development of efficient hybrid finite element modelling for simulation of ultrasonic Non-Destructive Evaluation," in *11th European Conference on Non-Destructive Testing*, 2014.

[60] Available: http://www.simposium.eu/

[61] Huthwaite, "Accelerated finite element elastodynamic simulations using the GPU," *Journal of Computational Physics,* vol. 257, pp. 687–707, 2014.

[62] S. W. Flax and M. O'Donnell, "Phase-aberration correction using signals from point reflectors and diffuse scatterers: basic principles," *IEEE Trans Ultrason Ferroelectr Freq Control,* vol. 35, pp. 758-67, 1988.

[63] M. O'Donnell and S. W. Flax, "Phase-aberration correction using signals from point reflectors and diffuse scatterers: measurements," *IEEE Trans Ultrason Ferroelectr Freq Control,* vol. 35, pp. 768-74, 1988.

[64] B. Beardsley, M. Peterson, and J. D. Achenbach, "A simple scheme for self-focusing of an array," *Journal of Nondestructive Evaluation,* vol. 14, pp. 169-179, Dec. 1995.

[65] K. W. Rigby, "Beamforming time delay correction for a multi-element array ultrasonic scanner using beamsum-channel correlation," U.S. Patent 5388461 A, 1994.

[66] L. Nock, G. E. Trahey, and S. W. Smith, "Phase aberration correction in medical ultrasound using speckle brightness as a quality factor," *Journal of Acoustical Society of America,* vol. 85, pp. 1819-33, May 1989.

[67] M. Karaman, A. Atalar, H. Koymen, and M. O'Donnell, "A phase aberration correction method for ultrasound imaging," *IEEE Trans Ultrason Ferroelectr Freq Control,* vol. 40, pp. 275-82, 1993.

[68] M. Fink and C. Dorme, "Phase aberration correction with ultrasonic time reversal mirrors," in *IEEE International Ultrasonics Symposium (IUS)*, 1994.

[69] C. Prada, E. Kerbrat, D. Cassereau, and M. Fink, "Time reversal techniques in ultrasonic nondestructive testing of scattering media," *Inverse Problems,* vol. 18, pp. 1761-1773, 2002.

[70] M. Fink, "Time reversal of ultrasonic fields. I. Basic principles," *IEEE Trans Ultrason Ferroelectr Freq Control,* vol. 39, pp. 5555-66, 1992.

[71] N. Chakroun, M. A. Fink, and F. Wu, "Time reversal processing in ultrasonic nondestructive testing," *IEEE Trans Ultrason Ferroelectr Freq Control,* vol. 42, pp. 1087-1098, 1995.

[72] G. D. Connolly, M. J. S. Lowe, J. A. G. Temple, and S. I. Rokhlin, "Correction of ultrasonic array images to improve reflector sizing and location in inhomogeneous materials using a ray-tracing model," *Journal of Acoustical Society of America,* 2010.

[73] O. Nowers, D. J. Duxbury, J. Zhang, and B. W. Drinkwater, "Novel ray-tracing algorithms in NDE: Application of Dijkstra and A* algorithms to the inspection of an anisotropic weld," *NDT & E International,* vol. 61, 2014.

[74] A. Apfel, J. Moysan, G. Corneloup, and B. Chassignole, "Simulations of the influence of the grain orientations on ultrasounds," in *16th WCNDT*, Montreal, Canada, 2004.

[75] Z. Fan and M. J. S. Lowe, "Investigation of ultrasonic array measurements to refine weld maps of austenitic steel welds," in *Review of Progress in Quantitative Nondestructive Evaluation*, 2012.

[76] J. Zhang, A. Hunter, B. W. Drinkwater, and P. D. Wilcox, "Monte Carlo inversion of ultrasonic array data to map anisotropic weld properties," *IEEE Trans Ultrason Ferroelectr Freq Control,* vol. 59, pp. 2487-97, Nov. 2012.

[77] A. Apfel, J. Moysan, G. Corneloup, T. Fouquet, and B. Chassignole, "Coupling an ultrasonic propagation code with a model of the heterogeneity of multipass welds to simulate ultrasonic testing," *Ultrasonics,* vol. 43, pp. 447-56, May 2005.

[78] C. Carpentier, C. Nageswaran, and Y. Y. Tse, "Evaluation of a new approach for the inspection of austenitic dissimilar welds using ultrasonic phased array techniques," in *ECNDT*, 2010.

[79] C. Nageswaran, C. Carpentier, and Y. Y. Tse, "Microstructural quantification, modeling and array ultrasonics to improve the inspection of austenitic welds," *Insight,* vol. 51, Dec. 2008.

[80] C. Nageswaran, C. Carpentier, and Y. Y. Tse, "Improving phased array ultrasonic testing using models to overcome austenitic weld distortion," in *JRC-NDE*, 2009.

[81] J. Camacho and C. Fritsch, "Phase coherence imaging of grained materials," *IEEE Trans Ultrason Ferroelectr Freq Control,* vol. 58, pp. 1006-1015, May 2011.

[82] P. M. Shankar, "Speckle reduction in ultrasound B-scans using weighted averaging in spatial compounding," *IEEE Trans Ultrason Ferroelectr Freq Control,* vol. 33, pp. 754-758, Nov. 1986.

[83] J. E. Wilhjelm, M. S. Jensen, S. K. Jespersen, B. Sahl, and E. Falk, "Visual and quantitative evaluation of selected image combination schemes in ultrasound spatial compound scanning," *IEEE Trans Med Imaging,* vol. 23, pp. 181-90, February 2004.

[84] M. Li and G. Hayward, "Ultrasound nondestructive evaluation (NDE) imaging with transducer arrays and adaptive processing," *Sensors,* vol. 12, pp. 42-54, Jan. 2012.

[85] C. H. Seo and J. T. Yen, "Sidelobe suppression in ultrasound imaging using dual apodization with cross-correlation," *IEEE Trans Ultrason Ferroelectr Freq Control,* vol. 55, pp. 2198-210, Oct. 2008.

[86] J. Shin and J. Yen, "Synergistic enhancements of ultrasound image contrast with a combination of phase aberration correction and dual apodization with cross-correlation," *IEEE Trans Ultrason Ferroelectr Freq Control,* vol. 59, pp. 2089-2101, Sep. 2012.

[87] G. Lind, "Reduction of Radar Tracking Errors with Frequency Agility," *IEEE Trans Aerospa and Electro Systems,* vol. AES-4, pp. 410-416, May 1968.

[88] L. L. Foldy, "The Multiple Scattering of Waves. I. General Theory of Isotropic Scattering by Randomly Distributed Scatterers," *Physical Review,* vol. 67, pp. 107-119, Feb. 1945.

[89] F. J. Margetan, R. B. Thompson, and I. Yalda-Mooshabad, "Modeling Ultrasonic Microstructural Noise in Titanium Alloys," in *Review of Progress in Quantitative Nondestructive Evaluation*, 1993, pp. 1735-1742.

[90] P. Rubbers, "An overview of Split Spectrum Processing," *NDT.net*, vol. 8, 2003.

[91] N. M. Bilgutay, R. Murthy, and K. Kaya, "Medical image enhancement using split spectrum processing," in *IEEE Ultrasonics Symposium (IUS)*, 1993, pp. 993-997.

[92] P. Karpur, P. M. Shankar, J. L. Rose, and V. L. Newhouse, "Split spectrum processing: Determination of the available bandwidth for spectral splitting," *Ultrasonics*, vol. 26, pp. 204–209, Jul. 1988.

[93] K. K. Yau, "Split-Spectrum Processing for Nondestructive Testing," *NDT.net*, vol. 2, no.8, 1997.

[94] A. Rodriguez, R. Miralles, I. Bosch, and L. Vergara, "New analysis and extensions of split-spectrum processing algorithms," *NDT & E International,* vol. 45, pp. 141–147, Jan. 2012.

[95] M. G. Gustafsson and T. Stepinski, "Split spectrum algorithms rely on instantaneous phase information-a geometrical approach (US NDE)," *IEEE Trans Ultrason Ferroelectr Freq Control,* vol. 40, pp. 659-665, Nov. 1993.

[96]   X. Li, N. M. Bilgutay, and J. Saniie, "Frequency diverse statistic filtering for clutter suppression," in *International Conference on Acoustics, Speech, and Signal Processing*, 1989, pp. 1349-1352.

[97]   G. E. Trahey, J. W. Allison, S. W. Smith, and O. T. von Ramm, "A quantitative approach to speckle reduction via frequency compounding," *Ultrasonic Imaging,* vol. 8, pp. 151-64, Jul. 1986.

[98]   J. R. Sanchez and M. L. Oelze, "An ultrasonic imaging speckle-suppression and contrast-enhancement technique by means of frequency compounding and coded excitation," *IEEE Trans Ultrason Ferroelectr Freq Control,* vol. 56, pp. 1327-1339, Jul. 2009.

[99]   R. G. Dantas and E. T. Costa, "Ultrasound speckle reduction using modified Gabor filters," *IEEE Trans Ultrason Ferroelectr Freq Control,* vol. 54, pp. 530-538, Mar. 2007.

[100]   Q. Tian and N. M. Bilgutay, "Statistical analysis of split spectrum processing for multiple target detection," *IEEE Trans Ultrason Ferroelectr Freq Control,* vol. 45, pp. 251-256, Jan. 1998.

[101]   P. Karpur, P. M. Shankar, J. L. Rose, and V. L. Newhouse, "Split spectrum processing: optimizing the processing parameters using minimization," *Ultrasonics,* vol. 25, pp. 204–208, Jul. 1987.

[102]   H. C. Sun and J. Saniie, "Nonlinear signal processing for ultrasonic target detection," in *IEEE Ultrasonics Symposium*, 1998, pp. 855-858.

[103]   Z. Liu, M. Lu, and M. Wei, "Structure noise reduction of ultrasonic signals using artificial neural network adaptive filtering," *Ultrasonics,* vol. 35, pp. 325–328, Jun. 1997.

[104]   G. Rui, L. Minghui, T. Lardner, and A. Gachagan, "Robust defect detection in ultrasonic nondestructive evaluation (NDE) of difficult materials," in *IEEE International Ultrasonics Symposium (IUS)*, 2012, pp. 467-470.

[105]   S. H. C. Ortiz, T. Chiu, and M. D. Fox, "Ultrasound image enhancement: A review," *Biomedical Signal Processing and Control,* vol. 7, pp. 419–428, Sep. 2012.

[106]   R. F. Wagner, S. W. Smith, J. M. Sandrik, and H. Lopez, "Statistics of Speckle in Ultrasound B-Scans," *IEEE Trans Sonics and Ultrason,* vol. 30, pp. 156-163, May 1983.

[107]   V. M. Narayanan, P. M. Shankar, and J. M. Reid, "Non-Rayleigh statistics of ultrasonic backscattered signals," *IEEE Trans Ultrason Ferroelectr Freq Control,* vol. 41, pp. 845-52, 1994.

[108]   P. M. Shankar, "A general statistical model for ultrasonic backscattering from tissues," *IEEE Trans Ultrason Ferroelectr Freq Control,* vol. 47, pp. 727-736, May 2000.

[109]   O. V. Michailovich and D. Adam, "A novel approach to the 2-D blind deconvolution problem in medical ultrasound," *IEEE Trans Med Imaging,* vol. 24, pp. 86-104, Jan. 2005.

[110]   T. Taxt, "Comparison of cepstrum based methods for radial blind deconvolution of ultrasound images," in *Computer-Based Medical Systems*, 1996, pp. 59-64.

[111]   J. S. Lee, "Digital image enhancement and noise filtering by use of local statistics," *IEEE Trans Pattern Anal Mach Intell,* vol. 2, pp. 165-168, 1980.

[112] Y. Chen, R. Yin, P. Flynn, and S. Broschat, "Aggressive region growing filtering for speckle reduction in ultrasound images," *Journal of The Acoustical Society of America,* vol. 103, 1998.

[113] S. Song and P. Que, "Wavelet based noise suppression technique and its application to ultrasonic flaw detection," *Ultrasonics,* vol. 44, pp. 188–193, Feb. 2006.

[114] G. Cincotti, G. Loi, and M. Pappalardo, "Frequency decomposition and compounding of ultrasound medical images with wavelet packets," *IEEE Trans Med Imaging,* vol. 20, pp. 764-71, Aug. 2001.

[115] S. H. Kay, *Fundamentals of Statistical Signal Processing: Estimation Theory v. 1 (Prentice Hall Signal Processing Series)*: Prentice Hall, 1993.

[116] P. Ganesan, G. D. Smith, and D. H. Yates, "Performance of Inconel Alloy 617 in Actual and Simulated Gas Turbine Environments," *Material and Manufacturing Process,* vol. 10, 1995.

[117] E. Menthe, A. Bulak, and J. Olfe, "Improvement of the mechanical properties of austenitic stainless steel after plasma nitriding," *Surface and Coatings Technology,* vol. 133–134, pp. 259–263, Nov. 2000.

[118] TWI Ltd., "Guidelines for generating array ultrasonic procedures for the inspection of dissimilar/austenitic welded components," 25 Jan. 2011.

[119] M. G. Gustafsson and T. Stepinski, "Studies of split spectrum processing, optimal detection, and maximum likelihood amplitude estimation using a simple clutter model," *Ultrasonics,* vol. 35, pp. 31–52, Feb. 1997.

[120] C. M. Bishop, "Neural networks and their applications," *Review of Scientific Instruments,* vol. 65, pp. 1803-1832, Jun. 1994.

[121] I. V. Tetko, D. J. Livingstone, and A. I. Luik, "Neural network studies. 1. Comparison of overfitting and overtraining," *Journal of Chemical Information and Modeling,* vol. 35, pp. 826-833, Sep. 1995.

[122] T. Xie, H. Yu, and B. Wilamowski, "Comparison between traditional neural networks and radial basis function networks," in *IEEE International Symposium on Industrial Electronics (ISIE)*, 2011, pp. 1194-1199.

[123] P. Courrieu, "Fast computation of moore-penrose inverse matrices," *Neural Information Processing - Letters and Reviews,* vol. 8, pp. 25-29, Aug. 2005.

[124] A. K. Jain, *Fundamentals of digital image processing.* vol. 3: Englewood Cliffs: prentice-Hall, 1989.

[125] P. Ramuhalli, M. S. Good, and *et al.*, "PNNL: Publication DetailsUltrasonic Characterization of Cast Austenitic Stainless Steel Microstructure: Discrimination between Equiaxed- and Columnar-Grain Material – An Interim Study," Pacific Northwest National Laboratory, Richland, WA2009.

[126] *pdist-pairwise distance between pairs of objects*. Available: http://uk.mathworks.com/help/stats/pdist.html